The Relationship Between Type Ia Supernovae and Their Host Galaxies

Yen-Chen Pan

Oriel College

University of Oxford

A thesis submitted for the degree of

Doctor of Philosophy

Trinity 2014

The Relationship Between Type Ia Supernovae and Their Host Galaxies

Yen-Chen Pan
Oriel College

A thesis submitted for the degree of Doctor of Philosophy
Trinity 2014

Abstract

This thesis studies the relationship between type Ia supernovae (SNe Ia) and their host galaxies. The sample consists of 527 SNe Ia with redshift $z < 0.09$ discovered by the Palomar Transient Factory (PTF). We obtained high-quality photometric and spectroscopic data of the host galaxies and determined their stellar mass ($M_{\rm stellar}$), star formation rate (SFR), gas-phase/stellar metallicity, stellar age and SN offset.

In the first part of the analysis, we compare the SN Ia photometric properties to the host parameters. Strong correlations between the SN Ia light-curve width (stretch) and the host age/mass/metallicity are found: fainter, faster-declining events tend to be hosted by older/massive/metal-rich galaxies. There is also some evidence that redder SNe Ia explode in higher metallicity galaxies. SNe Ia in higher-mass/metallicity galaxies also appear brighter after stretch/colour corrections than their counterparts in lower mass hosts, and the stronger correlation is with gas-phase metallicity suggesting this may be the more important variable. We also compare the host stellar mass distribution to that in galaxy targeted SN surveys and the high-redshift untargeted Supernova Legacy Survey (SNLS). The difference between each stellar mass distribution can be explained by an evolution in the galaxy stellar mass function, coupled with a SN delay-time distribution proportional to t^{-1}. Finally, we found no significant difference in the mass–metallicity relation of our SN Ia hosts compared to field galaxies, suggesting any metallicity effect on the SN Ia rate is small.

In the second part of the analysis, we compare the SN spectral features to the host parameters. We find that SNe Ia with higher Si II λ6355 velocities tend to explode in more massive galaxies. We study the strength of the high-velocity component of the Ca II NIR absorption, and find that SNe Ia with a stronger high-velocity component are preferentially hosted by galaxies with a low $M_{\rm stellar}$, a blue colour, and a high SFR, and are therefore likely to arise from the youngest progenitor systems. When combined with other studies, our results support the scenario that these high-velocity features are related to an interaction between the SN ejecta and a circumstellar medium (CSM) local to the SN.

Declaration

I declare that no part of this thesis has been accepted or submitted for any degree or diploma or other qualification at any other university. This thesis is the result of my own work unless otherwise stated below.

The measurement of SN photometry was done by Mark Sullivan and Kate Maguire. The SN spectral fitting code was written by Mark Sullivan. The measurement of SN spectral features was done in collaboration with Kate Maguire.

The material in Chapter 2, 3 and 4 was published in the paper *"The host galaxies of Type Ia supernovae discovered by the Palomar Transient Factory"*, Pan Y.-C. et al., 2014, MNRAS, 438, 1391. The material in Chapter 5 and 6 will appear in the paper *"Type Ia Supernova Spectral Features in the Context of Their Host Galaxy Properties"*, to be submitted to MNRAS.

Yen-Chen Pan
June 2014

Acknowledgements

I am enormously grateful to both my supervisor Mark Sullivan and Isobel Hook. Thanks Mark for nearly four years of inexhaustible guidance and tutoring. You taught me how to do good science and show me what a good scientist should look like. Without you I would not be able to finish this thesis. I am fortunate to have you as my supervisor during the time in Oxford. Thanks Isobel for your further professional advice and suggestion. These supports are invaluable to me. Thanks both of you for spending time on reading this thesis and making it better. Thanks Kate Maguire for all the helpful advice on my research and sharing valuable observing skills with me. I enjoy the time we observed at WHT.

Thanks my great friends Josh, Eric, Wilson, Yun-Ju, Tao-Hsin and Fu-lien. I really enjoy the time I spent in Oxford with you guys. They are wonderful memories to me. I would like to give particular thank you to Josh Ko, who leads me to the world of Macintosh. Thanks for sharing useful computing skills and knowledges.

Finally, I would like to give a huge thank you to my parents, Chien-Yu and all my family members in Taiwan for your strong support. It is great to have your back and let me focus on my own research.

Contents

List of Figures

List of Tables

Chapter 1

Introduction

Type Ia supernovae (SNe Ia) are remarkable cosmological standardisable candles that can be used to measure cosmological parameters. Their extremely bright luminosities are found to be systematically correlated with their light curve parameters, such as light curve width and SN colour. These correlations allow them to be standardised, making them extraordinary tools in probing the cosmic expansion. The universe was found to expand with an accelerating speed by using distant SNe Ia, and they provide importance evidence of the existence of dark energy.

SNe Ia are believed to be the result of the thermonuclear explosion of an accreting carbon-oxygen white dwarf star in a close binary system. Recent studies have constrained the size of the primary star to be consistent with a compact object. However, the nature of the companion star that donates material is not yet clear. The various possibilities include the classical single degenerate and double degenerate scenarios, or more variations on these themes. This limited understanding of the SN Ia progenitor systems may ultimately provide a limit in their cosmological use — and as SN surveys become increasingly more precise, reducing the systematic uncertainties becomes the most important issue in improving SN distance estimates.

This thesis concerns the astrophysical effects of host galaxies on SN properties.

SN Ia host galaxies have long been a useful tool to probe the progenitor system. By studying the global properties of the host environment of SNe Ia, we can place constraints on the SN progenitors. In this work, we will investigate the relations between SN photometric/spectroscopic properties and their host galaxies. In the following sections, we will introduce the SN Ia astrophysics and their recent development, and the problems we would like to address in this thesis.

1.1 SN classification

Supernovae are classified mainly based on their spectra and light curves. Minkowski (1941) introduced two classes of supernova, Type I and II, based on their optical spectra. Type I SNe are defined by the absence of hydrogen signature in their optical spectra (except for the contamination from the host galaxies), whereas the Type II supernovae present prominent hydrogen in their spectra. A subset of Type I supernovae showing a deep absorption trough around 6150 Å in their early-time and maximum-light spectra are further classified as Type Ia supernovae (Wheeler & Harkness, 1990). The rest of the Type I supernovae are subdivided into two subclasses, Type Ib and Type Ic, depending on the presence or absence of He I lines, respectively. They are believed to be related to core-collapse supernovae but with their hydrogen envelope or both hydrogen and helium envelopes being stripped away.

Type II supernovae are typically divided into four types. Type IIP supernovae show a plateau phase with an extremely slow decline rate on their optical light curves after the maximum light. By contrast, Type IIL supernovae show a steep and linear decline in their light curves after maximum light. Type IIb supernovae are a mixture of Type Ib and II supernovae in the sense that they are similar to Type II (with hydrogen lines) in the early-time spectra, but show signatures of Type Ib (with helium lines) in their late-time spectra. Type IIn supernovae feature the presence of narrow

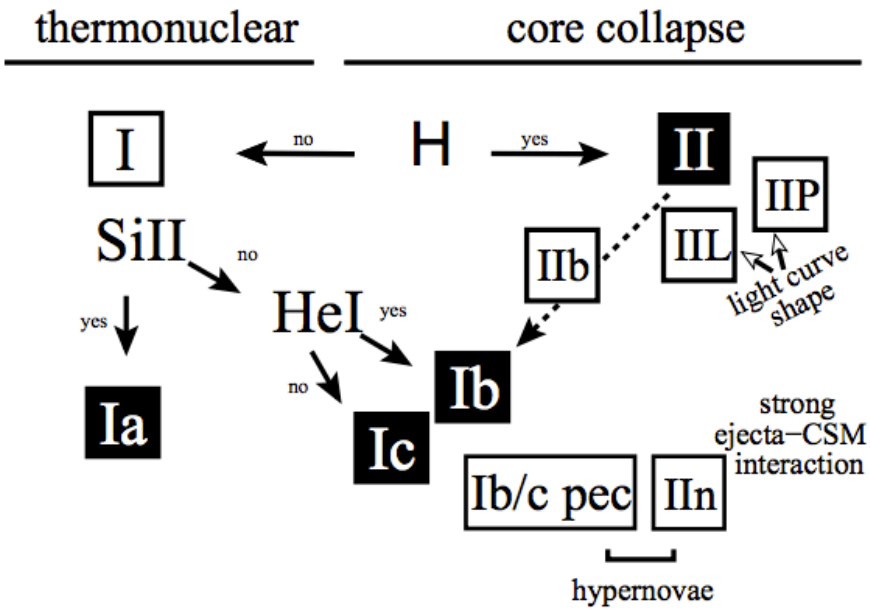

Figure 1.1: The SN classification scheme (taken from Turatto, 2003).

emission lines in their spectra. Their spectra are dominated by strong Balmer emission lines without broad absorptions. A supernova classification scheme can be found in Fig. 1.1. A review of supernova classification can be found in Filippenko (1997) and Turatto (2003).

1.2 SN light curves and spectra

Most SNe Ia show remarkable homogeneity in their light curves and spectra. The observed SN luminosity is mainly powered by the radioactive decay, from ^{56}Ni, which is the dominant product synthesised during the thermonuclear process, to ^{56}Co, and then to the stable ^{56}Fe, with exponential time scale of 9 d and 114 d, respectively (Colgate & McKee, 1969; Maoz et al., 2013). The SN peak bolometric luminosity is approximately equal to the energy deposited by the radioactive decay, and is correlated with the mass of ^{56}Ni by Arnett's Rule (Arnett, 1979, 1982). The light curve rises to maximum in about 2–3 weeks, declines about 3 mag in the first month, and then drops ∼1 mag per month afterwards. The SN Ia peak luminosities also show

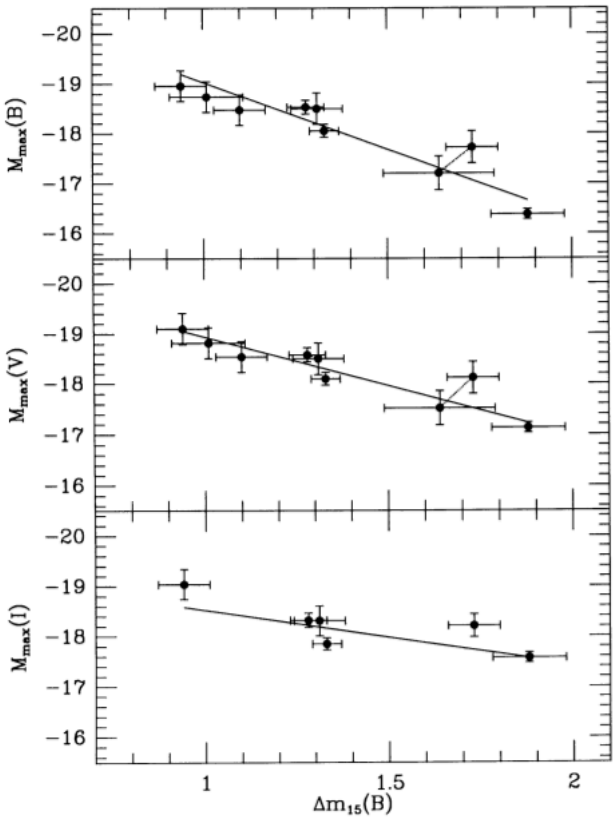

Figure 1.2: The SN Ia peak luminosity as a function of light curve decline rate measured as Δm_{15}, which represents the amount of magnitudes that the B-band light curve drops 15 days after maximum light taken from (Phillips, 1993).

a tight relation with the light curve width, the so-called width-luminosity relation (WLR; Phillips, 1993; Phillips et al., 1999). Brighter SNe Ia generally have broader light curves and slower decline rate than their fainter counterparts (see Fig. 1.2). The origin of the WLR is believed to be connected to the amount of ^{56}Ni synthesised during the thermonuclear process. Brighter SNe Ia have a higher ^{56}Ni mass and therefore have a higher temperature. The higher temperature will lead to a higher opacity and longer diffusion time, and causes broader light curves (Hoeflich et al., 1996).

The early-time spectra of SNe Ia are dominated by P Cygni profiles of singly-ionized intermediate-mass elements such as Si II, S II, Ca II and Mg II, and some iron-peak elements (i.e. Fe and Co) at near-UV wavelengths (Filippenko, 1997). The Si II λ6355 line is the strongest and most remarkable feature in the early-time spectra.

At late-time phases (∼1 month after the maximum light), as the SN photosphere recedes into the ejecta, the envelope becomes more transparent, and the spectra are dominated by the emission lines of iron-group elements (e.g., [Fe II], [Fe III] and [Co II]), entering the so-called 'nebular phase'.

Despite the fact that the majority of SNe Ia show great homogeneity in their peak luminosities and spectral properties (Branch & Tammann, 1992), there is a fraction of peculiar SNe Ia which present more heterogeneous properties (Li et al., 2000). The most famous of its kind is SN 1991bg (Filippenko et al., 1992a; Leibundgut et al., 1993; Turatto et al., 1996). Compared to normal SNe Ia, 91bg-like objects are subluminous, with a light curve decline that is unusually fast. They are also redder than normal SNe Ia. Their spectra at maximum light are characterised by a deep trough at $\sim 4200\,\text{Å}$ (produced by the Ti II line), together with other intermediate-mass elements. The expansion velocity ($\sim 10,000\,\mathrm{km\,s^{-1}}$) is slightly lower than normal SNe Ia ($11,000 - 13,000\,\mathrm{km\,s^{-1}}$). By contrast, objects like SN 1991T represent another subclass of peculiar SNe Ia (Filippenko et al., 1992b; Phillips et al., 1992). 91T-like SNe Ia are brighter and more energetic than normal SNe Ia, and show a broader light curve with a slower decline rate. Unlike normal SNe Ia, the pre-maximum light curve of SN 1991T did not show Si II or Ca II lines, instead, they were dominated by iron-group elements. However, the spectra start to resemble that of normal SNe Ia a few months after maximum light.

1.3 Progenitor system

Despite a good empirical understanding of SN Ia light curves and spectra, the nature of the progenitor system is still an open question. The proposed progenitor model should be able to pass all the observational constraints discussed in Section 1.2. For a review of SN Ia progenitor systems, see Hillebrandt & Niemeyer (2000), Maoz et al.

(2013) and Hillebrandt et al. (2013). Below we briefly summarise recent developments.

SNe Ia are believed to be triggered from the thermonuclear burning in a degenerate stellar core (Hoyle & Fowler, 1960). Given the fact that hydrogen and helium are absent in their spectra, and their occurrence in both young and old stellar populations, they are most likely the disruption of white dwarfs (WD) with a carbon-oxygen (C+O) core. This is also supported by the recent observations of SN 2011fe, a SN Ia exploding in nearby M101, which constrained the size of the primary star to be consistent with the compact object (Nugent et al., 2011; Bloom et al., 2012a). The unstable thermonuclear runaway can be explained by the physical nature of degenerate gas. When the degenerate gas is heated, it does not expand and cool like normal gas, and the nuclear reaction rates steeply depend on the temperature. An explosion burning front is produced as the carbon core of the WD is ignited and destroys the WD. The increase of temperature and pressure is generally associated with the accumulation of accreted mass on the WD. The carbon will be ignited in a non-rotating C+O WD when the WD mass approaches the Chandrasekhar mass $M_{ch} \sim 1.4\,M_{\odot}$ (Arnett, 1969).

However, a typical C+O white dwarf has a mass around 0.6 $M_{\odot}$ (Homeier et al., 1998). Binary evolution is therefore a necessary channel for the WD to accumulate the mass and reach a total mass $\sim M_{ch}$. This can be achieved by either the accretion from a non-degenerate star; the so-called the single-degenerate model (SD; Whelan & Iben, 1973), or by the merging of two WDs, the so-called double-degenerate model (DD; Iben & Tutukov, 1984; Webbink, 1984).

In the single-degenerate scenario, the companion star can be a main sequence, subgiant, helium or red giant star. We illustrate a possible evolutionary path of the single-degenerate model in the left panel of Fig. 1.3. In this simplified picture, two main-sequence stars with different masses are considered in a binary system. The more massive star (denoted as the primary star) in the binary system will evolve to a

AGB star with a degenerate carbon-oxgen core prior to the less-massive star (denoted as the secondary star). A common-envelope forms if the system is wide enough for the Roche-lobe overflow to occur. During the common-envelope evolution, the separation of the binary system shrinks considerably and the common-envelope is ejected. After the outflow of the common-envelope, the carbon-oxygen WD core of the primary star remains, and the secondary star has evolved to a red-giant star and fills its Roche-lobe. Mass transfer begins between the WD and the secondary star. The WD accretes matter on its C+O core from the secondary star until its mass approaches $\sim M_{ch}$ and explodes as a SN Ia. However, the challenge of this picture is that to get the accreting WD to actually grow in mass needs a very small range in mass accretion rate ($\sim$ a factor of three) to allow the stable nuclear burning of hydrogen to helium on WD. There exists a class of binary systems which have been identified as promising candidates, the so-called supersoft X-ray sources, which present such accretion rate that can burn the hydrogen steadily (van den Heuvel et al., 1992; Kahabka & Ergma, 1997). At low accretion rate, the WD may undergo nova eruptions and lose more mass by the outburst than the mass accreted on it (Nomoto, 1982). At very high accretion rates, it could form a red giant-like envelope around the WD and stop the growth of mass on WD (Nomoto et al., 1979). Alternatively, the donor could be a helium star, which accreted a helium layer on the WD. The possible detonations in the helium layer will drive a strong shock into the C+O core and trigger a secondary carbon detonation (Woosley & Weaver, 1994). This channel is related to some sub-Chandrasekhar models.

Compared to the single-degenerate scenario, the double-degenerate scenario has the advantage that it naturally explains the lack of hydrogen in the SN Ia spectra. We illustrate the simplified evolutionary path of double-degenerate scenario in the right panel of Fig. 1.3. The initial evolution is similar to single-degenerate scenario considering two main-sequence stars with difference masses in the binary system.

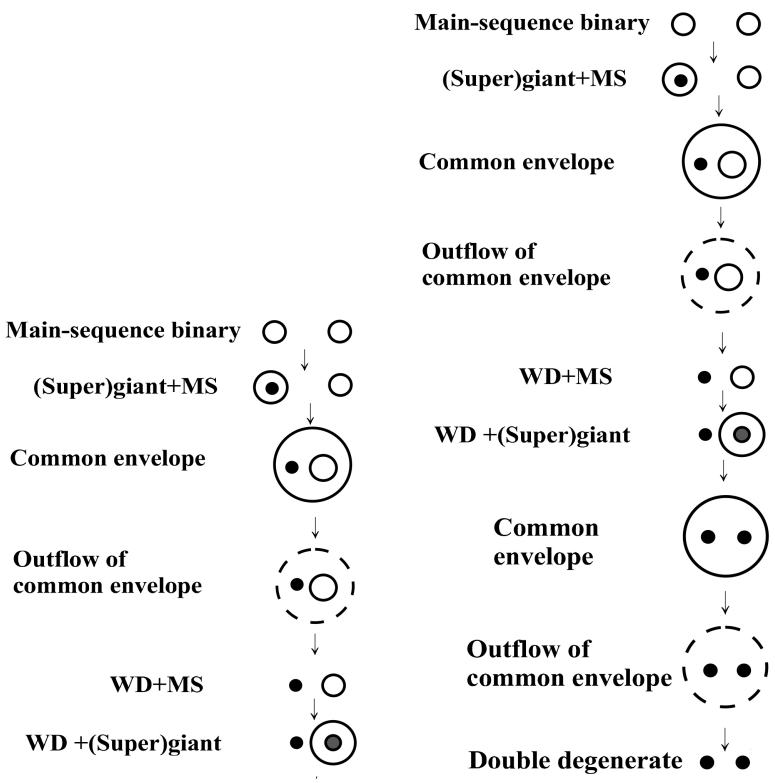

Figure 1.3: Illustration of binary evolution for single-degenerate (left) and double-degenerate (right) channels of SNe Ia (Yungelson, 2005).

However, the double-degenerate scenario is thought to experience a second common-envelope evolution due to the evolution of the secondary star to become a AGB star with a degenerate carbon-oxygen core. In this picture, the secondary star also evolves to a carbon-oxygen WD, and the separation of the two WDs shrinks by dissipating the gravitational wave radiation. When the total mass of two C+O WDs exceeds the M_{ch}, the more massive WD is thought to tidally disrupt and accrete the lower-mass WD. However, the challenge of this picture is that such a merger was thought to cause the burning in the outer layers instead of central burning. An off-centre carbon ignition will occur and lead to the burning of carbon into O, Ne and Mg. For WDs with such a composition, this will result in gravitational instability due to the electron capture on Mg and Ne, and cause an accretion-induced collapse that will change the WD into a neutron star (Nomoto & Iben, 1985).

There is a varying degree of evidence supporting both the single-degenerate scenario (e.g., Sternberg et al., 2011; Dilday et al., 2012) and the double-degenerate scenario (e.g., Schaefer & Pagnotta, 2012). This observational evidence implies that the SNe Ia may not be a result of a single channel. With more precise studies, SNe Ia were found to show quite diverse properties (e.g., with respect to their host environment). A multi-channel scenario may be necessary to explain the observed diversity of SNe Ia.

1.4 Cosmological use

The most profound implication of SN Ia study is its use in measuring the cosmological parameters. Studies of SNe Ia revealed that the universe is expanding with an accelerating speed (Riess et al., 1998; Perlmutter et al., 1999; Riess et al., 2007; Kessler et al., 2009; Sullivan et al., 2011b; Suzuki et al., 2012; Rest et al., 2013; Betoule et al., 2014). This has provided evidence of the existence of 'dark energy' (Huterer & Turner, 1999).

Despite the fact that SNe Ia are not perfect standard candles (Branch & Tammann, 1992), they can be standardised via the tight correlation between SN Ia light curve width and luminosity (Phillips, 1993) and between SN Ia optical colour and luminosity (Riess et al., 1996; Tripp, 1998). Brighter SNe Ia tend to have broader, slower evolving light curves and are bluer than fainter SNe Ia. When these empirical relations are applied to the SN Ia datasets, the scatter of peak luminosity can be reduced to $\sim 0.15\,\mathrm{mag}$ (Jha et al., 2007; Guy et al., 2007; Conley et al., 2008). Fig. 1.4 shows an example of a Hubble diagram from a recent study (Suzuki et al., 2012). They used very distant SNe Ia discovered by Hubble Space Telescope (HST) Cluster Supernova Survey with a redshift interval $0.6 < z < 1.4$, together with other data compilations ranging from low-z to high-z to constrain the cosmological param-

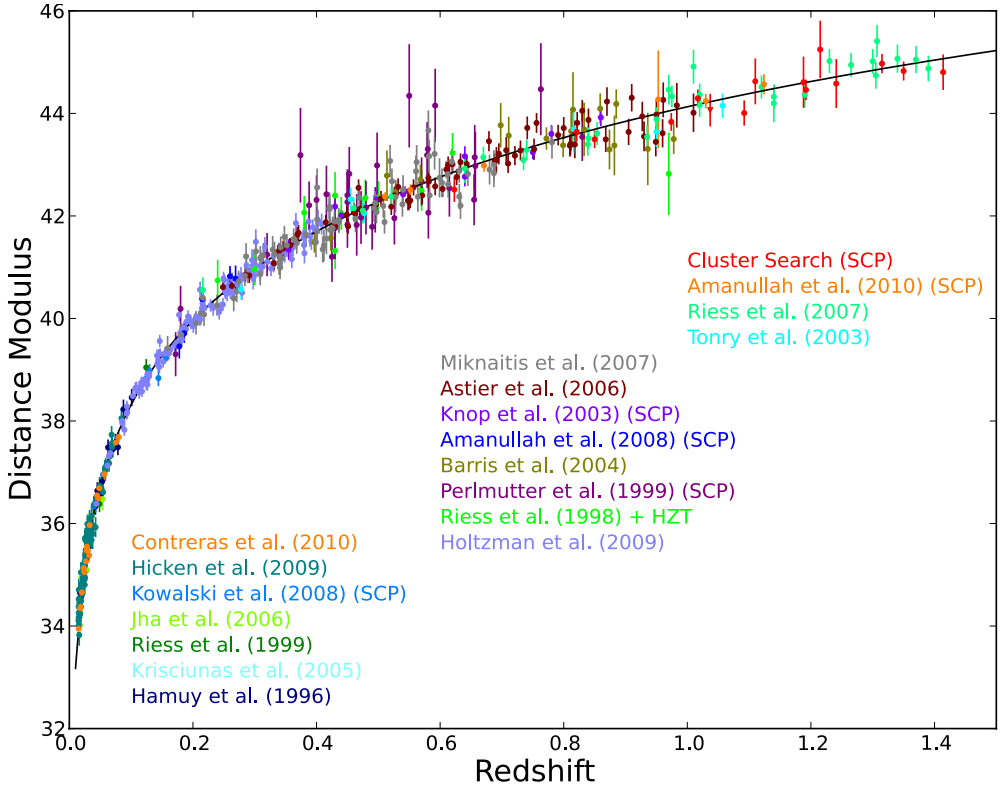

Figure 1.4: The Hubble diagram reproduced from Suzuki et al. (2012). Different data sets of SNe Ia are colour-coded in the plot. The solid line represents the best-fit cosmology for a flat ΛCDM universe. They found the dark energy density $\Omega_\Lambda = 0.729 \pm 0.014$.

eters. They found a matter density $\Omega_m = 0.271 \pm 0.014$ for a flat ΛCDM model and a dark energy equation-of-state $w = -1.013^{+0.068}_{-0.073}$ for a flat wCDM model. A more recent study by Betoule et al. (2014) revealed similar results. They performed a joint analysis of SNe Ia observations obtained by SDSS-II and SNLS (Supernovae Legacy Survey) to constrain the cosmological parameters. They found a matter density $\Omega_m = 0.295 \pm 0.034$ for a flat ΛCDM model and a dark energy equation-of-state $w = -1.027 \pm 0.055$ for a flat wCDM model.

To improve SNe Ia as distance indicators, it is of great importance to reduce the uncertainties in the luminosities. For example, the photometric calibration uncertainties of SN Ia light curves are long known to be the dominant source of systematic error. Recent progress in improving the photometric calibration procedure can be found in Betoule et al. (2013), which applied flat-field corrections to improve the uniformity of different SN Ia surveys when comparing the photometry in overlapping fields. The host environments were also found to play a role in affecting the precision of the SN Ia cosmology. The SN Ia luminosities were found to be systematically correlated with host galaxy properties (e.g., host stellar mass; Sullivan et al., 2010). By directly using the host information in the cosmological fits, the systematic uncertainties introduced by the host environments are reduced (Sullivan et al., 2011b). Understanding these systematic effects will become critical for the future, larger samples (e.g., Dark Energy Survey; Bernstein et al., 2012).

1.5 Host galaxies

In Section 1.3 and 1.4 we have discussed the SN Ia progenitors and the usage of SNe Ia in cosmological studies. We also illustrated the challenges of the current SN Ia studies. Given the diverse behaviours observed in SNe Ia, different approaches are necessary to put constraints on the properties of their progenitors, as there was no di-

rect observation at the time of this work. When it comes to cosmological use, previous studies indicated that the SN Ia luminosities show systematic trends with their host environments, which could therefore introduce a bias in the distance measurement.

Host galaxy study is a useful tool in addressing these problems. Study of the host galaxies and environments of various types of supernovae has long been a profitable route to probe astrophysical effects in the SN population. For example, studying the correlation between core-collapse supernovae and host galaxy star-formation rate (SFR) to constrain the SN progenitors (Anderson & James, 2008; Anderson et al., 2012). The observed properties of SNe Ia are also known to correlate with the physical parameters of their host galaxy stellar populations. For example, SNe Ia in elliptical or passively evolving galaxies are intrinsically fainter than SNe Ia in spiral or star-forming galaxies, and possess narrower, faster evolving (or lower 'stretch') light curves (Hamuy et al., 1995, 1996; Riess et al., 1999; Hamuy et al., 2000; Howell, 2001; Gallagher et al., 2005; Sullivan et al., 2006). Host stellar mass ($M_{\rm stellar}$) was also found to be correlated with SN luminosities (Kelly et al., 2010; Sullivan et al., 2010; Lampeitl et al., 2010). More massive galaxies tend to host intrinsically fainter SNe Ia than low-mass galaxies.

The two primary competing explanations are that either progenitor metallicity or progenitor age (or a combination of both) play a role in controlling SN Ia luminosities – but directly measuring either is extremely difficult. Indirect information can be obtained on metallicity from the ultraviolet (UV) SN spectra (e.g. Hoeflich et al., 1998; Lentz et al., 2000), and while this has provided useful insights into evolution within SN Ia populations (Ellis et al., 2008; Foley et al., 2008; Maguire et al., 2012; Foley et al., 2012a), the interpretation of any individual event is extremely complex even with very high quality data (Mazzali et al., 2013). There is currently no technique to estimate the age of the progenitor star from the SN spectrum.

Thus many studies have instead focused on detailed spectroscopic studies of the

host galaxies of the SNe Ia rather than the events themselves, assembling statistical samples with which to search for correlations between the physical parameters defining the host galaxies, and the SN Ia properties. Such global host galaxy properties are believed to represent reasonable tracers of the SN progenitor star, at least in a statistical sense (Bravo & Badenes, 2011). Common spectroscopic measurements include star formation rates and gas phase metallicity measured from nebular emission lines (Gallagher et al., 2005; D'Andrea et al., 2011; Stanishev et al., 2012; Johansson et al., 2013; Childress et al., 2013a; Rigault et al., 2013; Pan et al., 2014), and stellar metallicity and age measured from individual spectral absorption indices or full spectrum fitting. (Gallagher et al., 2008; Stanishev et al., 2012; Johansson et al., 2013; Pan et al., 2014).

A number of intriguing results have arisen from these studies. Intrinsically fainter SNe Ia (specifically those with faster light curves) are preferentially located in massive/older galaxies than in younger/lower-mass systems. Galaxies with stronger star-formation also tend to host slower, brighter SNe Ia than passive galaxies. From a cosmological perspective, 'corrected' SN Ia luminosities also show a dependence on various parameters correlated with host galaxy stellar mass ($M_{\rm stellar}$) and metallicity, in the sense that brighter SNe Ia tend to be found in massive/metal-rich galaxies. There are also emerging trends that massive, or metal-rich, galaxies host redder SNe Ia. These residual trends between SN luminosity and host galaxy properties can be accounted for at the level required by current cosmological analyses. For example, a correction for the relation between host $M_{\rm stellar}$ and Hubble residuals (e.g., Fig. 1.5) was used in the cosmological fit (Conley et al., 2011; Sullivan et al., 2011b; Suzuki et al., 2012).

SN Ia spectral features are also important in understanding the properties of the progenitor system, providing the only direct tracer of the material in the SN ejecta. Benetti et al. (2005) showed that SNe Ia can be divided into three different

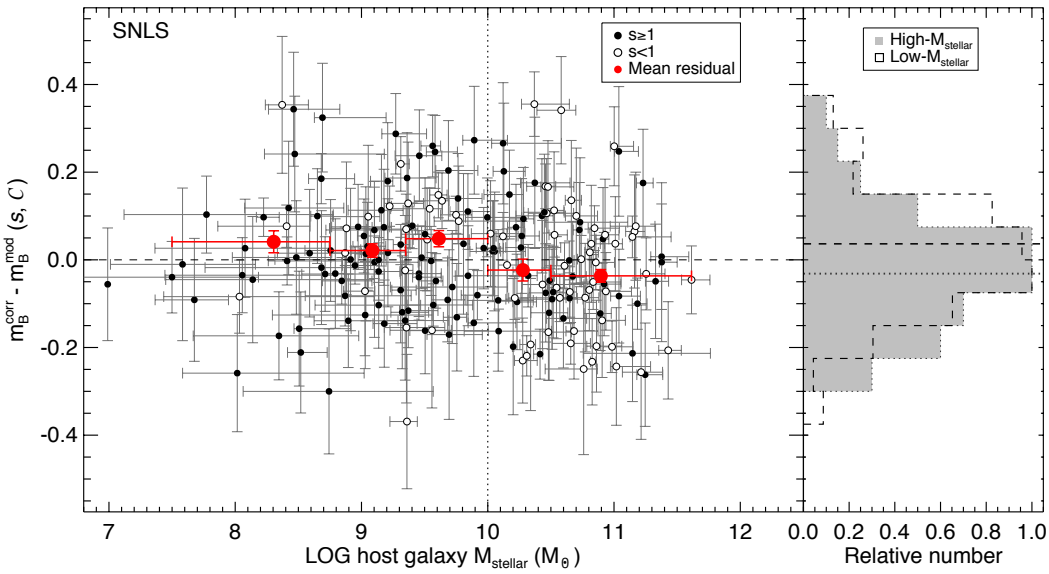

Figure 1.5: The Hubble residuals as a function of host stellar mass ($M_{\rm stellar}$) from Sullivan et al. (2010). Hosts with $s < 1$ (see Section 4.2 for a definition of SN stretch s) are shown as open circles, and those with $s \geq 1$ as filled circles. The red circles are the mean residuals in bins of host $M_{\rm stellar}$. The error bars on these points represent the bin width in $M_{\rm stellar}$, and the weighted error on the mean. The histograms in the right-hand side show the total residuals for SNe Ia in low and high $M_{\rm stellar}$ hosts.

groups according to their spectral properties: A 'FAINT' group, such as SN 1991bg-like events; a 'HVG' group, which present a high velocity gradient in their Si II λ6355 velocity evolution; and a 'LVG' group, which present a low velocity gradient in their Si II λ6355 velocities. Such studies indicate that SNe Ia are not drawn from a one-parameter family from the perspective of their spectral properties. Wang et al. (2009) divided SNe Ia into two groups according to the photospheric velocities measured from Si II λ6355 absorption. They found that SNe Ia with high Si II λ6355 velocities (high-$v_{\rm Si\,II}$; defined as $v_{\rm Si\,II} \geq 12,000\,{\rm km\,s^{-1}}$) have a different extinction law than normal-velocity events (normal-$v_{\rm Si\,II}$; defined as $v_{\rm Si\,II} < 12,000\,{\rm km\,s^{-1}}$). By applying different values of R_V to each group, the dispersion in the corrected SN peak luminosities can be reduced. Many spectral indicators have also been found to correlate with SN luminosity, and can be used for distance estimation (Nugent et al., 1995; Bronder et al., 2008; Bailey et al., 2009; Blondin et al., 2011; Walker et al., 2011; Silverman

et al., 2012a).

However, there are fewer studies addressing the relationship between SN Ia spectral features and their host galaxies. Foley (2012) studied the relation between Ca II H&K velocity and host $M_{\rm stellar}$, and found SNe Ia in massive galaxies have lower Ca II H&K velocities, although Maguire et al. (2012) suggested this could be caused by underlying relations between light-curve width and $M_{\rm stellar}$ (e.g., Sullivan et al., 2010), and between light-curve width and Ca II H&K velocity (see Maguire et al., 2012, Maguire et al. 2014). Wang et al. (2013) found that high-$v_{\rm Si\,II}$ SNe Ia and normal-$v_{\rm Si\,II}$ SNe Ia may originate from different populations with respect to their radial distributions in their host galaxies. High-$v_{\rm Si\,II}$ SNe Ia tend to concentrate in the inner regions of their host galaxies, whereas the normal-$v_{\rm Si\,II}$ SNe Ia span a wider range of radial distance. Their result was interpreted as evidence for the existence of two distinct populations of SNe Ia.

As well as photospheric spectral features, 'high-velocity features' (HVFs) in SN Ia spectra have also been studied (Wang et al., 2003; Gerardy et al., 2004; Mazzali et al., 2005a,b; Childress et al., 2013c, 2014). The physical origin of these HVFs is not yet clear, but it is generally thought to be related to an abundance or density enhancement in the SN ejecta, or interactions between the SN ejecta and a circumstellar medium (CSM) local to the SN. Some interesting properties have been found for these HVFs. For example, Childress et al. (2014) show the strength of the HVFs is connected to the decline rate of the SN light curve: slower declining SNe have stronger HVFs. They also found SNe Ia with stronger HVFs have lower Si II λ6355 photospheric velocities, while the high-$v_{\rm Si\,II}$ SNe Ia discussed above show no distinct HVFs in their maximum-light spectra. HVFs could also provide different angles to investigate the properties of CSM local to the SN. Sternberg et al. (2011) and Maguire et al. (2013a) used the narrow Na I D features as probes for CSM and found the SNe presenting blue-shifted Na I D tend to be found in late-type galaxies. Foley et al. (2012b) found these SNe

with blue-shifted Na I D generally have higher ejecta velocities and redder colours at maximum light. Understanding the properties of these HVFs could provide some clues to their relations with any CSM and therefore the SN progenitor system.

1.6 An outline of the thesis

The main purpose of this thesis is to study the relationship between SNe Ia and their host galaxies. By studying the SN Ia host environments, we expect to have a better understanding of the properties of their progenitor systems, and any systematic uncertainties that host parameters could have on the SN distances.

A plan of the thesis follows. We present the SN Ia and host galaxy observations in Chapter 2. We define the SN sample studied in this work, and discuss the data reduction of the photometric/spectroscopic data. The techniques of SN light curve fitting are also presented.

In Chapter 3, we present our spectral fitting method to fit the SN Ia host spectrum. The active galactic nucleus (AGN) diagnostic as applied to our SN Ia host galaxies is also discussed. We present methods to determine the host galaxy parameters, such as host galaxy stellar mass ($M_{\rm stellar}$), star formation rate (SFR), gas-phase metallicity, stellar metallicity, stellar age, and SN offset (i.e., position of the SN relative to the centre of the host galaxy). These host parameters are obtained by measuring both photometric and spectroscopic data.

In Chapter 4, we investigate the relations between SN photometric properties and host parameters. We compare the SN stretch, optical colour and SN luminosity (as parameterised by Hubble residual) with the host $M_{\rm stellar}$, SN offset, SFR, gas-phase/stellar metallicity, and stellar age.

In Chapter 5, we present our methods to fit the SN Ia spectrum. We measure the key spectral features, such as the pseudo-equivalent widths (pEW) and velocities of

Si II λ6355 and Ca II near infrared (NIR) triplet. The SN high-velocity feature (HVF) is particularly of interest in this thesis. We measure the HVFs by decomposing the photospheric-velocity feature (PVF) and HVF in the Ca II NIR line profile.

In Chapter 6, we study the relations between SN spectral properties and host parameters. As in Chapter 4, we compare pEW and velocities of SN Si II λ6355 and Ca II NIR features with host parameters such as $M_{\rm stellar}$, SFR and SN offset. The properties of SN high-velocity features from Ca II NIR line are investigated. We discuss the possible scenarios for producing these HVFs.

In Chapter 7, we summarise our main findings and conclusions, and illustrate the potential future SN Ia host studies based on this thesis. Throughout this thesis, we assume $\rm H_0 = 70\,km\,s^{-1}\,Mpc^{-1}$ and a flat universe with $\Omega_{\rm M} = 0.3$.

Chapter 2

Observations and data reduction

In this chapter, we present the observations of both SN sample and their host galaxies, including both the photometric and spectroscopic data. We will define our SN parent sample and present the techniques used for the SN light curve fitting. The procedure for host galaxy spectroscopic data reduction is also shown in the later section.

2.1 SN observations

The SNe Ia studied in this work were discovered by the Palomar Transient Factory (PTF; Rau et al., 2009; Law et al., 2009), a project which operated from 2009–2012 and used the CFH12k wide-field survey camera (Rahmer et al., 2008) mounted on the Samuel Oschin 48-inch telescope (P48) at the Palomar Observatory. The observational cadences used to discover the SNe ranged from hours up to ~ 5 days. PTF operated in either the R or g' band (hereafter $R_{\rm P48}$ and $g_{\rm P48}$), switching from $g_{\rm P48}$ band around new moon to $R_{\rm P48}$ band when the sky was brighter. Multi-colour light curves were not obtained by default for all SNe using the P48; instead they were assembled via triggered observations on other robotic facilities, e.g., the Liverpool Telescope (LT; Steele et al., 2004), the Palomar 60-in (P60; Cenko et al., 2006) and the Las Cumbres Observatory Global Telescope Network (LCOGT; Brown et al., 2013)

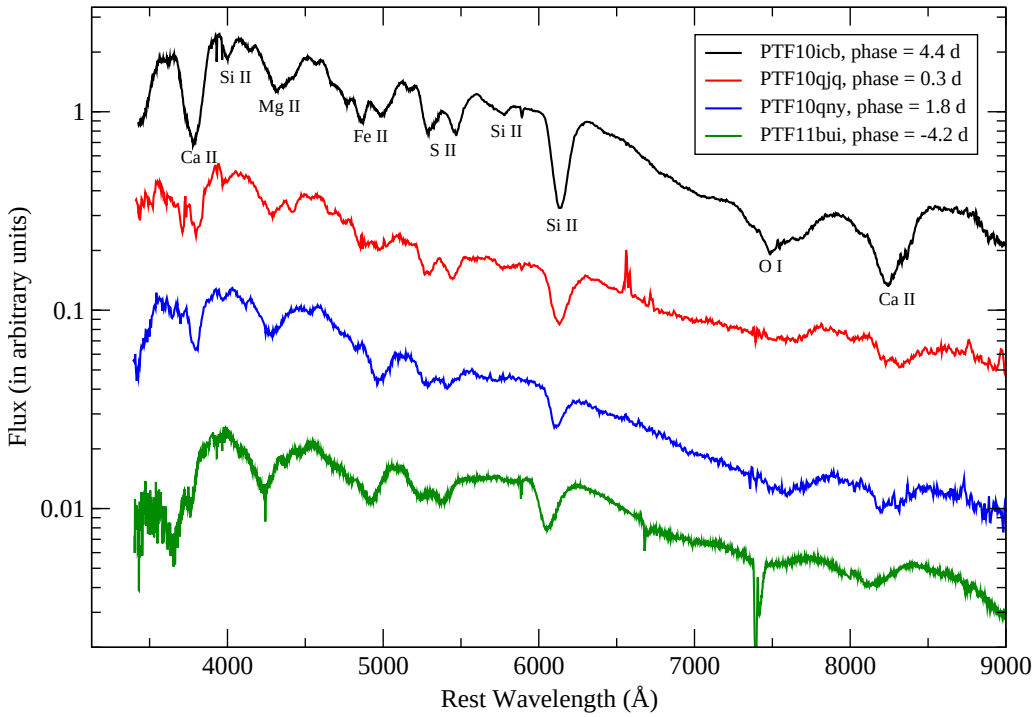

Figure 2.1: Examples of typical SN Ia spectrum around maximum light discovered by Palomar Transient Factory (PTF). The key spectral features are marked in the top spectrum.

Faulkes Telescopes (FTs; clones of the LT). SN candidates were identified in image subtraction data and ranked using both simple cuts on the detection parameters and a machine learning algorithm (Bloom et al., 2012b), and then visually confirmed by members of the PTF collaboration or, from mid-2010 onwards, via the citizen science project 'Galaxy Zoo: Supernova' (Smith et al., 2011).

Promising SN candidates were sent for spectroscopic confirmation using a variety of telescope/instrument combinations. These included: The William Herschel Telescope (WHT) and the Intermediate dispersion Spectrograph and Image System (ISIS), the Palomar Observatory Hale 200-in and the DouBle SPectrograph (DBSP), the Keck-I telescope and the Low Resolution Imaging Spectrometer (LRIS), the Keck-II telescope and the DEep Imaging Multi-Object Spectrograph (DEIMOS), the Gemini-N telescope and the Gemini Multi-Object Spectrograph (GMOS), the Very Large Telescope and X-Shooter, the Lick Observatory 3m Shane telescope and the Kast

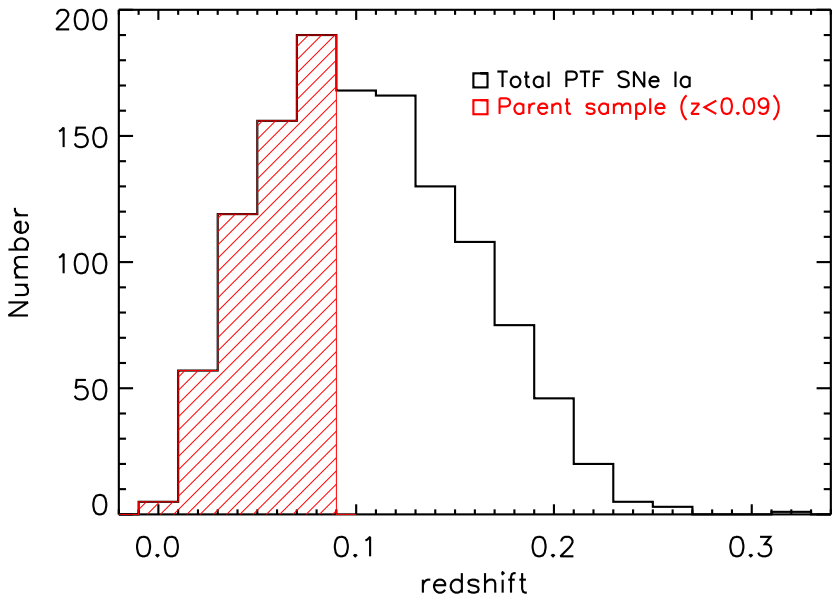

Figure 2.2: A comparison of the redshift distribution of complete SN Ia sample discovered by PTF (1249 events) and the parent sample used in this study (527 events).

Dual Channel Spectrograph, the Kitt Peak National Observatory 4m telescope and the Ritchey-Chretien Spectrograph, and the University of Hawaii 88-in and the Supernova Integral Field Spectrograph (SNIFS). In Fig. 2.1 we show a few examples of typical SN Ia spectrum around maximum light in our sample. All of the spectra used to confirm the SNe in this work as SN Ia are available from the WISeREP archive (Yaron & Gal-Yam, 2012).

2.1.1 SN parent sample

The full PTF SN Ia sample comprises $\sim$ 1250 spectroscopically confirmed events. However, many of these are at relatively high redshift and thus have poor quality P48 light curves. In that case no multi-colour information is available. Thus we need to define a parent sample of high-quality SNe Ia from which targets for host galaxy studies can be selected.

In this work we restricted our SNe to a redshift (z) of $z < 0.09$. The motivation for this was to define a sample less susceptible to selection effects: the median redshift of

all PTF SNe Ia is 0.1, and at $z = 0.09$, a typical SN Ia has a peak apparent magnitude of $R_{\rm P48} \simeq 18.5$, $\simeq 2.5$ mag above the PTF detection limit of 21 (a typical SN Ia at $z = 0.09$ has $R_{\rm P48} = 21$ at 13 days before maximum light). We apply this redshift constraint, giving a parent sample of 527 SNe Ia. Fig. 2.2 shows a comparison of redshift distribution of the complete SN Ia sample discovered by the PTF and the parent sample used in this work. The redshifts of the complete sample of SNe Ia discovered by the PTF span a wide range up to $z \sim 0.3$. By contrast, the parent sample ($z < 0.09$) in this work includes about half of the complete sample. In the later sections, we will discuss how we further select our SNe from this parent sample in host galaxy photometric/spectroscopic studies using various criteria.

A caveat is that any biases that exist in the selection of the PTF sample will also be present in our parent sample. The potentially most serious of these is the difficulty in finding SNe on very bright galaxy backgrounds, where the contrast of the SN over the host galaxy is low. This can occur in the cores of galaxies (e.g., Shaw, 1979) but also more generally for faint events in bright host galaxies (e.g., Perrett et al., 2010), which of course are also likely to be the most metal rich. However, with modern image subtraction techniques this is only an issue when the SN brightness drops to $< 10\%$ of that of the host background (Perrett et al., 2010), and the redshift cuts used in our sample definition mean this is unlikely to occur for normal SNe Ia.

2.2 SN light curve fitting

Optical light curves of our SNe Ia in *gri* were obtained at the LT, the P60, and the FTs. In all cases, reference images were made by stacking data taken >1 year after the SN explosion, which was then subtracted from the images containing SN light to remove the host galaxy. We measure the SN photometry using a point-spread-function (PSF) fitting method [1]. In each image frame, the PSF is determined from

[1]The SN photometry presented in this work was measured by K. Maguire and M. Sullivan.

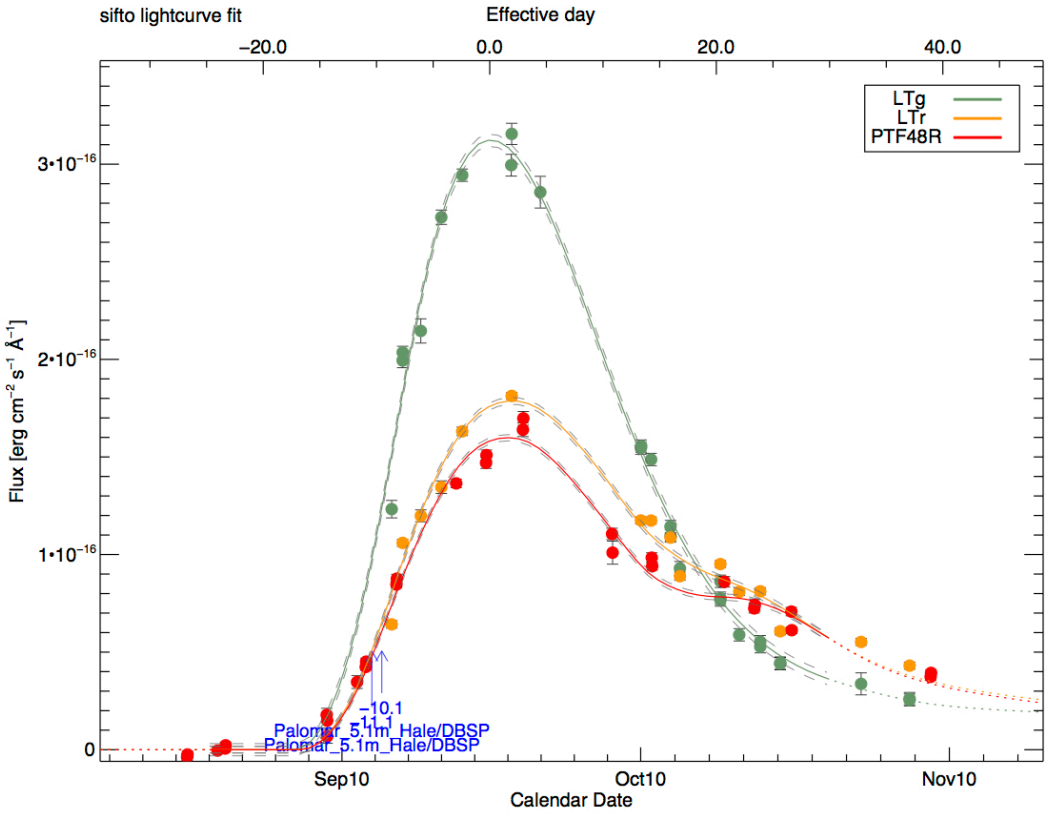

Figure 2.3: An example showing the SN light curve fitting by SiFTO. Here the P48 $R_{\rm P48}$ (shown in red filled circles) and LT *gr* light curves (shown in green and orange filled circles) of PTF10ubm were fit (the best fit is shown in solid line). The blue texts inside the plot indicate the dates and instruments of the SN spectroscopic observations. In this case, two SN spectra were taken using the Palomar 5.1-m Hale/DBSP instrument.

nearby field stars, and this average PSF is then fit at the position of the SN event weighting each pixel according to Poisson statistics, yielding a SN flux and flux error.

The SiFTO light curve fitting code (Conley et al., 2008) was used to fit the light curves. SiFTO works in flux space, manipulating a model of the spectral energy distribution (SED) and synthesising an observer-frame light curve from a given spectral time-series in a set of filters at a given redshift, allowing an arbitrary normalisation in each observed filter (i.e., the absolute colours of the template being fit are not important and do not influence the fit). The time-axis of the template is adjusted by a dimensionless relative 'stretch' (s) factor to fit the data, where the input template is

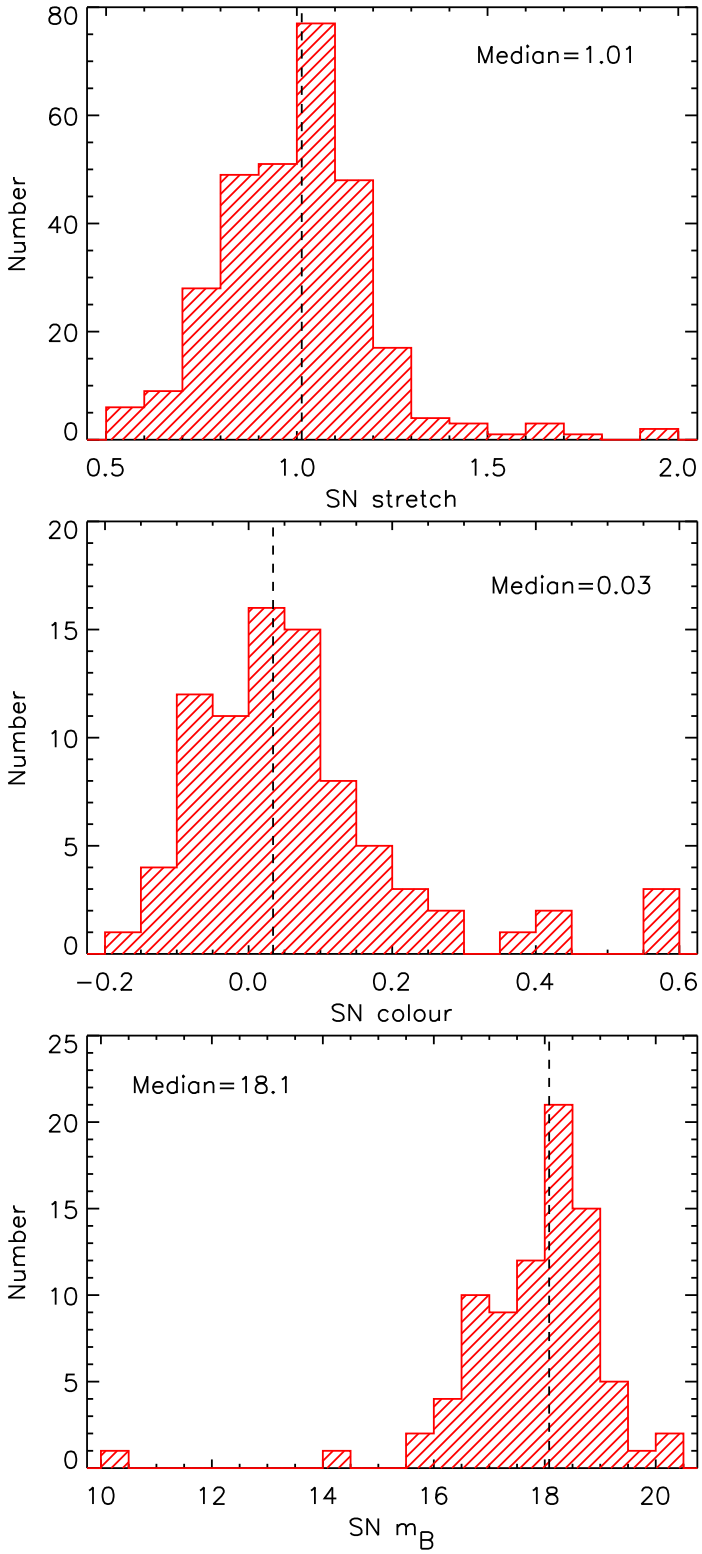

Figure 2.4: The SN stretch (s), colour ($\mathcal{C}$) and B-band apparent magnitude (m_B) distribution of our parent sample derived by SiFTO light curve fitting code. The dashed line in each panel represents the median value of the distribution.

defined to have $s = 1$. Once the observer-frame SiFTO fit is complete, a second step can be used to estimate rest-frame magnitudes in any given set of filters, provided there is equivalent observer-frame filter coverage, and at any epoch. This is performed by adjusting the template SED at the required epoch to have the correct observed colours from the SiFTO fit, correcting for extinction along the line of sight in the Milky Way, de-redshifting, and integrating the resultant SED through the required filters. This process is essentially a cross-filter k-correction, with the advantage that all the observed data contribute to the SED shape were used. Fig. 2.3 shows an example of SN light curve fitting by SiFTO.

We used SiFTO to determine the time of maximum light in the rest-frame B-band, the stretch, the rest-frame B-band apparent magnitude at maximum light m_B, and the $B - V$ colour at B-band maximum light, $\mathcal{C}$. When estimating the final SN colour via the template SED adjustment, filters that are very close in effective wavelength can introduce discontinuities in the adjusted spectrum. Thus we remove the P48 $R_{\rm P48}$ and $g_{\rm P48}$ filters in this process where data from the LT, P60, or FTs are also available. Note that the P48 filters are always used to estimate the stretch and time of maximum light. Fig. 2.4 shows the distribution of SN stretch (s), colour ($\mathcal{C}$) and B-band apparent magnitude (m_B) of our parent sample. The median of the distribution is $s = 1.01$, $\mathcal{C} = 0.03\,\mathrm{mag}$ and $m_B = 18.1\,\mathrm{mag}$, respectively. In Table A.4 we summarise the SN Ia photometric measurements in this work.

2.3 SN spectroscopic data reduction

The SN spectroscopic data in this work was reduced by the members in PTF collaboration. I contributed part of the spectroscopic reduction for the spectra taken at William Herschel Telescope (WHT). A total of ~ 260 spectra were reduced during 2010–2013. These SN spectra were taken at WHT using ISIS. ISIS is a dual-armed

spectrograph, and the R300B and R158R gratings are used in the blue and red arms, respectively. The 5300 dichroic was used. An example of a SN spectrum taken at WHT is shown in Fig. 2.5.

The data reduction pipeline[2] is written in IRAF [3]. We follow standard procedures. Firstly, we combine a stack of bias and flat-field images taken at the same night as our SN observation using the IRAF task IMCOMBINE. These calibration images were taken with the same slit width and binning (in spatial axis) as our target. The raw data is then processed through bias subtraction and flat-fielding. The cosmic-ray removal (using LACOSMIC; van Dokkum, 2001) and a wavelength calibration are also performed. The IRAF task APALL is then used to extract the 1-D spectrum from each 2-D frame. We checked the wavelength calibration of our spectrum by examining the 6300.3 Å line in the red arm and 5199/5577 Å lines in the blue arm from the sky background. An offset in each arm is computed from these sky lines and then used to tweak the spectrum in wavelength space. A (relative) flux calibration is performed with a telluric-correction by comparing to standard stars. We generally took 2–3 standard stars per night at the beginning, middle and end of the observation, and used the one nearest to our target (nearest in observing time) for flux calibration. 'Error' spectra are derived from a knowledge of the CCD properties and Poisson statistics, and are tracked throughout the reduction procedure. As all the spectra were taken with dual-arm spectrographs with a dichroic, with different wavelength coverages and dispersions, they need to be combined to produce the final spectrum. This was performed by rebinning to a common dispersion, and combining (with weighting) to form a final contiguous spectrum.

[2]The ISIS pipeline used in this work is written by M. Sullivan.

[3]The Image Reduction and Analysis Facility (IRAF) is distributed by the National Optical Astronomy Observatories, which are operated by the Association of Universities for Research in Astronomy, Inc., under cooperative agreement with the National Science Foundation.

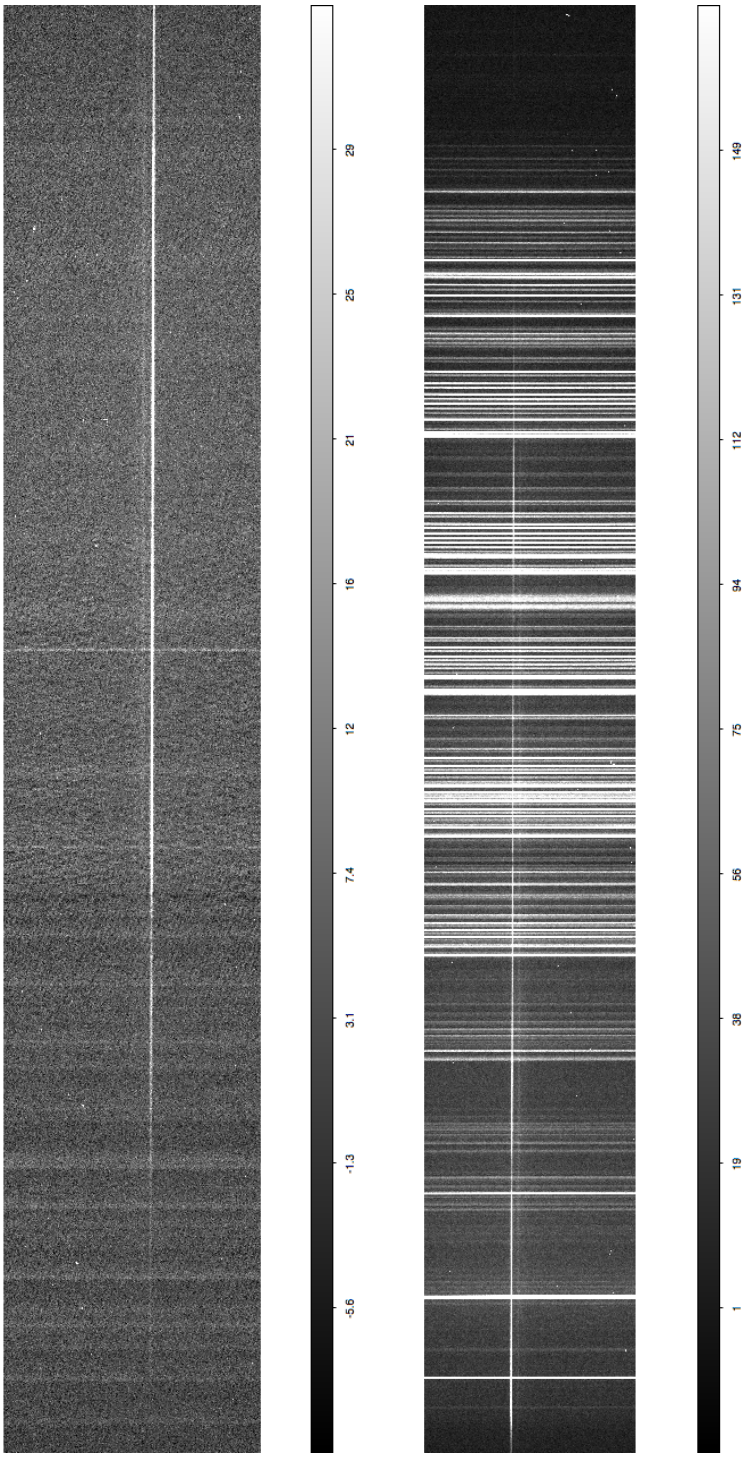

Figure 2.5: An example of SN spectrum taken at William Herschel Telescope (WHT) using ISIS. The R300B and R158R gratings are adopted for the blue (left panel) and red arms (right panel). The spatial axis is in the horizontal direction and the dispersion axis is in the vertical direction. The bright trace along dispersion axis in each panel is the light from the targeted SN (PTF11cao in this case). The fainter trace which is in several pixels offset from the SN trace shows the light from the SN host galaxy.

2.4 Host observations

In this work we investigate the properties of host galaxies using both photometric and spectroscopic data. The host galaxy photometry is principally derived from the SDSS database, but some data are also taken from the Liverpool Telescope (LT). The spectroscopy of host galaxies plays a critical role in this study, as it reveals important host properties including star-formation rate (SFR), gas-phase/stellar metallicity and stellar age. We will present the observation of the host photometric/spectroscopic data and the procedure of the data reduction in the following sections.

2.4.1 Host photometry

We use broad-band photometry of the SN Ia host galaxies to estimate host parameters such as stellar mass ($M_{\rm stellar}$) or star-formation rate (SFR). We use SDSS (York et al., 2000) *ugriz* photometry where available for our sample. The host galaxies were identified by searching for the nearest background galaxies in SDSS images at the SN position. The 'model magnitude' is adopted, where each object in the two-dimensional SDSS images is fit by a matched galaxy model to get the optimal measurement of its total flux. There are 438 out of 527 events in our parent sample that have available SDSS photometry. Of the 89 events for which SDSS photometry is not available, 79 lie outside the SDSS footprint, and the remaining 10 SNe Ia have no host galaxy visible in the SDSS images. The host-less events are listed in Table 2.1. Most of these host-less SNe Ia have normal or relatively higher stretches. Of the 7 SNe Ia with known stretches, 5 have stretches $s > 1$. The spectra of these events are similar to normal SNe Ia. SNe Ia which are distant from their host galaxies, or show no visible host galaxies at their locations, have long been an interesting topic in the SN Ia literature (e.g., Sullivan et al., 2011a; Maguire et al., 2011), as they may explode in the distant halo components from the host galaxies (which could be globular clusters) or in very

Table 2.1: The host-less SNe Ia in this work.

SN name	redshift	SN stretch (s)	SN colour ($\mathcal{C}$)
09ads	0.06	···	···
09akt	0.05	0.9	···
09eiy	0.06	1.4	···
10lxp	0.08	1.1	···
10oiv	0.05	1.7	···
10qnn	0.08	1.3	···
10qyx	0.06	0.9	-0.09
10xgc	0.05	1.4	···
10xk	0.08	···	···
10zej	0.04	···	···

faint galaxies (e.g., dwarf galaxies). The stars in these environments are likely to originate from very old or metal-poor stellar populations, and it would be interesting to see if these SNe Ia show peculiar properties in these extreme environments. This would be an interesting avenue of investigation in future work.

Five of our SNe (PTF09hqp, PTF09ifh, PTF10hjw, PTF10nlg and PTF10zgy) lie outside the SDSS footprint but have available LT photometry. For these we instead use the LT $g'r'i'$ images (similar to SDSS) taken as part of the SN photometric follow-up campaign, calibrated using observations of either Smith et al. (2002) standard stars, or of the SDSS stripe 82 (Ivezić et al., 2007). The host photometry is measured by SEXTRACTOR (Bertin & Arnouts, 1996). In each band, we first scale each image by comparing the flux of some bright stars found in the same field. The IRAF code IMCOMBINE is then used to combine (average) the stack of images in each band and produce a final image for photometric measurement. We adopt dual-image mode in SEXTRACTOR, ensuring the same consistent aperture is used in each filter. The FLUX_AUTO option is selected to estimate the total count of the object using SEXTRACTOR's automatic aperture photometry routine. Finally we convert the integrated flux of host galaxy to apparent magnitude using

$$\text{Magnitude} = -2.5\log(\text{Flux}) + \text{Z}_\text{p} \tag{2.1}$$

Table 2.2: The statistics of host galaxy observation.

sample	Num. of SN
Total SNe Ia in PTF	1249
Parent sample in this study ($z < 0.09$)	527
Hosts photometric observation (SDSS+LT)	443
Hosts spectroscopic observation	82

where the flux is the counts per second of host galaxy enclosed by the aperture. The Z_p represents the zero-point of the LT image. It is related to the characteristics of the instrument and varies with the condition of the observation.

Fig. 2.6 shows the distribution of host galaxy photometry in *ugriz* derived from SDSS or LT. We also present the distribution of host $M_{\rm stellar}$ and SFR of our parent sample determined by Z-PEG (see Section 3.3.1 for a complete discussion) in Fig. 2.7 using these photometry. The median of the host $M_{\rm stellar}$ and SFR of our parent sample is $2.5 \times 10^{10}\,{\rm M}_\odot$ and $1.9\,{\rm M}_\odot\,{\rm yr}^{-1}$, respectively.

2.4.2 Host spectroscopy

For the host galaxy spectroscopic study, we only observed host spectra for those 'older' SNe Ia, i.e., those SNe Ia which had already faded by the time the host galaxy spectrum was taken. We took these at >1 year after the SN explosion. We had sufficient telescope time to observe 82 host galaxy spectra, selected at random from the parent sample. The host galaxies of the SNe Ia were identified by inspecting images taken by the SDSS. Most of the host galaxies in our sample can be identified unambiguously, except PTF09dav where its likely host galaxy lies $\sim 41\,{\rm kpc}$ from the SN (Sullivan et al., 2011a). A summary of host photometric and spectroscopic samples can be found in Table 2.2.

All of our host galaxy spectra were obtained using spectrographs operating in long-slit mode on four different facilities. Table 2.3 summarises the instruments and setups used for our spectroscopic data. Generally, our strategy was to place the slit

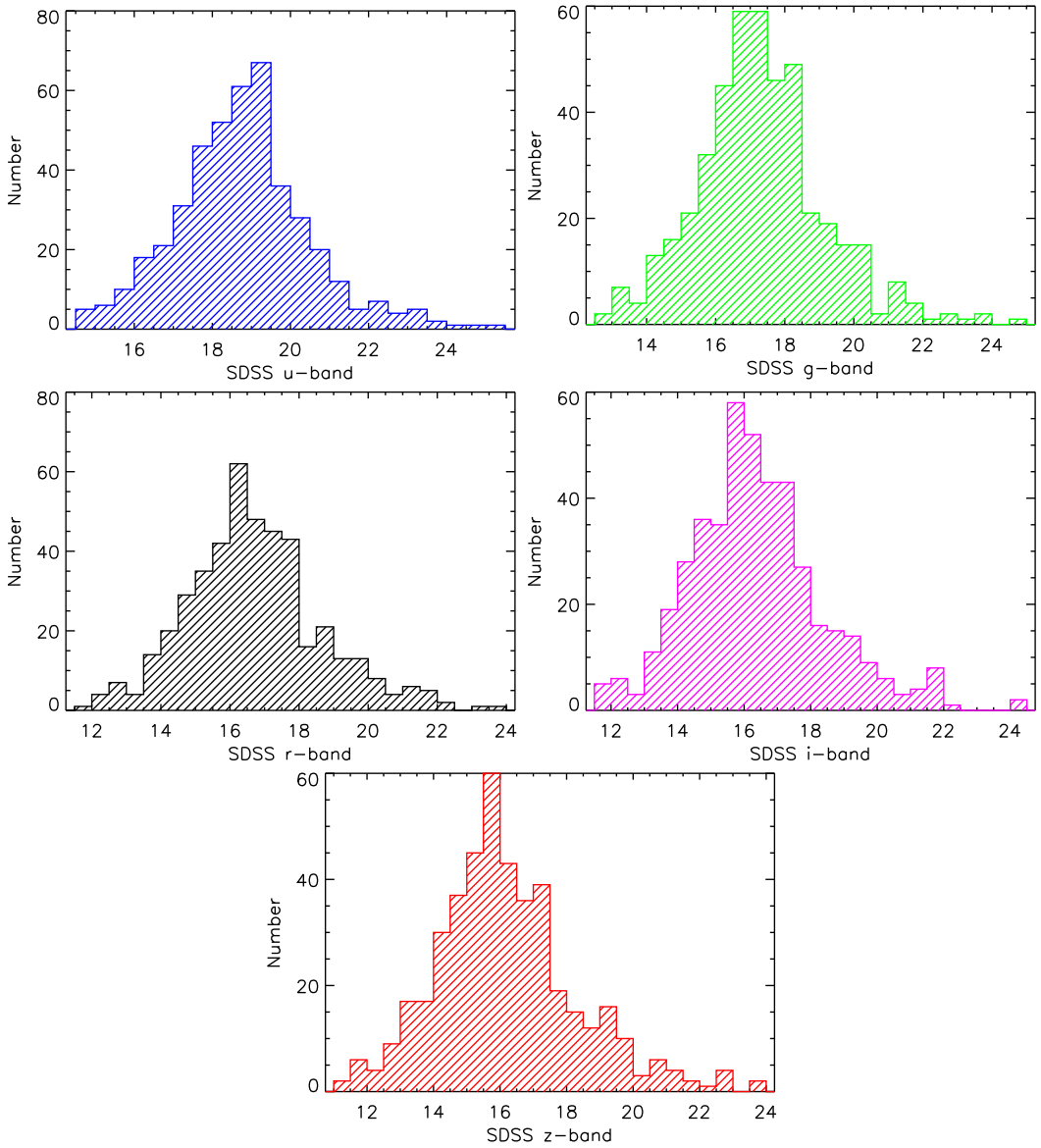

Figure 2.6: The distribution of SN host galaxy photometry in SDSS *ugriz* of the parent sample in this work.

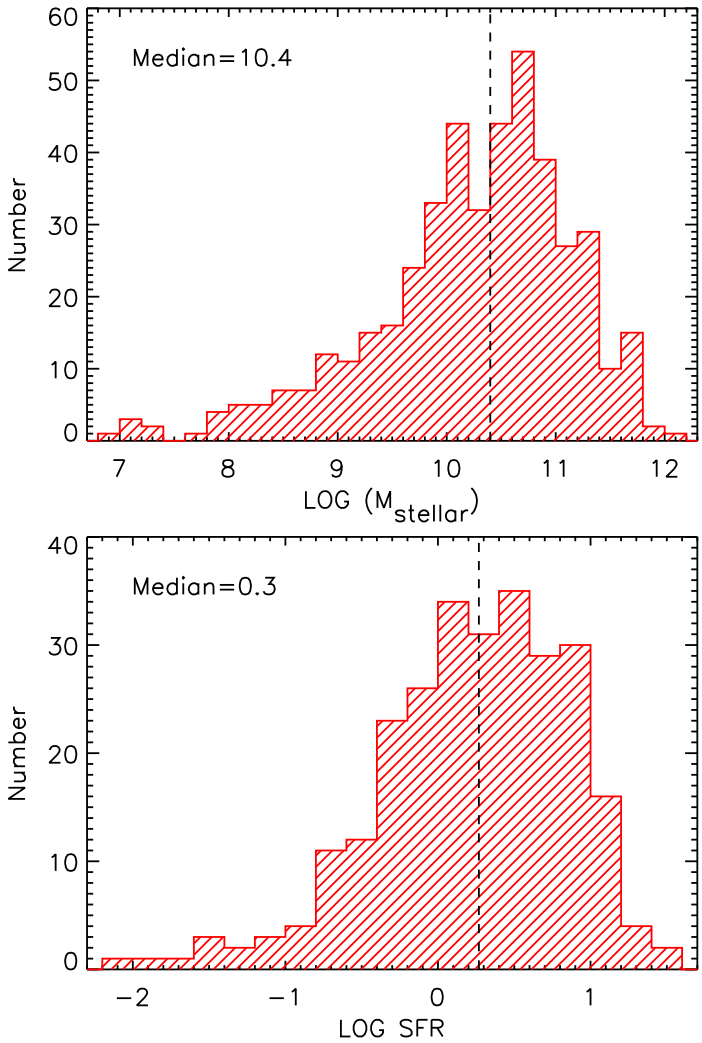

Figure 2.7: The host stellar mass ($M_{\rm stellar}$, in $M_\odot$) and star-formation rate (in $M_\odot\,yr^{-1}$) of our parent sample determined by Z-PEG (see Section 3.3.1). The dashed line in each panel represents the median value of the distribution.

through both the positions of the SN and the centre of the host galaxy. Thus we were careful to ensure that the observations were taken at low airmass to avoid losses due to not observing at the parallactic angle. The median airmass of the spectroscopic data in this work is ~ 1.15. Note that by placing the slit through both the SN position and the centre of the host galaxy, the spectra will be dominated by light from the central regions of the host galaxies, which are generally the brightest part of galaxies.

Most of our SN Ia host galaxy spectra were taken at the Gemini Observatory during 2010–2012 (59 out of 82 hosts), using both Gemini North and Gemini South. We used GMOS (Hook et al., 2004) with a 3600–9400 Å wavelength coverage provided using two different settings (B600 and R400 gratings). Two exposures in each setting were taken, with a ~ 100 pixel shift in wavelength space in order to cover the gaps between the detectors (the GMOS array is composed of three CCDs). The gaps in each exposure will be replaced by the same areas in the other exposure. Total integration times were around two hours per source. Fig. 2.8 shows an example of the two-dimensional spectroscopic data taken at Gemini observatory using the GMOS spectrograph.

There were 18 SN Ia host spectra taken at the 4.2-m WHT using ISIS, providing a 3000–10000 Å wavelength coverage. ISIS is a dual-armed spectrograph, and we used the R300B and R158R gratings in the blue and red arms, respectively. The 5300 dichroic was used.

Two host galaxy spectra (PTF10ygu and PTF11bas) were taken with the 3-m Shane telescope at the Lick Observatory, using the Kast Spectrograph (Miller & Stone, 1993) providing 3000–11000 Å wavelength coverage. Here, the 300/7500 grating was used for the red arm and 600/4310 grism for the blue arm, using the D55 dichroic.

Finally the 10-m telescope Keck-I telescope was used to observe three fainter ($m_r \geq 20$) host galaxies (PTF10hdv, PTF10rab and PTF11pfm) using LRIS (Oke et al., 1995) with a 3200–10000 Å wavelength coverage. LRIS is also a dual-armed

Table 2.3: The instrumental setups used for the spectroscopic data.

Telescope	Spectrograph	Gratings/Grisms (Red)	(Blue)	Dichroic	λ coverage (Å)
Gemini	GMOS	R400	B600	–	3600–9400
WHT	ISIS	R158R	R300B	5336 Å	3000–10000
Lick	Kast	300/7500	600/4310	5500 Å	3000–11000
Keck	LRIS	400/8500	600/4000	5696 Å	3200–10000

spectrograph. The 400/8500 grating was used for the red arm and the 600/4000 grism for the blue arm, with the D560 dichroic. In Table A.1 we summarise the information of the host spectroscopic observations in this work.

2.5 Host spectroscopic data reduction

Similar to the SN spectroscopic data reduction discussed in Section 2.3, we reduced the host spectroscopic data using a custom data reduction pipeline written in IRAF. For data taken at the Gemini Observatory, we also used some tasks from the Gemini IRAF package. Our pipeline follows standard procedures, including bias subtraction, flat-fielding, cosmic-ray removal (using LACOSMIC; van Dokkum, 2001) and a wavelength calibration. The IRAF task APALL is then used to extract the 1-D spectrum from each 2-D frame, and a relative flux calibration performed with a telluric-correction by comparing to standard stars. As all the spectra in our sample are taken either with a spectrograph with two different grating settings (Gemini), or with dual-arm spectrographs with a dichroic (WHT, Lick, Keck), red and blue spectra for each object, with different wavelength coverages and dispersions, need to be combined to produce the final spectrum. As already discussed in Section 2.3, it was achieved by rebinning to a common dispersion, and combining to form a final contiguous spectrum.

We test our relative flux calibration by comparing synthetic photometry measured from our final host spectra, with SDSS photometry of the same objects. The SDSS

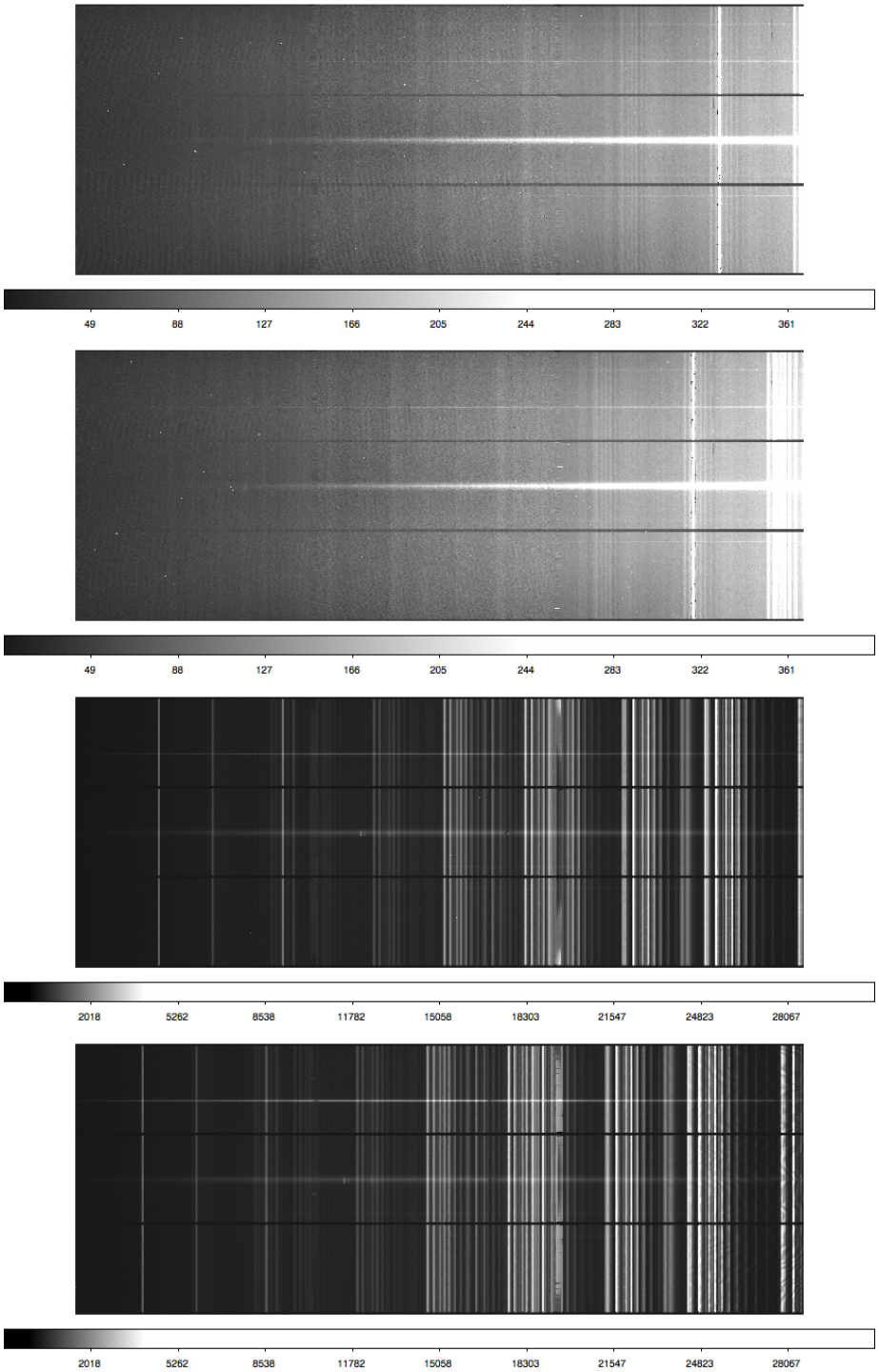

Figure 2.8: Example of two-dimensional spectroscopic data taken at Gemini Observatory using the GMOS spectrograph. The top two panels show the spectra taken with the B600 grating ($\sim 3400 - 6000\,\text{Å}$). There is a $\sim$ 100 pixels offset between two exposures to cover the gaps between 3 CCD chips. The bright trace close to the central part of CCD is the light from the host galaxy (PTF09dxw in this case). The bottom two panels are the same as the top two panels, but using the R400 grating ($\sim 5000 - 9400\,\text{Å}$) instead.

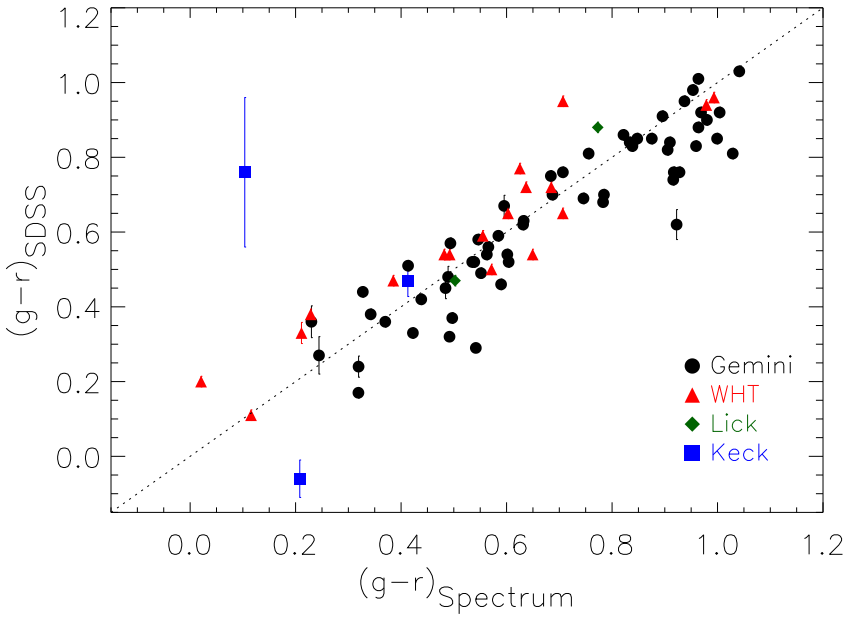

Figure 2.9: The $g-r$ colour derived from our host galaxy spectra, compared with that determined from the SDSS broad-band photometry. The line of equality is shown in dotted line.

model magnitudes are used here. Fig. 2.9 shows the $g-r$ colour of our spectra plotted against the $g-r$ colour from the SDSS photometry. Overall our data show a good consistency with the SDSS photometry: the r.m.s. scatter is 0.12 mag, with a mean offset of 0.01 mag.

We correct our absolute flux calibration using the same SDSS photometry (this is important for host galaxy parameters measured based on absolute line strength, for example $M_{\rm stellar}$ and SFR). Again, we measure a synthetic SDSS r-band magnitude for our observed spectra, and compare to the SDSS photometry, scaling our observed spectra so the two magnitudes are equal.

Finally, we apply a correction for foreground galactic extinction prior to de-redshifting the spectra into the rest-frame. The latest calibration (Schlafly & Finkbeiner, 2011) is used, and the typical Milky Way value $R_V = 3.1$ is assumed, using a Cardelli, Clayton, & Mathis (1989, CCM) law. Although redshift estimates based on the original SN classification spectrum are available, we confirm these using emission and

absorption lines in the galaxy spectra; the two redshift measures are consistent in all cases. In Fig. 2.10 we show some examples of the host galaxy spectrum in our sample.

2.6 Summary

We have presented both the photometric and spectroscopic observations of our SN Ia sample and their host galaxies. The procedure of spectroscopic data reductions were also shown. We defined the SN parent sample of this work by restricting the redshift to $z < 0.09$ from the whole SN Ia sample in the Palomar Transient Factory (PTF). The SN Ia light curve parameters were determined using the SiFTO light curve fitting code. We derived SN stretch, $B - V$ colour and B-band apparent magnitude.

In the next chapter, we will present the method to fit our host galaxy spectrum. The techniques used to determine the host parameters will be discussed as well. The host stellar mass ($M_{\rm stellar}$), star-formation rate (SFR), gas-phase/stellar metallicity , stellar age and SN offset are determined.

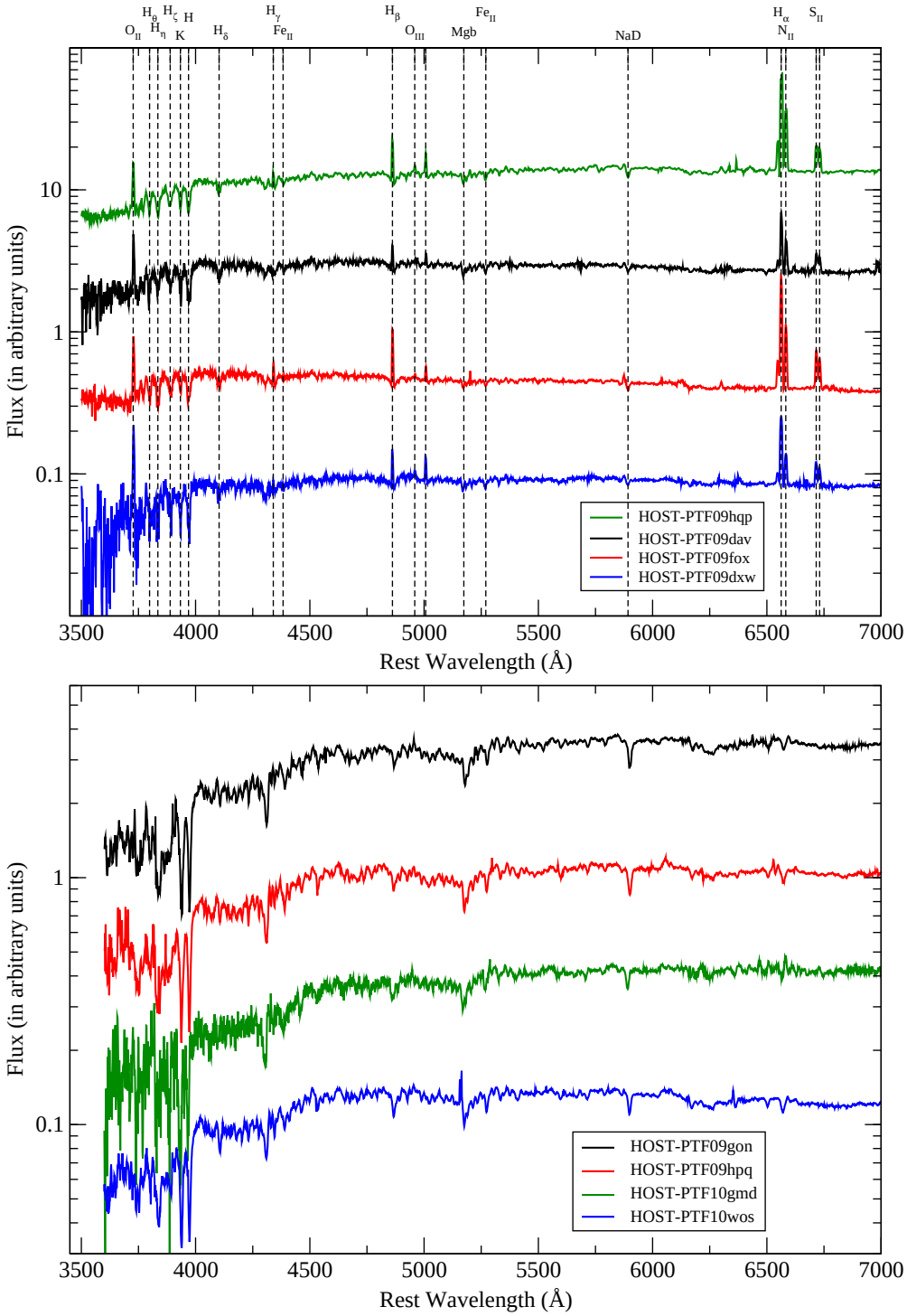

Figure 2.10: Examples of host galaxy spectrum in our sample. Top: We present some star-forming galaxies and marked several remarkable line features found in the spectrum. Bottom: We present some passive galaxies in our sample which show weak or no emission lines in their spectra.

Chapter 3

Host galaxy parameter determination

Having described the sample and data that make up our host galaxy sample, we now discuss the techniques used to fit the SN Ia host galaxy spectra, and estimate various physical parameters such as the stellar mass ($M_{\rm stellar}$), star formation rate (SFR), gas-phase/stellar metallicity, stellar age and SN offset. We use various techniques, including emission line measurements to determine SFRs and gas-phase metallicities, spectral fitting to determine stellar metallicities and ages, and broad-band photometric fitting to determine stellar masses.

3.1 Spectral measurement

A typical galaxy spectrum is composed of two components: emission lines and stellar continuum. Emission lines are generally formed from the interstellar gas inside the galaxy that is ionised or excited by hot stars or an active galactic nucleus (AGN), and the stellar continuum is formed from all the star light in the galaxy, with numerous absorption lines caused by the stellar atmospheres. For star-forming galaxies, there are prominent emission lines on top of the stellar continuum. By contrast, passive galaxies usually show weak or no emission lines, and the spectra are dominated by the stellar absorptions. As emission lines reflect the gas properties of the galaxy, we

can use them to estimate parameters such as SFR and gas-phase metallicity. In this work, we measure several key features, such as [O II], Hβ, Hα, [O III] and [N II] lines. By contrast, the stellar continuum reflects the properties of the stellar populations inside the galaxy, and it can be used to estimate parameters like stellar metallicity and age.

The emission line measurement is complicated by stellar absorptions beneath, especially for those with strong absorptions (e.g., the hydrogen Balmer lines). Without considering the flux 'eaten' by the stellar absorption, the strength of the emission lines can be underestimated. (e.g., Tremonti et al., 2004). Therefore, previous studies usually subtract the stellar continuum from the observed spectrum before measuring the emission lines (e.g., Tremonti et al., 2004; Kewley & Ellison, 2008). To achieve this, the stellar continuum is firstly fit by a stellar population model, with the emission lines masked out from the spectrum during this fitting. The emission lines will then be measured after subtracting the synthetic stellar continuum from the observed spectrum (i.e., using the residual spectrum).

In this study, we adopt similar techniques. The emission lines and stellar continuum of the host galaxy spectrum were fit using the Interactive Data Language (IDL) codes PPXF (Cappellari & Emsellem, 2004) and GANDALF (Sarzi et al., 2006). PPXF fits the line-of-sight velocity distribution (LOSVD) of the stars in the galaxy in pixel space using a series of stellar templates. The advantage of working in pixel space is that emission lines and bad pixels are easily excluded when fitting the continuum. Before fitting the stellar continuum, a list of emission lines is used to mask out the potential contamination. Table 3.1 lists all the emission lines we masked out during the fitting. The stellar templates are based on the MILES empirical stellar library (Sánchez-Blázquez et al., 2006; Vazdekis et al., 2010), giving a wavelength coverage of 3540 Å to 7410 Å with a spectral resolution of 2.51 Å, and a variety of different metallicities and ages. A total of 276 templates are selected with $[M/H] = -1.71$ to

+0.22 in 6 steps and ages ranging from 0.079 to 14.12 Gyr in 46 steps. The $[M/H]$ here represents the logarithmic difference between the relative metal abundance of the star (elements heavier than helium) and the relative metal abundance of the Sun, which is computed as

$$[\mathrm{M/H}] = \log(\mathrm{M/H})_{\mathrm{star}} - \log(\mathrm{M/H})_{\mathrm{sun}} \tag{3.1}$$

where the $(\mathrm{M/H})_{\mathrm{star}}$ is the relative metal abundance of the star, and the $(\mathrm{M/H})_{\mathrm{sun}}$ is the relative metal abundance of the Sun. We use all the templates provided by MILES library except the templates with the lowest metallicity ($[M/H] = -2.32$, where only templates with ages above 10 Gyr are acceptable), and with ages far older than our Universe (15.84 and 17.78 Gyr). Table 3.2 list all the $[M/H]$ and ages of the stellar templates used in this study.

After measuring the stellar kinematics with PPXF, the emission lines and stellar continuum are simultaneously fit by GANDALF. GANDALF treats the emission lines as additional Gaussian templates. Through an iterative fitting process, GANDALF locates the best velocities and velocity dispersions of each Gaussian template and also the optimal combination of the stellar templates which have already been convolved with the LOSVD (previously determined by PPXF). This results in the emission lines and stellar continuum being fit simultaneously to each spectrum. We required all the Balmer lines to have the same line width and velocity offset. The same strategy is also performed for all the forbidden lines (e.g., Tremonti et al., 2004). By doing this, we can better constrain those weak nebular lines using the strong lines (e.g., Hα and [N II] λ6584).

Extinction is handled using a two-component reddening model. The first component assumes a diffusive dust throughout the whole galaxy that affects the entire spectrum including emission lines and the stellar continuum, while the second is a

Table 3.1: List of emission lines considered during the PPXF/GANDALF fitting. The relative strength required during the spectral fitting is shown in the last column.

Line	Rest wavelength (Å)	Relative strength
[O II]	3727.23	
[Ne III]	3868.69	
[Ne III]	3967.40	
Hζ	3889.05	0.037×Hα
Hϵ	3970.07	0.056×Hα
Hδ	4101.73	0.091×Hα
Hγ	4340.46	0.164×Hα
[O III]	4363.15	
He II	4685.74	
[Ar IV]	4711.30	
[Ar IV]	4740.10	
Hβ	4861.32	0.350×Hα
[O III]	4958.83	0.350×[O III] λ5007
[O III]	5006.77	
[N I]	5197.90	
[N I]	5200.39	
He I	5875.60	
[O I]	6300.20	
[O I]	6363.67	0.333×[O I] λ6300
[N II]	6547.96	0.340×[N II] λ6584
Hα	6562.80	
[N II]	6583.34	
[S II]	6716.31	
[S II]	6730.68	
[Ar III]	7135.67	

Table 3.2: The stellar templates selected from MILES stellar library. A total 276 templates (with a combination of 6 different stellar metallicities and 46 different stellar ages) are used for the spectral fitting.

[M/H]	Age (Gyr)
-1.71	0.08, 0.09, 0.10, 0.11, 0.13, 0.14, 0.16, 0.18
-1.31	0.20, 0.22, 0.25, 0.28, 0.32, 0.35, 0.40, 0.45
-0.71	0.50, 0.56, 0.63, 0.71, 0.79, 0.89, 1.00, 1.12
-0.40	1.26, 1.41, 1.58, 1.78, 2.00, 2.24, 2.51, 2.82
+0.00	3.16, 3.55, 3.98, 4.47, 5.01, 5.62, 6.31, 7.08
+0.22	7.94, 8.91, 10.0, 11.2, 12.6, 14.1

local dust component around the nebular regions, and therefore affects only the emission lines. These two components are determined by comparing the observed spectra to the un-reddened stellar templates. They are free to float while fitting the spectrum. However, we place a constraint on the intrinsic relative strength of the multiplets of some emission lines prior to the reddening caused by the dust, which are listed in the last column of Table. 3.1. These values are computed under the Case B condition (assuming an optically thick nebula) at T = 10,000 K (Osterbrock, 1989). Among these ratios, the Balmer decrement (e.g., the Hα λ6563 to Hβ λ4861 line ratio) is the most important and effective in determining the extinction originating from the local dust. The local dust component is constrained only if the Balmer decrement can be measured. For galaxies without Balmer lines in their spectra, only the diffusive dust component is fit (26 out of 82 hosts).

Calzetti (1997) found the relation between the colour excess of the nebular gas $E(B-V)_g$ and the stellar continuum $E(B-V)_s$ can be expressed as

$$E(B-V)_s = 0.44 \times E(B-V)_g \tag{3.2}$$

This implies the fact that the regions of stellar continuum suffer lower reddening than the emission lines (which are originate from nebular gas). In Fig. 3.1 we plot the relation between the colour excess from the local dust component and diffusive dust component determined by GANDALF. Our measurements follow a similar trend as Calzetti's relation in the sense that the $E(B-V)_s$ is less than about half of $E(B-V)_g$. In Fig. 3.2 we show the distribution of the dust extinction (A_v) originating from the Milky Way and the host galaxies. These values are computed assuming a $R_v = 3.1$ and Cardelli, Clayton, & Mathis (CCM; 1989) reddening law. We found most of our host galaxies have $A_v \leq 1.5$ mag, which indicates they do not suffer severe dust extinction.

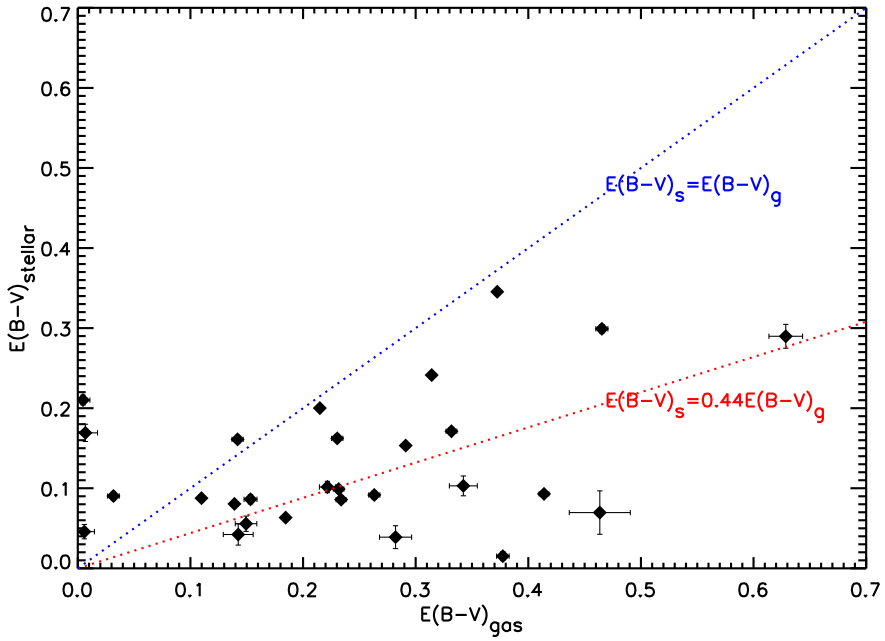

Figure 3.1: The colour excess of the diffusive dust component $E(B-V)_s$ which affects both the stellar continuum and emission lines, as a function of the nebular gas component $E(B-V)_g$, which affects only the emission lines. The red dotted line represents the relation derived by Calzetti (1997). The line of equality is shown in blue dotted line.

To ensure the emission lines in our spectrum are well-measured, we required a S/N $>$ 3 (S/N is defined as the ratio of line amplitude to the noise of the spectrum) for emission lines used in the determination of the host parameters. In Fig. 3.3 and Fig. 3.4 we show examples of the observed spectrum and the best-fit stellar population models for star-forming and passive galaxies, respectively.

3.2 AGN contamination

Our next task is to check for active galactic nuclei (AGN) activity in our host galaxies. In galaxies hosting an AGN, non-thermal emission from the AGN can dominate over emission from the hot stars, leading to a different ionisation source for the nebular H II regions. This in turn means that the stellar continuum and emission line measurements in Section 3.1 cannot be interpreted predominantly as the properties

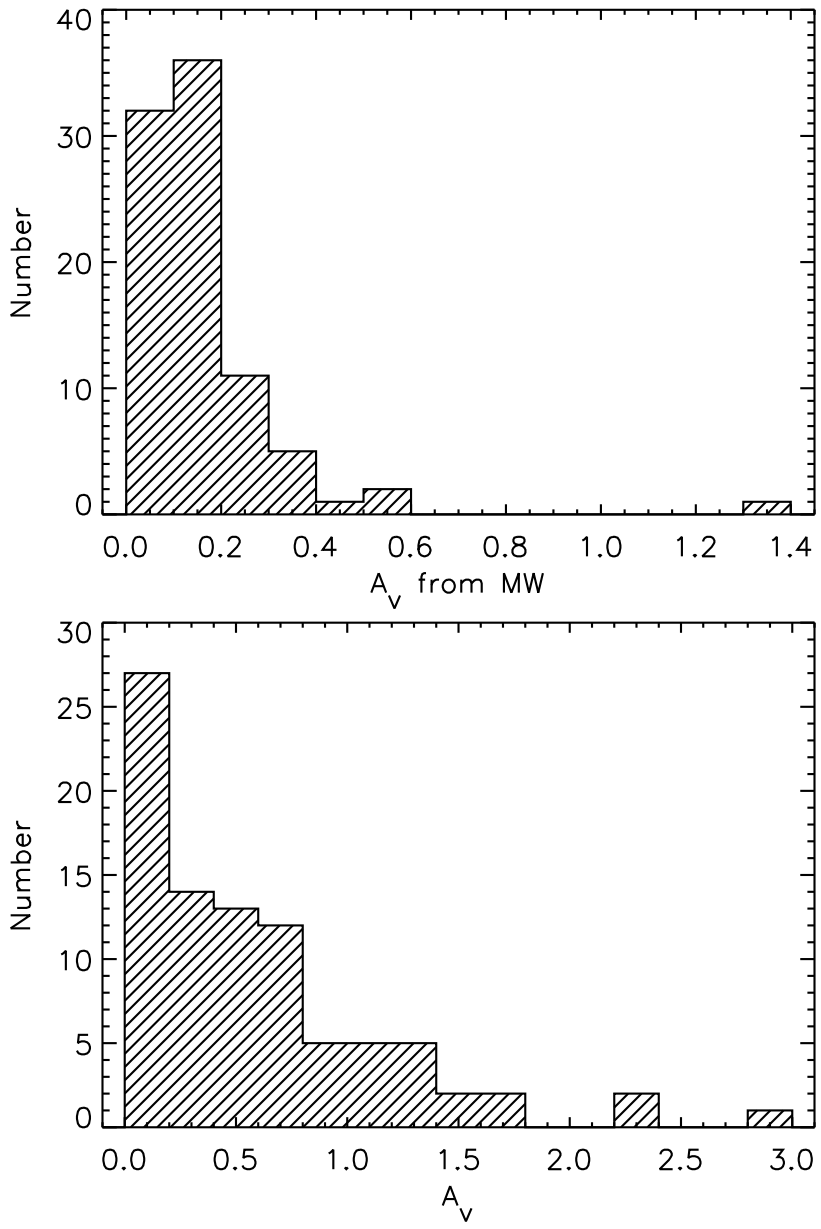

Figure 3.2: Top panel: The distribution of extinction (A_v) contribution from the Milky Way at the coordinates of SNe using $E(B-V)$ derived by Schlafly & Finkbeiner (2011), assuming $R_v = 3.1$. Bottom panel: Same as top panel, but considering the extinction originating from the host galaxies.

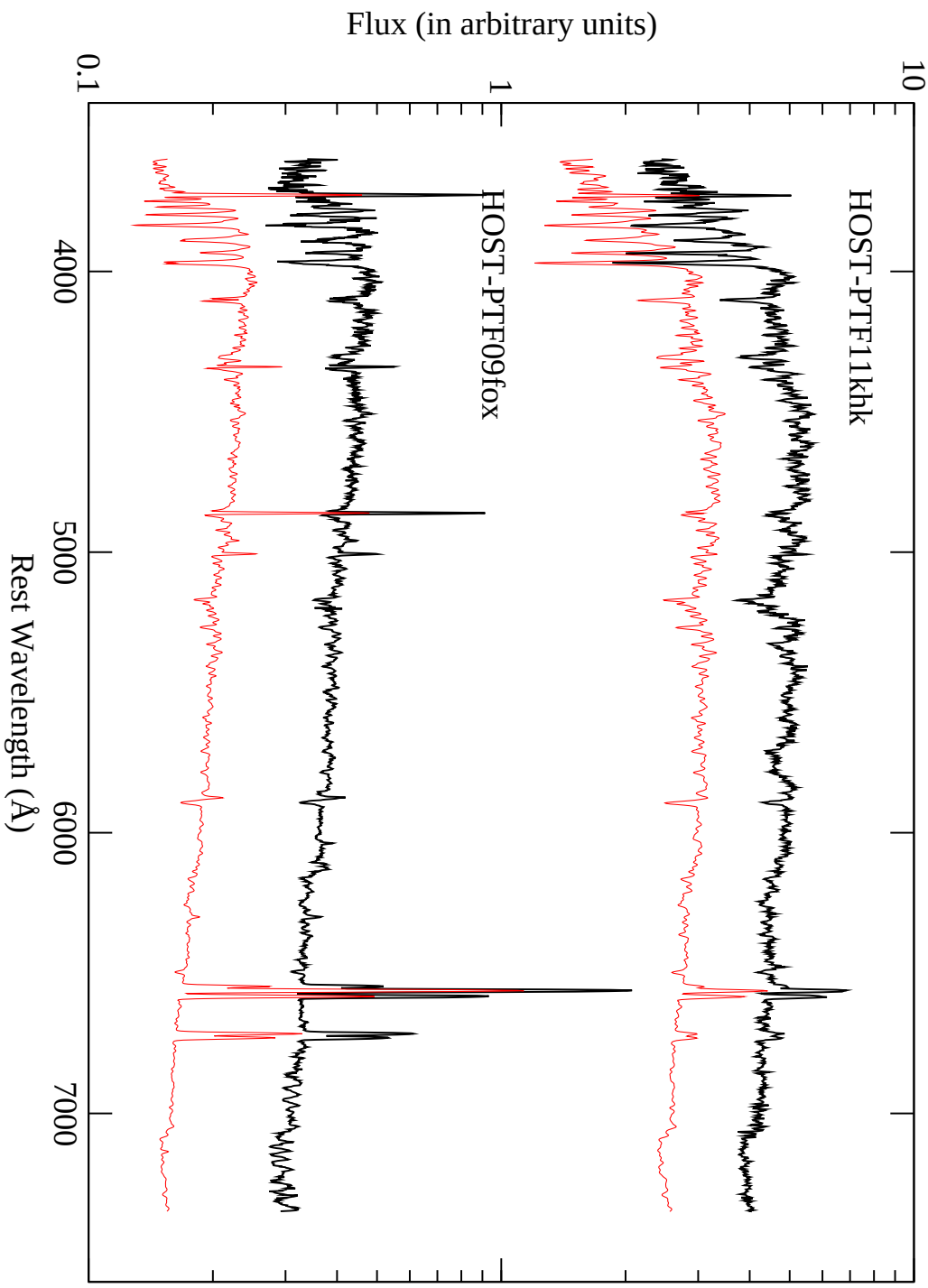

Figure 3.3: The examples of spectral fitting by GANDALF in this work: the host galaxies of PTF11khk and PTF09fox. The black and red lines represent the observation and best-fit, respectively. These are typical star-forming galaxies in our sample.

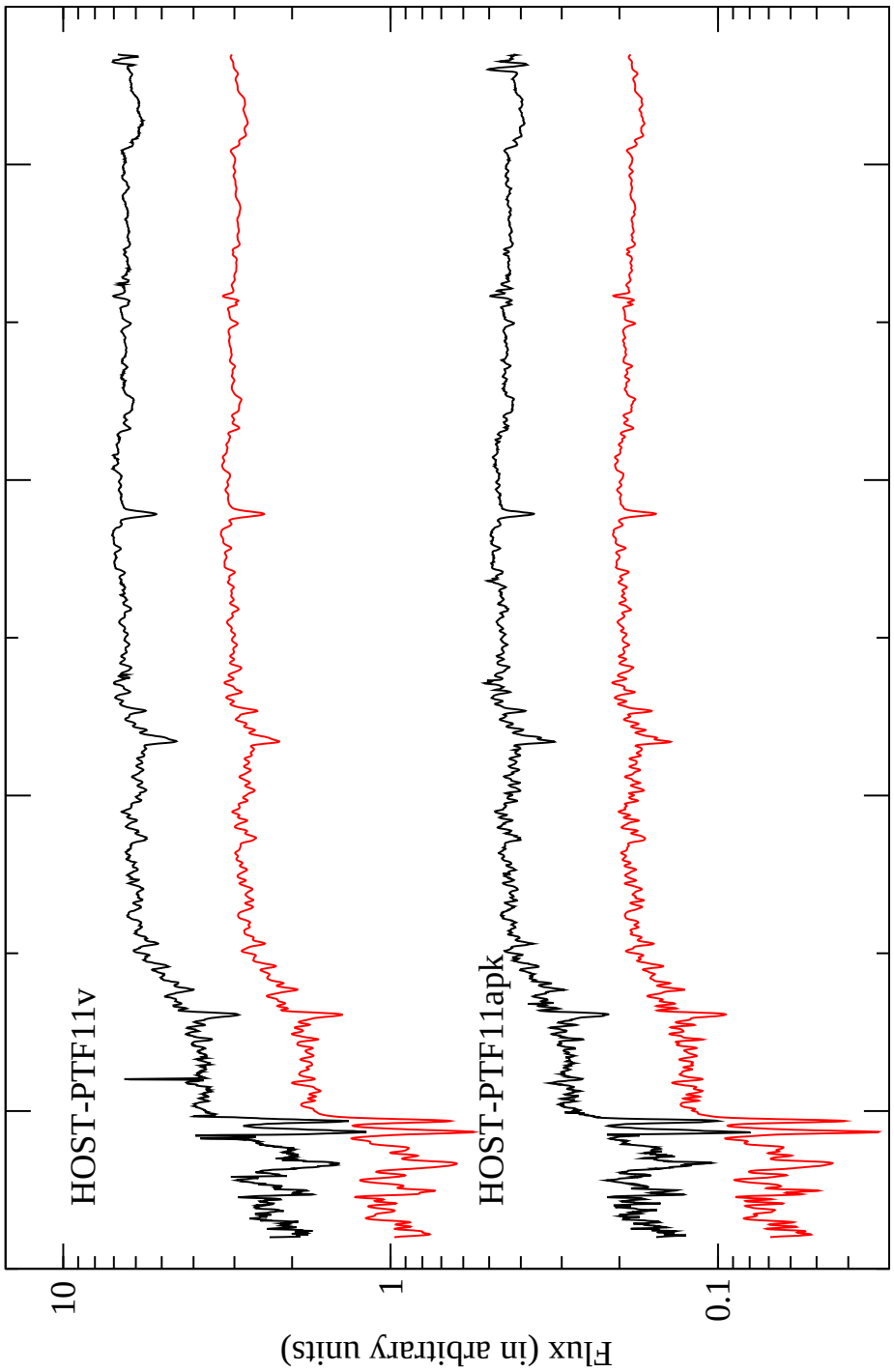

Figure 3.4: The same as Fig. 3.3, but with PTF11v and PTF11apk instead. These are galaxies showing little or no emission lines in their spectra.

of stars and nebular gas inside the galaxy.

Conventionally, two pairs of strong emission lines involving both high ionisation and low ionisation lines are selected to separate the photoionisation caused by different excitation mechanisms. Here we adopt the diagnostics proposed by Baldwin, Phillips, & Terlevich (1981, the so-called BPT diagram) to classify our host galaxies. The two most popular line ratios [O III]/Hβ and [N II]/Hα are used. These lines are strong and visible in the optical spectrum. They are also less affected by the reddening, giving their short separations in wavelength space. In Fig. 3.5 we plot our host galaxies in the BPT diagram according to these line ratios. The galaxies are divided into two groups using either the criteria proposed by Kewley et al. (2001) or Kauffmann et al. (2003). Any galaxies lying to the right of these lines in Fig. 3.5 are regarded as potential AGN host galaxies. We adopt the Kewley et al. criterion in this work: a galaxy will be identified as a AGN if

$$\log\left([\mathrm{O\,III}]/\mathrm{H}\beta\right) > \frac{0.61}{\log\left([\mathrm{N\,II}]/\mathrm{H}\alpha\right) - 0.47} + 1.19 \tag{3.3}$$

where [N II] is the flux of λ6584 line, and [O III] the λ5007 line. However, this requires the four emission lines to be well detected. For those spectra with only [O III] and Hβ or [N II] and Hα available, 'two-line' methods can be used (Miller et al., 2003): a galaxy will be identified as a AGN if

$$\log\left([\mathrm{N\,II}]/\mathrm{H}\alpha\right) > -0.2 \tag{3.4}$$

or

$$\log\left([\mathrm{O\,III}]/\mathrm{H}\beta\right) > 0.8 \tag{3.5}$$

Note that these two-line criteria are more conservative than Kewley et al. criterion.

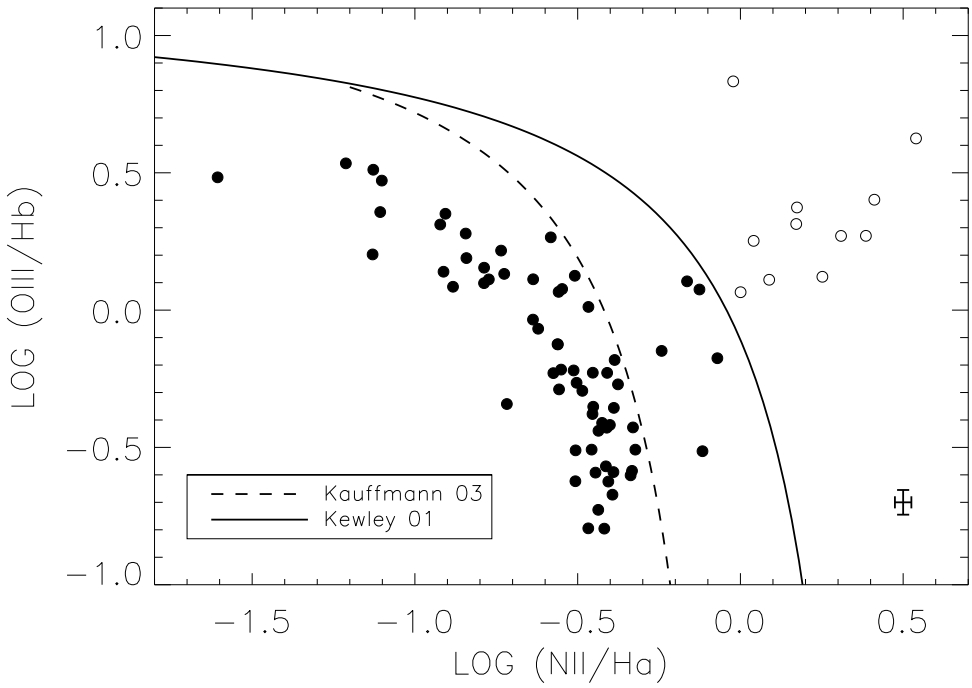

Figure 3.5: The BPT diagram (Baldwin et al., 1981) used to identify the AGN host galaxies in our sample. Two different criteria are over-plotted: Kewley et al. (2001) and Kauffmann et al. (2003). The galaxies which lie on the right hand side of Kewley 01 criteria will be regarded as potential AGN host galaxies in this work (the open circles). Normal star-forming galaxies are plotted in filled circles. The representative error is shown in the bottom-right corner.

There are 11 (3 by the two-line methods) galaxies in our sample identified as AGN, and these are discarded from the sample for further emission line analyses. A further 5 galaxies would have been excluded based on the Kauffmann et al. criterion. We have checked that including these objects does not affect our results. In Fig. 3.6 we show the examples of host spectra in our sample which were identified as potential AGN hosts.

3.3 Determination of host parameters

Having measured the emission lines of the SN hosts, and removed galaxies likely hosting AGN from our sample, we now turn to the estimation of various host galaxy physical properties: the host galaxy stellar mass ($M_{\rm stellar}$), the star-formation rate

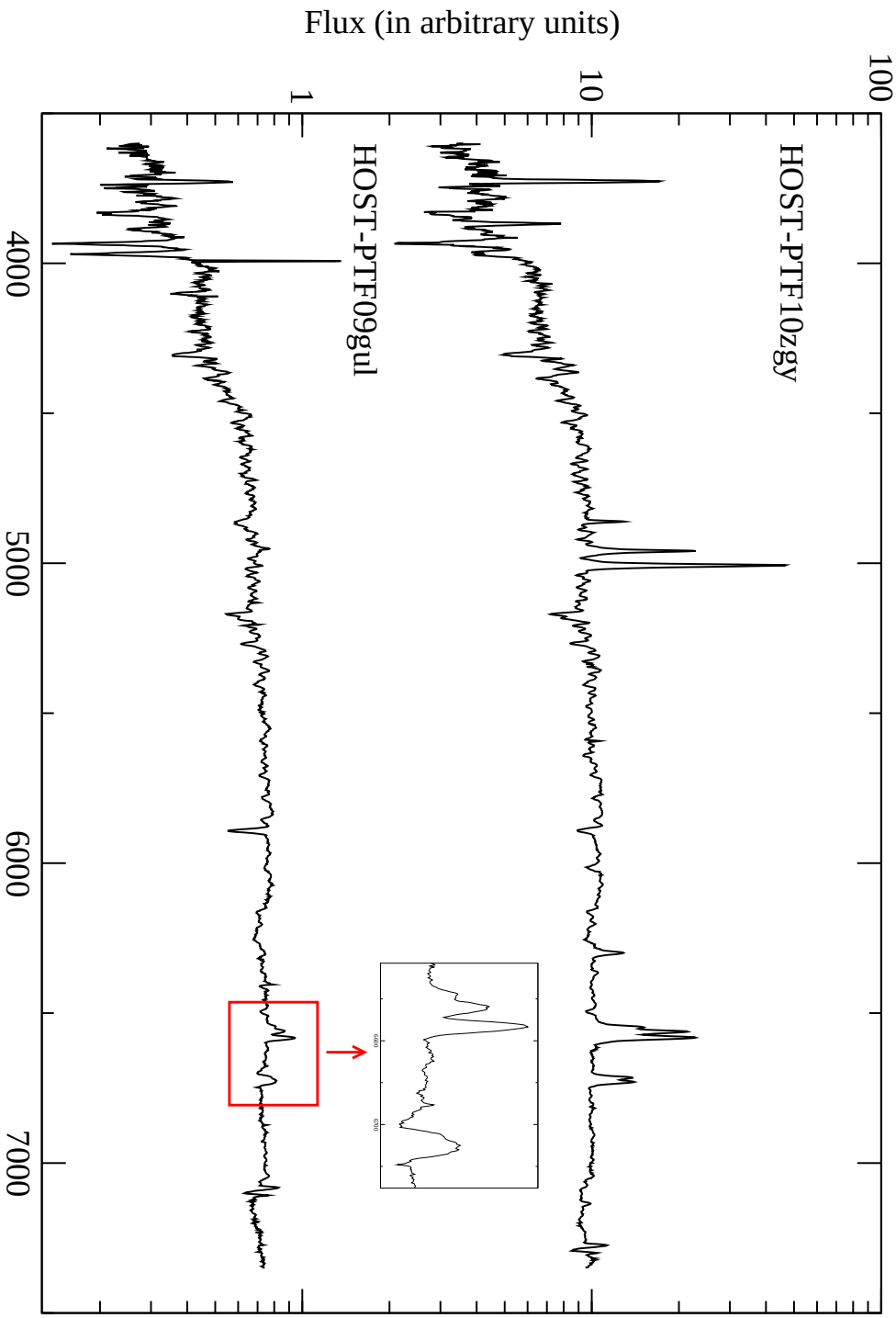

Figure 3.6: The examples AGN host galaxies in this work: PTF10zgy and PTF09gul. The sub-plot enlarges the region of ∼6500–6800 Å (enclosed by the red box).

(SFR), the gas-phase metallicity, the mean stellar metallicity and age, and the SN-host offset.

3.3.1 Host stellar mass

The first parameter of interest is the stellar mass of the host galaxies. We use the photometric redshift code Z-PEG (Le Borgne & Rocca-Volmerange, 2002), which is based on the spectral synthesis code PÉGASE.2 (Fioc & Rocca-Volmerange, 1997), to estimate $M_{\rm stellar}$. The wavelength coverage of Z-PEG stellar library ranges from far-ultraviolet (far-UV) to near-infrared (NIR). Z-PEG fits the observed galaxy colours (Section 2.4.1) with galaxy SED templates corresponding to 9 different types (SB, Im, Sd, Sc, Sbc, Sb, Sa, S0 and E). These templates are computed on the basis of evolution scenarios of star formation. The metal enrichment is also taken into account depending on the evolution scenarios. We assume a Salpeter (1955) IMF. The choice of IMF will not affect our final results as long as the same IMF is used throughout the study. The galactic dust extinction in the Milky Way is corrected using measurements from Schlafly & Finkbeiner (2011). A foreground dust screen varying from a colour excess of $E(B-V) = 0$ to 0.2 mag in steps of 0.02 mag is also used during the fitting.

Z-PEG is used to locate the best-fitting SED model (in a χ^2 sense), with the redshift fixed at the redshift of the SN host galaxy measured from our spectra. The current $M_{\rm stellar}$ and the recent SFR, averaged over the last 0.5 Gyr before the best fitting time step, are recorded. Error bars on these parameters are taken from their range in the set of solutions that have a similar χ^2 (as in Sullivan et al., 2006).

The main uncertainty in this procedure is the choice of SED libraries used in the χ^2 fitting. We use the standard Z-PEG libraries for ease of comparison to previous results in the literature. However we note that improved stellar masses can be obtained by the use of more recent templates (Johansson et al., 2013), particularly those that include an improved treatment of the thermally-pulsing Asymptotic Giant Branch

stage of stellar evolution (Maraston, 2005). A fuller discussion of the uncertainties associated with this stellar population modelling can be found in Childress et al. (2013a). These authors conservatively concluded that the maximal systematic error is $\sim 0.4\,\mathrm{dex}$ in M_{stellar}, which should be borne in mind when interpreting our results.

3.3.2 Star formation rate

The SFR of a galaxy can be estimated using nebular lines in the spectrum, with Hα the most popular choice due to its intrinsic strength and location in the redder part of the spectrum, leading to a lower susceptibility to dust extinction. As this emission line is produced from ionising photons generated by the most massive ($> 10\,\mathrm{M}_{\odot}$), youngest stars ($< 20\,\mathrm{Myr}$), the SFR estimated is a nearly instantaneous measure (Kennicutt, 1998). We adopt the conversion of Kennicutt (1998), which used evolutionary synthesis models to relate the luminosity of the Hα line, $L(\mathrm{H}\alpha)$, to the SFR via

$$\mathrm{SFR} = 7.9 \times 10^{-42} \times L(\mathrm{H}\alpha)\ M_{\odot}\,\mathrm{yr}^{-1} \tag{3.6}$$

with $L(\mathrm{H}\alpha)$ measured in $\mathrm{erg\,s}^{-1}$. The relation assumes a case B recombination at $\mathrm{T_e} = 10,000\,\mathrm{K}$ and a Salpeter (1955) IMF. Brinchmann et al. (2004) studied the likelihood distribution of the conversion factor between $L(\mathrm{H}\alpha)$ and SFR, and found a ~ 0.4 dex variation between massive and low-mass galaxies, with the most massive galaxies producing smaller Hα luminosity than low-mass galaxies for the same SFR. The Kennicutt (1998) conversion factor is close to the median value of their study. As a result, and following D'Andrea et al. (2011), we further add a $0.2\,\mathrm{dex}$ uncertainty in our SFR measurements.

The left panel of Fig. 3.7 shows a comparison between the SFRs derived from the Hα line to that estimated by Z-PEG. The mean difference in log(SFR) is $\sim 0.25\,\mathrm{dex}$,

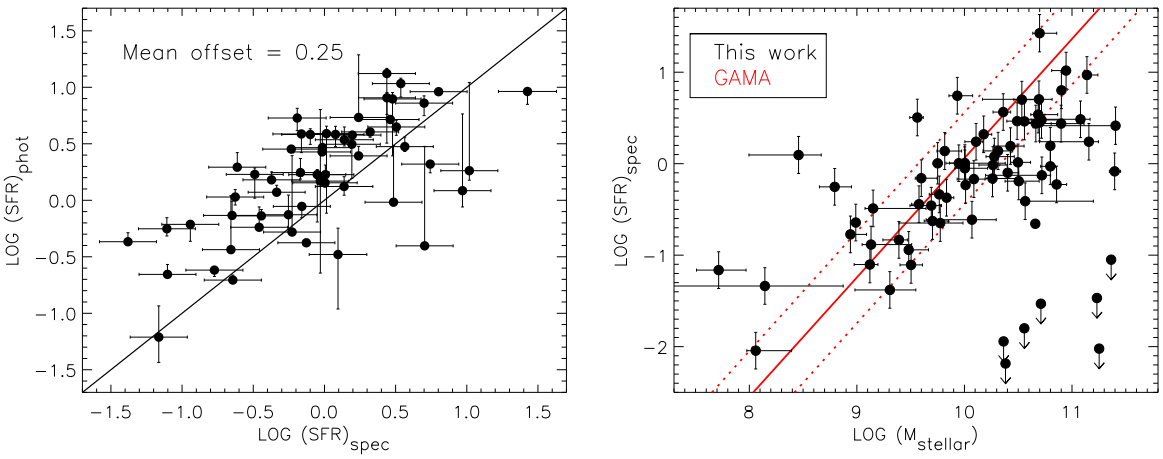

Figure 3.7: Left: A comparison of the star formation rates (SFRs) derived from Hα luminosities ($\mathrm{SFR_{spec}}$) to those measured from broad-band photometry using Z-PEG ($\mathrm{SFR_{phot}}$). The solid line shows the 1:1 relation. Right: The SFR measured from Hα as function of the host M_{stellar}. The relation determined by the Galaxy And Mass Assembly survey (GAMA; Foster et al., 2012) is over-plotted. The dotted line shows the 1-σ range of the GAMA relation. Some passive galaxies with a low SFR for their M_{stellar} (i.e. a low specific SFR) can be seen for large M_{stellar}.

with the SFRs from Z-PEG systematically larger than those from the Hα luminosity. A similar offset using similar techniques was also found by Smith et al. (2012). This offset is perhaps not surprising; Z-PEG determines SFRs averaged over the last 0.5 Gyr, while Hα-based measures determine the instantaneous SFRs.

The relation between the spectroscopic SFRs and M_{stellar} for our sample is shown in the right panel of Fig. 3.7. We over-plot the relation determined by the Galaxy And Mass Assembly survey (GAMA; Foster et al., 2012), which used a similar method as ours for estimating the SFR. Our results show good consistency with this relation, although we also sample some massive galaxies with lower SFRs than the linear relation would predict.

3.3.3 Gas-phase metallicity

There are various methods for calibrating the the gas-phase metallicity determined by emission line ratios (for a review see Kewley & Ellison, 2008, hereafter KE08). The

direct method is to measure the ratio of the [O III] λ4363 line to a lower excitation line to estimate the electron temperature (T_e) of the gas, and then convert it to the metallicity — the so-called T_e-based metallicity. The disadvantage is that this [O III] line is very weak and difficult to detect unless a very high S/N spectrum can be acquired; in our sample for only three spectra was the [O III] λ4363 line detected (PTF09dzq, PTF10hdn, and PTF10zgy). Instead, the empirical metallicity calibrations are popular alternatives by fitting the relations between direct T_e metallicities and the strong-line ratios like [N II]/Hα, [N II]/[O II] or R_{23} (([O II] + [O III]λ4959, 5007)/Hβ). One of the disadvantages of R_{23} method is that it is double-valued with metallicity. It gives both low-metallicity ('lower-branch') and high-metallicity ('higher-branch') estimate. Therefore an additional line ratio (e.g., [N II]/[O II]) is necessary to break this degeneracy. In this study we use indirect metallicity calibrations, and, following the recommendation of KE08, adopt the empirical relations from Pettini & Pagel (2004, hereafter PP04). PP04 fit the relations between various emission line ratios and the T_e-based metallicity measurement for a sample of H II regions.

The PP04 'N2' method uses the ratio of [N II] λ6584 to Hα. As these lines are very close in wavelength space, this is a (nearly) reddening-free method, and covers both the upper-branch ($\log([\mathrm{N\,II}]/[\mathrm{O\,II}]) > -1.2$) and lower-branch ($\log([\mathrm{N\,II}]/[\mathrm{O\,II}]) < -1.2$) metallicities. The gas-phase metallicity $12 + \log(\mathrm{O/H})$ is given by

$$12 + \log(\mathrm{O/H}) = 9.37 + 2.03 \times \mathrm{N2} + 1.26 \times \mathrm{N2}^2 + 0.32 \times \mathrm{N2}^3 \tag{3.7}$$

where N2 is the [N II]/Hα line ratio. The PP04 relation is only valid for $-2.5 < \mathrm{N2} < -0.3$. Gas-phase metallicities for 53 galaxies in our sample can be derived using this method.

For those galaxies outside the valid range of the PP04 'N2' method, we follow the Kewley & Dopita (2002, hereafter KD02) method. Unlike the empirical PP04 cali-

bration, the KD02 technique is derived based on stellar evolution and photoionisation models. For the upper branch metallicities, we use the ratio of [N II] and [O II] λ3727, which is given by

$$\log\left([\mathrm{N\,II}]/[\mathrm{O\,II}]\right) = 1107 - 532Z + 96.4Z^2 - 7.8Z^3 + 0.24Z^4 \tag{3.8}$$

where Z is the gas-phase metallicity $12+\log(\mathrm{O/H})$. The equation above is computed assuming an ionisation parameter $q = 2\times10^7\,\mathrm{cm\,s^{-1}}$, although as KD02 pointed out, this relation is insensitive to the ionisation parameter for $\log([\mathrm{N\,II}]/[\mathrm{O\,II}]) > -1.2$. We solve for Z using the IDL task FZ_ROOTS.

For the lower-branch metallicity, KD02 recommend averaging two methods based on the R_{23} ratio: the McGaugh (1991, hereafter M91) and Kobulnicky & Kewley (2004, hereafter KK04) relations, which are given by

$$12+\log(\mathrm{O/H})_{\mathrm{M91}} = 12-4.944+0.767x+0.602x^2-y(0.29+0.332x-0.331x^2) \tag{3.9}$$

and

$$12+\log(\mathrm{O/H})_{\mathrm{KK04}} = 9.40+4.65x-3.17x^2-\log q(0.272+0.547x-0.513x^2) \tag{3.10}$$

where $x = \log R_{23}$ and $y = \log([\mathrm{O\,III}]\lambda4959,5007/[\mathrm{O\,II}])$. The quantity q represents the ionisation parameter. The detail of determining the ionisation parameter can be found in KE08. For the 29 galaxies where metallicities are unavailable via the PP04 N2 method, 19 can be calibrated following KD02. The 10 other galaxies show no detectable emission lines available for the metallicity calibration.

As previous studies have noted, offsets may exist between these different metallicity calibrations. Here we convert all the metallicities to the PP04 N2 calibration using the conversion provided by KE08. However, we still found small systematics between

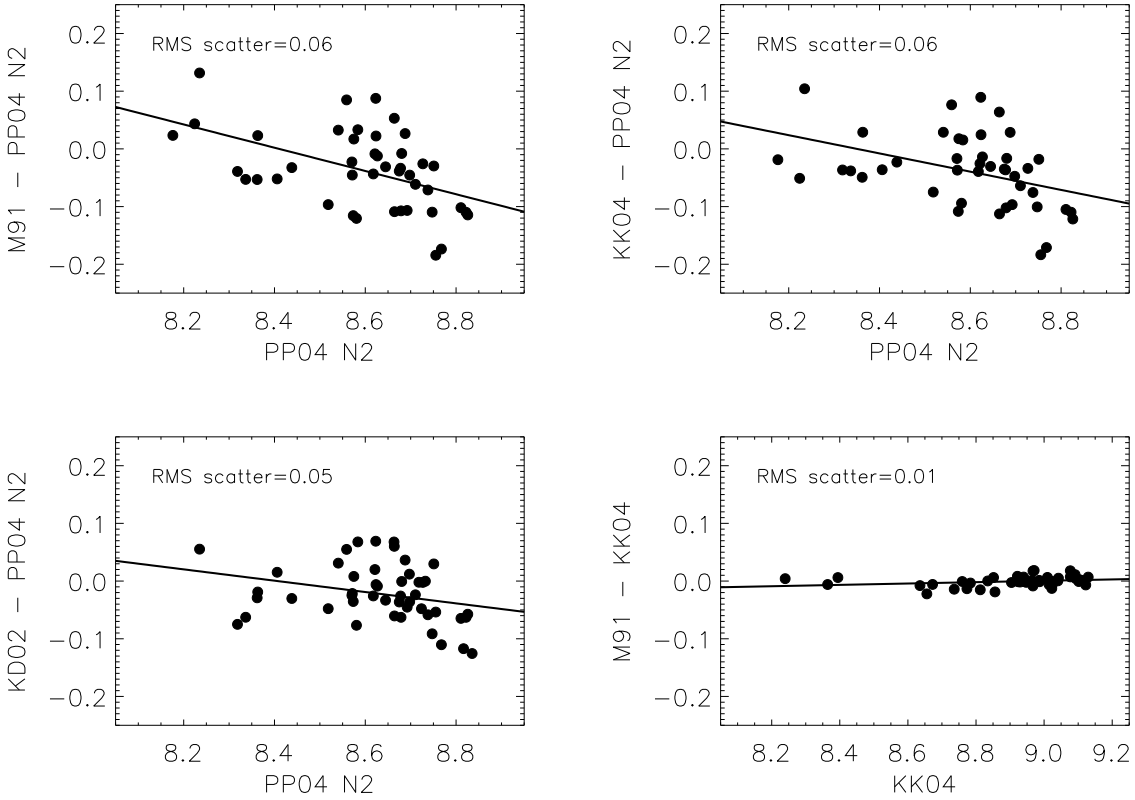

Figure 3.8: The metallicity conversions used in this work. We convert the metallicities derived by M91, KK04 and KD02 to PP04 N2, which is the calibration used for our host galaxy data. In each plot we use the best linear fit (solid line) and scatter to represent the accuracy of the conversion.

Table 3.3: The linear equations performed in Fig. 3.8. The parameter Δ is the offset between metallicities (Z) from three different calibrations (M91, KK04 and KD02) and PP04 N2.

metallicity (Z_i)	offset ($\Delta_i = Z_i - Z_{\rm PP04N2}$)
$Z_{\rm KD02}$	$\Delta_{\rm KD02} = -0.098 Z_{\rm N2} + 0.826$
$Z_{\rm M91}$	$\Delta_{\rm M91} = -0.202 Z_{\rm N2} + 1.696$
$Z_{\rm KK04}$	$\Delta_{\rm KK04} = -0.158 Z_{\rm N2} + 0.321$

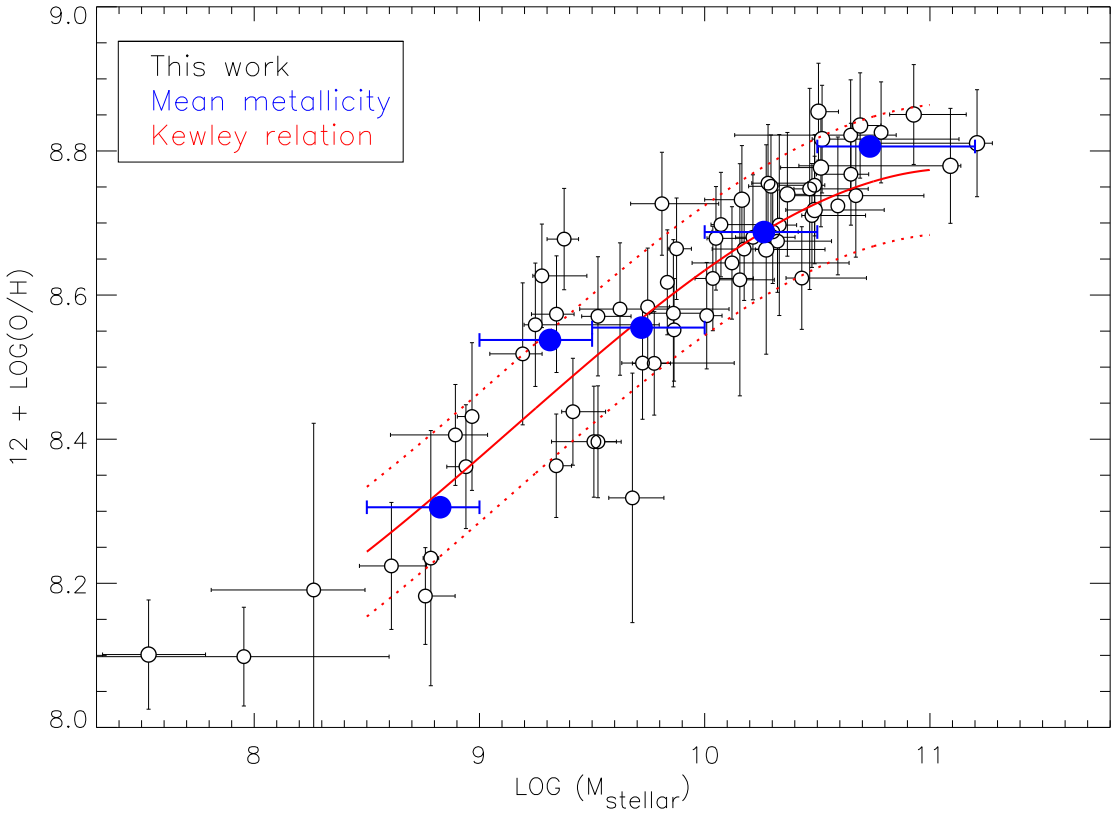

Figure 3.9: The $M_{\rm stellar}$–metallicity relation derived for our host galaxy sample. The red solid line is the best fit of mass–metallicity relation from KE08 using the PP04 N2 metallicity calibration. The red-dotted lines represent the rms residuals from the best fit to field galaxies. The mean metallicity (blue filled-circle) in each bin is also computed.

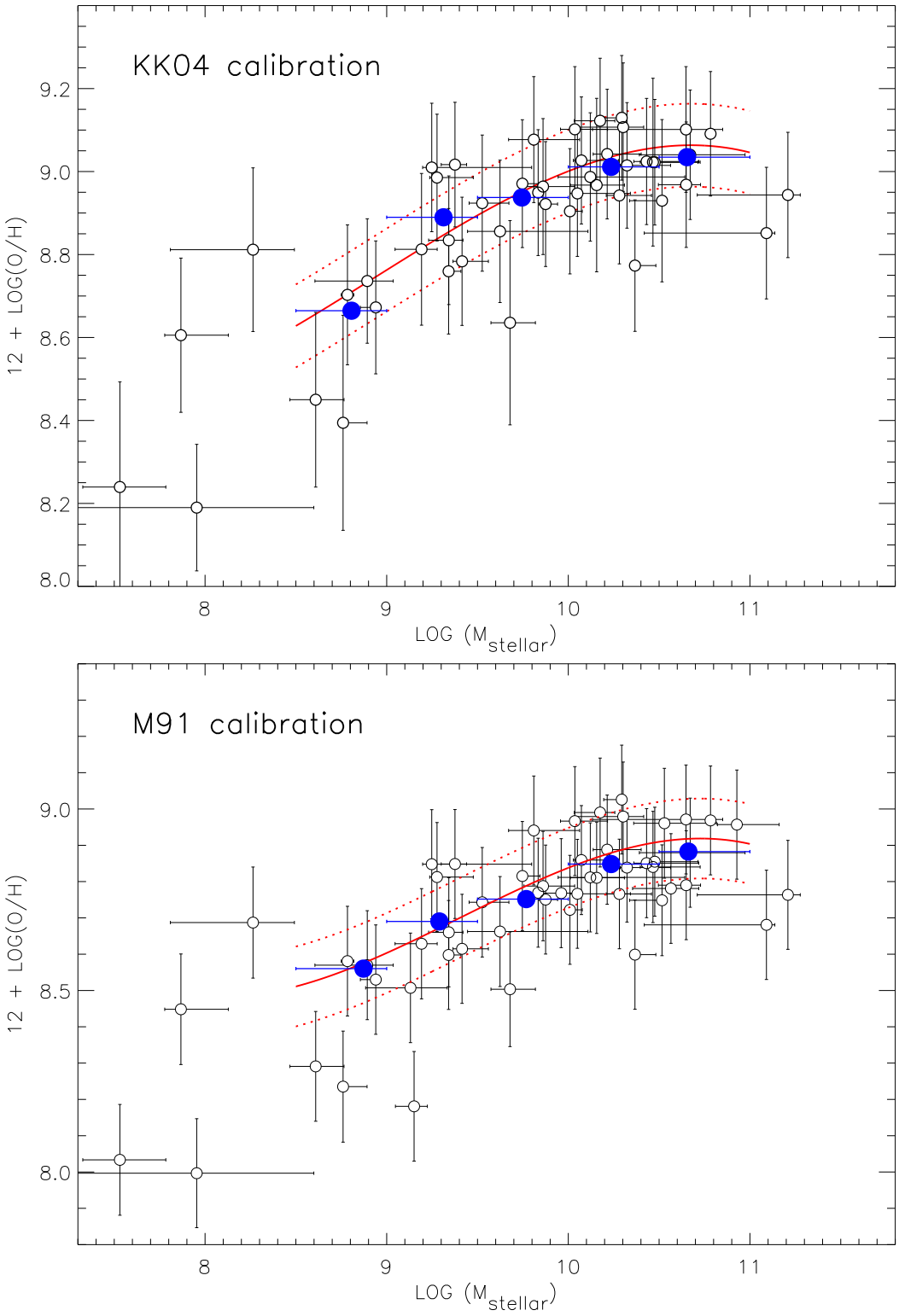

Figure 3.10: The same as Fig. 3.9, but considering the KK04 (top panel) and M91 (bottom panel) metallicity methods.

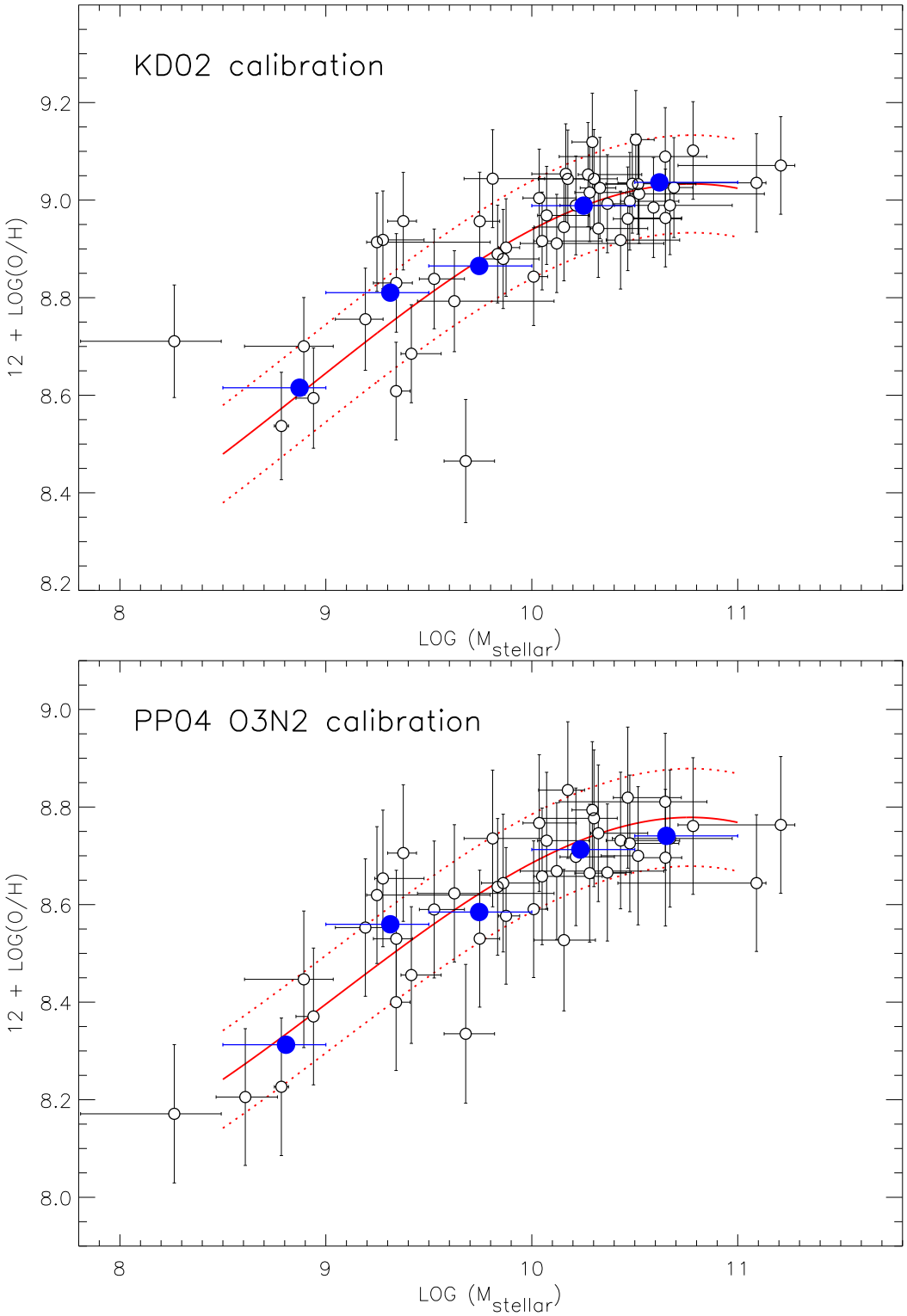

Figure 3.11: The same as Fig. 3.9, but considering the KD02 (top panel) and PP04 O3N2 (bottom panel) metallicity methods.

different metallicity calibrations after applying the KE08 conversions. For galaxies where it is possible to make more than one metallicity measurement, we compare the results directly. This is shown in Fig. 3.8; the different calibrations after applying a linear fit compare well. It is also obvious that the metallicities calibrated by similar methods (e.g., M91 and KK04; R_{23} method) have the least dispersion after the conversion. The observed rms scatters are (this work/KE08): 0.06/0.07, 0.06/0.07, 0.05/0.05 and 0.01/0.02 for the M91–PP04, KK04–PP04, KD02–PP04 and M91–KK04 relations, respectively. The best-fitting linear trends (the difference between two different metallicity calibrations) are applied to our metallicity measurements, although they have no significant effects on the final results. In Table 3.3 we list the linear equations used in this work. Finally, in Fig. 3.9 we plot our metallicities as a function of $M_{\rm stellar}$ (the 'mass–metallicity relation'). The mass–metallicity relation studied by KE08 using the PP04 N2 method is over-plotted for comparison. For consistency, in this plot we have adopted the same IMF (Kroupa, 2001) and cosmology ($\rm H_0 = 72\,km\,s^{-1}\,Mpc^{-1}$ and $\Omega_{\rm M} = 0.29$) as used by KE08 for the measurement of $M_{\rm stellar}$. Apart from the PP04 N2 calibration, we also test the mass–metallicity relation using other calibrations, including KK04 and M91 calibrations in Fig. 3.10, and KD02 and PP04 O3N2 calibrations in Fig. 3.11. It is clear that our SN Ia host galaxies follow a very similar mass–metallicity relation as that of KE08.

3.3.4 Stellar metallicity and age

The stellar metallicity and age are normally determined using absorption features in the spectrum. One widely used method is the Lick/IDS system (Worthey, 1994; Trager et al., 1998). Recently, with the availability of high-quality model templates, the 'full spectrum fitting' method has become a popular alternative (e.g. Cid Fernandes et al., 2005; Koleva et al., 2009) to study the stellar populations, as it exploits more spectral information than just individual line indices.

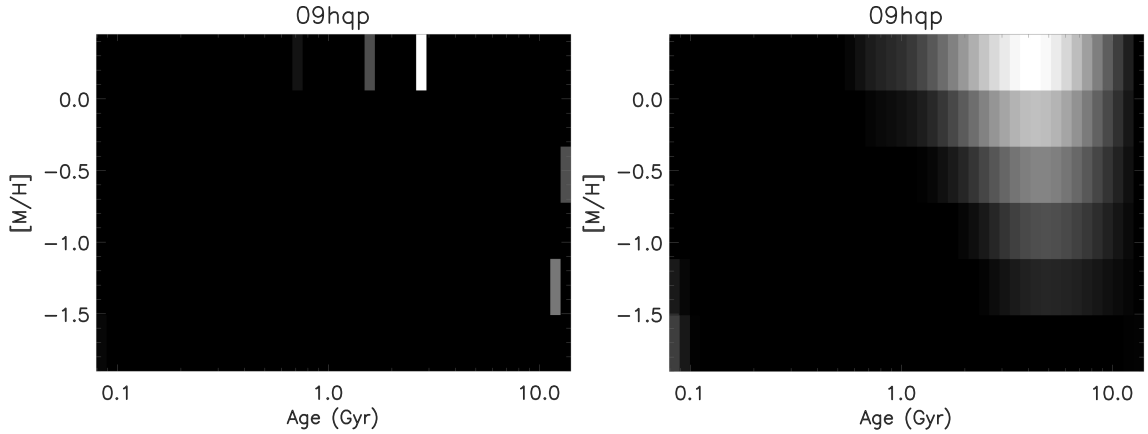

Figure 3.12: A grid of total 276 stellar templates (a combination of 6 metallicities and 46 ages) used for PPXF fitting. The weight of each template is represented by the strength of the colour. The templates with more weights are brighter. We present here the PPXF fitting for PTF09hqp without regularisation (left panel) and with regularisation (right panel).

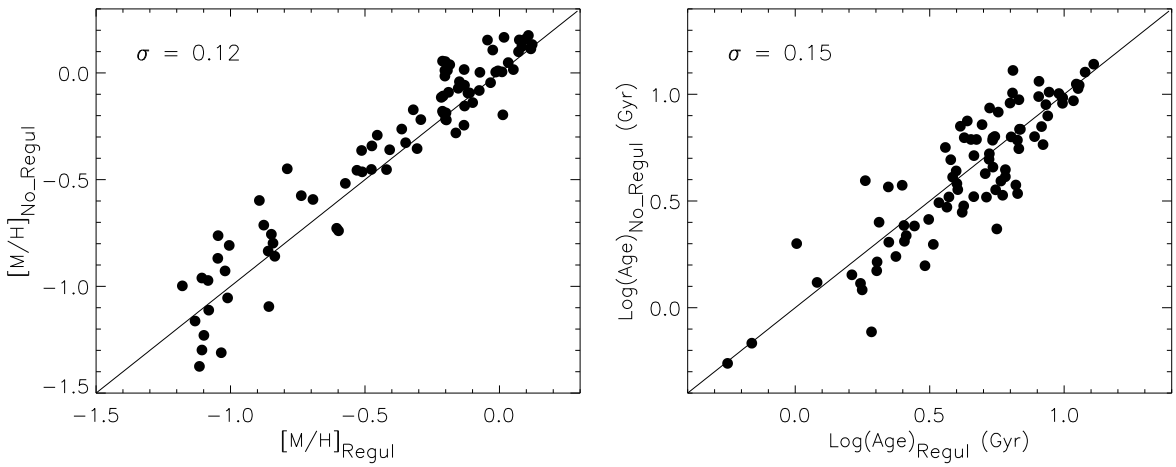

Figure 3.13: Left panel: The comparison of mean stellar metallicities determined with or without regularisation. The line of equality is shown in solid line. Right panel: The same as left panel, but using mean stellar ages instead.

In this study we use PPXF to fit the stellar continuum of our host spectra. Basically the procedure is the same as described in Section 3.1 but fits only the stellar continuum component. The same MILES templates described are used. One feature of PPXF is the linear regularisation performed during the fit, which can help smooth the weights of the best-fit templates (the weights are the output of the fitting process). However, this feature must be used with caution, as it is a trade-off between the smoothness and goodness of the fit. Following the procedure described in Press et al. (1992), the regularisation parameter for each host galaxy was determined such that the resulting fit was consistent with the observations, but also gave a smooth star formation history. An example of the effect of regularisation on spectral fitting can be seen in Fig. 3.12. We found the solution without regularisation being performed is dominated by few stellar templates with quite distinct properties. By contrast, we get a smoother solution of model templates after performing the regularisation, which makes more sense and is closer to the real physical situation. We estimate the stellar metallicity and age by performing a weighted-average of all the model templates, given by

$$\langle \log t \rangle = \sum_{i=1}^{N} w_i \times \log t_i \tag{3.11}$$

and

$$\langle [\mathrm{M/H}] \rangle = \sum_{i=1}^{N} w_i \times [\mathrm{M/H}]_i, \tag{3.12}$$

where $\log t_i$, $[\mathrm{M/H}]_i$ and w_i represent the stellar age, stellar metallicity and weight of the ith template. The $\langle \log t \rangle$ and $\langle [\mathrm{M/H}] \rangle$ are the mass-weighted age and metallicity over the N templates used to fit the spectrum. Here we estimated the uncertainty by examining the dispersion between the results with and without regularisation (Fig. 3.13). An uncertainty of 0.12 dex and 0.15 dex was determined and added to [M/H] and stellar age, respectively.

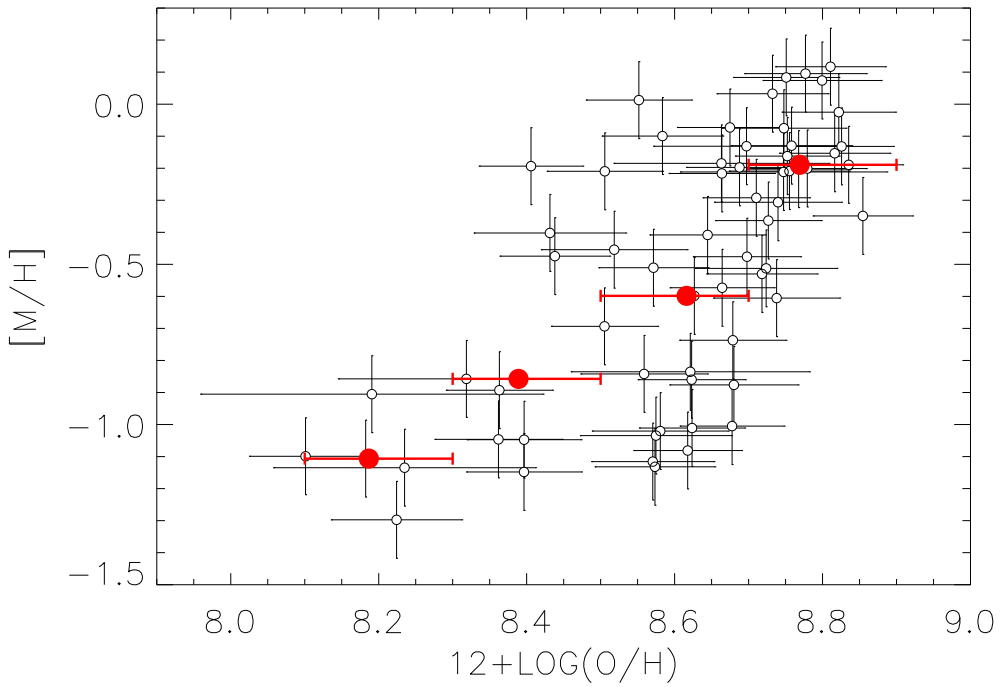

Figure 3.14: The host stellar metallicity as a function of gas-phase metallicity. The median metallicity in each bin with bin size = 0.2 dex is computed and shown as red filled-circles.

As the stellar ages and metallicities of the SN Ia hosts determined in this work are weighted by the mass of their stellar populations, they are most sensitive to the dominant populations (based on their masses) inside the host galaxies. This method may not be optimal to estimate the age and metallicity of the SN Ia progenitor as there is evidence that the SN Ia rate is also proportional to the star formation rate of the host galaxy (Mannucci et al., 2005, 2006; Sullivan et al., 2006; Smith et al., 2012); i.e., SNe Ia are more easily found in younger stellar populations. A more sophisticated method/weighting which considers the star formation history of each stellar population may be necessary to precisely constrain the age and metallicity of the SN Ia progenitor. Previous studies (e.g., Johansson et al., 2013) adopted the simple luminosity-weighted host parameters (i.e., they may be dominated by the youngest stellar populations), and our results in later sections are consistent with these studies.

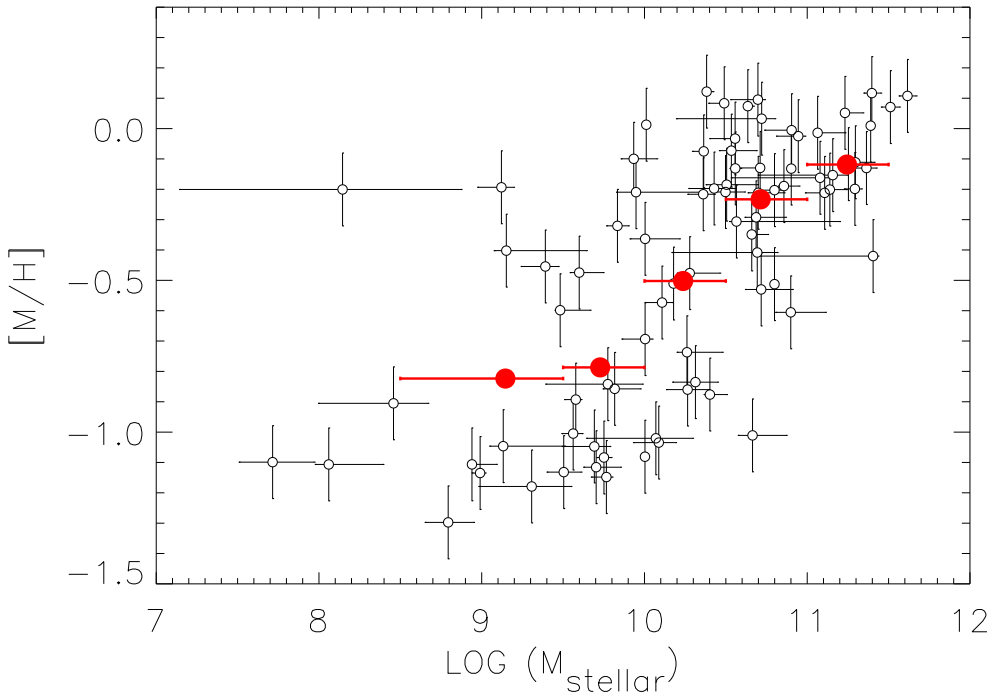

Figure 3.15: The host stellar metallicity as a function of $M_{\rm stellar}$. The mean metallicity in each bin is computed and shown as red filled-circles.

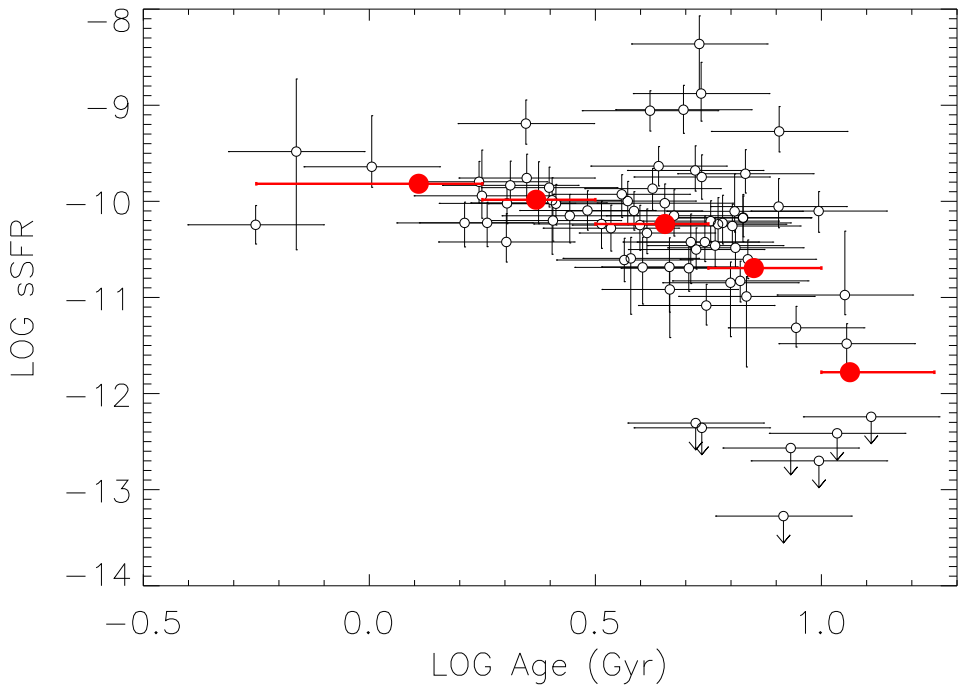

Figure 3.16: The host stellar age as a function of specific star-formation rate (sSFR). The mean metallicity in each bin is computed and shown as red filled-circles.

A comparison between the host gas-phase and stellar metallicities can be found in Fig. 3.14. It is clear that the two metallicities scale with each other with a positive Pearson correlation coefficient ~ 0.67. Similar to gas-phase metallicity, the stellar metallicities also present a tight relation with host $M_{\rm stellar}$ as shown in Fig. 3.15. In Fig. 3.16, we plot the host stellar age as a function of specific star-formation rate (sSFR), the SFR per unit $M_{\rm stellar}$ (Guzman et al., 1997). As expected, there is a strong trend that galaxies with older stellar populations tend to have a lower sSFR than young populations.

3.3.5 SN offset

We measure the SN offset ($\rm R_{SN}$) from its host galaxy. $\rm R_{SN}$ is defined as the separation (i.e., radial distance) between the SN position and the host galaxy centre. The coordinate of the SN position was measured as a product of P48 SN photometry procedure (Section 2.2) using a point-spread-function (PSF) fitting method, and the centre of host galaxy was estimated using SEXTRACTOR (Bertin & Arnouts, 1996) on the $R_{\rm P48}$ or $g_{\rm P48}$ reference images. Fig. 3.17 shows examples of the reference images used in this work. We examine the potential hosts in the reference images by crosschecking the same field in SDSS database. By doing this, we can check the object type identified by the SDSS database and avoid measuring objects other than galaxies. Therefore we only measured the hosts which are covered by the SDSS footprint.

These offsets are projected offsets, and so we investigate the possibility of deprojecting the offsets using our data. We can approximately deproject the SN offset using the position angle and axial ratio of the host galaxy measured by SEXTRACTOR. Following the procedure described in Hakobyan et al. (2009), the coordinates of SN

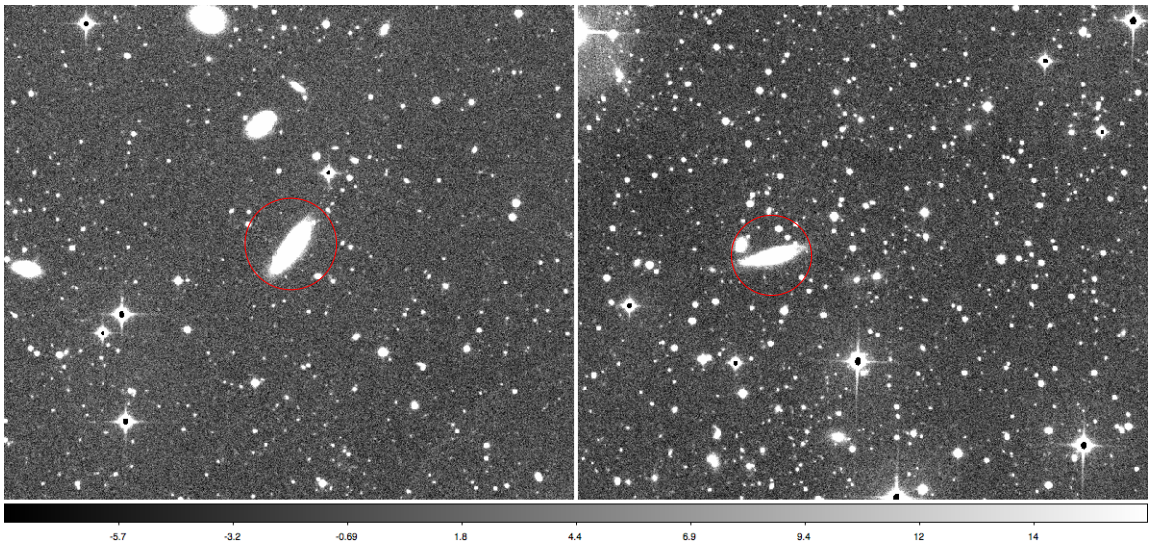

Figure 3.17: Examples of P48 R-band images. The red open circles mark the host galaxies of PTF10ygu (left panel) and PTF10fxl (right panel).

with respect to its host galaxy can be represented as

$$\begin{aligned} U &= \Delta\alpha \sin\theta + \Delta\delta \cos\theta \\ V &= \Delta\alpha \sin\theta - \Delta\delta \cos\theta \end{aligned} \tag{3.13}$$

where U and V are the coordinates of SN along major and minor axes of host galaxies, respectively. $\Delta\alpha$ and $\Delta\delta$ are the SN offsets in Right ascension and Declination from the centre of the host galaxy in the equatorial coordinate system. θ is the position angle of the host galaxy measured from north through the east. The radial distance of SN relative to the host centre can then be computed as

$$R_{SN} = U^2 + (\frac{V}{\cos i})^2 \tag{3.14}$$

where the angle i represents the inclination of the host galaxy, which is given by (Hubble, 1926):

$$\cos^2 i = (q^2 - q_0^2)/(1 - q_0^2) \tag{3.15}$$

where q represents the axial ratio of the host galaxy (i.e., the length of minor axis to major axis), and q_0 is the minimum axial ratio that the galaxy should be considered as edge-on (i.e., $i = 90°$). Here we choose to use the conventional value $q_0 = 0.2$ (Tully & Fisher, 1977) to compute the inclination of our host galaxies.

This correction is only valid for disk galaxies with moderate inclinations, and no corrections should be made for elliptical galaxies or disk galaxies with very large inclinations (i.e., nearly edge-on). Compared to other SN studies using host galaxies with very low-redshift (e.g., $z < 0.05$ in Wang et al. (2013)), our host galaxies are generally more distant and smaller in their apparent sizes (e.g., the median of the width of our host galaxies along their major axes is $\sim 0.13'$, compared to the galaxies studied in Wang et al. (2013) of a typical size $\sim 1.3'$). This introduces difficulties in classifying these galaxies and thus further increases the uncertainties in deprojecting the SN offsets. Furthermore, we found our results presented in later sections are not sensitive to the correction, and therefore no deprojection is applied for the host galaxies in this work. We also measure a typical size of each of the host galaxies R_{gal}, defined as the radius at which 90% of the flux from the galaxy is enclosed. We then use R_{gal} to normalise the SN offset.

3.4 Summary

In this chapter, we have presented the methods to fit the host galaxy spectrum. The stellar continuums and emission lines were fit by IDL code PPXF and GANDALF, using the stellar model templates provided by the MILES empirical stellar library. We also performed the AGN diagnostics to eliminate the potential AGN host galaxies in our sample from emission line analysis.

We have determined the host stellar mass ($M_{stellar}$) using the photometric data from the SDSS database. The photometric redshift code ZPEG was used to fit the

host photometry. The star-formation rates (SFRs) were determined from the Hα luminosity. We estimated the gas-phase metallicities using the PP04 N2 empirical calibration. The mean (mass-weighted) stellar metallicities and ages were determined by fitting the full stellar continuum with PPXF. Finally, we measured the SN offset from its host centre.

In the next chapter, we will investigate the relations between SN light curve parameters and their host galaxies. The effect of host parameters on SN stretch, colour and luminosity will be discussed.

Chapter 4

SN luminosities and host parameters

Having measured various physical parameters of the PTF SN Ia host galaxies from their spectra and broad-band photometry, we now compare these parameters with the photometric properties of the SNe. We take each of the three key SN Ia properties in turn – stretch (light curve width), optical colour, and luminosity – and compare with the $M_{\rm stellar}$, the SN offset, the gas-phase metallicity $12 + \log({\rm O/H})$, the stellar metallicity [M/H], the stellar age, and the specific SFR (sSFR, defined as ${\rm SFR}/M_{\rm stellar}$). Compared to the SFR, the sSFR is a more appropriate indicator to measure the relative star-formation activity of a galaxy as it measures the star-formation relative to the underlying galaxy stellar mass.

4.1 Host spectral sample

As described in Section 2.1.1, the SN Ia parent sample in this work consists of 527 events with redshift $z < 0.09$. There are 82 SNe Ia in the parent sample for which spectra of their host galaxies are available. The host spectroscopic observations and data reduction are discussed in Section 2.4. We presented the techniques used to fit the host spectrum, and determine the host parameters, in Chapter 3. Here we define these 82 SNe Ia as our host spectral sample, and they will be our main interest in the

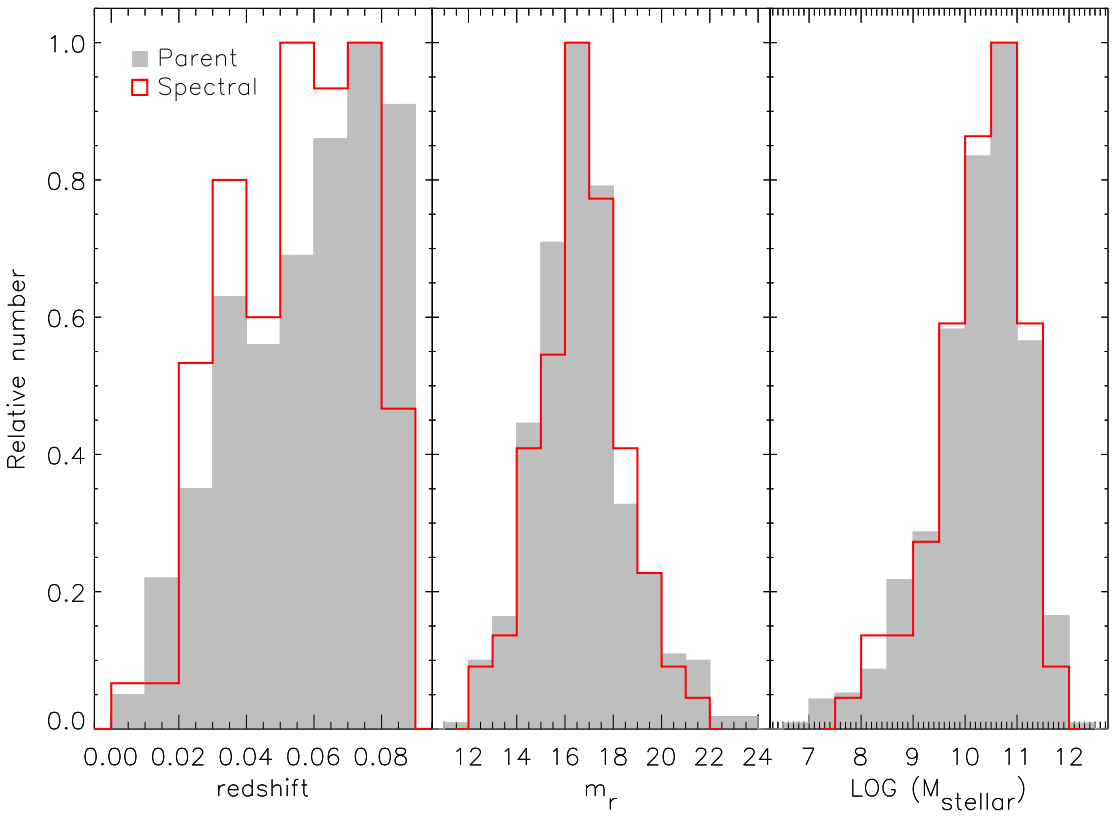

Figure 4.1: The normalised distribution in SN redshift, SDSS r-band host galaxy apparent magnitude (m_r), and host galaxy stellar mass ($M_{\rm stellar}$) of our host spectral sample (82 SNe Ia). The PTF SN Ia parent sample is shown as the filled grey histogram (527 SNe Ia in the redshift histogram, and 443 events in the m_r and $M_{\rm stellar}$ panels), and our host spectral sample as the open red histogram.

following sections.

Fig. 4.1 shows a comparison of the distributions of our host spectral sample and parent PTF sample in redshift, host galaxy r-band apparent magnitude (m_r), and host galaxy stellar mass, $M_{\rm stellar}$. The parent sample shown in Fig. 4.1 contains the 527 $z < 0.09$ PTF SNe Ia, although only 443 of these have Sloan Digital Sky Survey (SDSS) or LT imaging data from which $M_{\rm stellar}$ estimates could be made (Section 2.4.1). A K-S test gives a 35, 77 and 99 percent probability that our host spectral sample and the larger PTF parent sample are drawn from the same population in redshift, m_r, and $M_{\rm stellar}$. Thus we find no strong evidence that our host spectral sample is biased with respect to the larger PTF parent sample.

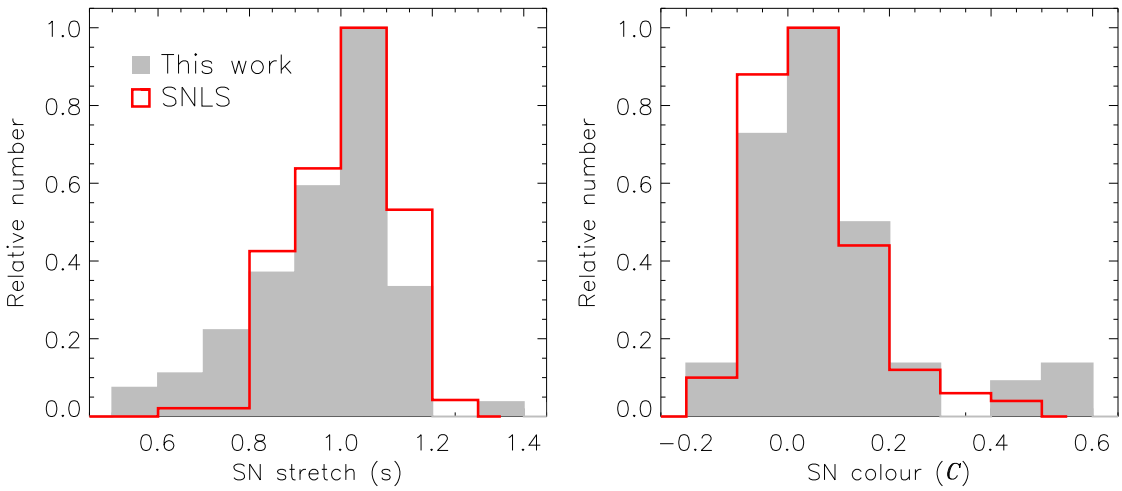

Figure 4.2: The grey filled histograms show the SN stretch (s) and colour ($\mathcal{C}$) distributions of our host spectral sample (see Section 2.2 for more details). The SNLS sample of Guy et al. (2010) at $z < 0.6$ is over-plotted in the red open histogram.

Fig. 4.2 shows the distribution of our SNe Ia in stretch and colour. As a comparison, we over-plot the higher-redshift Supernova Legacy Survey (SNLS) sample studied by Guy et al. (2010) for SNLS events at $z < 0.6$ where the SNLS sample is more complete (Perrett et al., 2010). We generally find a good agreement in the stretch and colour distributions, although our sample probes faster (lower stretch) and redder SNe Ia than SNLS.

In the later sections, we will assess the significance of various relations between the SN light curve properties and their host galaxies. In each case we split the sample into two groups. A value of $\log(\mathrm{M/M_\odot}) = 10.0$ is used to split between the high- and low-M_{stellar} sample, and $12 + \log(\mathrm{O/H}) = 8.65$ and $[\mathrm{M/H}] = -0.5$ are used (based on the mass-metallicity relation in Fig. 3.9 and relation between gas-phase and stellar metallicities in Fig. 3.14) to split between high- and low-metallicity hosts. For the stellar age, SFR and sSFR, the split points were selected to make approximately equally sized sub-groups (e.g., Sullivan et al., 2010). The weighted mean of the measurements in each group are calculated. The error of the weighted-mean was corrected to ensure a $\chi^2_{\mathrm{red}} = 1$. The linear fitting is performed by using the Monte Carlo Markov Chain

(MCMC) method LINMIX (Kelly, 2007). To examine the correlation of the relations, both the Pearson and Kendall correlation coefficients are also calculated.

4.2 SN Ia stretch

The stretch of a SN Ia is a direct measurement of its light curve width, a key parameter in the calibration of SNe Ia as distance estimators (Phillips, 1993) — brighter SNe Ia have slower light curves (a broader width or higher stretch) than their fainter counterparts. We can directly relate the SN stretch (s) derived from SiFTO (Section 2.2) to the SN light curve decline rate (Δm_{15}: total amount in magnitudes a SN decays in its B-band light curve over the 15 days past peak luminosity; Phillips, 1993), via the relation provided by Conley et al. (2008):

$$\Delta m_{15} = 1.00 - 1.63 \times (s-1) + 2.03 \times (s-1)^2 - 1.82 \times (s-1)^3 \quad (4.1)$$

Here we restrict our analysis to SNe Ia with $0.7 < s < 1.3$, typical of SNe Ia that are used in cosmological analyses (Conley et al., 2011). This removes one high-stretch and five low-stretch (sub-luminous) SNe from our SN spectral sample, including the peculiar event PTF09dav (Sullivan et al., 2011a).

The SN stretch as a function of the host spectral parameters can be found in Fig. 4.3 and Fig. 4.4. The trend calculated for each case is listed in Table 4.1. When comparing with $M_{\rm stellar}$, we recover the trend seen by earlier studies that lower stretch ($s < 1$) SNe Ia are more likely to be found in massive galaxies than higher stretch ($s \geq 1$) SNe Ia (Howell et al., 2009; Neill et al., 2009; Sullivan et al., 2010). The SNe Ia in the high-$M_{\rm stellar}$ bin ($\log(M/M_\odot) > 10$) are fainter than those in low-mass galaxies ($\log(M/M_\odot) < 10$) at 4.3σ significance. Bearing in mind that gas-phase and stellar metallicity strongly correlate with $M_{\rm stellar}$ (e.g. Tremonti et al., 2004; Gallazzi et al., 2005), a similar trend is expected between stretch and metallicity, which is

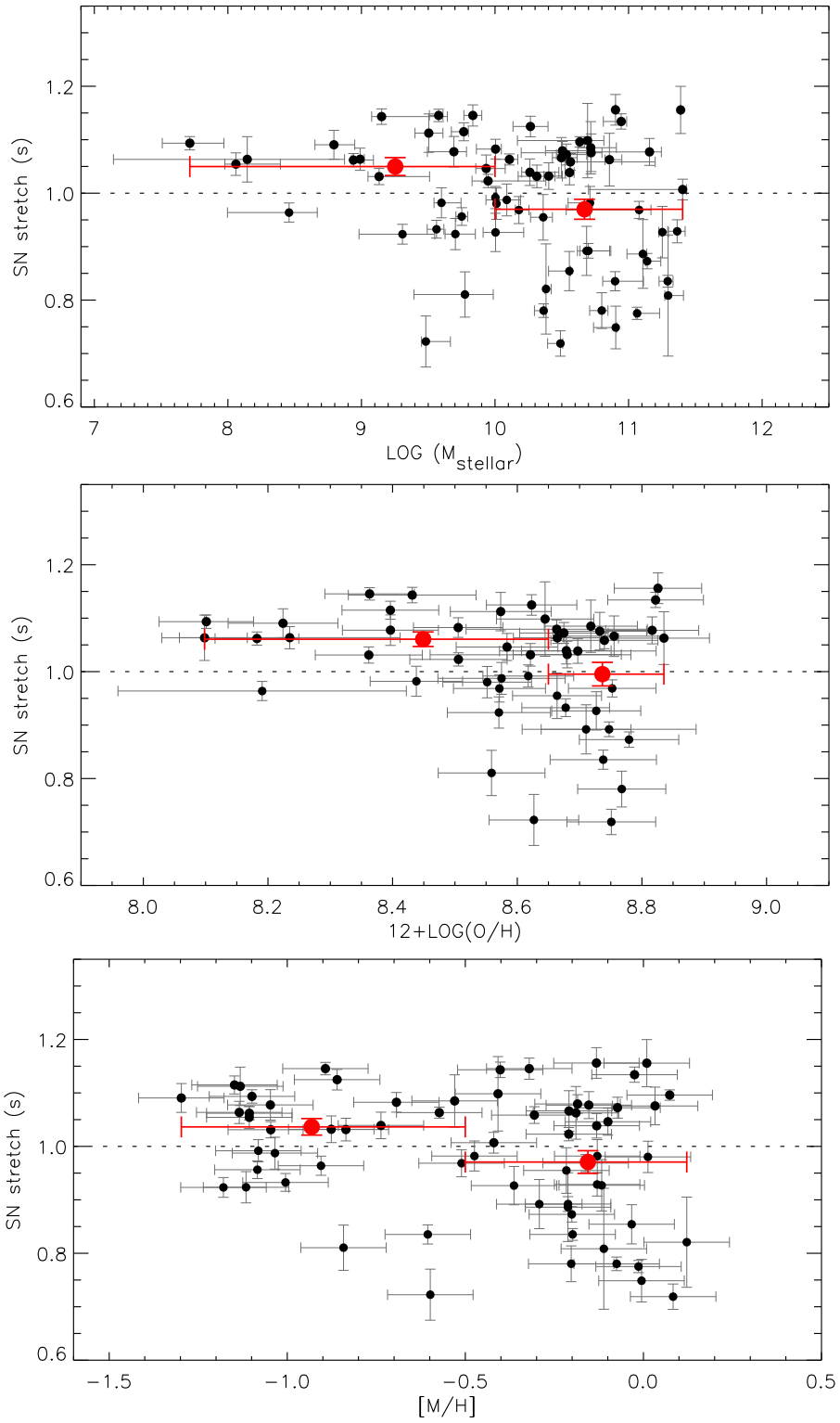

Figure 4.3: The SN stretch s as a function of host $M_{\rm stellar}$ (top panel), gas-phase metallicity (middle panel), mass-weighted mean stellar metallicity (bottom panel). The red solid circles represent the mean stretch in bins of host parameters.

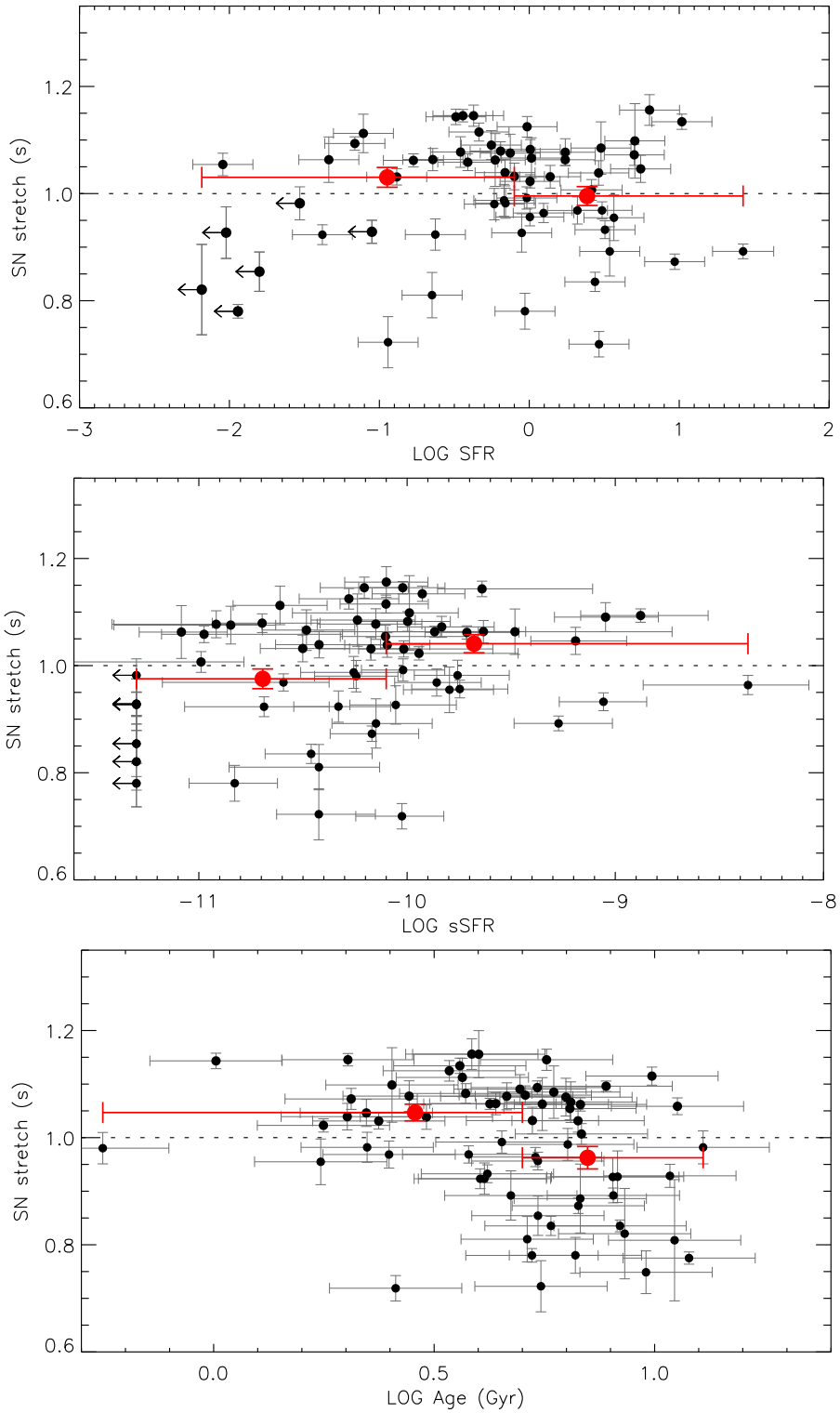

Figure 4.4: The SN stretch s as a function of host SFR (top panel), specific SFR (sSFR; middle panel), and mass-weighted mean stellar age (bottom panel). The red solid circles represent the mean stretch in bins of host parameters.

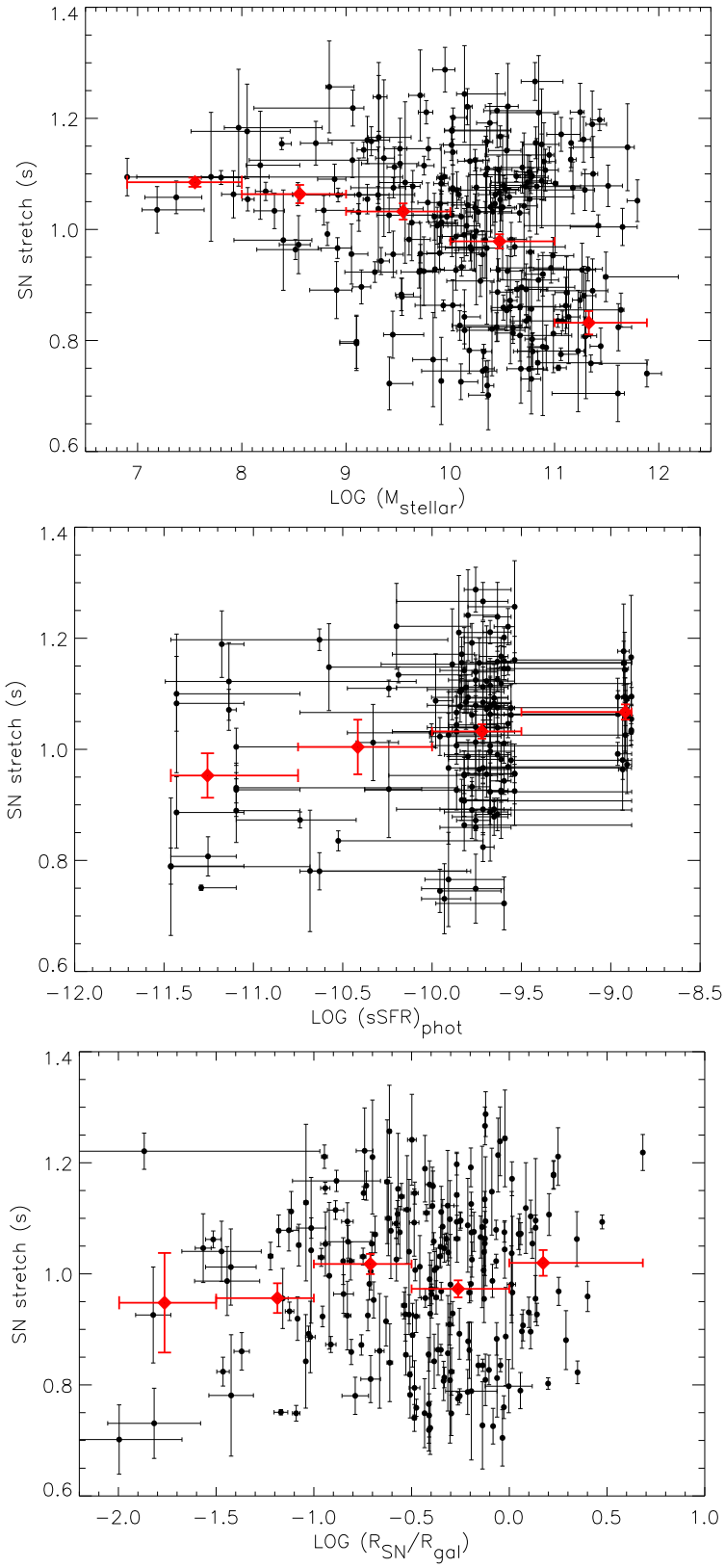

Figure 4.5: The SN stretch s as a function of host $M_{\rm stellar}$ (top panel), specific SFR (sSFR; middle panel) determined by Z-PEG, and SN offset (bottom panel) for the PTF parent sample. The red solid circles represent the mean stretch in the bin of host parameters.

both observed here (middle and bottom panels in Fig. 4.3) and has previously been described in the literature: low-metallicity galaxies preferentially host brighter SNe Ia (before light curve shape correction) than metal-rich galaxies (Gallagher et al., 2005; D'Andrea et al., 2011; Johansson et al., 2013; Childress et al., 2013a). The SNe Ia in metal-rich galaxies are fainter than their counterparts at 2.5σ significance for both gas-phase and stellar metallicities. The data also show that higher-stretch SNe Ia preferentially explode in younger galaxies (at 3.2σ significance), to the extent that there are few low stretch SNe in hosts with mass-weighted mean ages of less than $\sim 4\,\mathrm{Gyr}$. This is consistent with the previous results of Gallagher et al. (2005) and Johansson et al. (2013), who used individual line indices to estimate the stellar ages of host galaxies. They also found the brighter SNe Ia appear to be explode in younger populations. The recent study of Rigault et al. (2013) showed that the relation between SN stretch and M_{stellar} is primarily driven by age, as measured by local SFR. We also see a moderate trend with sSFR in the sense that galaxies with a higher sSFR tend to host brighter SNe Ia (at 3.1σ significance). No significant correlation is found with SFR.

Apart from the 82 SNe in our host spectral sample, we also show the relations with host parameters determined by photometric data (e.g., M_{stellar} and sSFR from Z-PEG, and the SN offset) in Fig. 4.5. It extends the sample size from 82 SNe Ia to the whole parent sample of this work. The top and middle panel of Fig. 4.5 show the SN stretch as a function of host M_{stellar} and sSFR determined by Z-PEG. Similar to the smaller spectral sample, we still see clear trends with the larger sample size. More massive or lower sSFR galaxies tend to host fainter SNe Ia than their counterparts. We do not see any trend with SN offset.

Table 4.1: The trend of SN stretch/colour with host parameters.

		SN stretch (s)		SN colour ($\mathcal{C}$)	
	Split point	N_{SN}	bin difference	N_{SN}	bin difference
$M_{\rm stellar}$	$10^{10}\,M_\odot$	68	0.08 (4.3σ)	55	0.05 (2.5σ)
12+log(O/H)	8.65	50	0.07 (2.5σ)	40	0.05 (2.5σ)
[M/H]	-0.5	67	0.07 (2.5σ)	55	0.06 (3.1σ)
Age	5 Gyr	67	0.08 (3.2σ)	55	0.01 (0.7σ)
SFR	$0.8\,M_\odot\,yr^{-1}$	65	0.03 (1.4σ)	52	0.03 (1.3σ)
sSFR	$7.9\times10^{-11}\,yr^{-1}$	65	0.08 (3.1σ)	52	0.03 (1.2σ)

4.3 SN Ia colour

We next examine the trends with SN Ia colour ($\mathcal{C}$). The colour is defined as the SN $B-V$ colour at B-band maximum light (Section 2.2). The SN colour is also a crucial parameter in calibrating their luminosities, as previous studies found that the SN optical colours are related to their peak luminosities in the sense that redder SNe Ia tend to be fainter than their bluer counterparts (Riess et al., 1996; Tripp, 1998). As for the stretch comparisons, we restrict the SNe to a typical colour range used in cosmological studies ($\mathcal{C} < 0.4$). This removes five red SNe Ia from our host spectral sample.

The SN colour as a function of the host spectral parameters can be found in Fig. 4.6 and Fig. 4.7. The SN colours as a function of $M_{\rm stellar}$ show a trend that SNe Ia in more massive galaxies are redder than those in low-mass galaxies (at 2.5σ significance). Both gas-phase and stellar metallicities also show correlations with SN colour with SNe Ia tending to be redder in galaxies of higher metallicity (at 2.5σ and 3.1σ significance, respectively). As star-forming galaxies are expected to contain more dust than passive galaxies, all other things being equal we would expect them to host redder SNe Ia. However, Fig. 4.7 does not show this effect; if anything SNe Ia in high-sSFR galaxies appear bluer ($\mathcal{C} < 0$) than those in low-sSFR galaxies. This may imply an intrinsic variation of SN colour with host environment that is greater than any reddening effect from dust. We do not see any trend with host stellar ages.

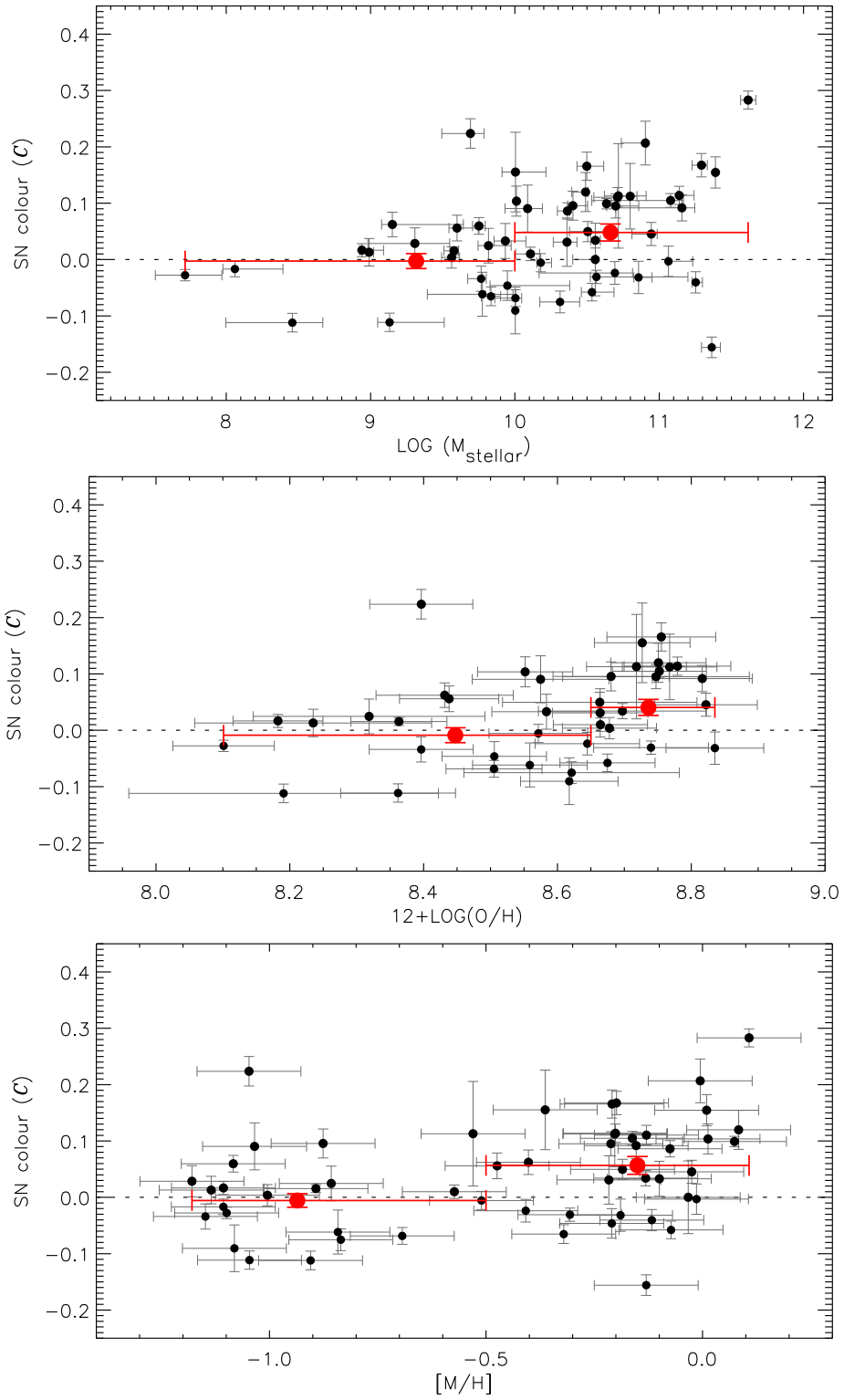

Figure 4.6: The SN colour $\mathcal{C}$ as a function of host $M_{\rm stellar}$ (top panel), gas-phase metallicity (middle panel), and mass-weighted mean stellar metallicity (bottom panel). The red solid circles represent the mean colour in bins of the host parameters.

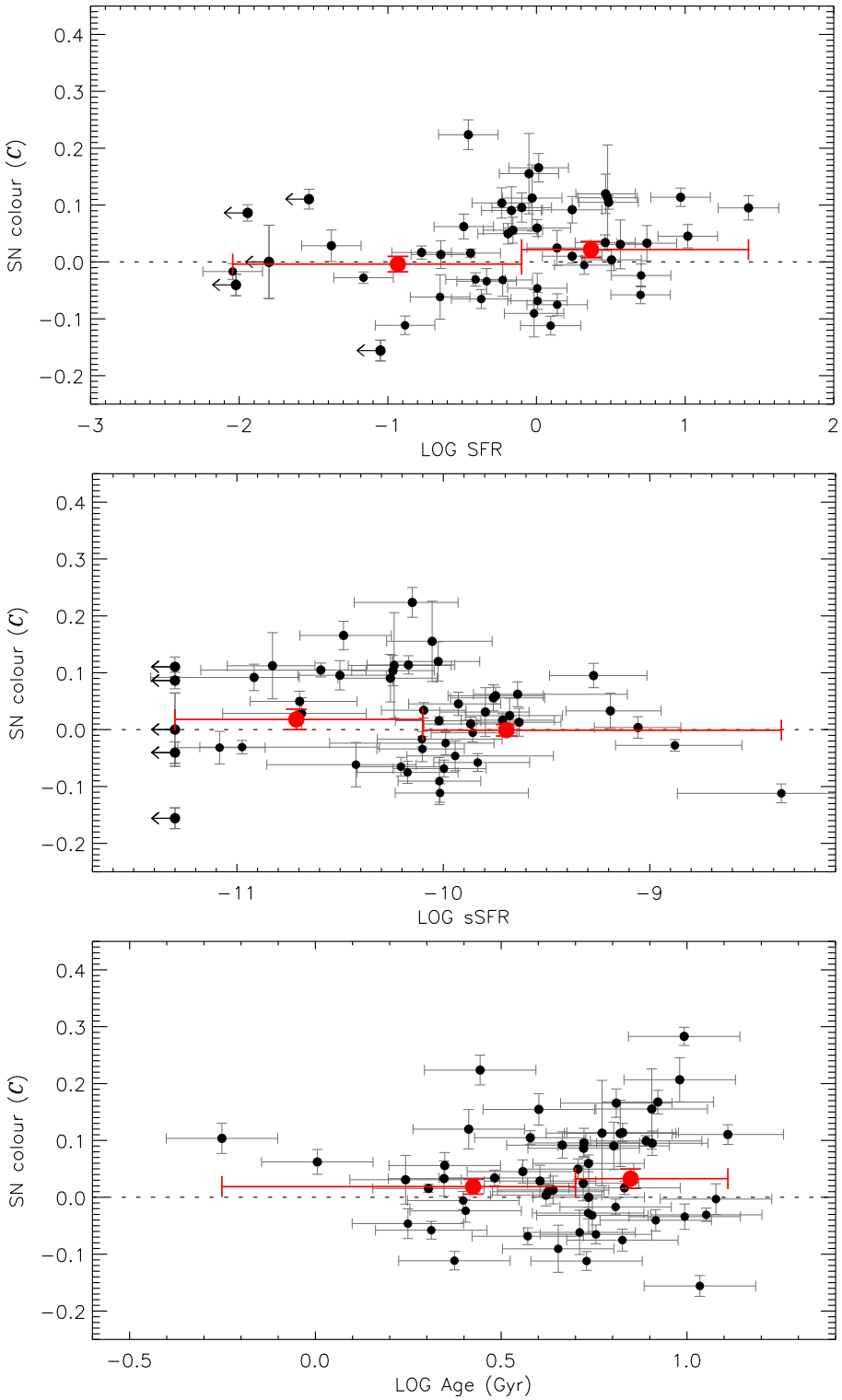

Figure 4.7: The SN colour $\mathcal{C}$ as a function of host SFR (top panel), sSFR (middle panel), and mass-weighted mean stellar age (bottom panel). The red solid circles represent the mean colour in bins of the host parameters.

In Fig. 4.8, we plot the SN colour as a function of the host parameters determined by Z-PEG (i.e., using host photometry). We do not see any trend with host sSFR or SN offset.

As we found in the beginning of this section, SNe Ia in high-metallicity and/or low-sSFR hosts appear to be redder. However, the SN colour discussed here (SiFTO $\mathcal{C}$) is not an 'intrinsic' SN colour, as dust extinction from the host galaxy may also contribute to the observed SN colour variation. Therefore it is useful to compare the SN colour measures to independent measures of host extinction to assess the effect of dust extinction from the host galaxies.

Fig. 4.9 shows the host colour excess $E(B-V)$ determined from the Balmer decrement as function of host parameters and SN colour. Mild correlations between $E(B-V)$ and the gas-phase metallicity/sSFR are found, with Pearson correlation coefficients of 0.39 and 0.36 for gas-phase metallicity and sSFR, respectively. However, we see no significant correlation with SN colour: the SN colour appears independent of the host galaxy $E(B-V)$. This independence becomes even more evident when including those red SNe Ia with $\mathcal{C} > 0.4$ previously excluded in this study.

There are two possibilities that could cause this. The first is that the bulk of the SN Ia colour variation is intrinsic to the SN event. Previous studies have shown that the SN Ia intrinsic colour could be altered systematically by changing the metallicity of the progenitor (Hoeflich, Wheeler, & Thielemann, 1998; Domínguez, Höflich, & Straniero, 2001). They showed that the line blanketing at shorter wavelength increases with the metallicity of the progenitor, and therefore results in redder SN Ia. There is some observational evidence for this: Childress et al. (2013a) recently showed that SNe Ia in high-metallicity hosts appear redder, and we also find a similar dependence of SN Ia colour on host gas-phase and stellar metallicities in Fig. 4.7.

A second possibility is that there is dust local to the SN explosion that affects the colour, for example circumstellar dust (Wang, 2005; Goobar, 2008; Amanullah &

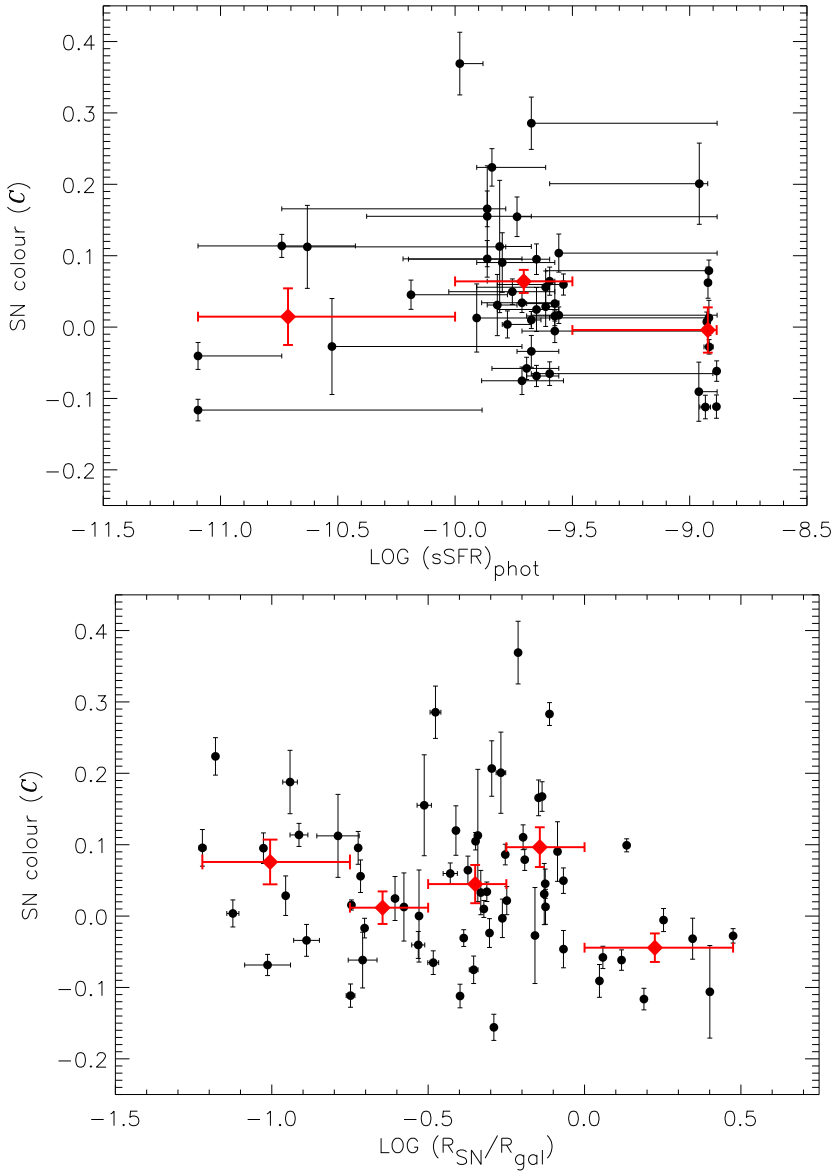

Figure 4.8: The SN colour $\mathcal{C}$ as a function of host specific SFR (sSFR; top panel) determined by Z-PEG, and SN offset (bottom panel) for the PTF parent sample. The red solid circles represent the mean stretch in bins of the host parameters.

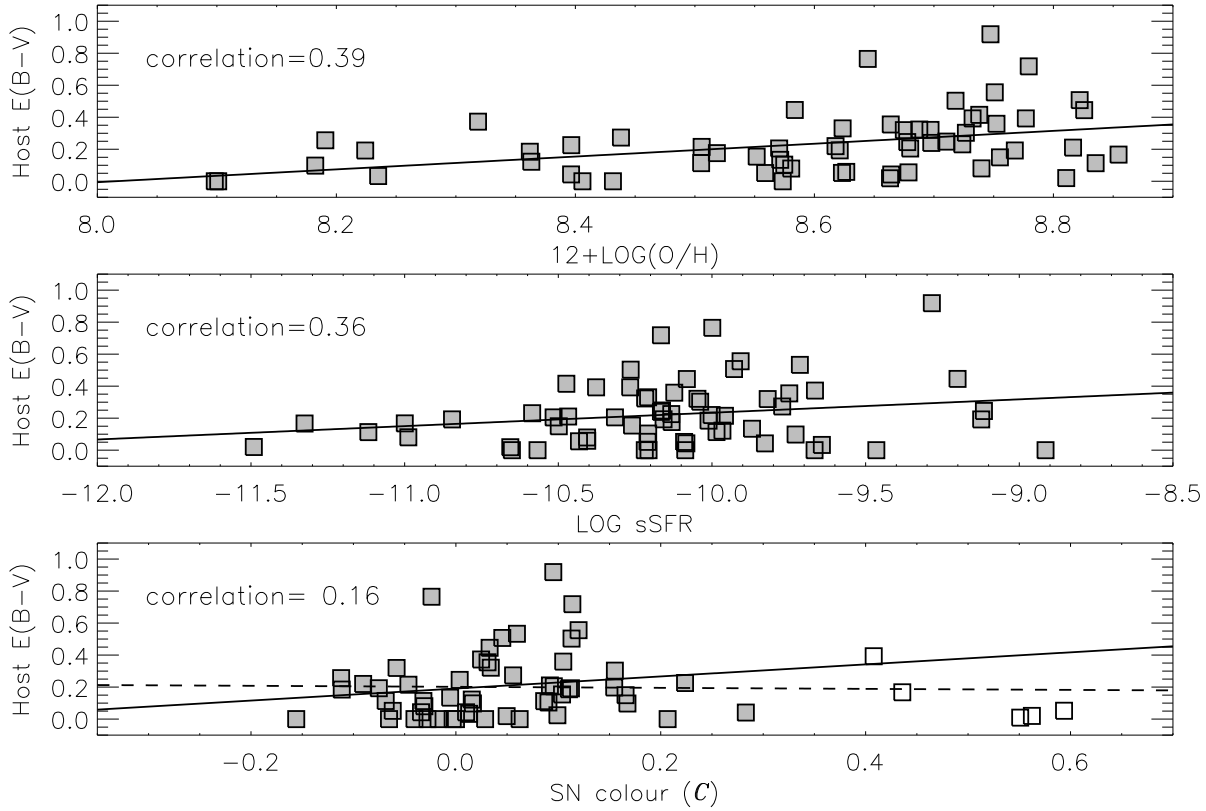

Figure 4.9: The colour excess of the host galaxies $E(B-V)$ as function of gas-phase metallicity, specific SFR and SN colour $\mathcal{C}$. The solid line in each panel represents the best linear fit to the data. The SNe with $\mathcal{C} > 0.4$ are shown in open squares in the lower panel, and the dashed line is the best linear fit to the data including these red SNe.

Goobar, 2011), that would not be traced by photons emerging from HII regions in the host galaxy. This interpretation is supported by evidence that the $B-V$ colour at maximum of SNe Ia correlates with the strength of narrow, blueshifted Na I D features in SN Ia spectra (Foley et al., 2012b; Maguire et al., 2013b), which likely trace the presence of circumstellar material (Patat et al., 2007; Sternberg et al., 2011).

4.4 SN luminosity

In this section we turn to the SN luminosity, which we parameterise by calculating the Hubble residual. This is defined as the difference between $m_B^{\rm corr}$, the observed

rest-frame B-band SN apparent magnitude (m_B; Section 2.2) corrected for stretch and colour, and $m_B^{\rm mod}$, the peak SN magnitude expected in our assumed cosmological model. At a fixed redshift, a brighter SN Ia therefore gives a negative Hubble residual. $m_B^{\rm corr}$ is given by

$$m_B^{\rm corr} = m_B + \alpha \times (s-1) - \beta \times \mathcal{C} \tag{4.2}$$

and $m_B^{\rm mod}$ by

$$m_B^{\rm mod} = 5\log_{10}\mathcal{D}_L\left(z;\Omega_{\rm M}\right) + \mathcal{M}_B, \tag{4.3}$$

where z refers to the cosmological redshift in the CMB frame, $\mathcal{D}_L$ is the c/H_0 reduced luminosity distance (in units of Mpc) with the c/H_0 factor (here c is the speed of light) absorbed into $\mathcal{M}_B$, the absolute luminosity of a $s=1$ $\mathcal{C}=0$ SN Ia (eqn. (4.2)). Explicitly, $\mathcal{M}_B = M_B + 5\log_{10}(c/H_0) + 25$, where M_B is the absolute magnitude of a SN Ia in the B-band. α, β and $\mathcal{M}_B$ are 'nuisance variables' to be derived from the cosmological fits. The best fit for the total N SNe was acquired by minimising

$$\chi^2 = \sum_N \frac{(m_B^{\rm corr} - m_B^{\rm mod})^2}{\sigma_{stat}^2 + \sigma_{int}^2} \tag{4.4}$$

where σ_{stat} is the total statistical uncertainty in $m_B^{\rm corr}$and $m_B^{\rm mod}$, and σ_{int} is the intrinsic dispersion of SN Ia luminosity.

The intrinsic dispersion is the quantity usually included in the total uncertainties so that the reduced χ^2 of the cosmological fit is equal to one. In this work, we do not add any intrinsic dispersion into the Hubble residual uncertainties as we are, in part, searching for variables which could generate this extra scatter. However, we are aware of the potential bias that this could introduce into the nuisance parameters (e.g., α and β) when comparing these results to studies including the intrinsic dispersion, and

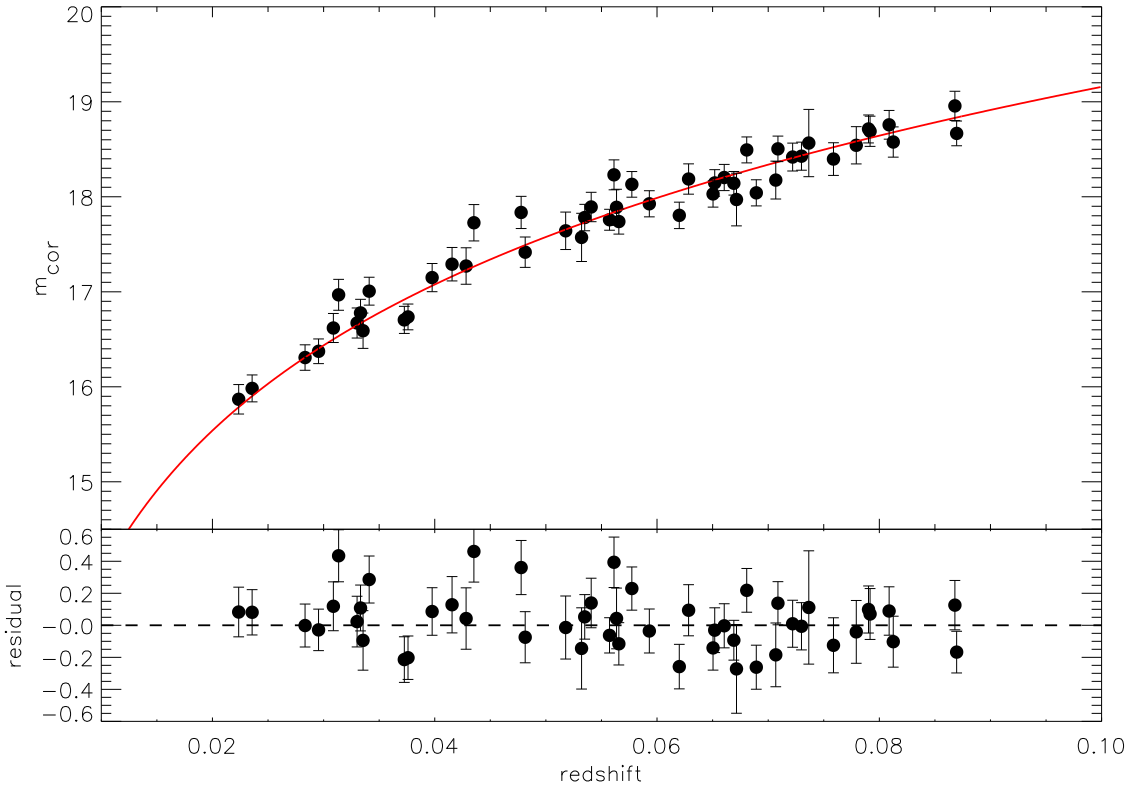

Figure 4.10: The top panel shows the Hubble diagram (SN B-band apparent magnitude after light curve correction as a function of redshift) in this work. The SN model magnitudes as a function of redshift are represented by the red solid line. The Hubble residuals (the difference between SN B-band apparent magnitude and model magnitude) are shown in the bottom panel.

Table 4.2: The best fit values of the nuisance variables α,β, SN Ia absolute magnitude M_B, and the rms scatter of the Hubble residuals in this work.

α	β	M_B (mag)	rms scatter (mag)
1.45 ± 0.12	3.21 ± 0.14	-19.16 ± 0.01	0.17

thus we caution such a comparison is not valid. To ensure our SNe are located in the smooth Hubble flow, we exclude SNe Ia with $z < 0.015$, removing one SN from our sample. In Fig. 4.10 we plot our results on the Hubble diagram. $\alpha = 1.45 \pm 0.12$ and $\beta = 3.21 \pm 0.14$ were obtained. The parameters from the cosmological fits are listed in Table 4.2. In the top two panels of Fig. 4.11, we show the SN luminosities as a function of stretch and colour before correcting for the colour-luminosity relation and stretch-luminosity relation, respectively. It is clear that the SN luminosities have a strong dependence on both the SN stretch and colour before the light curve corrections are performed. In the bottom panels of Fig. 4.11, we can see that the corrected SN luminosities show no significant trend with either SN stretch or colour.

The Hubble residuals as a function of host $M_{\rm stellar}$ are shown in Fig. 4.12. We see only a weak trend that is consistent with that expected based on earlier work, in the sense that more massive galaxies preferentially host brighter SNe Ia after stretch and colour corrections. However, the trend in our data taken in isolation is not significant: the Hubble residuals of low-$M_{\rm stellar}$ and high-$M_{\rm stellar}$ bins have a weighted average of 0.057 ± 0.038 mag and -0.028 ± 0.028 mag respectively, a difference of 0.085 ± 0.047 mag. There is a $\sim 91\%$ probability the slope is negative based on 10,000 MCMC realisations.

Figs. 4.13 and 4.14 show the Hubble residuals as a function of gas-phase and stellar metallicity respectively. A trend with gas-phase metallicity can be seen in the same sense as with stellar mass: higher-metallicity galaxies tend to host brighter SNe Ia after stretch and colour corrections. The differences are more significant than with $M_{\rm stellar}$: the Hubble residuals of the high-metallicity and low-metallicity bins

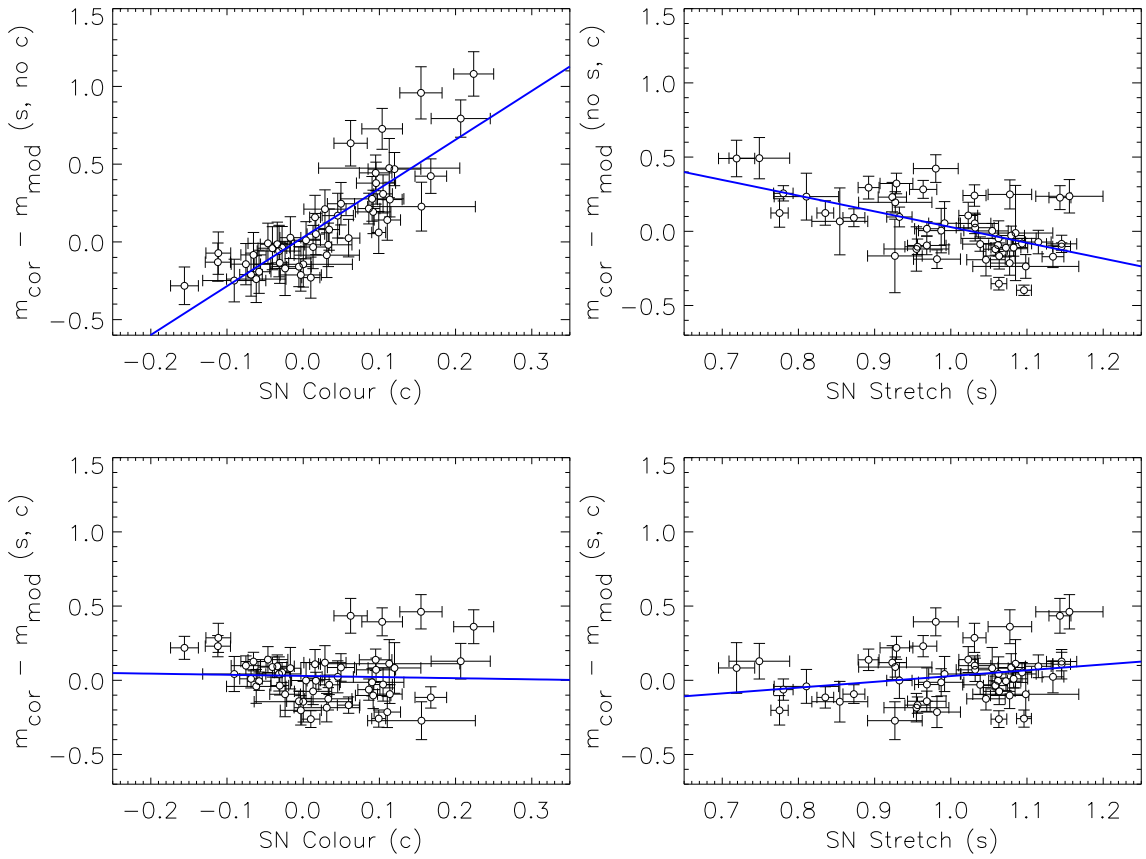

Figure 4.11: Top-left: Hubble residuals as a function of SN colour $\mathcal{C}$ before the colour-luminosity relation is applied. Top-right: Hubble residuals as a function of SN stretch s before the stretch-luminosity relation is applied. Bottom-left: Hubble residuals as a function of SN colour $\mathcal{C}$ after the complete light curve correction. Bottom-right: Hubble residuals as a function of SN stretch s after the complete light curve correction The linear fit in each panel is shown as a blue solid line.

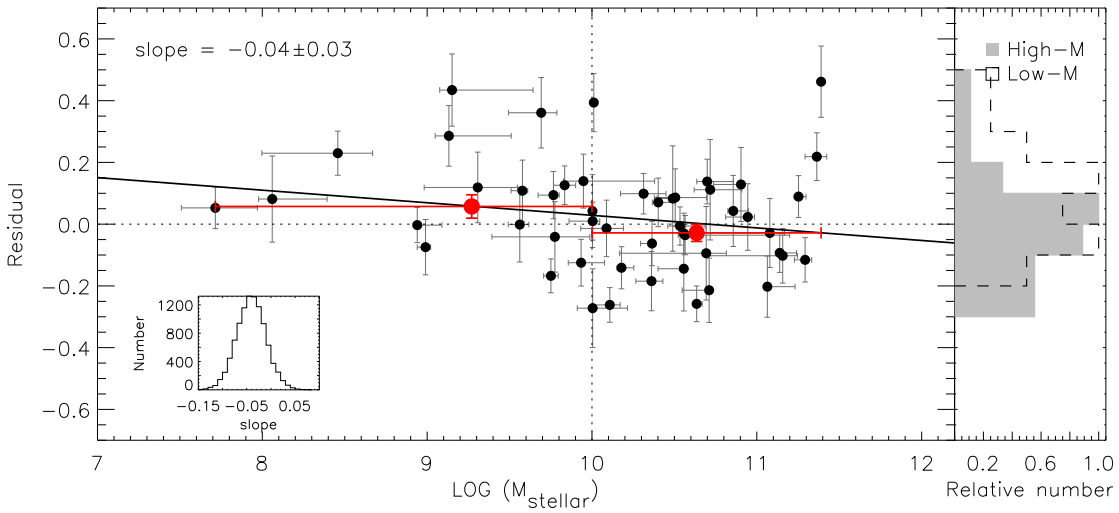

Figure 4.12: Hubble residuals as a function of host galaxy $M_{\rm stellar}$. The vertical dashed line represents the criterion used to split our sample into high-$M_{\rm stellar}$ and low-$M_{\rm stellar}$ galaxies. The red filled circles represent the weighted-mean of the residuals in bins of $M_{\rm stellar}$, and their error bars are the width of the bins and the error of the weighted mean. The histogram on the right shows the distribution of residuals in high-$M_{\rm stellar}$ (filled histogram) and low-$M_{\rm stellar}$ (open histogram). The distribution of the slopes best fit to the data from 10,000 MCMC realisations is shown in the inset. The solid line represents the mean slope determined from the distribution.

have a weighted average of -0.047 ± 0.030 mag and 0.068 ± 0.035 mag, respectively, a difference of 0.115 ± 0.046 mag. Fitting a straight line using the LINMIX method gives a $\sim$ 98% probability the slope is negative. The correlation coefficient is $\sim$ 2 times larger than the relation between Hubble residuals and $M_{\rm stellar}$. We see no trend with stellar metallicity. The Hubble residuals as function of host stellar age are shown in Fig. 4.15; no significant trends are seen. Fig. 4.16 and Fig. 4.17 show the Hubble residuals as function of sSFR determined by Hα luminosity and Z-PEG, respectively. We do not see a significant trend. However, there is a hint that fainter SNe Ia tend to reside in galaxies with higher sSFRs. The trends calculated for Hubble residuals with host parameters are listed in Table 4.3.

Many of the relations shown in this section have been studied by different authors using independent samples of SNe Ia. Since $M_{\rm stellar}$ is the most straightforward variable to measure, requiring only broad-band imaging, the most common comparison

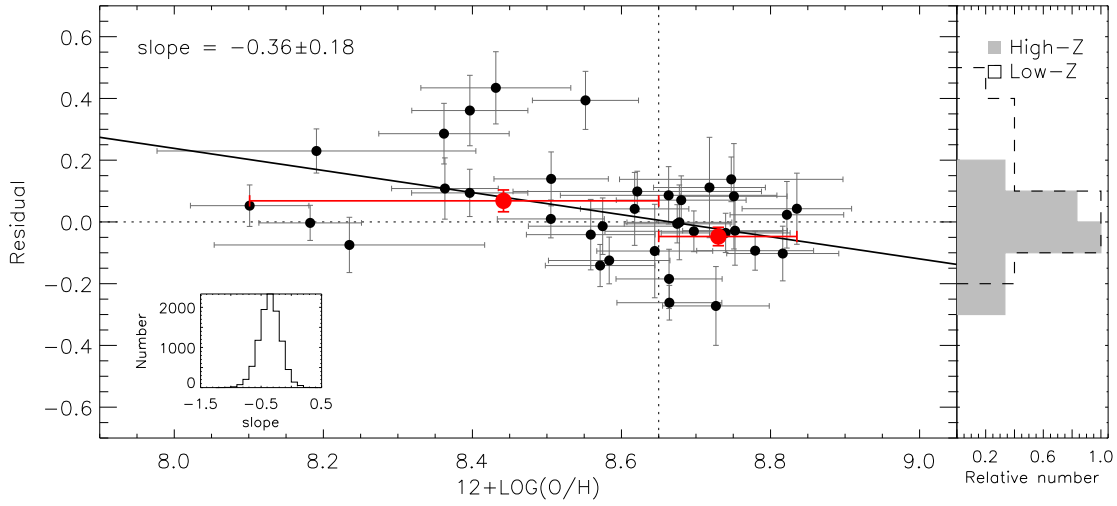

Figure 4.13: As Fig. 4.12, but considering gas-phase metallicity instead of $M_{\rm stellar}$.

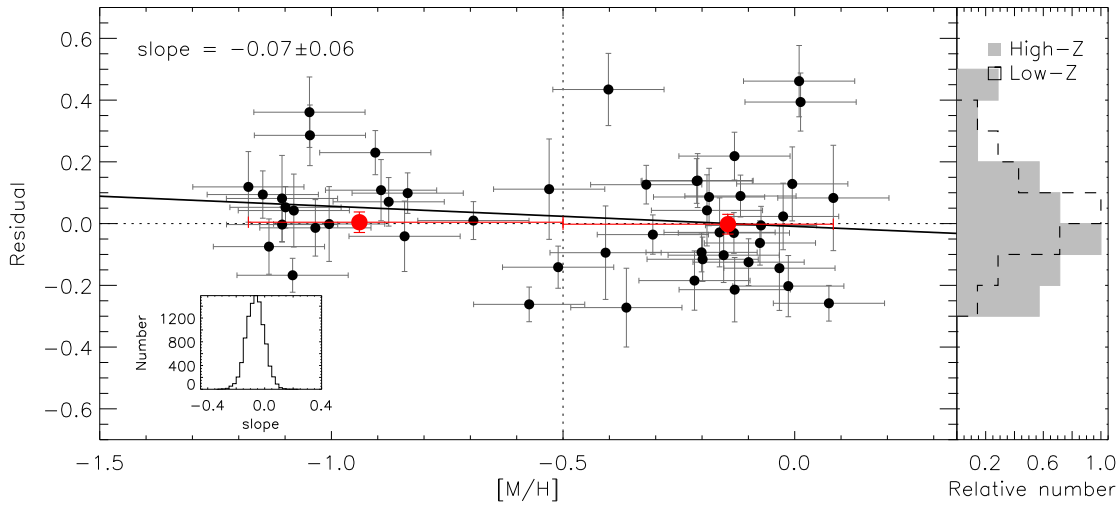

Figure 4.14: As Fig. 4.12, but considering stellar metallicity instead of $M_{\rm stellar}$.

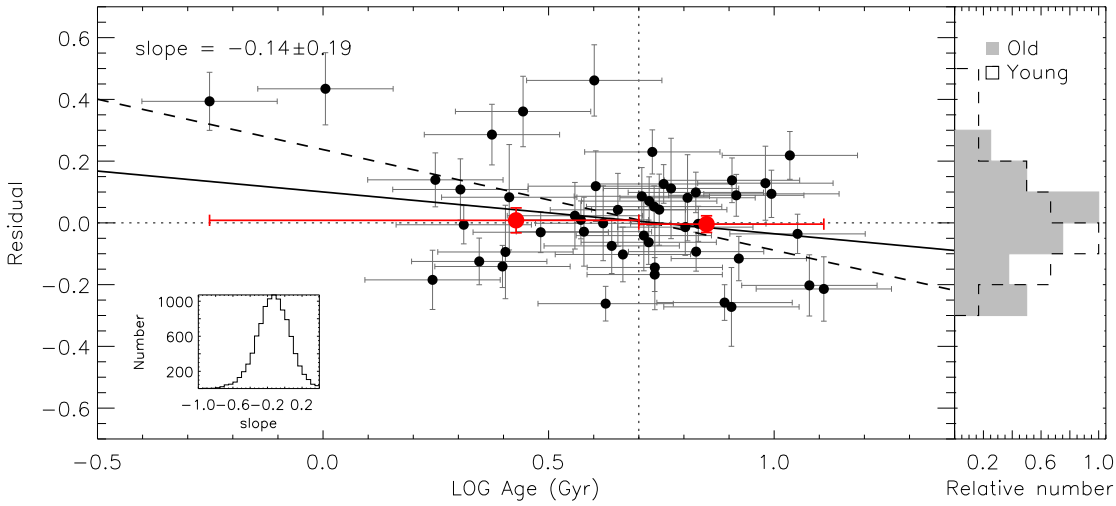

Figure 4.15: As Fig. 4.12, but considering stellar age instead of $M_{\rm stellar}$. Here the dashed line includes the two SNe in the youngest host galaxies, which cause a significant trend with Hubble residual, and which otherwise is not present.

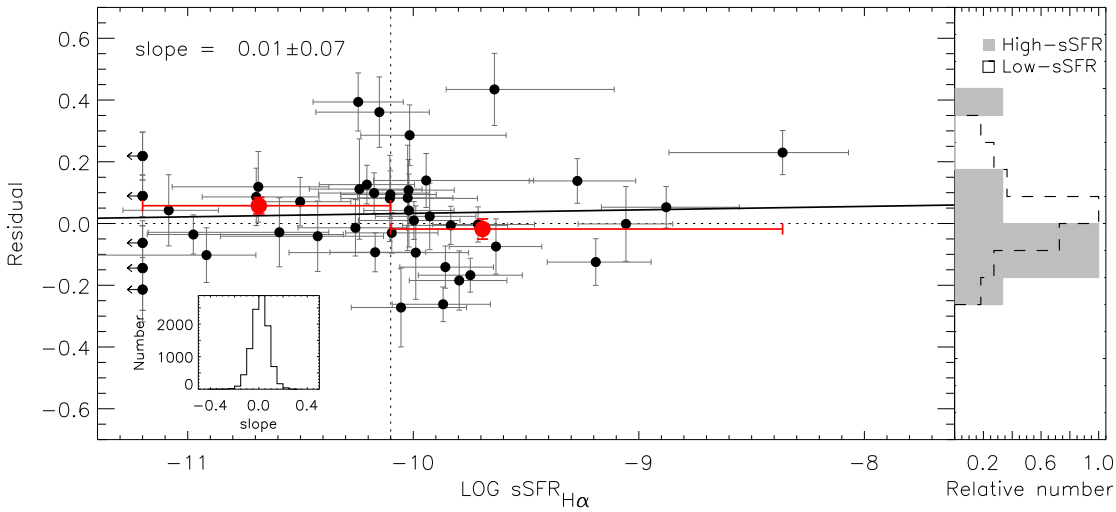

Figure 4.16: As Fig. 4.12, but considering specific star-formation rate instead of $M_{\rm stellar}$.

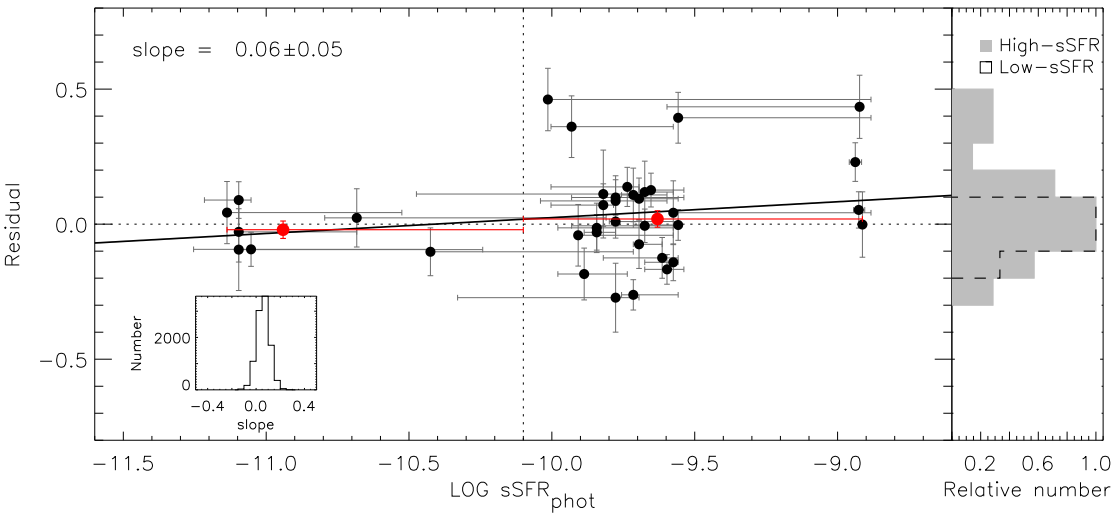

Figure 4.17: As Fig. 4.12, but considering specific star-formation rate (determined by Z-PEG) instead of $M_{\rm stellar}$.

has been between Hubble residual and $M_{\rm stellar}$, which has been examined with a variety of samples over a large redshift range (Kelly et al., 2010; Sullivan et al., 2010; Lampeitl et al., 2010; Gupta et al., 2011; Johansson et al., 2013; Childress et al., 2013a). These studies all find that more massive galaxies host brighter SNe after corrections for light curve shape and colour have been made. The size of the difference is usually around 0.1 mag, with a transition mass of around $10^{10}\,M_{\odot}$. Our result is consistent with these earlier studies, although at a reduced significance due to a smaller dataset.

However, one of the primary goals of this work is to study the metallicity of the SN host galaxies rather than just $M_{\rm stellar}$. Although some studies convert $M_{\rm stellar}$ into metallicity using average mass-metallicity relations (e.g., Sullivan et al., 2010), it is obviously more useful to measure the metallicity directly. The first study of this kind was Gallagher et al. (2005) who compared the Hubble residuals for 16 local SNe Ia with the gas-phase metallicity of their hosts; no significant trends were seen. D'Andrea et al. (2011) studied a larger sample of ∼40 SNe Ia host galaxies from the SDSS-II SN survey, finding SNe Ia in high-metallicity galaxies to be ~ 0.1 mag ($\simeq 4.9\sigma$) brighter than those in low-metallicity galaxies after corrections, consistent

Table 4.3: The trend of Hubble residuals with host parameters.

	Split point	N_{SN}	bin difference (mag)	linear trend	probability of negative slope	correlation Pearson	correlation Kendall
$M_{\rm stellar}$	$10^{10}\,M_\odot$	50	0.085 (1.8σ)	-0.041 ± 0.030	91.3%	−0.19	−0.13
12+log(O/H)	8.65	36	0.115 (2.5σ)	-0.358 ± 0.176	98.1%	−0.36	−0.22
[M/H]	−0.5	50	0.006 (0.1σ)	-0.065 ± 0.063	85.1%	−0.13	−0.09
Age	5 Gyr	48	0.012 (0.3σ)	-0.135 ± 0.193	75.7%	−0.14	−0.04
$(\mathrm{sSFR})_{\mathrm{H}\alpha}$	$7.9 \times 10^{-11}\,\mathrm{yr}^{-1}$	48	0.075 (1.8σ)	0.011 ± 0.069	42.7%	0.06	−0.02
$(\mathrm{sSFR})_{\mathrm{phot}}$	$7.9 \times 10^{-11}\,\mathrm{yr}^{-1}$	37	0.039 (0.9σ)	0.059 ± 0.053	12.9%	0.21	0.13

with the results based on $M_{\rm stellar}$. Using the low-redshift SNe studied by the SNfactory, Childress et al. (2013a) derived the gas-phase metallicity from 69 SNe Ia hosts and found a ~ 0.1 mag ($\simeq 2.9\sigma$) difference between high-metallicity and low-metallicity hosts. Our results are in good agreement (a 0.115 mag difference between high- and low-metallicity hosts). Compared to a metallicity simply converted from host $M_{\rm stellar}$, the SN Ia luminosity shows a stronger dependence on the metallicity derived via direct emission-line measurements.

For stellar metallicity studies, Gallagher et al. (2008) studied 29 early-type SN Ia host galaxies by measuring the Lick indices from the SN Ia host spectra. They found the host stellar metallicity correlates with the Hubble residual at $\simeq$98 per cent confidence level, although this technique is not directly comparable to ours. Johansson et al. (2013) also derived the host stellar metallicity by measuring the absorption line indices from the SN Ia host spectra, but did not find a significant trend. We also find no significant trend in our data.

Gupta et al. (2011) determined the mass-weighted average age of 206 SN Ia host galaxies by fitting their broad-band photometry. They found a weak correlation between the Hubble residuals and host age at $\sim 1.9\sigma$. Johansson et al. (2013) measured the light-weighted age for the SNe Ia host galaxies using the absorption line indices but found no significant trend; again we find no trend in our data.

Sullivan et al. (2010) measured photometric-based sSFRs and found that SNe Ia in low-sSFR hosts appear brighter than those in high-sSFR hosts at $\simeq 2.6\sigma$ significance after s and $\mathcal{C}$ corrections. Similar trends have also been found using spectroscopy-based sSFRs (D'Andrea et al., 2011; Childress et al., 2013a). Rigault et al. (2013) have shown that at least some of the trends with host $M_{\rm stellar}$ may be driven by SNe in locally passive environments: SNe in massive galaxies with locally passive environments are systematically brighter than those in locally star forming environments by ~ 0.09 mag. We do not see these trends in our dataset although this may be due to

the relatively small sample size.

4.5 The effect of metallicity on SN Ia luminosities

The peak luminosity of SNe Ia is powered by the radioactive decay of ^{56}Ni synthesised during the explosion. Timmes et al. (2003) showed that the observed scatter in metallicity could introduce a 25% variation in the mass of ^{56}Ni synthesised by SNe Ia. Metal-rich stars tend to synthesize more neutron-rich (and stable) ^{58}Ni instead of the ^{56}Ni that powers the SN Ia luminosity. As a result, and all other variables being equal, intrinsically fainter SNe Ia are expected to explode in higher-metallicity environments.

However, Bravo & Badenes (2011) showed that SN Ia metallicities can be reasonably estimated by the host galaxy metallicity, and are better represented by gas-phase metallicity than by stellar metallicity. In this study we used the host gas-phase metallicity as a proxy for the progenitor metallicity to study the metallicity effects on SNe Ia. Fig. 4.18 shows the dependence of Hubble residuals on metallicities based on different calibrations. The relative metallicity conversions we derived in Section 3.3.3 were not applied here, therefore the number of hosts which are available for different metallicity calibrations could be different. The results showed a good consistency between different calibrations. The slopes range from -0.74 to -1.13, with the Pearson correlation coefficients ranging from -0.42 to -0.51. This suggests that the correlation between Hubble residual and gas-phase metallicity is independent of the calibration methods at least at the level of precision probed here.

Following the procedure described in Hook et al. (1994), the Kendall rank correlation coefficients between Hubble residual, gas-phase metallicity, $M_{\rm stellar}$ and stellar age are listed in Table 4.4. Our results show that the SN Ia luminosity has the strongest dependence on the host gas-phase metallicity compared to $M_{\rm stellar}$ or stellar

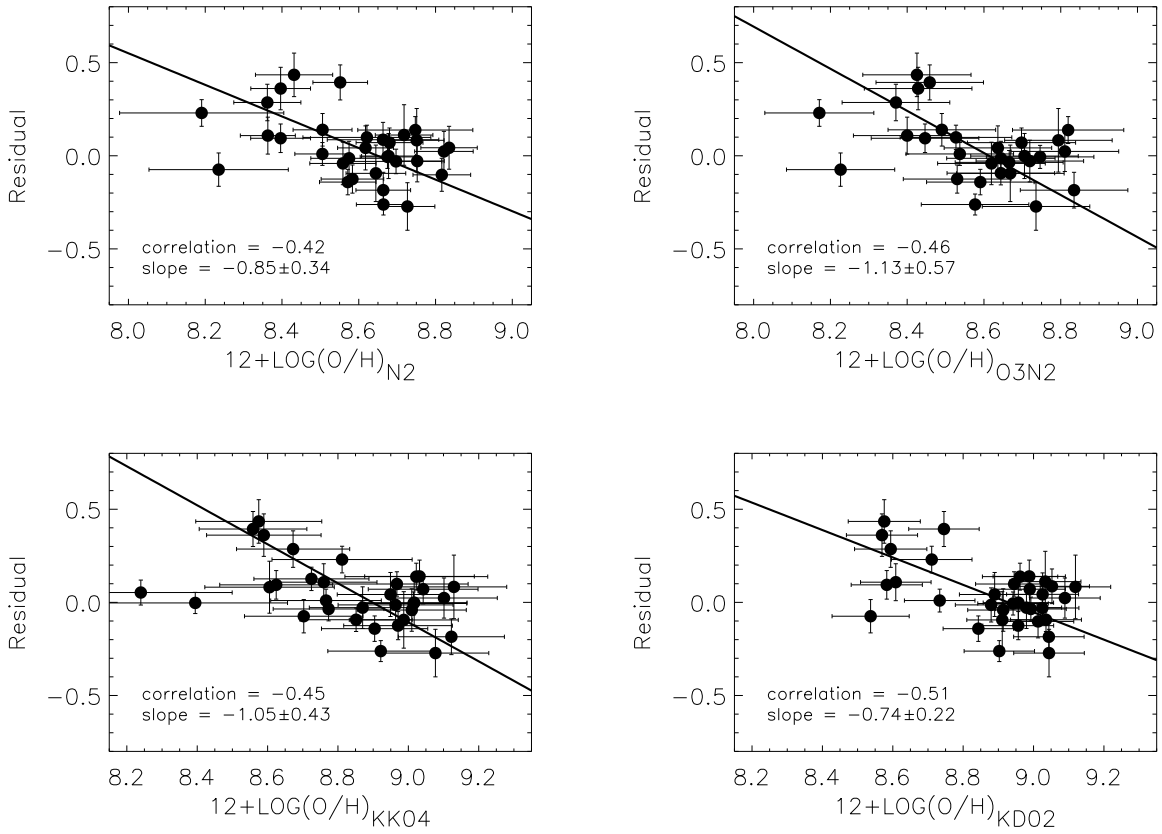

Figure 4.18: The Hubble residuals as function of host galaxy gas-phase metallicity using four different calibrations. The best linear fit is shown in solid line in each panel.

Table 4.4: Kendall rank correlation coefficients between Hubble residual (HR), gas-phase metallicity, $M_{\rm stellar}$ and stellar age.

	HR	12+log(O/H)	$M_{\rm stellar}$	Age
HR	–	−0.22	−0.13	−0.04
12+log(O/H)		–	0.49	0.03
$M_{\rm stellar}$			–	0.35
Age				–

age. We also found that the correlation coefficient between Hubble residuals and $M_{\rm stellar}$ is similar to the value multiplicatively combining the correlation coefficients of the Hubble residual–metallicity and $M_{\rm stellar}$-metallicity relations, from which it can be inferred that the correlation between Hubble residuals and $M_{\rm stellar}$ may be a consequence of the Hubble residual–metallicity relation and the strong correlation between $M_{\rm stellar}$ and metallicity.

Hayden et al. (2013) applied the fundamental metallicity relation (FMR) to the SN Ia host galaxies using broad-band colours alone. They found the scatter of the Hubble residual is greatly reduced by using the FMR instead of just the $M_{\rm stellar}$, which in turn implies that metallicity may be the underlying cause of the correlation between Hubble residual and $M_{\rm stellar}$. By directly measuring the gas-phase metallicity of SN Ia host galaxies we can also show that it has a more significant effect on SN Ia luminosity than $M_{\rm stellar}$ or stellar age.

4.6 The host stellar mass distribution

Unlike galaxy-targeted supernova surveys that are biased towards surveying brighter and more massive galaxies, the host galaxies in PTF should represent a wider range of SN environments. A key test of this is the host galaxy stellar mass distribution (Fig. 4.1; Section 2.4.1), the form of which should be a combination of the underlying galaxy stellar mass function and the mean SN Ia rate as a function of stellar mass, and which should be able to be reproduced from a qualitative knowledge of both. We

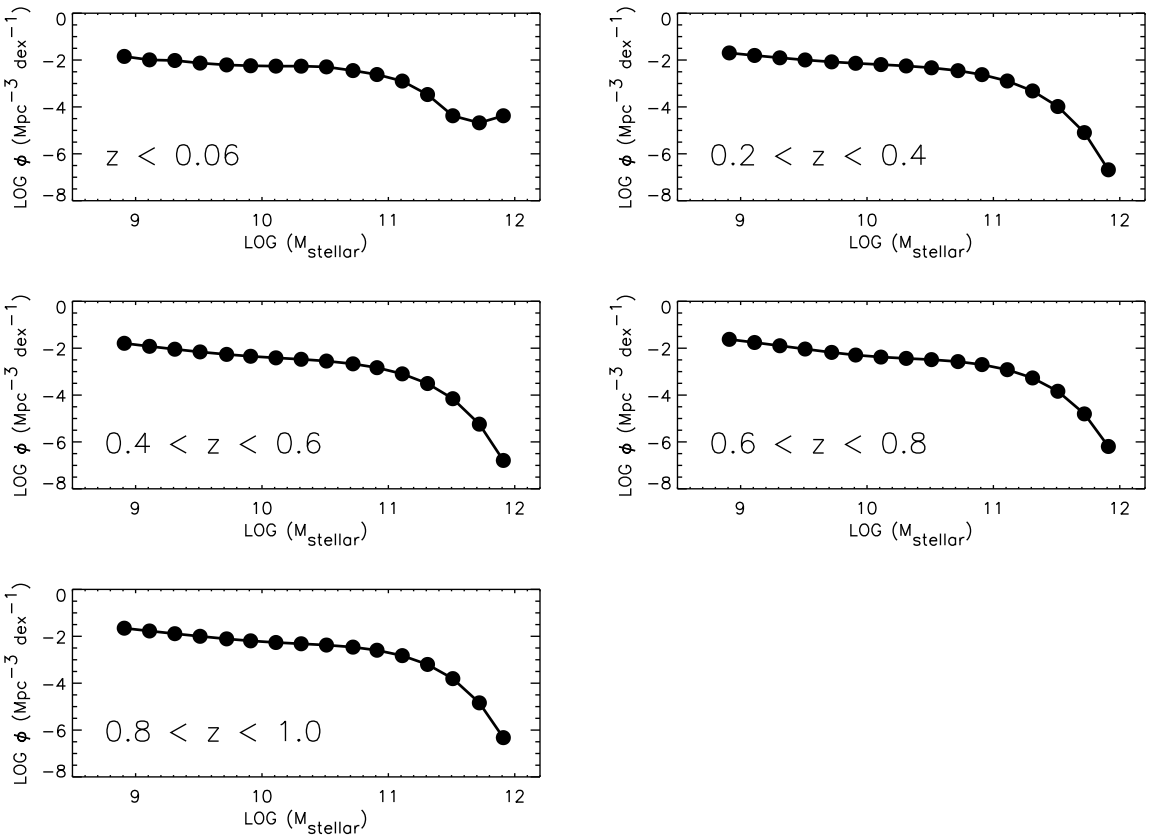

Figure 4.19: The galaxy stellar mass function (GSMF) ϕ used in this work. Top left: The GSMF studied from Baldry et al. (2012) with $z < 0.06$. Top right to bottom: The GSMFs studied from Drory et al. (2009) in different redshift ranges: $0.2 < z < 0.4$, $0.4 < z < 0.6$, $0.6 < z < 0.8$, and $0.8 < z < 1.0$.

examine this in this section.

We begin with the galaxy stellar mass function (GSMF) in the local universe, defined as the number of galaxies per logarithmic bin in stellar mass. For this study we adopt the GSMF of Baldry et al. (2012, top-left panel in Fig. 4.19), the redshift range of which ($z < 0.06$) is similar to this work. In each bin in stellar mass, we multiplied the GSMF by the stellar mass in that bin to obtain the stellar mass distribution. We then over-plot the observed SN Ia host galaxy stellar mass distribution. We compare both to a SN Ia host mass distribution drawn primarily from galaxy-targeted searches (the low-z sample compilation of Conley et al., 2011). The result can be seen in the upper left panel of Fig. 4.20.

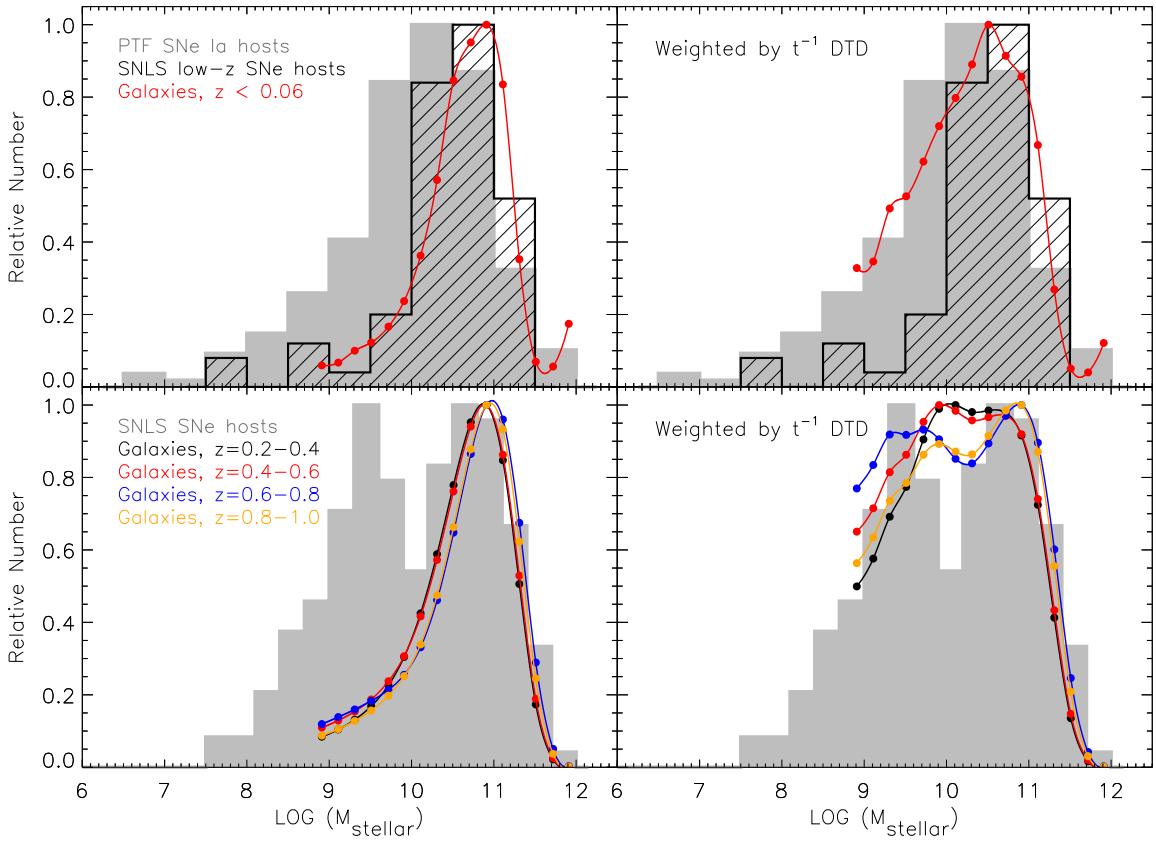

Figure 4.20: Upper left: The stellar mass distribution of PTF SN Ia host galaxies (grey histogram) compared to the low-redshift SN Ia host sample of Conley et al. (2011) (black histogram). The red solid line with filled circles is the predicted distribution based on the stellar mass function of local galaxies ($z < 0.06$; Baldry et al., 2012). Upper right: The same plot as the upper left panel, but with the predicted SN Ia stellar mass distribution produced by weighting each bin by a t^{-1} DTD. Lower left: The stellar mass distribution of the SNe Ia host galaxies in the SNLS sample of Sullivan et al. (2010) (grey histogram). The lines with filled circles in different colours represent the mass contributions derived from the galaxy stellar mass functions in different redshift ranges studied from Drory et al. (2009). Lower right: The same plot as left panel, but with prediction weighted by the t^{-1} DTD.

The host stellar mass distribution for the galaxy-targeted SN Ia sample is similar to that expected based on the GSMF, but is obviously different to our PTF sample at smaller stellar masses. However, this test assumes that the SN Ia rate is simply proportional to the stellar mass of the host. While this may be approximately correct in the more massive systems, it is known to be incorrect in lower stellar mass systems which have a larger fraction of younger potential progenitor systems or higher sSFRs (Fig. 3.7) — the SN Ia rate is not simply proportional to stellar mass (e.g. Mannucci et al., 2005, 2006; Sullivan et al., 2006; Smith et al., 2012). In practise, a delay-time distribution (DTD; the distribution of times between the progenitor star formation and the subsequent SN Ia explosion) with the SN Ia rate proportional to t^{-1} is favoured by most recent data (e.g. Maoz & Mannucci, 2012). If we assume this DTD, and the relation between $M_{\rm stellar}$ and galaxy age determined by Gallazzi et al. (2005), a revised distribution of SN Ia host galaxy stellar masses can be formed by weighting each mass bin by a t^{-1} DTD.

The results are shown in Fig. 4.20 (upper right): the effect of the t^{-1} DTD is to increase the contribution from SNe in less massive (younger) galaxies. A reduced χ^2 is calculated between galaxy stellar mass distribution and SN Ia host galaxy stellar mass distribution. The reduced χ^2 drops from 24.6 to 2.4 after considering a t^{-1} DTD to the galaxy stellar mass distribution. Indeed, assuming a t^{-1} DTD and a simple scaling between stellar mass and age allows an excellent reproduction of the observed host galaxy stellar mass distribution.

A similar comparison can be made to the stellar mass distribution from the SNLS sample (Sullivan et al., 2010). As seen in the lower panels of Fig. 4.20, the SNLS sample contains more lower stellar-mass galaxies than our PTF sample even though the selection of SNe should be similar. Using the GSMF of Drory et al. (2009) over $0.2 < z < 1.0$, and the same technique as above, again a good agreement between the observed host galaxy $M_{\rm stellar}$ distribution and that derived from the GSMF is

achieved. Thus the difference in the stellar mass distributions of the PTF and SNLS host galaxies can be explained by evolution in the field galaxy population from which the hosts are drawn where there is an excess in low-mass galaxies for the stellar mass distributions at high redshifts.

4.7 The mass–metallicity relation of SN Ia host galaxies

As well as impacting on the observed photometric properties of SNe Ia (see Section 4.4), the metallicity of the progenitor star may also impact on the SN Ia rate. An increased rate with lower metallicity may be expected as stars with a lower metallicity generally form more massive white dwarfs and therefore may more easily approach the Chandrasekhar mass limit (Kistler et al., 2011). A decreased rate with lower metallicity may be expected in some single degenerate scenarios as the lower metallicity inhibits accretion onto the white dwarf due to lower opacities in the wind (Kobayashi et al., 1998; Kobayashi & Nomoto, 2009). Observationally, there is some evidence that prompt SNe Ia are more prevalent (or explode with a brighter luminosity) in metal-poor systems (Cooper, Newman, & Yan, 2009).

Such effects may impact on the observed SN Ia host mass–metallicity relation; if any of the putative metallicity effects lead to SNe Ia preferentially occurring in low or high metallicity galaxies, then the mass–metallicity relation for SN Ia hosts would be offset from that of field galaxies (e.g., at fixed galaxy stellar mass, the SN Ia host galaxies may systematically have lower or higher metallicities than the field galaxies). We compare our mass–metallicity relation with those derived for field galaxies (Fig. 3.9), and compare the use of four different gas-phase metallicity calibrations in Fig. 4.21. We fit these mass–metallicity relations using the same functional form as described in KE08 at $8.5 < \log M < 11.0$. Note that although we estimate $M_{\rm stellar}$

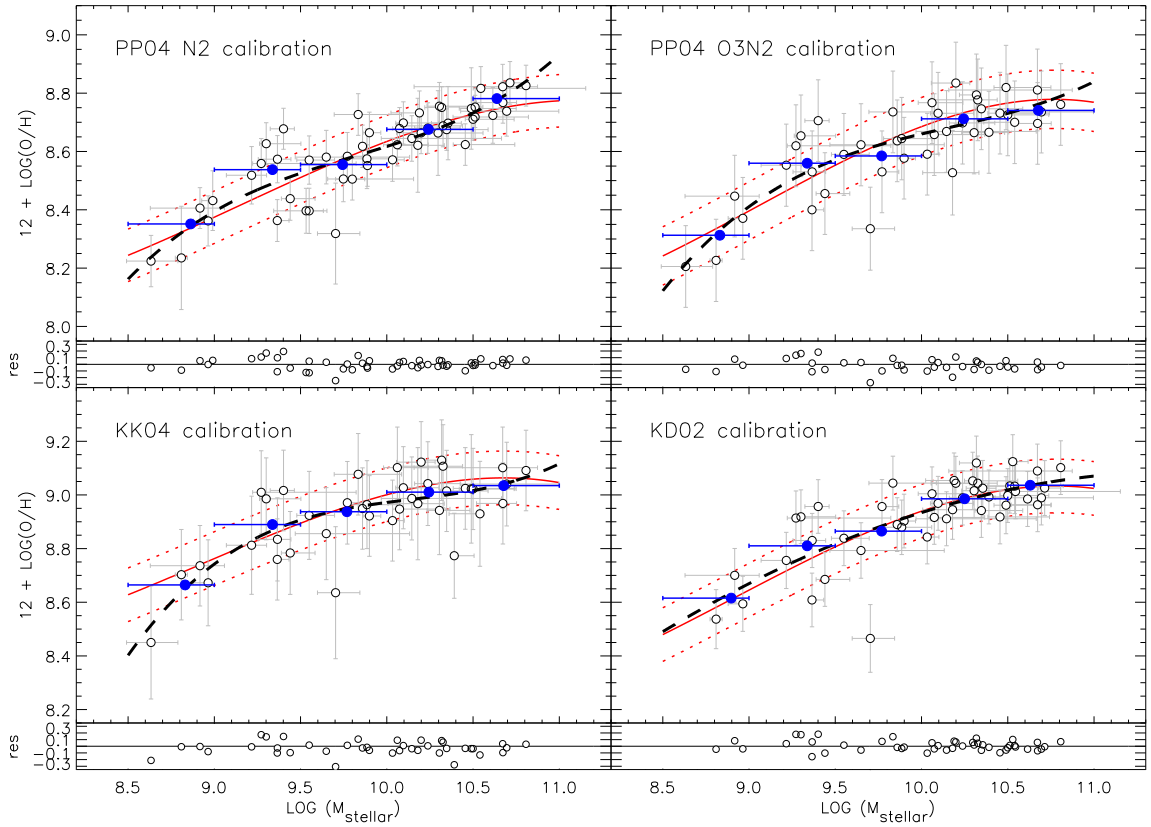

Figure 4.21: The mass–metallicity relations compared by different metallicity calibrations. Upper panels: PP04 N2 (left) and PP04 O3N2 (right) calibrations. Lower panels: KK04 (left) and KD02 (right) calibrations. The open circles show the measurements in this work. The blue filled-circle is the mean metallicity in bins of $M_{\rm stellar}$. The best fit to field galaxies given by Kewley & Ellison (2008) with the range of one rms scatter was over-plotted (in red line and red dashed-line, respectively). The black dashed-line is the best fit to the measurements in this work. The sub-plot in the bottom of each panel represents the residuals of our measurements from KE08's best fit.

by fitting broad-band photometry instead of using the spectroscopic indices of KE08, previous work has shown that the two different approaches provide consistent results (0.001 dex; Smith et al., 2012). Thus the different $M_{\rm stellar}$ determination techniques should have a negligible effect on our results.

The SN Ia host mass–metallicity relations are consistent with the fits from KE08, with a weighted mean offset of ~ 0.01 dex ($\lesssim 1\sigma$ significance; see Table 4.5 for more details). This is consistent with Childress et al. (2013b), who found that SN Ia hosts in their sample also show a good agreement with the field galaxy mass–metallicity

Table 4.5: The mean offset of mass-metallicity relations derived from SN Ia hosts in this work and field galaxies from KE08 using four different metallicity calibrations.

	PP04 N2	PP04 O3N2	KK04	KD02
mean offset	0.016 ± 0.013	-0.009 ± 0.015	-0.012 ± 0.015	0.011 ± 0.013

relation.

However, this comparison has one potential systematic — at fixed $M_{\rm stellar}$, other variables may affect the SN Ia rate, for example the number of young stars (or the SFR). Indeed, Mannucci et al. (2010) showed that the observed mass–metallicity relation could be a projection of a more general relation between $M_{\rm stellar}$, gas-phase metallicity, and SFR, which together can be described using a fundamental metallicity relation (FMR). The FMR can be defined as the relation between gas-phase metallicity and $\log(\mathrm{M_{stellar}}) - \alpha \times \log(\mathrm{SFR})$, where α is a parameter determined to minimise the scatter of the metallicities. Mannucci et al. (2010) found $\alpha = 0.32$ produced the minimum dispersion in metallicity.

We therefore construct the FMR for the 61 SN Ia hosts with a measure of $M_{\rm stellar}$, SFR and gas-phase metallicity. For comparison, we also determined the FMR for SDSS field galaxies using the same parent sample as Mannucci et al. (2010). Similar quality cuts as described in Mannucci et al. (2010) have been performed. We select galaxies within a similar redshift range as our host sample ($0.03 < z < 0.1$, with a median $z \sim 0.07$), and remove the potential AGN host galaxies using the technique described in Section 3.2. In addition, we applied aperture corrections to the SDSS sample by comparing the SDSS r-band model magnitude to fibre magnitudes. A total of 130,941 SDSS galaxies passed our criterion. The results are shown in Fig. 4.22. We found no significant difference between the FMR for SN Ia hosts and that of the SDSS galaxies. The weighted mean offset between the SNe Ia hosts and best-fit from SDSS galaxies is 0.005 ± 0.011 dex (a difference of $\sim 0.5\sigma$). The comparisons of the $M_{\rm stellar}$–SFR and metallicity–SFR relation are shown in Fig. 4.23 and Fig. 4.24. We

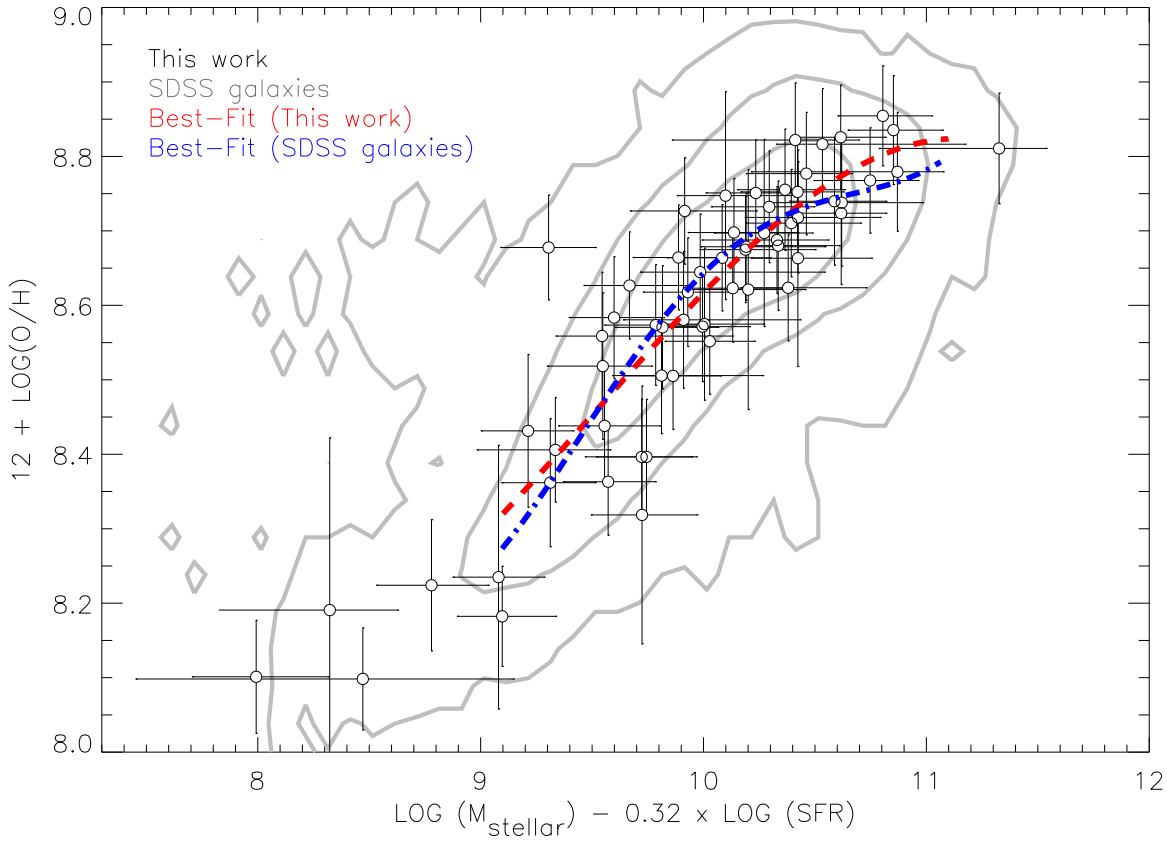

Figure 4.22: The fundamental metallicity relation (FMR) derived from our data. The open circles show the measurement of our SN hosts. The red dashed line is the best-fit to it. The grey contours show the sample including 68%, 95% and 99.7% of SDSS galaxies from Mannucci et al. (2010). The blue dot-dashed line is the best fit to the SDSS galaxies.

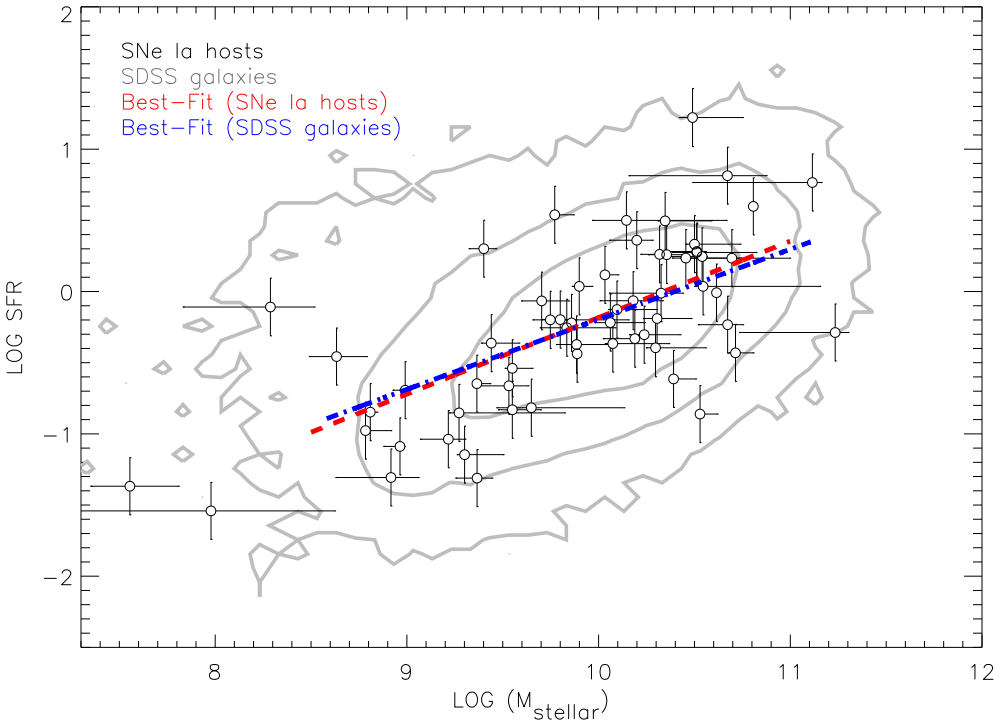

Figure 4.23: The SFR (in units of $M_{\odot}\,yr^{-1}$) as a function of $M_{\rm stellar}$ of our sample. The symbols are the same as in Fig. 4.22.

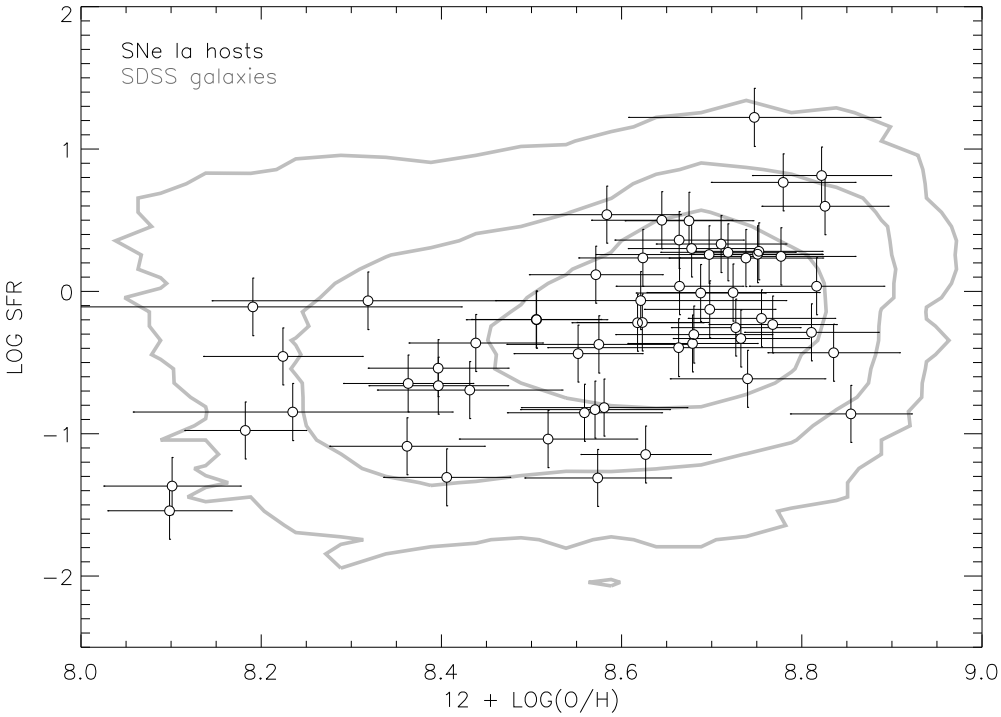

Figure 4.24: The SFR (in units of $M_{\odot}\,yr^{-1}$) as a function of gas-phase metallicity. The symbols are the same as in Fig. 4.22.

also see no significant difference between our SN Ia hosts and normal field galaxies.

In previous sections we have shown that the metallicity has a significant effect on SN Ia luminosity and colour by altering the mass of ^{56}Ni and the opacity of the SN envelope during the explosion. However, the metallicity effect may not be directly related to the SN Ia rate via these relations. Instead, it was thought to show strong correlations with the SN pre-explosion properties such as the mass and stellar wind of the WD (Kobayashi et al., 1998; Kobayashi & Nomoto, 2009; Kistler et al., 2011). By examining both the mass–metallicity relation and the FMR of SN Ia host galaxies, we find a good agreement with the same relations derived from field galaxies, suggesting SN Ia host galaxies and normal field galaxies follow similar relations. This in turn suggests that the effect of metallicity on the SN Ia rate may not be the dominant variable and may be too small to alter the observed SN Ia rate. The other possibility is that the parameter space explored in this work may not be sufficient to detect any metallicity effect. For example, Kobayashi & Nomoto (2009) showed that the metallicity should have a significant effect on systems with an iron abundance [Fe/H] ≤ -1. However, the metallicities with this range usually exist in very low-mass galaxies (e.g., $\log(M/M_{\odot}) < 9$), and are not well constrained by the mass–metallicity relation studied in this work.

4.8 Summary

In this chapter, we have focused on the 82 SN Ia selected from our parent sample with available host spectroscopic data, and we examined the relationships between the SNe Ia and their hosts. The host galaxy parameters compared here were determined from both photometric and spectroscopic data, including star-formation rates (SFRs), stellar masses ($M_{\rm stellar}$), gas-phase and stellar metallicities, and stellar ages for the host galaxies. Below we list our main findings.

Previously observed correlations between SN Ia properties and their host parameters are recovered in this work. We show that the SN light-curve width (stretch) has a strong dependence on host stellar mass, metallicity, specific star-formation rate and stellar age. Fainter, faster evolving (lower stretch) SNe Ia tend to be hosted by massive/metal-rich/passive/older galaxies than brighter, slow evolving (higher stretch) SNe Ia.

For the SN Ia colour, we have shown that redder SNe Ia have a tendency to explode in more massive and metal-rich galaxies. However, we found no relation between SN colour and the colour excess of the host galaxies as measured from the Balmer decrement, suggesting that the bulk of the SN Ia colour variation is intrinsic and not dependent on host galaxy extinction. No significant trends were found with star-formation rate, stellar age or SN offset.

The dependence of the SN Ia Hubble residuals on host parameters was also investigated. We saw a mild trend that SNe Ia in massive galaxies tend to be brighter than those in low-mass galaxies after light-curve shape and colour corrections. However, SN Ia luminosities show a stronger dependence on gas-phase metallicity. SNe Ia in metal-rich galaxies are ~ 0.1 mag brighter than those in metal-poor galaxies after light-curve shape and colour corrections. This dependence does not depend on different metallicity calibrations. The correlation derived between Hubble residual and gas-phase metallicities is about two times stronger than for stellar mass. This implies that the host galaxy metallicity may be the underlying cause of the well-established relation between SN Ia luminosity and stellar mass. There was also a hint that SNe Ia hosted by galaxies with a lower specific star-formation rate are brighter than their counterparts after the light curve corrections.

We showed that the stellar mass distribution of the PTF and SNLS SN Ia host galaxies are quite different, with SNLS possessing many more low-mass host galaxies than PTF. However this can be understood and reproduced by a combination of a

redshift-dependent galaxy stellar mass function (GSMF), and a SN Ia rate inversely proportional to the age of the galaxy (a t^{-1} DTD). This implies the difference in the stellar mass distribution of the PTF and SNLS hosts can be explained by the evolution of field galaxies from which there is an excess in low-mass galaxies for the stellar mass distribution at high redshifts.

Finally, we compared the mass-metallicity relation for the SN Ia hosts to that of field galaxies drawn from SDSS. We found no significant difference between the two relations, a result that is not sensitive to the metallicity calibrations adopted. In addition, we derived the fundamental metallicity relation (FMR; Mannucci et al., 2010) for the SN Ia hosts and also found it to be similar to that measured from field galaxies. This suggests that metallicity has a negligible effect on the SN Ia rate.

Chapter 5

SN spectral measurement

In chapter 3 and 4 we have determined the host galaxy parameters from both spectroscopic and photometric data and investigated their effects on SN Ia luminosities. However, given the fact that the spectroscopic data contains crucial information about SN Ia properties, it would be important to extend our analysis to the SN spectral features. The next step would be to investigate the relations between SN Ia spectral features and their host parameters.

In this chapter, we discuss our method to measure the SN spectral features. The key features of interest are the pseudo-equivalent widths (pEW) and velocities of Si II λ6355 and the Ca II near infrared (NIR) triplet. The SN high-velocity feature (HVF), in particular, is of interest to this work. The HVFs are known to exhibit in SN spectra with much higher velocities than that associated with main SN line forming regions (i.e., photosphere). Therefore in the later sections we will decompose the HVF and photospheric-velocity feature (PVF) in the Ca II NIR lines, and investigate their properties with host parameters.

Table 5.1: The SN spectral sample selection in this work.

	Criterion	Num. of SNe left
PTF parent sample	$z < 0.09$	527
Spectral phase cut	$-5\,\mathrm{d} \leq t \leq 5\,\mathrm{d}$	160
Redshift derived from host	–	143
LC quality cut	–	133
Spectrum quality cut	–	123
(In SDSS)	–	101

5.1 The SN spectral sample

We have defined a host galaxy spectral sample (82 SNe Ia) from our parent sample in chapter 4 and studied their relations with SN luminosities. To investigate the dependence of SN spectral features on host parameters, here we define a new subset from the parent sample. We focus on the SNe Ia with well-observed optical spectra near maximum light, and measure the key spectral features. Several criteria were used.

The SN selected from the parent sample have redshift $z < 0.09$, and this ensures that the Ca II near infrared triplet that we study here is included in the spectral coverage (typically 3500 – 9500 Å). Secondly, we restricted the phases of SN spectroscopic observations to be within 5 rest-frame days relative to B-band maximum light, where the variation in the SN spectral velocities with phase show only a relatively mild and linear trend (discussed further in Section 5.3). We then restrict to the SNe where the redshifts can be estimated from host galaxy features rather than from SN template fitting, as spectral velocities are significantly more uncertain in the latter case. Finally, we exclude 20 SNe Ia from our sample which have only a poor quality (low S/N) spectrum or light curve. In total, 123 events passed the above criteria and enter our final SN spectral sample. We summarise our sample selection in Table 5.1.

Of the 123 SNe Ia, 101 have host galaxies and available photometry in the Sloan Digital Sky Survey (SDSS), which we use for an M_{stellar} determination (Section 3.3.1). A further two events lie outside of the SDSS footprint but their M_{stellar} can be de-

termined using LT images (see Section. 2.4.1) taken as part of the SN photometric follow-up campaign. The remainder of the 20 SNe without photometric host data lie outside of the SDSS footprint.

5.2 Line measurement

Here we present the method to measure the line features of our SN spectral sample. We started by fitting the Si II λ6355 doublet, a prominent line in SN Ia spectra with little contamination from other features. We apply a correction for foreground galactic extinction to the SN spectrum and correct it into the rest-frame. We define (by hand) continuum regions either side of the feature, and fit a straight line pseudo-continuum across the absorption feature. The feature is then normalised by dividing it by the pseudo-continuum. A double-Gaussian fit is performed to the normalised Si II λ6355 doublet line in velocity space using the MPFIT package (Markwardt, 2009). The centres of the two Gaussians have a fixed velocity difference corresponding to the difference in the wavelengths of the doublet (λ6347 Å and λ6371 Å), the same width, and peaks fixed by the ratio of their oscillator strengths (here the ratio $\sim$2:1). The resulting fit then gives the velocity of the feature, together with the pEW.

We then fit the complex Ca II NIR feature (λ8498 Å, λ8542 Å and λ8662 Å, the strength ratio $\sim$1:9:5). This is a more complicated task as the Ca II high-velocity component can be strong around SN maximum light, and thus we fit for both photospheric velocity and high-velocity components in the absorption complex (total six components). To achieve this, we force each triplet in the photospheric velocity and high-velocity components to have the same velocities, widths and relative strengths. The Si II λ6355 velocity and width derived from the previous fit are used as initial guesses for the photospheric component of Ca II NIR line. We then require the velocity of the Ca II NIR photospheric component to be within 25% of the Si II λ6355

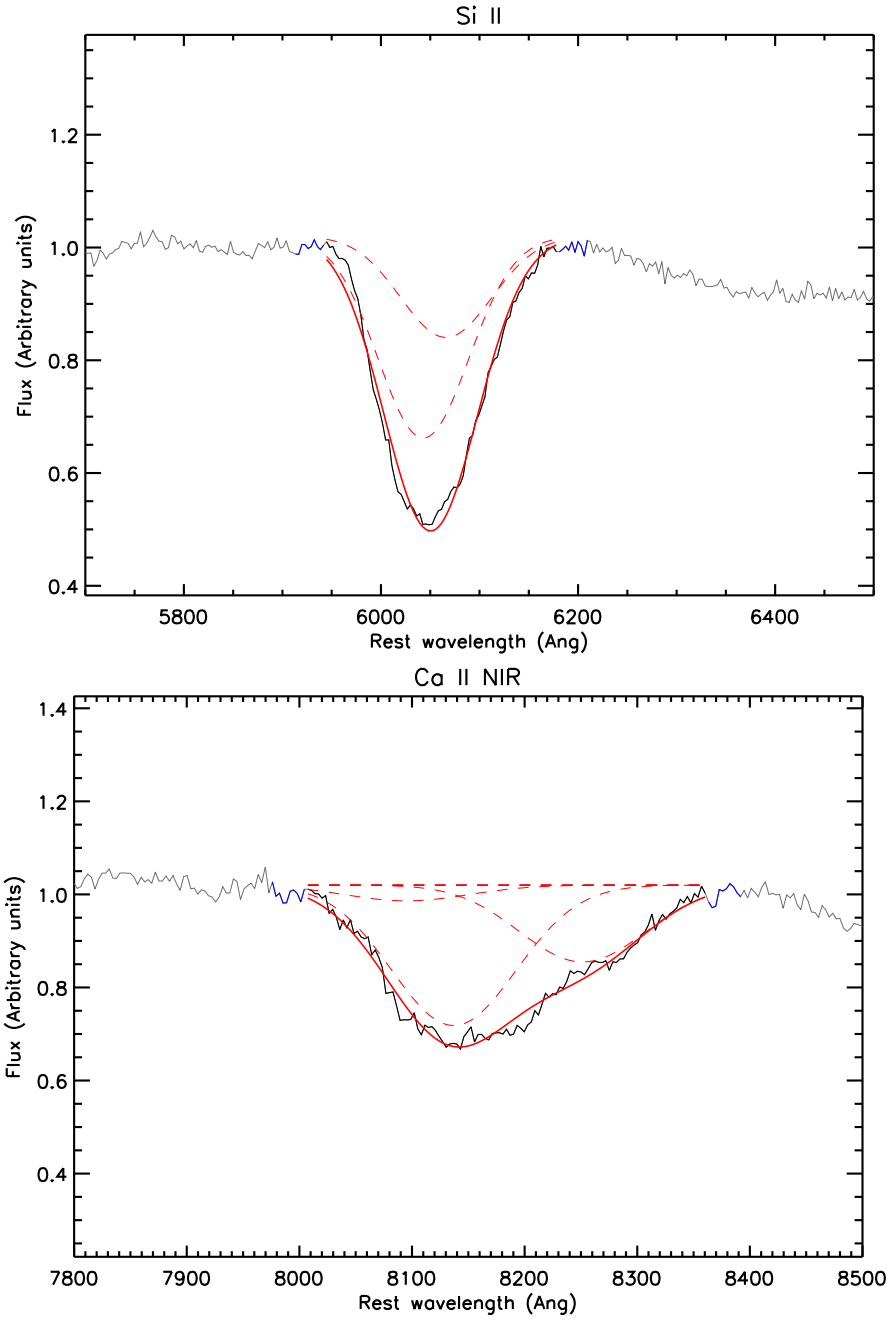

Figure 5.1: The Si II λ6355 line (top) and Ca II NIR line (bottom) from PTF10bjs. The black solid line shows the range we fit the line profile. The blue continuum regions near the left and right side of the line profile are the regions we select to fit the pseudo-continuum. The red solid line is the best fit to the line profile, which is the superposition of all the line components used for the fitting (represented in dashed lines).

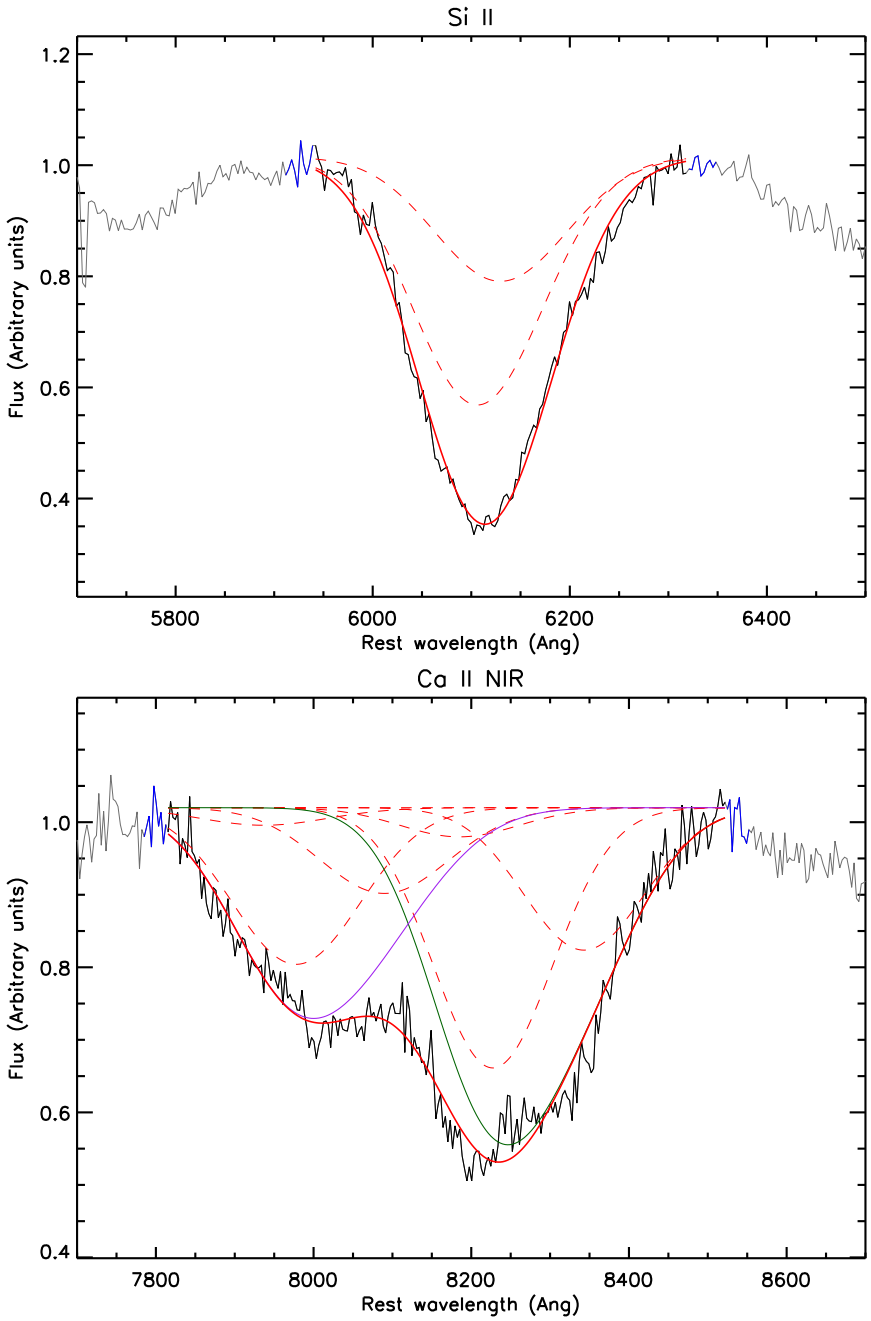

Figure 5.2: The same as Fig. 5.1, but for PTF09qn. The green curve represents the superposition of all the components in photospheric-velocity feature (PVF). The purple curve represents the superposition of all the components in the high-velocity feature (HVF).

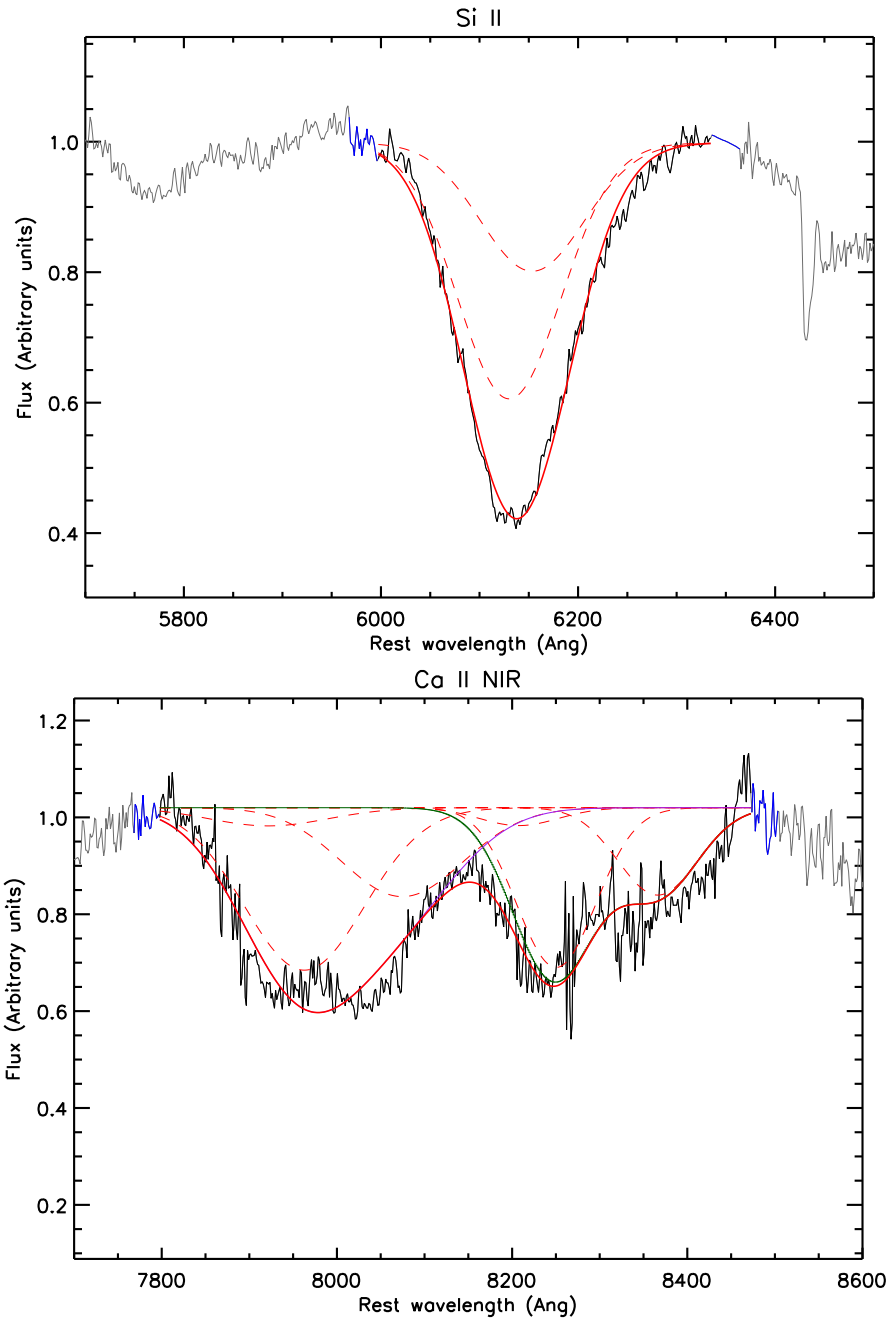

Figure 5.3: The same as Fig. 5.2, but for PTF09dlc.

velocity, and the Ca II NIR high-velocity component to be larger than the Si II λ6355 velocity by at least 2500 km s^{-1}. No other constraints are applied during the fit. We also include O I λ8446 line when fitting the Ca II NIR complex, with the constraint that its velocity is within 10% of the Si II λ6355 line. A strong O I λ8446 feature can be seen in cooler SN spectra such as the subluminous 1991bg-like objects. We found the contribution of O I λ8446 line is small for most of our SNe Ia. We focus on the Ca II NIR line measurement in this work although the Ca II H&K line (λ3933 Å and λ3968 Å) is also available in our data. This is due to the potential contamination from the Si II λ3858 line in the Ca II H&K feature, which makes the Ca II H&K measurement become uncertain (see Section 6.1.1 for a discussion).

To ensure our measurements of these absorption lines are not sensitive to the locations we selected for deriving the pseudo-continuum, we randomly move the red and blue pseudo-continuum regions by up to 10Å with respect to the original location, and re-fit the line profile. This random process is repeated 200 times. The final values reported in this work are the mean of the measurements from all the iterations, and the uncertainty is the standard deviation. From Fig. 5.1 to Fig. 5.3 we present three typical examples of the line measurements in this work. The order of figures are arranged in the sense that the strength of the high-velocity feature (HVF) component in Ca II NIR line (defined in Section 6.3) increases from Fig. 5.1 to Fig. 5.3.

5.3 Phase correction

In Section 5.1, we restricted the phases of our SN spectral sample to be within 5 days of the B-band maximum light. Over this phase range, SN Ia spectral velocities generally show a mild and linear trend (Silverman et al., 2012b). This can also be seen in our sample in Fig. 5.4, which shows the Si II λ6355 velocity as a function of phase. The velocity evolution shows a relatively linear variation within $\pm$5 d of B-

band maximum light. We therefore apply linear phase corrections to each spectral feature, and correct all our measurements to SN maximum light as follows. The spectral features as function of phases are shown in Fig. 5.4 to Fig. 5.9.

For SNe with more than one spectrum within ± 5 d, we fit a straight line to these measurements. The spectral feature at maximum light can then be estimated using the slope of the straight line (i.e., the gradient of the spectral feature). For those SNe with single spectrum we use the straight line fit to the velocity–phase diagram of all the SNe (i.e., the linear fit shown in Fig. 5.4 to Fig. 5.9). The gradient/correction of each spectral feature in this work can be found in Table 5.2, and the measurements of all the SN spectral features studied in this work (after phase correction) can be found in Table A.5. We also test if our results in later chapters are sensitive to these phase corrections. We found our conclusions are still valid without applying the phase corrections to the SN spectral parameters.

Fig. 5.11 shows the comparisons of the Si II λ6355 velocity ($v_{\rm Si\,II}$), redshift, normalised SN offset ($\rm R_{SN}/R_{gal}$) and $M_{\rm stellar}$ distributions in this work and the sample used in Wang et al. (2013) and Childress et al. (2014). Here, we only show the 123 'Branch-Normal' SNe Ia used in Wang et al. (2013). We determined the $M_{\rm stellar}$ for the hosts studied in Wang et al. (2013) using the same method described in Section 3.3.1, with 74 out of 123 events having available SDSS photometry for comparison to our sample.

The Wang et al. (2013) $M_{\rm stellar}$ distribution is very different from this work. This is almost certainly due to the selection of the SN sample used by Wang et al. (2013), which were discovered by the Lick Observatory Supernova Search (LOSS), designed as a galaxy-targeted survey. A Kolmogorov-Smirnov (K-S) test gives a $< 1\%$ probability that $M_{\rm stellar}$ distributions of Wang et al. (2013) and this work are drawn from the same underlying population.

We also see a large difference in the $v_{\rm Si\,II}$ distributions, with Wang et al. (2013)

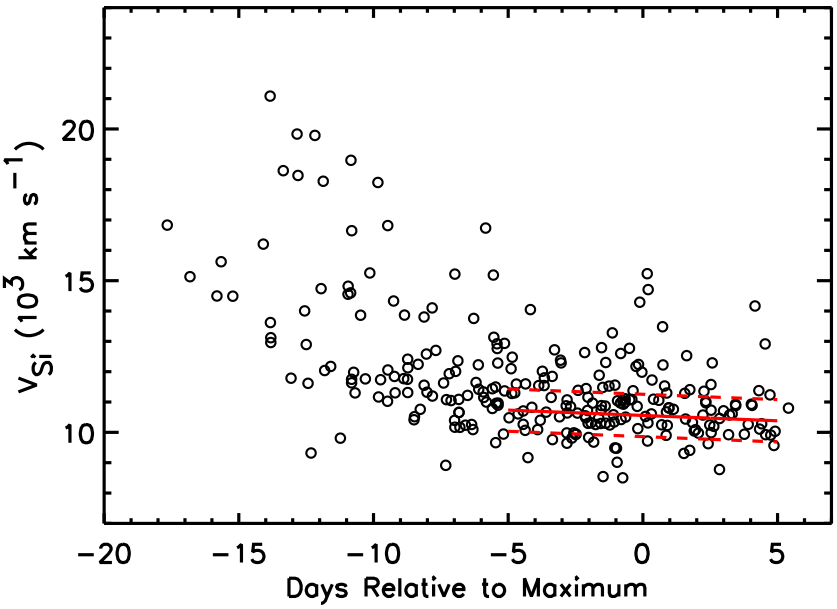

Figure 5.4: The Si II λ6355 velocity as a function of the phase of the SN Ia spectroscopic observation. The red solid line shows a linear fit to data with phases from −5d to +5d. The dashed lines show the 1-σ range relative to the fit.

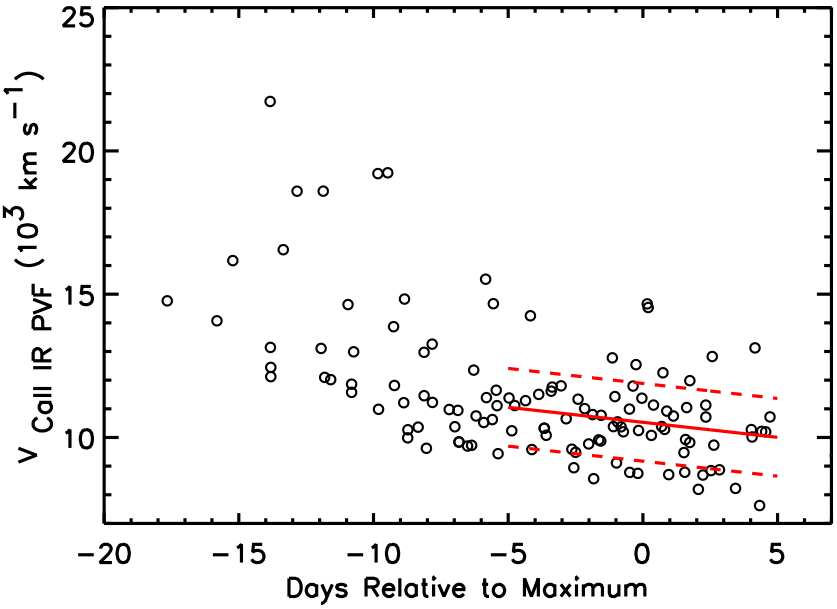

Figure 5.5: The same as Fig. 5.4, but showing the velocity of Ca II NIR photospheric-velocity feature (PVF) instead.

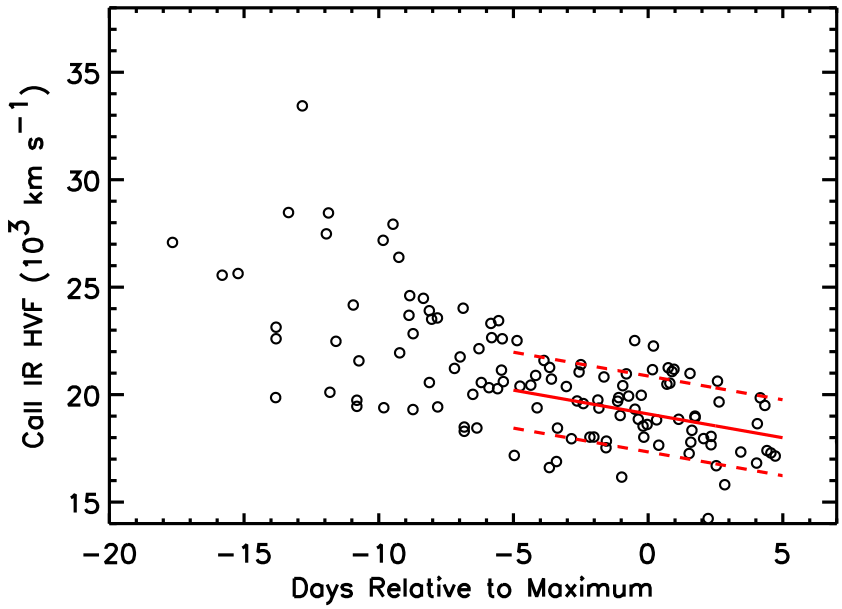

Figure 5.6: The same as Fig. 5.4, but showing the velocity of Ca II NIR high-velocity feature (HVF) instead.

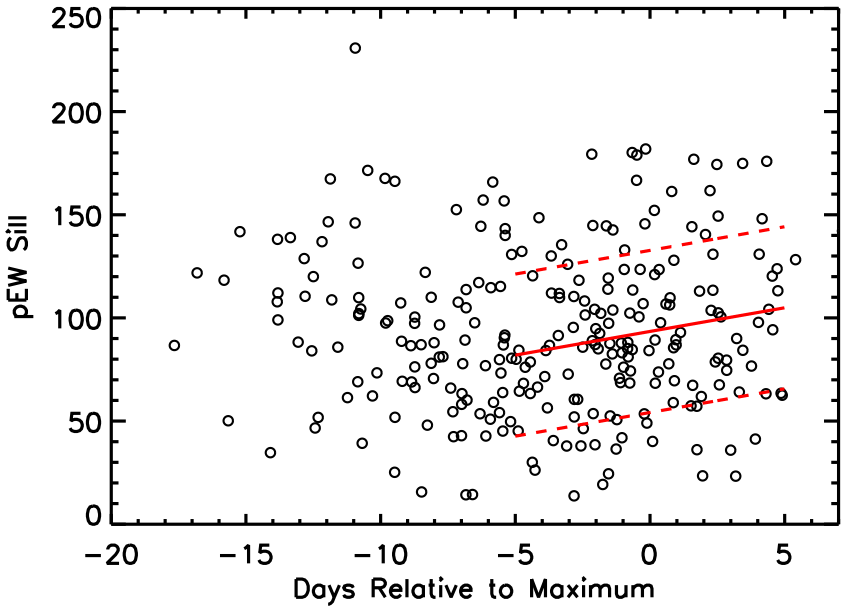

Figure 5.7: The same as Fig. 5.4, but showing pseudo-equivalent width (pEW) of Si II λ6355 instead.

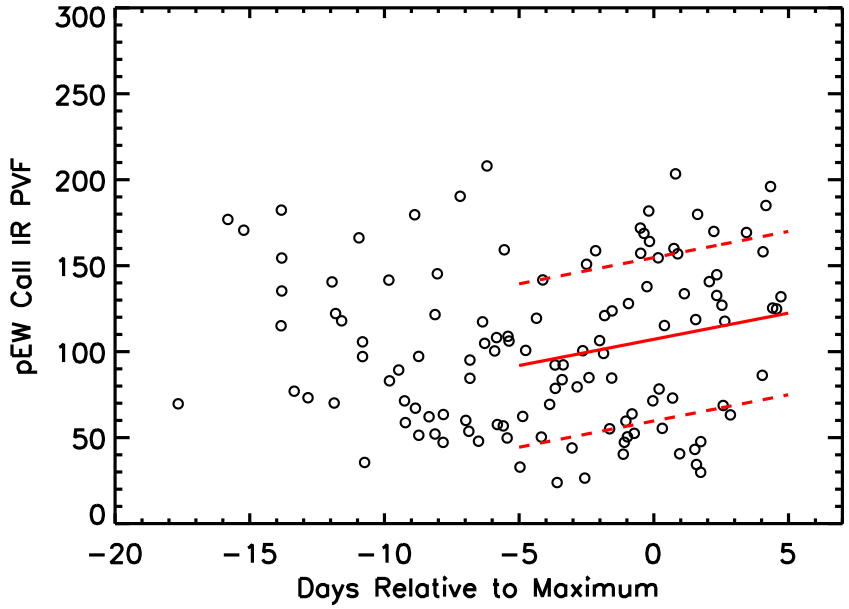

Figure 5.8: The same as Fig. 5.4, but showing pseudo-equivalent width (pEW) of Ca II NIR photospheric-velocity feature (PVF) instead.

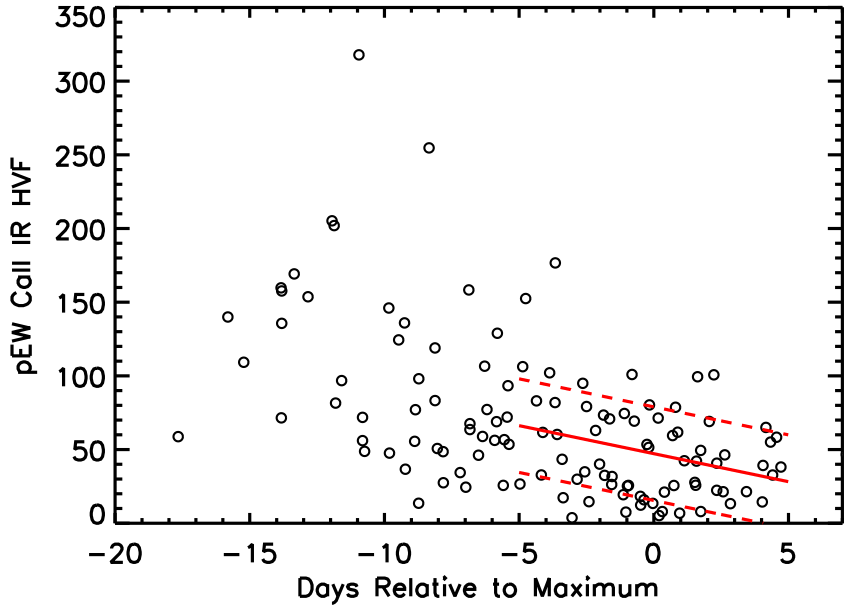

Figure 5.9: The same as Fig. 5.4, but showing pseudo-equivalent width (pEW) of Ca II NIR high-velocity feature (HVF) instead.

Table 5.2: The gradient of SN spectral features in this work.

Feature	Gradient
Si II λ6355 velocity	-37 ± 23 km s^{-1}d^{-1}
Ca II NIR velocity (PVF)	-107 ± 64 km s^{-1}d^{-1}
Ca II NIR velocity (HVF)	-224 ± 75 km s^{-1}d^{-1}
Si II λ6355 pEW	$+2.3 \pm 1.2$ Å d^{-1}
Ca II NIR pEW (PVF)	$+3.1 \pm 1.1$ Å d^{-1}
Ca II NIR pEW (HVF)	-3.8 ± 1.5 Å d^{-1}

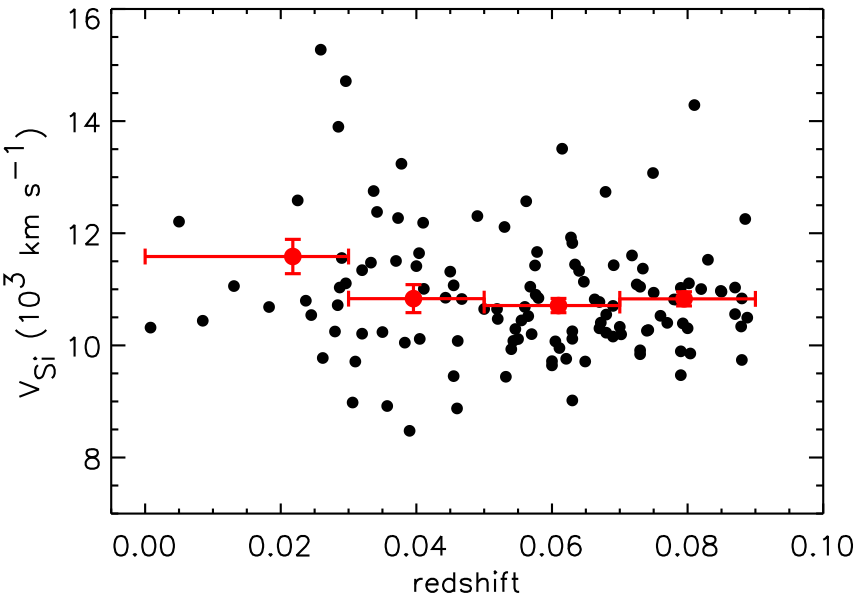

Figure 5.10: The SN Si II λ6355 velocities as a function of redshift. The red solid circles are the mean $v_{\rm Si\,II}$ in each redshift bin.

having a larger fraction of SNe Ia with high $v_{\rm Si\,II}$. Our $v_{\rm Si\,II}$ distribution is consistent with that of Childress et al. (2014). We find no evidence for a redshift evolution in $v_{\rm Si\,II}$ in our sample (see Fig. 5.10), making the small redshift difference between our sample and that of Wang et al. (2013) unlikely to drive the offset in Fig. 5.11. We discuss the possible origin of the $v_{\rm Si\,II}$ discrepancy in Section 6.1.2. The SN radial distribution of this work is consistent with that of Wang et al. (2013), despite the slightly different definitions (Section 3.3.5).

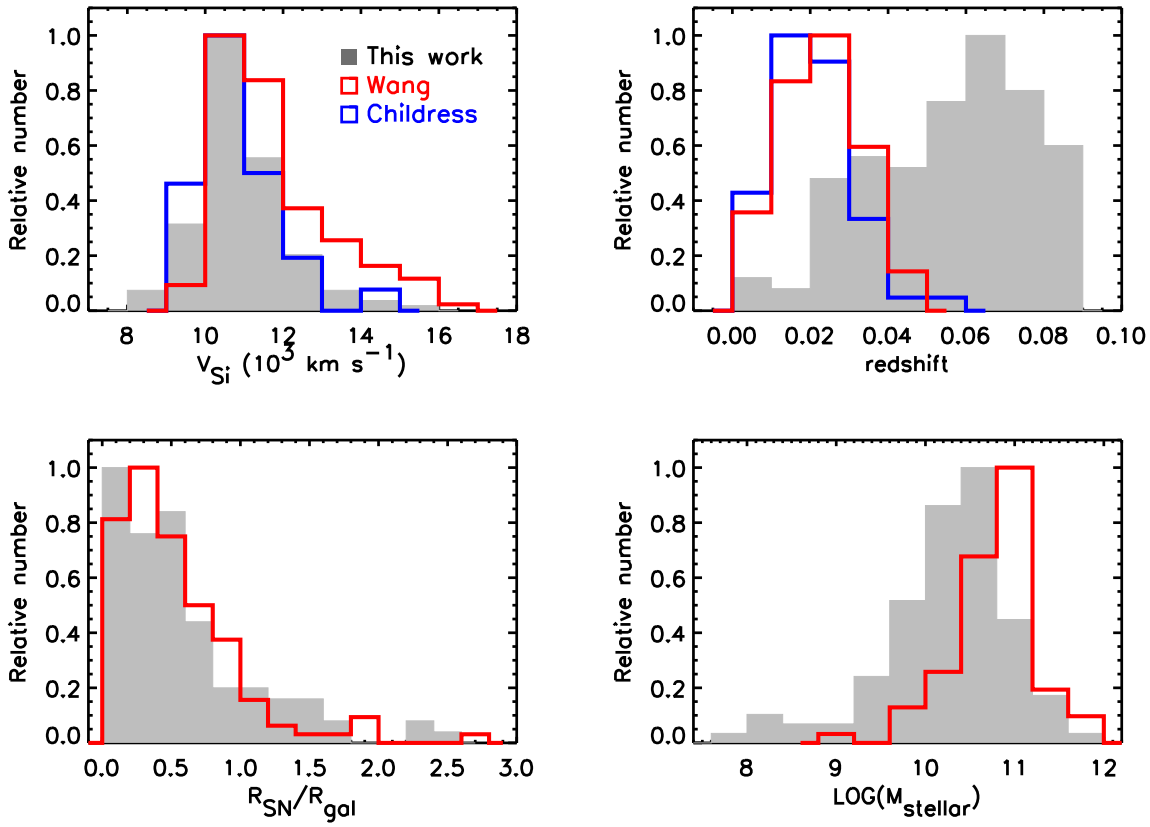

Figure 5.11: The distribution of the SN Si II λ6355 velocity, redshift, host galaxy offset, and host stellar mass ($M_{\rm stellar}$) of our samples (filled histogram). For comparison, the samples used in Wang et al. (2013) and Childress et al. (2014) are also shown in red and blue, respectively.

5.4 Summary

In this chapter, we selected a sample of SN to measure their spectroscopic properties. We presented the method to measure the SN spectral features, such as the pseudo-equivalent widths (pEW) and velocities of Si II λ6355 and the Ca II near infrared (NIR) triplet. We also decomposed the photospheric-velocity feature (PVF) and high-velocity feature (HVF) in Ca II NIR line and made a separate measurement. The correction to the variation of SN spectral features on phases were also performed. In the next chapter, we will start investigating the dependence of these SN spectral features on the host galaxy parameters.

Chapter 6

SN spectral features and host parameters

Having measured the spectral features from our SN spectral sample, we now examine the relations between these features and the host galaxy parameters. We split our analysis into two parts. The first concerns the properties of the photospheric features and velocities, namely the Si II λ6355 and Ca II NIR photospheric velocities ($v_{\rm Si\,II}$ and $v_{\rm Ca\,II\,NIR}$). The second part concerns the strength of the high-velocity features present in the Ca II NIR absorption.

6.1 Photospheric features and host parameters

In this section, we will discuss the properties of SN spectral features that are associated with the SN Ia photosphere, and their dependence on host galaxy parameters.

6.1.1 Stellar mass

We begin by examining trends with host galaxy stellar mass ($M_{\rm stellar}$). Fig. 6.1 shows $v_{\rm Si\,II}$ as a function of $M_{\rm stellar}$. There is a broad trend that high-$v_{\rm Si\,II}$ SNe Ia ($v_{\rm Si\,II} \geq 12000\,{\rm km\,s^{-1}}$) tend to reside in massive galaxies, whereas the normal-$v_{\rm Si\,II}$ SNe Ia ($v_{\rm Si\,II} < 12000\,{\rm km\,s^{-1}}$) are found in galaxies of all mass. In our sample, high-$v_{\rm Si\,II}$ SNe Ia only occur in galaxies with $\log({\rm M/M_\odot}) > 9.5$. Fig. 6.2 (top panel) shows the

cumulative distribution function of host galaxy $M_{\rm stellar}$ for both high- and normal-$v_{\rm Si\,II}$ SNe Ia. The two distributions are different particularly at the low-$M_{\rm stellar}$ end. The cumulative distribution function of $v_{\rm Si\,II}$ for SNe Ia in high and low-$M_{\rm stellar}$ hosts is also shown in Fig. 6.2 (bottom panel). The distribution of high-$M_{\rm stellar}$ hosts ($\log(\rm M/M_\odot) > 10$) is different from low-$M_{\rm stellar}$ hosts due to additional SNe at high $v_{\rm Si\,II}$.

The classical K-S test is less sensitive when testing two distributions that vary mainly in their tails, and indeed gives a p-value of 0.25 that the normal- and high-$v_{\rm Si\,II}$ SN $M_{\rm stellar}$ distributions are drawn from the same underlying population (i.e., they are not two distinct populations). The same test gives a p-value of 0.06 that low-$M_{\rm stellar}$ and high-$M_{\rm stellar}$ hosts have $v_{\rm Si\,II}$ distributions drawn from the same population. Drawing 17 SNe Ia, the size of the high-$v_{\rm Si\,II}$ sample, with replacement and at random from the full PTF sample, only in 4.7% of iterations do all the selected SNe have $M_{\rm stellar}$ greater than $4.36 \times 10^9\,M_\odot$ (the minimum $M_{\rm stellar}$ of the high-$v_{\rm Si\,II}$ SNe Ia in this work). Finally, a linear fitting performed by LINMIX (Kelly, 2007) shows a non-negative slope at 91% probability.

These results are suggestive, but not conclusive, that high-$v_{\rm Si\,II}$ SNe Ia prefer high-$M_{\rm stellar}$ host galaxies, and of a more general relationship between $v_{\rm Si\,II}$ and $M_{\rm stellar}$. We investigate if the trend holds when adding additional high-redshift $0.09 \leq z < 0.15$ PTF SNe Ia (our primary sample has $z < 0.09$; Section 5.1). This larger sample has more significant trends: the linear fitting prefers a non-negative slope at 97% probability.

Previous studies found some evidence that $v_{\rm Ca\,II\,H\&K}$ correlates with $M_{\rm stellar}$, in the sense that SNe Ia in more massive galaxies tend to have lower $v_{\rm Ca\,II\,H\&K}$ (e.g., Foley, 2012; Maguire et al., 2012); note this is opposite to the trends with $v_{\rm Si\,II}$ in Fig.6.1. Maguire et al. (2012) suggested that this trend is caused by an underlying relationship between SN light curve shape and Ca II H&K velocity, in the sense that

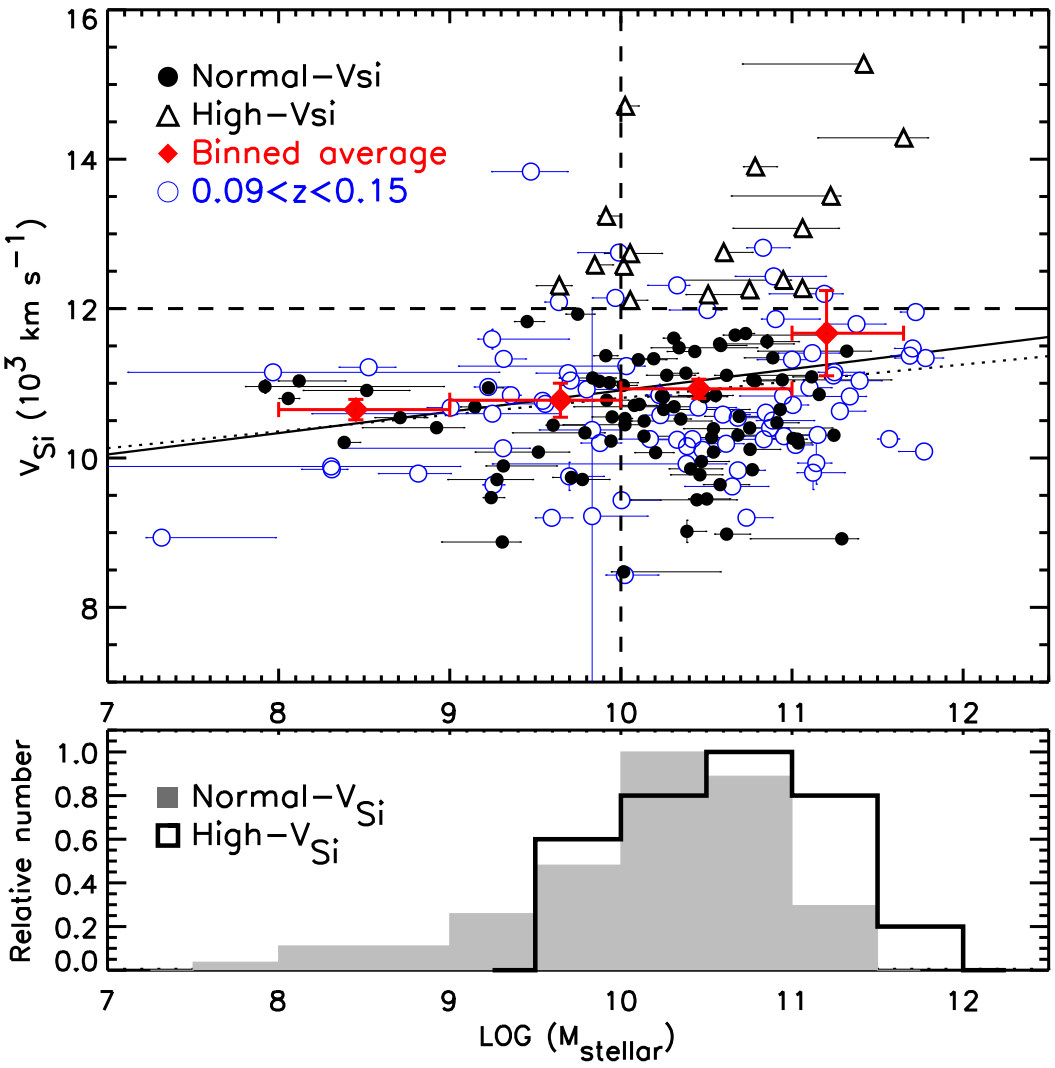

Figure 6.1: The Si II λ6355 velocities ($v_{\mathrm{Si\,II}}$) as a function of M_{stellar}. The high-$v_{\mathrm{Si\,II}}$ SNe Ia (with $v_{\mathrm{Si\,II}} \geq 12000\,\mathrm{km\,s^{-1}}$) are shown as open triangles, and the normal-$v_{\mathrm{Si\,II}}$ SNe Ia are shown as filled circles. The red diamonds represent the mean velocities in bins of M_{stellar}, and their error bars are the width of the bins and the error on the mean. The vertical and horizontal dashed lines represent the criterion used to split the sample in velocity and M_{stellar} space, respectively. The solid line is the linear fit to the data in the plot (filled circles plus open triangles). We overplot the SNe with $0.09 < z < 0.15$ in open blue circles for comparison. The linear fit to all the data (including those $0.09 < z < 0.15$) is shown in dotted line. The bottom histograms show the M_{stellar} distributions of high-$v_{\mathrm{Si\,II}}$ and normal-$v_{\mathrm{Si\,II}}$ SNe Ia.

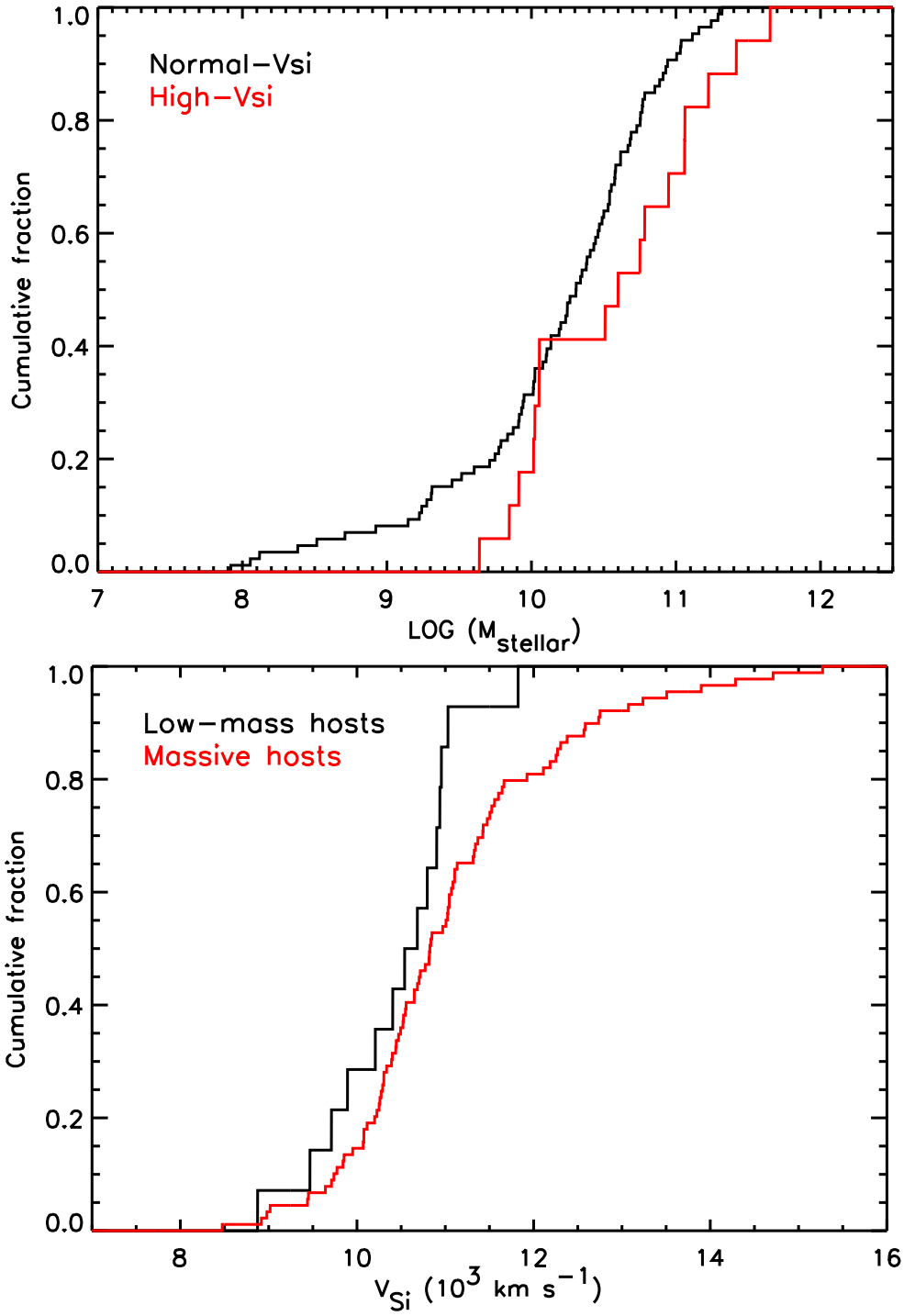

Figure 6.2: Top panel: The cumulative fractions of host $M_{\rm stellar}$ of high-$v_{\rm Si\,II}$ and normal-$v_{\rm Si\,II}$ SNe Ia. Bottom panel: The cumulative fractions of $v_{\rm Si\,II}$ of SNe Ia in massive and low-mass host galaxies.

SNe with higher stretches tend to have higher Ca II H&K velocities (which is also seen in this work; Fig. 6.3). They found the trend between Ca II H&K velocity and $M_{\rm stellar}$ disappeared after removing the correlation between SN light curve shape and Ca II H&K velocity.

However, Foley (2013) argued the contribution of the Si II λ3858 line to the Ca II H&K feature is important, and may make the measurement of the Ca II H&K line uncertain. They suggested the blue component of the Ca II H&K feature is caused by the Si II λ3858 feature for most SNe Ia, and that therefore the correlation between SN light curve shape and $v_{\rm Ca\,II\,H\&K}$ observed in Maguire et al. (2012) could be due to the strong correlation between Si II λ3858 and excitation temperature, and therefore the SN light curve shape. Childress et al. (2014) found the HVFs are stronger in higher stretch SNe Ia, supporting the idea proposed by Maguire et al. (2012). However, they also showed the Si II λ3858 line does have some impact on the Ca II H&K line. In summary, these results implies the trend between $v_{\rm Ca\,II\,H\&K}$ and $M_{\rm stellar}$ may not be unambiguously caused by the intrinsic property of Ca II feature itself.

Clearly a problem with these analyses is the use of the Ca II H&K, which is a difficult feature to model accurately. Here we use Ca II NIR line instead, as it provides us a cleaner measurement of Ca II velocity feature without contamination from other features (e.g., Si); we are also able to decompose the high-velocity and photospheric-velocity components. Fig. 6.4 shows the Ca II NIR velocity of these photospheric and high-velocity components as a function of $M_{\rm stellar}$. Similar to our $v_{\rm Si\,II}$ analysis, SNe with the highest photospheric $v_{\rm Ca\,II\,NIR}$ also tend to reside in massive galaxies. This may not be surprising given the strong correlation between Si II λ6355 velocities and Ca II NIR PVF velocities (Fig. 6.5). The high-velocity $v_{\rm Ca\,II\,NIR}$ shows no significant trend with $M_{\rm stellar}$, although there is suggestion that SNe with low $v_{\rm Ca\,II\,NIR}$ are deficient in lower-mass galaxies. Maguire et al. (2014) showed that the SNe with strong HVFs (i.e., $\rm R_{HVF} > 1$) generally have higher Ca II velocities. If the hosts with

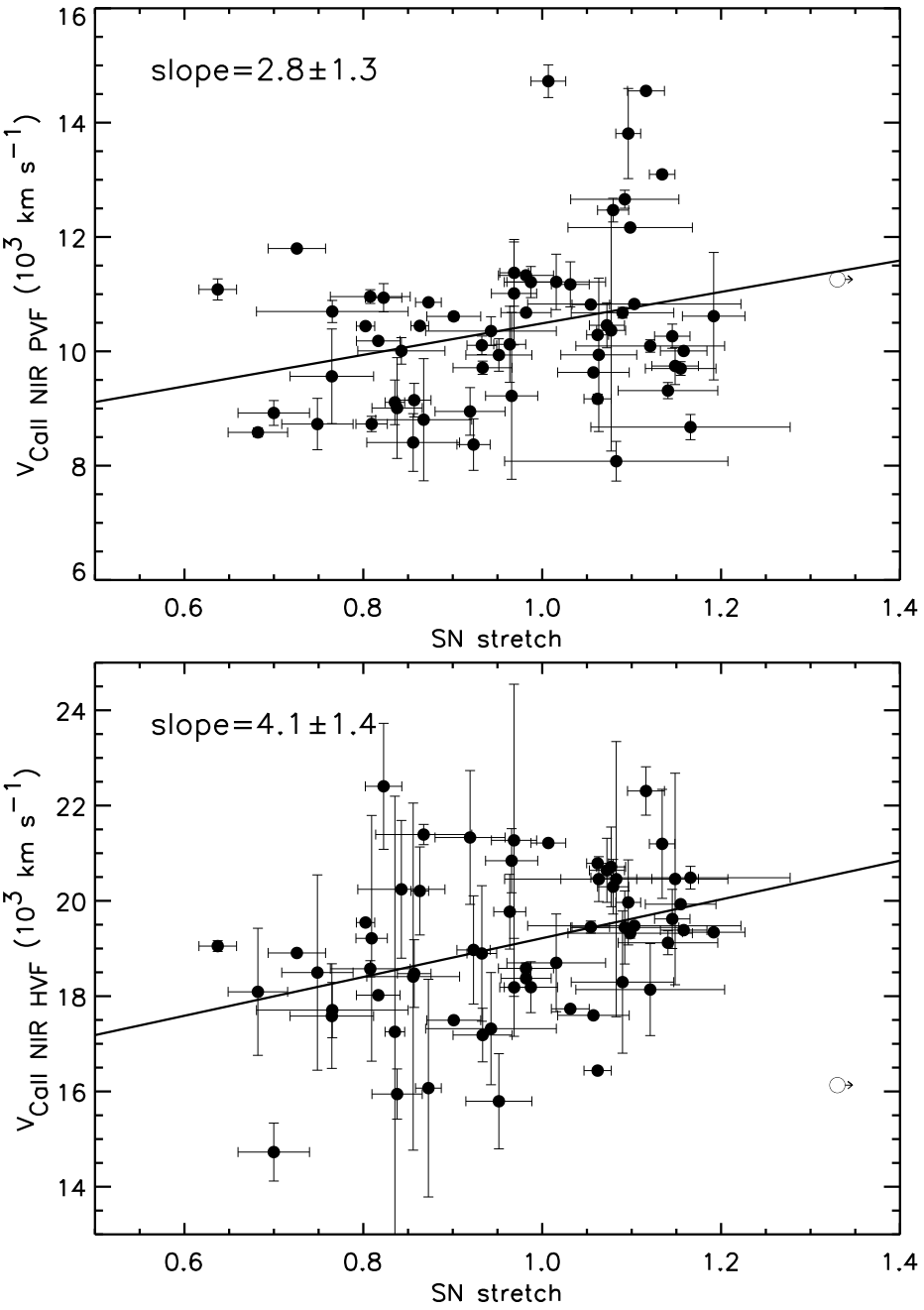

Figure 6.3: The upper panel shows the Ca II NIR velocities of photospheric-velocity feature (PVF) as a function of SN stretch. The lower panel shows the Ca II NIR velocities of high-velocity feature (HVF) as a function of SN stretch. The solid line in each panel shows the best linear fit to the data. The open circle shows one outlier in the plot: PTF09dhx ($s = 1.7$, $v_{\mathrm{Ca\,II\,NIR}} = 11,258$ and 16,132 km s^{-1} for PVF and HVF, respectively.

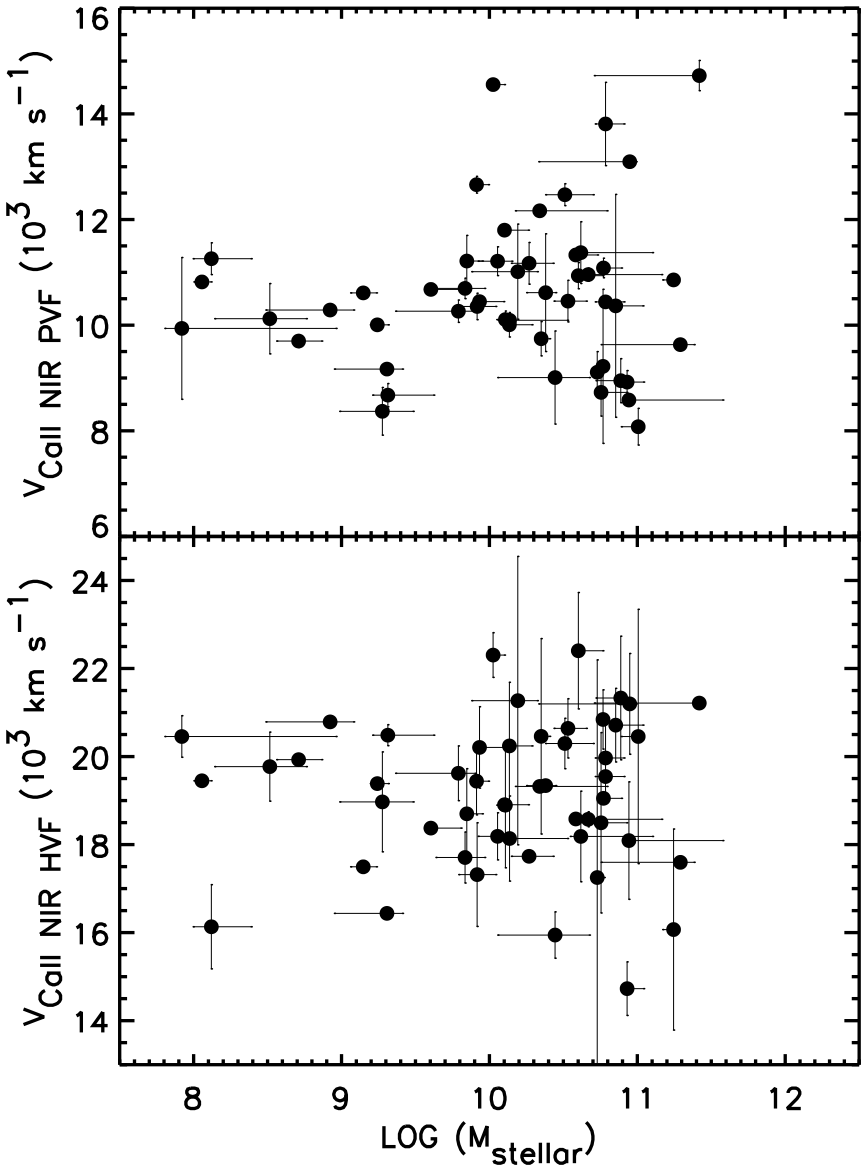

Figure 6.4: The upper panel shows the Ca II NIR velocities of photospheric feature (PVF) as a function of $M_{\rm stellar}$. The lower panel shows the Ca II NIR velocities of high-velocity feature (HVF) as a function of $M_{\rm stellar}$.

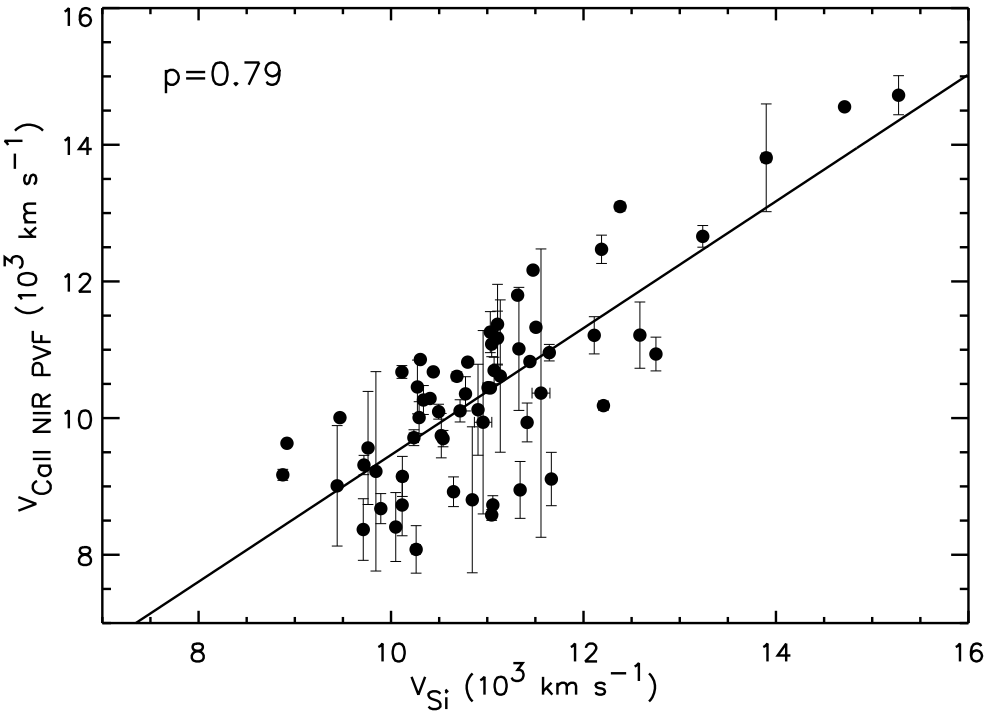

Figure 6.5: The Si II λ6355 velocities as a function of Ca II NIR PVF velocities. The solid line shows the best linear fit to the data. A Pearson correlation coefficient gives a value of $p = 0.79$ to the relation.

lower $M_{\rm stellar}$ ($\log(\rm M/M_\odot) < 10$) are dominated by SNe with strong HVFs (as we will see in Section 6.3), we will expect the SNe in low $M_{\rm stellar}$ galaxies have higher Ca II NIR HVF velocities. That might explain the tendency for the low-mass galaxies in our sample to lack SNe with low Ca II NIR HVF velocities.

6.1.2 SN offset

Wang et al. (2013) found evidence for two distinct populations of SNe Ia with respect to their radial distributions in the host galaxies. They found that the high-$v_{\rm Si\,II}$ SNe Ia are concentrated in the inner regions of their host galaxies, whereas the normal-$v_{\rm Si\,II}$ SNe Ia span a wide range of radial distance. We next examine this trend in our sample in Fig. 6.6, showing $v_{\rm Si\,II}$ as a function of the normalised SN offset, $\rm R_{SN}/R_{gal}$ (see Section 3.3.5). The high-$v_{\rm Si\,II}$ SNe Ia in the PTF sample also appear deficient in the outer regions of their hosts compared to the normal-$v_{\rm Si\,II}$ SNe Ia, which are found

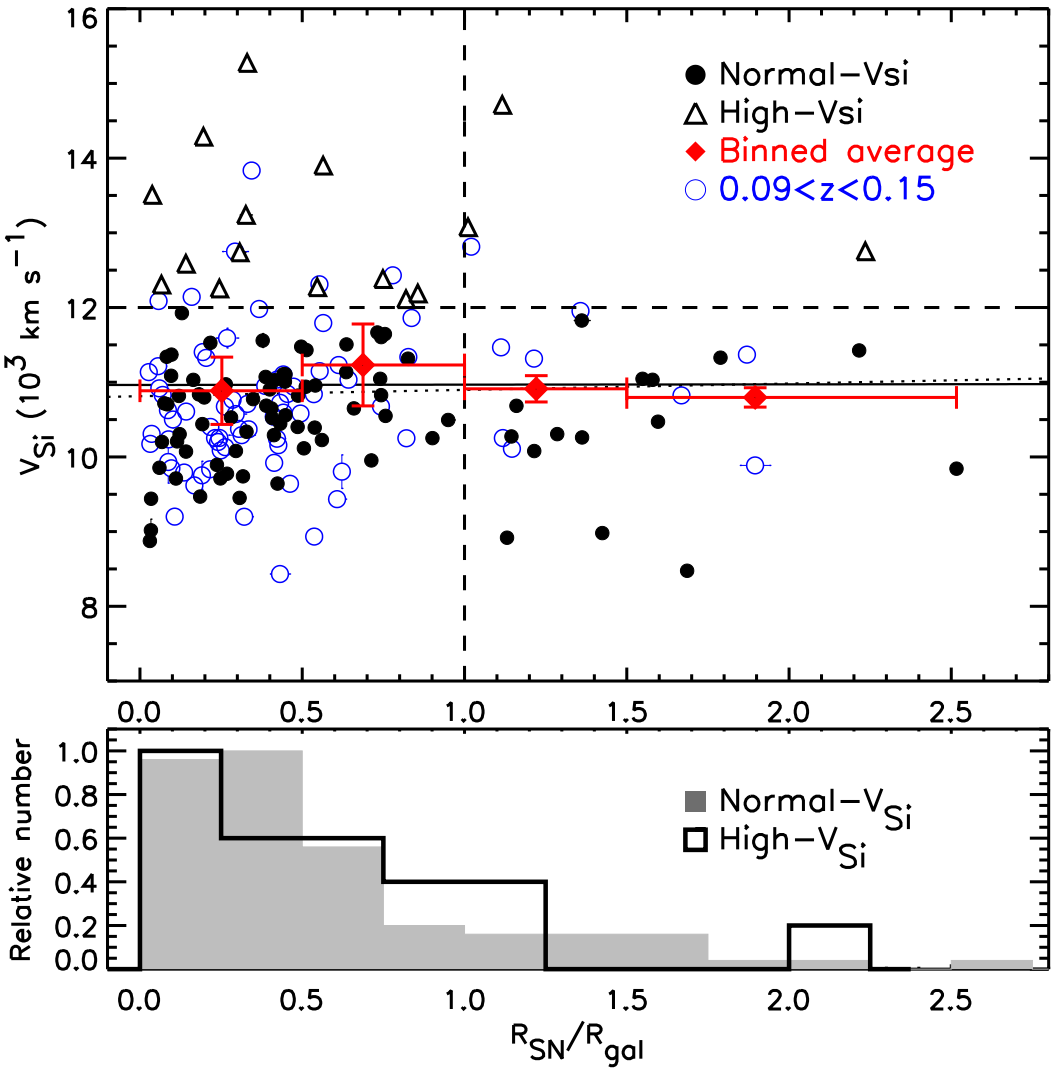

Figure 6.6: As Fig. 6.1, but considering the R_{SN}/R_{gal} ratio instead of $M_{stellar}$. R_{SN} and R_{gal} are defined in Section 3.3.5.

at all radii. The only high-$v_{Si\,II}$ SN at a large radius (PTF09djc; $v_{Si\,II}$= 12751 km s^{-1}, R_{SN}/R_{gal}= 2.2) resides in the outskirts of an extended galaxy, with no potential host found at the SN position to the SDSS photometric limit ($r \simeq 22$ mag).

However, in our sample the trend is not statistically significant. We found that the locations of 81% of the high-$v_{Si\,II}$ SNe Ia and 82% of the normal-$v_{Si\,II}$ SNe Ia are within $R_{SN}/R_{gal} = 1$, which implies the high-$v_{Si\,II}$ SNe Ia are similar to the normal-$v_{Si\,II}$ SNe Ia with respect to their radial distribution, although the normal-$v_{Si\,II}$ SN sample size is much larger. Fig. 6.7 shows the cumulative distribution functions of

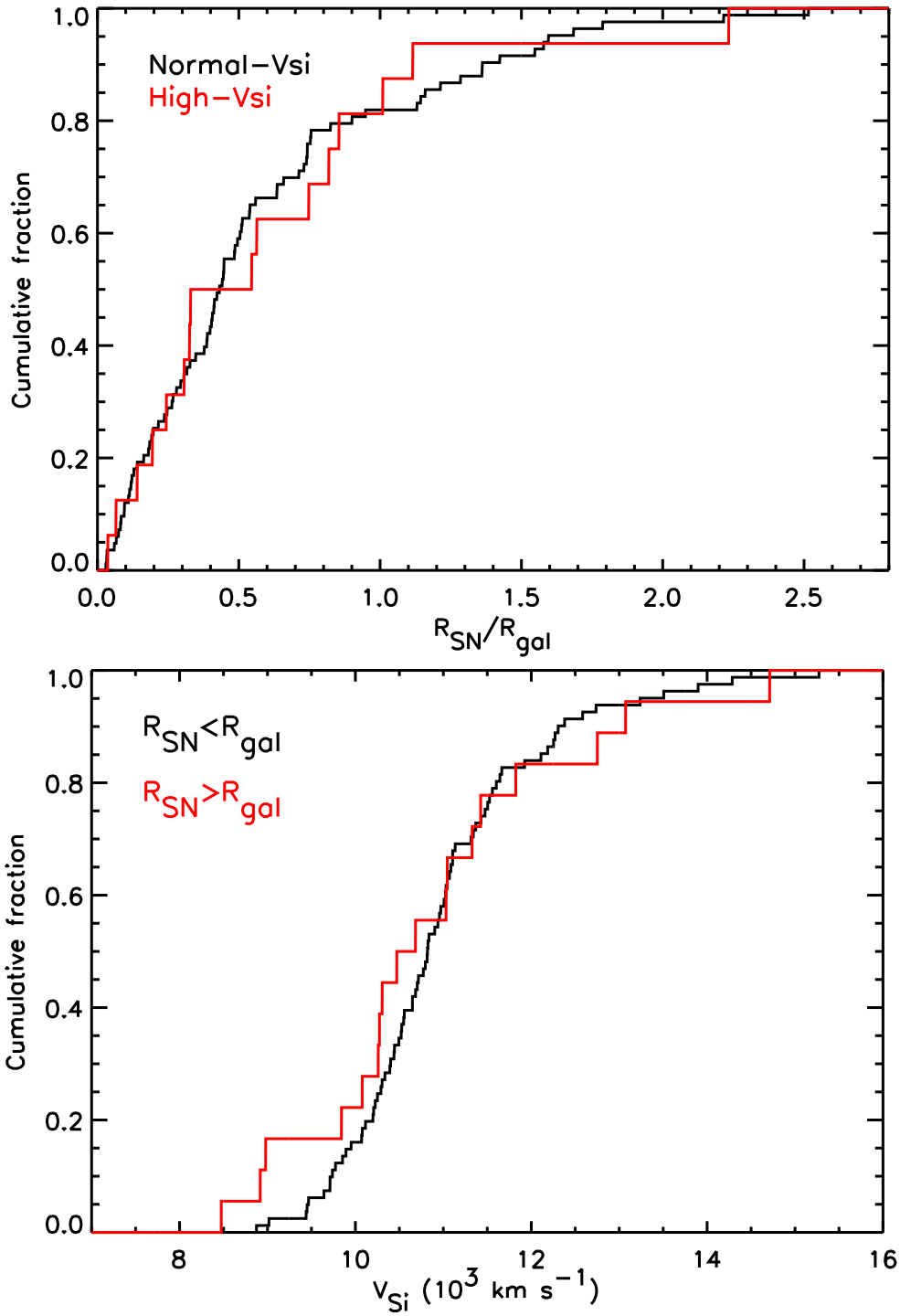

Figure 6.7: Top panel: The cumulative fractions of R_{SN}/R_{gal} of high-$v_{Si\,II}$ and normal-$v_{Si\,II}$ SNe Ia. Bottom panel: The cumulative fractions of in $v_{Si\,II}$ of SNe Ia in larger radial distance and smaller radial distance.

R_{SN}/R_{gal} for high-$v_{Si\,II}$ and normal-$v_{Si\,II}$ SNe Ia, and $v_{Si\,II}$ for SNe at $R_{SN}/R_{gal} > 1$ and $R_{SN}/R_{gal} < 1$. We do not see significant differences in the distributions; a K-S test gives p=0.90 that high-$v_{Si\,II}$ SNe Ia and normal-$v_{Si\,II}$ SNe Ia are drawn from the same population in R_{SN}/R_{gal}. This value is larger than that for the Wang et al. (2013) sample ($p = 0.005$). Repeating the same analysis as Section 6.1.1 and randomly selecting 16 SNe from the full sample, in only 4.9% of cases do all the selected SNe have R_{SN}/R_{gal} smaller than 1.1 (the maximum R_{SN}/R_{gal} of the high-$v_{Si\,II}$ SNe Ia). However, this test excludes the outlier PTF09djc. We see very similar results when including all PTF SNe Ia up to $z < 0.15$, and thus conclude that there is no strong evidence in our sample that high-$v_{Si\,II}$ SNe Ia prefer the inner regions of their host galaxies.

One explanation for the differing level of significance, despite the similar overall sizes of this and the Wang et al. (2013) sample, is that the PTF sample has a smaller fraction of high-$v_{Si\,II}$ SNe Ia (15%; 18 high-$v_{Si\,II}$ SNe and 105 normal-$v_{Si\,II}$ SNe) compared to Wang et al. (2013) (33%; 40 high-$v_{Si\,II}$ SNe Ia and 83 normal-$v_{Si\,II}$ SNe Ia). This may be because the Wang et al. (2013) sample is biased towards massive galaxies (Fig. 5.11; Section 5.3), whereas PTF is untargeted. If high-$v_{Si\,II}$ SNe Ia occur more frequently in massive galaxies (e.g., Fig. 6.1; Section 6.1.1), we would expect more high-$v_{Si\,II}$ SNe Ia to be discovered in a galaxy-targeted survey such as LOSS.

We test this hypothesis by attempting to reproduce the $v_{Si\,II}$ distribution of Wang et al. (2013) using the PTF sample, by matching the Wang et al. selection in $M_{stellar}$. We generate synthetic SN samples by selecting 123 events (the size of the Wang et al. sample) from the PTF sample, with the probability of a SN being selected weighted by its $M_{stellar}$, using the $M_{stellar}$ distribution from Wang et al. (2013). We repeated this procedure 10,000 times and determined the mean $v_{Si\,II}$ distribution. The result is shown in Fig. 6.8.

Weighting by $M_{stellar}$ clearly alters the $v_{Si\,II}$ distribution of our synthetic sample,

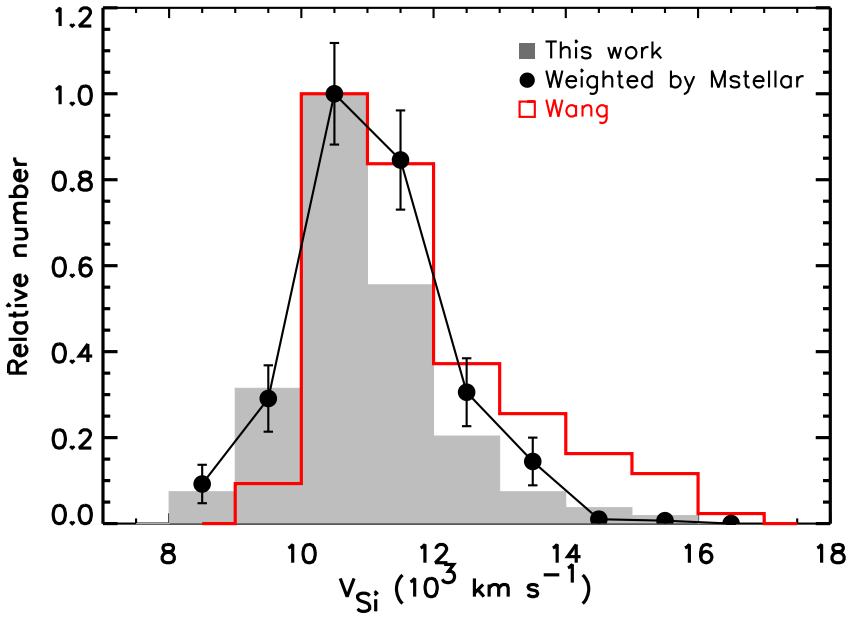

Figure 6.8: The comparison of the $v_{\rm Si\,II}$ distributions in the PTF sample (filled histogram) compared with the Wang et al. (2013) sample (open red histogram). The filled circles connected by solid lines show the distribution of our sample weighted by the $M_{\rm stellar}$ of Wang et al. (2013), in an attempt to account for the selection differences seen in Fig. 5.11.

as expected. The distribution in $v_{\rm Si\,II}$ between 8000 and 13000 km s^{-1}, after weighting by $M_{\rm stellar}$, is now consistent with Wang et al. (2013). However, the distribution is still inconsistent at $v_{\rm Si\,II} > 13000$ km s^{-1}. Thus although the selection bias in $M_{\rm stellar}$ may explain some of the difference, it is clear that either some other variable is also at work, or our tests of the selection effects do not capture all the effects.

6.1.3 Other host parameters

Of the 123 SN Ia host galaxies in our SN spectral analysis, 41 events have spectral parameters measured in Chapter 3. In Fig. 6.9, we present the $v_{\rm Si\,II}$ as a function of these other host parameters, including specific star formation rate (sSFR), gas-phase metallicity, stellar metallicity and stellar age. The sample size is smaller than for the investigations related to $M_{\rm stellar}$ or $\rm R_{SN}/R_{gal}$, and we do not find any significant trends between $v_{\rm Si\,II}$ and these host properties.

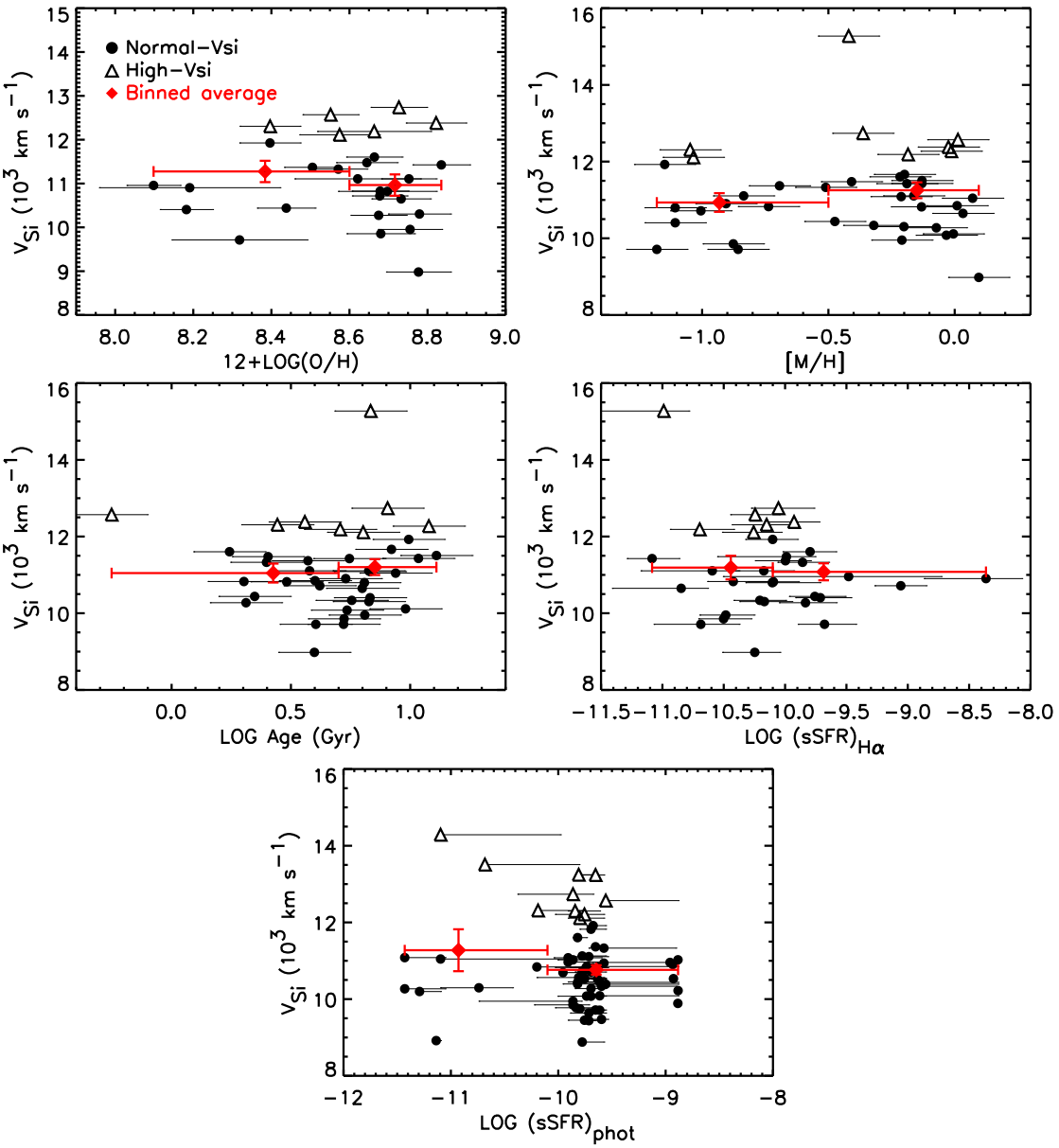

Figure 6.9: The Si II λ6355 velocity ($v_{\rm Si\,II}$) as a function of gas-phase metallicity (upper left), stellar metallicity (upper right), stellar age (middle left), specific star-formation rate derived from Hα luminosity (middle right), and specific star-formation rate derived from Z-PEG (bottom). The red diamonds represent the mean of $v_{\rm Si\,II}$ in bins of each of the host parameters, and the error bars are the width of the bins and the error of the mean.

6.2 Silicon velocity and metallicity

Wang et al. (2013) found that high-$v_{\rm Si\,II}$ SNe Ia appear concentrated in the inner regions of their host galaxies, whereas normal-$v_{\rm Si\,II}$ SNe Ia span a wider range of radial distance. Observations have shown that negative metallicity gradients are common in both the Milky Way and many external galaxies, in the sense that the heavy-element abundances decrease systematically outward from the centre of galaxies (Henry & Worthey, 1999). Therefore we would expect these high-$v_{\rm Si\,II}$ SNe Ia are more likely to originate from metal-rich populations. In this work we did not find any significant trends between high-$v_{\rm Si\,II}$ SNe Ia and radial position. However, we did observe a stronger trend that high-$v_{\rm Si\,II}$ SNe Ia tend to explode in more massive galaxies. According to the galaxy mass-metallicity relation (Tremonti et al., 2004; Kewley & Ellison, 2008), massive galaxies are generally more metal-rich than low-mass galaxies, and thus the stellar populations in the inner regions of galaxies may be similar to massive galaxies with respect to their metallicities. By using the $M_{\rm stellar}$ as a different approach, we suspect metallicity may be a potential variable in making high-$v_{\rm Si\,II}$ SNe Ia different from normal-$v_{\rm Si\,II}$ SNe Ia.

Lentz et al. (2000) showed that the C+O layer metallicity in SN Ia explosions could play a role in affecting the observed Si II λ6355 velocity. The blue-shifted velocities of the silicon features increase with C+O layer metallicity due to the increasing opacity in the C+O layer moving the features blueward and causing larger line velocities. The number of metallicity measurements from host spectroscopic data in this work do not have sufficient statistical power to reveal if metallicity is important factor in altering the $v_{\rm Si\,II}$. However, given the tight relation between $M_{\rm stellar}$ and metallicity, it offers a possible explanation that high-$v_{\rm Si\,II}$ SNe Ia could originate from more metal-rich populations than normal-$v_{\rm Si\,II}$ SNe Ia.

6.3 High-velocity features and host parameters

Having examined the relations between SN photospheric features and host parameters, we now discuss the HVFs seen in the Ca II NIR feature. Following the procedure in Childress et al. (2014), we quantify the strength of the HVFs using the ratio (R_{HVF}) of the pEWs of the Ca II NIR photospheric-velocity component to the pEW of the high-velocity component, which is computed as

$$R_{HVF} = \frac{\text{pEW(HVF)}}{\text{pEW(PVF)}} \tag{6.1}$$

SNe Ia with a larger R_{HVF} will present stronger relative absorption in the high-velocity component. We define SNe Ia with $R_{HVF} > 1.0$ as having strong HVFs.

Fig. 6.10 shows R_{HVF} as a function of the SN stretch (s), $v_{Si\,II}$, and $M_{stellar}$. The SNe in the plot are further colour-coded into three populations: normal-$v_{Si\,II}$ SNe Ia, high-$v_{Si\,II}$ SNe Ia and SNe Ia with strong HVFs. We see a clear trend that nearly all SNe Ia with strong HVFs (or large R_{HVF}) have high stretches ($s \geq 1.05$), as expected (Childress et al., 2014). There is one outlier in the plot with very high stretch but weak HVFs: PTF09dhx ($s = 1.7$, $R_{HVF} = 0.32$). By contrast, SNe Ia with high-$v_{Si\,II}$ have relatively weak HVFs and intermediate stretches ($0.8 < s < 1.1$). We also confirm that SNe Ia with strong HVFs have normal Si II λ6355 velocities ($v_{Si\,II} < 12000\,\mathrm{km\,s^{-1}}$), already noted by Childress et al. (2014). In Fig. 6.11 we plot the SN Si II λ6355 velocity as a function of SN stretch, which provides us a different angle in understanding the relation between SN stretch and these HVFs. We found no trend between Si II λ6355 velocities and SN stretch. However, we confirm what we already found: The SNe Ia with strong HVFs have high stretches but normal Si II λ6355 velocities.

The lower panels of Fig. 6.10 show the relations between SN stretch, $M_{stellar}$ and R_{HVF}. In contrast to high-$v_{Si\,II}$ SNe Ia, which are likely to reside in massive galaxies,

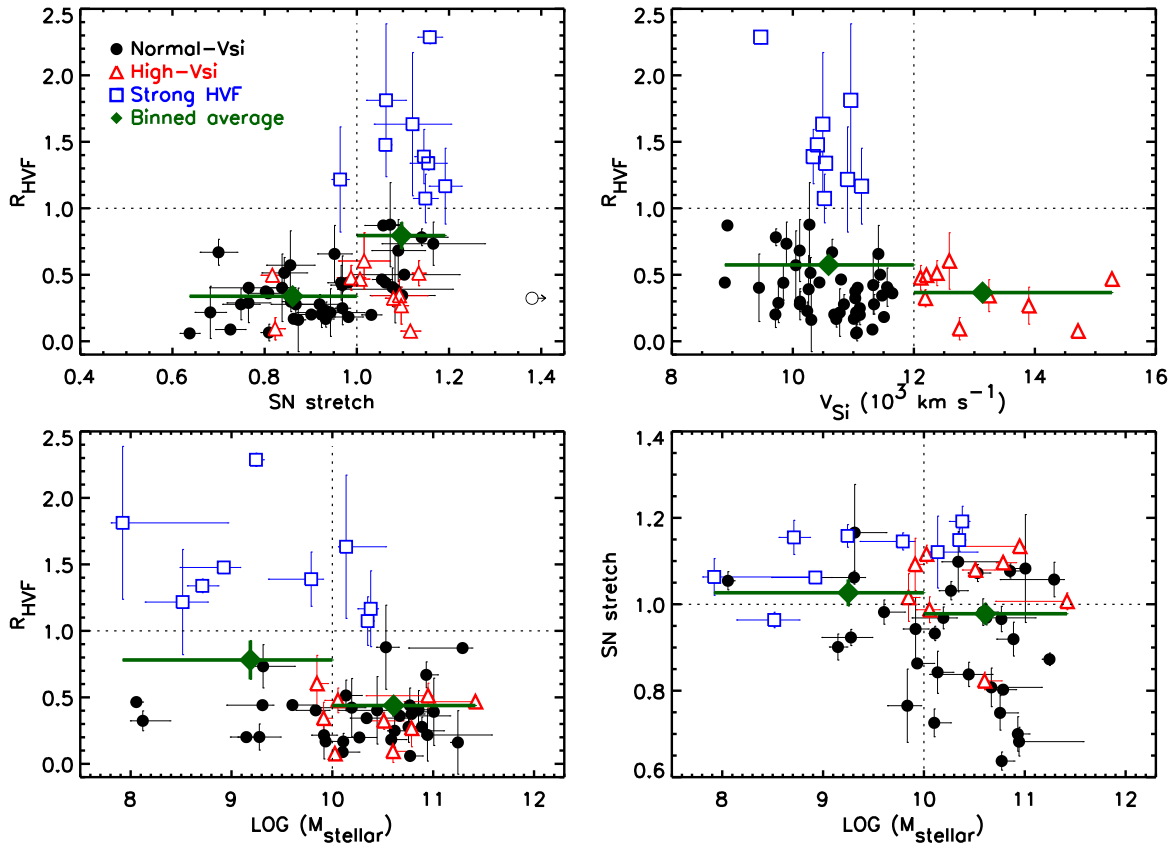

Figure 6.10: The ratio of the pEW of the high-velocity Ca II NIR feature to the photospheric Ca II feature, R_{HVF} as a function of various parameters. Upper left is the SN stretch, upper right the Si II λ6355 velocity, and lower left the $M_{stellar}$. The SN stretch is plotted against $M_{stellar}$ in the lower-right panel. Only SNe with Ca II NIR features are plotted. The solid circles, open triangles and open squares represent the normal-$v_{Si\,II}$ SNe Ia, high-$v_{Si\,II}$ SNe Ia and strong HVFs (i.e., a large R_{HVF}) respectively. The solid green diamonds represent the mean R_{HVF} in each bin. The open circle in R_{HVF}–stretch plot shows one outlier in the plot: PTF09dhx ($s = 1.7$, $R_{HVF} = 0.32$).

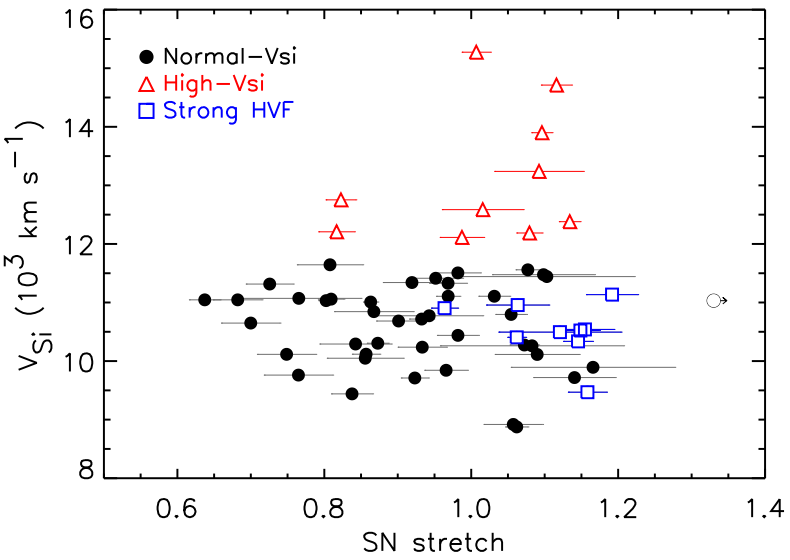

Figure 6.11: The Si II λ6355 velocities as a function of SN stretch. The same colour code is used in the plot as Fig. 6.10.

here we find that SNe Ia with strong HVFs are preferentially to be found in low-mass galaxies. The K-S test gives a p-value 0.009 that the host $M_{\rm stellar}$ distributions of strong HVFs and weak HVFs are drawn from the same population. Thus SNe Ia with high-$v_{\rm Si\,II}$ appear different in terms of their host galaxies to SNe Ia with high-velocity Ca II NIR features.

In Fig. 6.12 we examine $\rm R_{HVF}$ as a function of the specific star-formation rate (sSFR) and $\rm R_{SN}/R_{gal}$. Here we use the sSFR determined by z-PEG instead of using the Hα luminosity to increase the sample size. The events with strong HVFs all reside in strongly star-forming galaxies, and indeed nearly all SNe in such galaxies display strong HVFs. By contrast, SNe with high-$v_{\rm Si\,II}$ tend to reside in galaxies with intermediate sSFRs: log(sSFR) ~ -9.7. For the relation between $\rm R_{HVF}$ and $\rm R_{SN}/R_{gal}$, we found all SNe with strong HVFs are located within $\rm R_{SN}/R_{gal} = 1$ of their host galaxies. As we will see in Section 6.4, these HVFs mostly come from late-type galaxies (spirals or irregulars). This strongly implies that SNe Ia with HVFs are less likely to originate from the old populations residing in the galactic halo distant from the host centre.

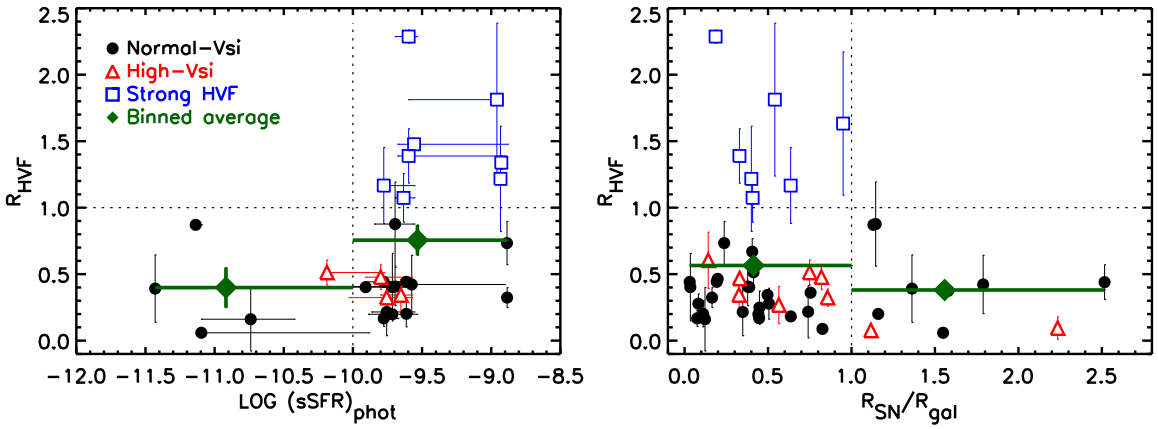

Figure 6.12: The same as Fig. 6.10 but with the sSFR derived from Z-PEG (left) and R_{SN}/R_{gal} (right).

6.4 The physical origin of HVFs

In this work, we found SNe Ia with strong HVFs present different properties to those with weak HVFs, probably implying a different origin. The physical origin of the HVFs in SNe Ia is not yet clear. They are common in SN Ia spectra, and many scenarios have been proposed by previous studies (Wang et al., 2003; Gerardy et al., 2004; Mazzali et al., 2005a,b; Tanaka et al., 2006; Childress et al., 2013c, 2014).

Wang et al. (2003) found a strong double-troughed absorption feature near 8000Å in the spectra of SN 2001el around the maximum light. The HVF in the absorption profile shows a higher degree of polarisation and different polarisation angle compared to the continuum, and was thought to be a kinematically distinct feature. Gerardy et al. (2004) found similar HVFs in SN 2003du during its early phases and at maximum light. Based on the model calculations, they found these HVFs can be caused by the interaction between the circumstellar material and the rapidly expanding SN ejecta. Mazzali et al. (2005b) found the HVFs (at least in the Ca II NIR feature) are common in early-phase SN Ia spectra despite the different strength and duration. It could be interpreted as an abundance or density enhancement. The abundance enhancement could result from an outer region of SN Ia dominated by Si or Ca. The

Table 6.1: The comparison of high-$v_{\rm Si\,II}$ SNe Ia with those with strong HVFs.

	High $v_{\rm Si\,II}$	Strong HVFs
SN stretch	$0.8 < s < 1.1$	$s > 1.0$
$v_{\rm Si\,II}$	–	< 12000 km s^{-1}
Host type	E to Sc	Sb/Sc/Irr
Host $M_{\rm stellar}$	massive	prefer low mass
Host sSFR	intermediate	high

density enhancement could be caused by either large-scale angular fluctuations or the sweeping up of circumstellar material by the SN ejecta with highest velocity.

Tanaka et al. (2006) presented spectral synthesis in three-dimensional space for the SN Ia early-time spectra. They suggested an orientation or viewing angle effect could be purely responsible for the presence of the HVFs in SN Ia spectra. Briefly speaking, the HVFs could be produced by either an abundance enhancement or a density enhancement, which could result from the SN explosion itself, or the interaction between SN ejecta and a circumstellar medium (CSM) — or both.

We confirmed that SNe Ia with strong HVFs are mostly brighter (with higher stretch) than those with weak HVFs. We found a strong trend that they are found in galaxies with a lower stellar mass and a stronger SFR. In Fig. 6.13 we plot the rest-frame colour-colour diagram (SDSS $g - r$ against $u - g$) of our host galaxies. Following the procedure described in Lamareille et al. (2006), we further classify our host galaxies into different Hubble types based on the criteria proposed by Strateva et al. (2001). The mean $u - r$ values for six different spectral types of galaxies are overplotted. Although the $u - r$ values used here have some uncertainty due to dust extinction in the galaxy, overall it provides a good idea of the Hubble types of our hosts. We can see that all the SNe Ia with strong HVFs concentrate toward the blue end with respect to the colours of their host galaxies. These galaxies are mostly classified as Sb/Sc/Irr galaxies, whereas the high-$v_{\rm Si\,II}$ SNe Ia are found in both late-type and early-type galaxies. This is consistent with Section 6.3, where we showed that SNe Ia with strong HVFs arise in galaxies with very strong SFRs, and

are therefore likely to be related to young stellar populations.

The CSM surrounding the SN progenitor system is thought to be a possible indication of a single-degenerate scenario. Using the narrow Na I D features as probes for CSM, Sternberg et al. (2011) and Maguire et al. (2013a) found an excess of SNe Ia with blueshifted narrow Na I D features compared to non-blushifted Na I D features, showing CSM around their progenitors. They further found the host galaxies of these SNe Ia are mostly late-type galaxies. If the HVFs observed in SN spectra are related to the interaction between the SN ejecta and a CSM, our work supports this interpretation: SNe Ia presenting strong HVFs tend to explode in galaxies with a low $M_{\rm stellar}$, a blue colour and a strong SFR. These trends show that they are very likely to originate from young stellar populations. This implies at least two different populations of SNe Ia, given the distinct properties of host galaxies between SNe Ia with strong HVFs and weak HVFs/high-$v_{\rm Si\,II}$ SNe Ia. The fact that the strength of the HVFs varies with host galaxy age also implies that they are unlikely to be caused solely by an orientation effect — or we would not expect any trend. In Table 6.1 we summarise the properties of high-$v_{\rm Si\,II}$ SNe Ia and SNe Ia with strong HVFs found in this work.

6.5 Summary

In this chapter we have analysed spectroscopic data of 123 SNe Ia selected from our parent sample. In particular, we focused on the velocity and pseudo-equivalent width of the Si II λ6355 and Ca II NIR absorptions. We investigated the relations between these SN spectral features and the host parameters, including the host $M_{\rm stellar}$, SN–host offset, SFR, metallicity and age. Below we summarise our main findings.

We find that high-$v_{\rm Si\,II}$ SNe Ia are preferentially found in massive host galaxies, whereas normal-$v_{\rm Si\,II}$ SNe Ia are found in hosts of all masses. There is also some

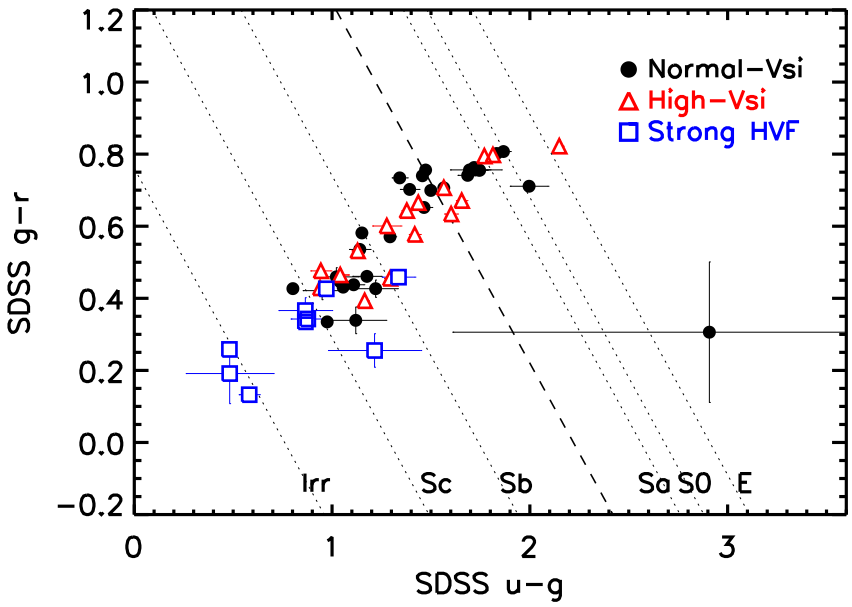

Figure 6.13: The rest-frame SDSS $g-r$ against $u-g$ of host galaxies in this work. The empirical relation studied by Strateva et al. (2001) is used to type the host galaxies. The dotted lines show the average $u-r$ for Irr(0.76), Sc(1.29), Sb(1.74), Sa(2.56), S0(2.68) and E(2.91) galaxies and the dashed line is the criterion to separate the late-type (left) and early-type (right) galaxies. The normal-$v_{\rm Si\,II}$ SNe Ia, high-$v_{\rm Si\,II}$ SNe Ia and SNe Ia with strong HVFs are shown in solid circles, open triangles and open squares, respectively.

evidence that these high-$v_{\mathrm{Si\,II}}$ SNe Ia are found in the inner regions of their host galaxies. However, this trend is not statistically significant in this work. The Ca II NIR PVF velocities also show similar trend on M_{stellar} in the sense that SNe Ia with higher Ca II NIR PVF velocities tend to be found in massive galaxies. By contrast, we found the SNe Ia with lower Ca II NIR HVF velocities were absent in low-mass galaxies.

We found SNe Ia with strong HVFs preferentially reside in late-type galaxies, with a lower M_{stellar}, a bluer colour and a stronger sSFR. SNe Ia with strong HVFs tend to be absent in high-mass galaxies in our sample. These trends strongly suggest that SNe Ia with strong HVFs originate from young stellar populations. Previous studies proposed a strong link between SN Ia HVFs and circumstellar material (CSM), and found that most of SNe Ia showing signatures of CSM explode in late-type galaxies. Our findings qualitatively support these findings, assuming that the HVFs are related to the interaction between the SN ejecta and a CSM local to the SN.

These findings also suggested at least two different populations of SNe Ia, given the different host galaxy properties between SNe Ia with strong HVFs and those with weak HVFs or high-$v_{\mathrm{Si\,II}}$ velocities.

Chapter 7

Conclusions

In this thesis, we studied the host galaxies of SNe Ia discovered by the Palomar Transient Factory (PTF). Our sample consists of 527 SNe Ia with redshift $z < 0.09$. We investigated the relations between the SN properties (estimated from either light curves or spectra) and the host galaxy parameters. Below we summarise our main results.

7.1 Summary of main results

- We showed that fainter SNe Ia (with lower stretch) tend to explode in massive galaxies, whereas the brighter SNe Ia (with higher stretch) can be found in both massive and low-mass galaxies. By directly measuring the gas-phase and stellar metallicity from the host galaxy, we also found these fainter SNe Ia tend to explode in metal-rich galaxies. Given the tight relation between stellar mass and metallicity (mass–metallicity relation), metallicity could be the underlying source driving the relation we see between host $M_{\rm stellar}$ and SN luminosity. Indeed, we found the SN luminosities after the stretch/colour corrections (as parameterised by Hubble residuals) show stronger correlation with host metallicity than with $M_{\rm stellar}$.

- The specific star-formation rate (sSFR) and stellar age were also found to correlate with SN luminosities. Fainter SNe Ia tend to explode in galaxies with lower specific star formation and older populations than their brighter counterparts. However, we did not see a significant trend between sSFR/stellar age and SN luminosities after the stretch/colour corrections. In this work we found the corrected SN luminosities show strongest correlation with the gas-phase metallicity, which suggests the metallicity is a more important factor in altering the SN luminosities.

- We have examined the effect of host parameters on SN colours. There is a mild trend that more massive and metal-rich galaxies tend to host redder SNe Ia. As we were not able to distinguish the contribution of the dust extinction from the host galaxies, the SN colour studied here may not be intrinsic. However, we found the SN colours show no correlation with reddening of the host galaxies as measured from the Balmer decrement. This suggests the bulk of the SN Ia colour variation may be intrinsic, or there could be dust local to the SN explosion (e.g., circumstellar medium) which can not be traced by photons from HII regions.

- We compared the mass–metallicity relation (M–Z relation) and the fundamental metallicity relation (FMR) for SN Ia hosts to that of field galaxies drawn from SDSS. No significant difference has been found between SN Ia hosts and field galaxies, which suggests the metallicity effect is negligible on SN Ia rate.

- We found the stellar mass distribution of SN Ia hosts can be reproduced by a combination of redshift-dependent galaxy stellar mass function (GSMF) and a SN Ia rate inversely proportional to the age of the galaxy (a t^{-1} DTD). This also explains the difference in the stellar mass distribution between PTF and SNLS SN Ia host galaxies, where there is an excess in low-mass galaxies at high-redshift (i.e., SNLS sample) due to the evolution in the field galaxy populations.

- We found the high-$v_{\rm Si\,II}$ SNe Ia ($v_{\rm Si\,II} \geq 12000\,{\rm km\,s^{-1}}$) preferentially to explode in massive galaxies, whereas the normal-$v_{\rm Si\,II}$ SNe Ia ($v_{\rm Si\,II} < 12000\,{\rm km\,s^{-1}}$) can be found in hosts of all mass. The same trend was also observed for the velocities of the photospheric-velocity feature (PVF) in Ca II NIR line. By contrast, the SNe Ia with lower velocities of the high-velocity feature (HVF) were absent in low-mass galaxies.

- We confirmed that the SNe Ia with strong HVFs are brighter (with higher stretch) than those with weak HVFs, and they also have normal Si II λ6355 velocities. We found that they tend to explode in late-type galaxies, with a lower $M_{\rm stellar}$, a bluer colour and a stronger SFR. Our findings support the idea that these HVFs could be related to the circumstellar medium (CSM) local to the SN explosion.

Previous studies have shown that SN Ia host galaxies are useful tools in understanding the progenitor systems. By studying the global properties of the host environments of SNe Ia, we can place broad constraints on the properties of progenitor systems. In this work, we found SNe Ia in different types of galaxies to have quite different properties. For example, SNe Ia found in metal-poor or young populations are intrinsically brighter than those in metal-rich or older populations. Furthermore, the SNe Ia presenting strong HVFs can only be found in late-type galaxies, whereas others show no preference in the morphology of their host galaxies. These trends imply that there could be at least two populations of SNe Ia originating from different stellar populations.

These results also have profound implications for SN Ia cosmology. SN Ia as distance indicators are an important and mature tool in determining the cosmic expansion. The trends found in this work could impact the precision of SN distances, considering galaxy evolution during cosmic time. The galaxies in the early universe should have a lower metal abundance than those in the local universe. For example,

the gas-phase metallicity of a galaxy at redshift $z \sim 0$ is about 0.2 dex higher than a galaxy at redshift $z \sim 1$ at a fixed stellar mass $\log(M/M_{\odot}) = 10$ (Savaglio et al., 2005). Given the dependence of SN luminosities on host metallicities studied in this work, this could introduce uncertainties on the SN distances.

In summary, this thesis has emphasised the important role of the host galaxies of SNe Ia in influencing the SN explosion properties, with SN Ia properties showing considerable dependence on their host galaxy parameters. From a cosmological perspective, the precision of the cosmology can be improved by correcting these biases introduced by host galaxies. It can also shed light on the properties of SN Ia progenitors. Therefore it is of great importance for future SN Ia surveys to study both the SNe and the galaxies in which they explode.

7.2 Future work

In this thesis, we have investigated the global properties of the SN Ia host environment by studying the host galaxy as a whole. Although host galaxy properties have proven to be a good proxy for the SN Ia progenitor, a few studies have suggested the investigation of the local environment could be better to constrain the nature of the progenitor system (Stanishev et al., 2012; Rigault et al., 2013). For example, Stanishev et al. (2012) studied host properties at the SN explosion site, using spatially-resolved two-dimensional maps of the host galaxies. They found no significant correlation between the local host properties and SNe Ia. However, their sample consists of only 6 SNe Ia which were all located in spiral galaxies. Rigault et al. (2013) measured local Hα emission at SN explosion site for 89 SNe Ia discovered by the Nearby Supernova Factory. They found the SNe Ia in locally star-forming regions are fainter than those in locally passive regions (after stretch/colour correction). These observations took advantages of the instruments equipped with integral

field unit (IFU), which is nowadays a common and popular tool in resolving the local properties of galaxies. From this work we already showed the tight relation between SN Ia and the global properties of their host environments. It would be promising to constrain the progenitor systems by studying the environments local to SN.

The other thing interesting but beyond the scope of this thesis would be the observations of very faint SN Ia host galaxies. In this work we have only three SN Ia hosts with $r > 20\,\mathrm{mag}$, and the faintest one has a $r \sim 22\,\mathrm{mag}$. Under the redshift range explored in this work, these faint host galaxies are generally very low-mass dwarf galaxies with extremely low metallicities. In Fig. 3.9 and 4.22, we can see that the mass–metallicity (M–Z relation) and fundamental metallicity relation (FMR) of SN Ia hosts compare well with that of field galaxies at $\log(\mathrm{M}/\mathrm{M}_{\odot}) > 8.5$. However, we do not have sufficient galaxies to constrain the low-mass tail of the relation. It would be interesting in the future to see how SNe Ia in extremely metal-poor environments compare with others, for example, the fundamental metallicity relation of low-mass galaxies (Mannucci et al., 2011). Telescopes with great light-gathering power such as Keck or Very Large Telescope (VLT) will be ideal to obtain the high-quality spectroscopic data of these faint galaxies.

In this thesis, we focused on two key SN spectral features, Si II λ6355 and the Ca II NIR triplet, and their relations with host properties. However, there are some other important spectral indicators we can take advantage of from the spectrum but did not address in this work. For example, the ratio of the pEW of Si II λ5972 to pEW of Si II λ6355, or the pEW of Si II λ4130, which were found to show strong correlation with SN photometric properties (Nugent et al., 1995; Bronder et al., 2008; Blondin et al., 2011; Walker et al., 2011). It would be interesting to investigate the relations between these spectral indicators and the host galaxy properties in the future.

Host galaxy observations will play an important role in future large surveys, such as Dark Energy Survey (DES) and the Large Synoptic Survey Telescope (LSST).

They will be used to precisely measure the redshifts of the SNe Ia, which is necessary to constrain their distances. In addition to providing accurate redshifts, these observations will enable us to probe any systematics by studying the correlations between SNe Ia and their host environments. The DES is expected to provide a large sample of ~ 4000 SNe Ia with redshifts $0.05 < z < 1.2$ (Bernstein et al., 2012). The spectroscopic follow-up programs will be organised to obtain the SN Ia host galaxy spectra of $\sim 20\%$ of the SN Ia sample in the later years of the survey, using multi-object spectrographs such as VIsible Multi-Object Spectrograph (VIMOS; Le Fèvre et al., 2003) or Fibre Multi-Object Spectrograph (FMOS; Kimura et al., 2010). Host information, such as star formation rate and metallicity, can then be determined for these SNe Ia. The LSST is another powerful tool in the future to probe the dark universe. It will provide $\sim 20,000$ square degrees of coverage in the southern sky (Ivezic et al., 2008). The survey will operate in six imaging bands ($ugrizy$), with a wavelength coverage $\sim$3200–10500 Å. LSST is expected to discover $\sim 250,000$ SNe Ia per year with redshift $0.45 < z < 0.7$. The instrument such as WEAVE (Dalton et al., 2012), Dark Energy Spectroscopic Instrument (DESI) and 4-metre Multi-Object Spectroscopic Telescope (4MOST; de Jong et al., 2012), which have thousands of spectroscopic fibres and provide a very large field-of-view, will be suitable for LSST to carry out the follow-up survey of both SNe Ia and their host galaxies. With such a large sample, LSST will be ideal to explore the subtle systematics in SN Ia luminosity.

Appendix A

Tables of measurements

Table A.1: The observing log for the host spectroscopic observations in this thesis.

SN name	Coordinate		Instrument	Exp. time[1]		redshift (z)[2]	
	(R.A.)	(Dec.)		(Blue)	(Red)	(Spec.)	(CMB)
PTF09dav	22:46:52.95	+21:38:21.5	Gemini+GMOS	3000	3000	0.0371	0.0359
PTF09dlc	21:46:30.02	+06:25:07.3	Gemini+GMOS	4000	4000	0.0672	0.0660
PTF09dnl	17:23:41.69	+30:29:51.0	Gemini+GMOS	3000	3000	0.0237	0.0236
PTF09dnp	15:19:25.34	+49:30:05.0	Gemini+GMOS	3600	3600	0.0370	0.0373
PTF09dxo	02:01:47.64	-07:05:34.4	Gemini+GMOS	4000	3000	0.0519	0.0510
PTF09dxw	23:44:50.66	+27:37:28.9	Gemini+GMOS	3000	3000	0.0293	0.0282
PTF09dza	21:03:31.68	-04:20:35.5	Gemini+GMOS	4000	4000	0.0832	0.0822
PTF09edr	00:11:42.89	+30:14:22.6	Gemini+GMOS	3000	3000	0.0857	0.0846
PTF09eoi	23:24:12.96	+12:46:46.6	Gemini+GMOS	3000	3000	0.0410	0.0398
PTF09fox	23:20:47.79	+32:30:06.1	Gemini+GMOS	3000	3000	0.0718	0.0707
PTF09foz	00:42:11.90	-09:52:54.8	Gemini+GMOS	3000	3600	0.0543	0.0532
PTF09gce	23:38:49.63	+28:16:13.8	Gemini+GMOS	3000	3000	0.0575	0.0564
PTF09gon	22:42:45.53	+05:09:28.8	Gemini+GMOS	4000	3600	0.0680	0.0668
PTF09gul	01:28:23.90	+33:51:40.7	Gemini+GMOS	3600	3600	0.0725	0.0716
PTF09hpl	01:21:29.18	+00:06:28.8	Gemini+GMOS	4000	3600	0.0781	0.0771
PTF09hpq	00:41:12.91	-09:09:00.4	Gemini+GMOS	4000	3600	0.0529	0.0518

PTF09hql	01:55:29.30	+13:13:50.9	Gemini+GMOS	3000	3000	0.0499	0.0490
PTF09hqp	03:10:30.61	+35:05:02.2	Gemini+GMOS	3000	3000	0.0218	0.0212
PTF09ifh	04:10:35.27	+27:23:32.1	Gemini+GMOS	3000	3000	0.0788	0.0784
PTF10aaiw	01:09:21.02	+15:44:06.7	Gemini+GMOS	4000	3600	0.0600	0.0589
PTF10accd	02:13:30.50	+46:41:38.4	Gemini+GMOS	4000	4000	0.0348	0.0341
PTF10acnz	11:44:56.31	+58:39:46.1	Gemini+GMOS	3600	3600	0.0615	0.0620
PTF10bxs	10:58:44.28	+32:27:08.3	Gemini+GMOS	3600	3600	0.0727	0.0737
PTF10duz	12:51:40.03	+14:26:29.4	Gemini+GMOS	3600	3600	0.0640	0.0650
PTF10fps	13:29:24.26	+11:47:49.2	Gemini+GMOS	4000	3600	0.0214	0.0224
PTF10fxl	16:52:48.63	+51:03:41.0	Gemini+GMOS	3600	3600	0.0296	0.0295
PTF10gmd	11:57:18.96	+57:11:58.6	Gemini+GMOS	3600	3600	0.0552	0.0557
PTF10gmg	16:24:58.54	+51:02:22.2	Gemini+GMOS	3600	3600	0.0628	0.0628
PTF10hdn	14:52:24.58	+47:28:34.3	Gemini+GMOS	3600	3600	0.0699	0.0703
PTF10hdv	12:07:45.43	+41:29:28.7	Keck+LRIS	1800	1800	0.0527	0.0535
PTF10hjw	12:52:18.00	-07:01:06.7	Gemini+GMOS	3600	3600	0.0417	0.0428
PTF10hml	13:19:50.66	+41:58:57.4	Gemini+GMOS	3600	3600	0.0534	0.0541
PTF10icb	12:54:49.78	+58:52:56.6	Gemini+GMOS	2400	2400	0.0085	0.0089
PTF10iyc	17:09:22.03	+44:23:30.1	Gemini+GMOS	3600	3600	0.0594	0.0593
PTF10jdw	15:41:59.95	+47:35:29.8	Gemini+GMOS	3600	3600	0.0766	0.0768
PTF10jtp	17:10:58.51	+39:28:28.9	Gemini+GMOS	3600	3600	0.0670	0.0669
PTF10mwb	17:17:50.04	+40:52:52.7	Gemini+GMOS	4000	4000	0.0310	0.0309
PTF10nkd	15:45:21.41	+52:13:50.5	Gemini+GMOS	3600	3600	0.0676	0.0678
PTF10nlg	16:50:34.55	+60:16:34.6	Gemini+GMOS	3600	3600	0.0562	0.0561
PTF10pvi[3]	22:02:02.42	+14:32:07.1	WHT+ISIS	3600	3600	0.0802	0.0790
PTF10qjl	16:39:59.23	+12:06:26.6	WHT+ISIS	1800	1800	0.0576	0.0577
PTF10qjq	17:07:12.36	+35:30:35.6	Gemini+GMOS	3600	3600	0.0284	0.0283
PTF10qkf	23:14:23.04	+10:45:17.3	WHT+ISIS	3600	3600	0.0804	0.0792
PTF10qkv[3]	17:11:52.75	+27:22:20.3	WHT+ISIS	1200	1200	0.0611	0.0610
PTF10qky[3]	22:17:49.08	+05:25:23.5	Gemini+GMOS	3600	3600	0.0742	0.0730
PTF10qny[3]	16:09:30.67	+22:20:10.0	Gemini+GMOS	4000	4000	0.0333	0.0335
PTF10qsc	21:34:21.12	-05:03:46.1	WHT+ISIS	3600	3600	0.0879	0.0868
PTF10qwg	02:42:09.96	+02:26:51.0	Gemini+GMOS	4000	3600	0.0679	0.0671
PTF10rab[3]	01:47:07.46	-00:02:58.9	Keck+LRIS	1800	1800	0.0850	0.0840

PTF10rbp[3]	01:16:37.78	-01:49:28.2	Gemini+GMOS	4000	4000	0.0823	0.0813
PTF10tce	23:19:09.74	+09:11:45.6	WHT+ISIS	5400	5400	0.0410	0.0398
PTF10trp	21:28:08.01	+09:51:14.0	Gemini+GMOS	4000	4000	0.0489	0.0478
PTF10twd	23:00:14.23	+20:47:59.3	Gemini+GMOS	4000	4000	0.0734	0.0722
PTF10ubm	00:01:59.23	+21:49:31.1	Gemini+GMOS	3600	3600	0.0701	0.0689
PTF10viq	22:20:19.46	+17:03:25.2	WHT+ISIS	1800	1800	0.0342	0.0330
PTF10wnm	00:22:03.70	+27:02:21.5	WHT+ISIS	2400	2400	0.0663	0.0652
PTF10wnq	00:49:10.10	+32:08:14.3	WHT+ISIS	2400	2400	0.0691	0.0681
PTF10wof[3]	23:32:41.42	+15:21:31.7	WHT+ISIS	3000	3000	0.0530	0.0518
PTF10wor	22:32:41.67	-09:27:46.8	Gemini+GMOS	4000	3600	0.0568	0.0556
PTF10wos	21:44:39.36	-05:25:22.4	Gemini+GMOS	4000	4000	0.0820	0.0809
PTF10xyt	23:19:02.43	+13:47:26.2	Gemini+GMOS	3600	3600	0.0490	0.0478
PTF10yer	21:29:01.37	-01:25:51.6	Gemini+GMOS	4000	4000	0.0528	0.0517
PTF10ygu[3]	09:37:29.83	+23:09:41.8	Lick+KAST	600	600	0.0259	0.0269
PTF10yux	23:24:13.92	+07:13:39.7	Gemini+GMOS	3600	3600	0.0578	0.0566
PTF10zbk	02:29:34.46	+22:20:00.2	Gemini+GMOS	4000	4000	0.0642	0.0634
PTF10zdk	02:14:07.37	+23:37:49.1	WHT+ISIS	2400	2400	0.0322	0.0314
PTF10zgy	02:38:43.77	+14:06:11.9	Gemini+GMOS	4000	4000	0.0443	0.0435
PTF11apk	10:21:00.53	+21:42:59.8	Gemini+GMOS	3600	3600	0.0405	0.0416
PTF11atu	15:31:14.91	-00:46:45.8	Gemini+GMOS	4000	4000	0.0774	0.0779
PTF11bas	13:16:47.78	+43:31:13.4	Lick+KAST	2400	2400	0.0863	0.0870
PTF11bju	11:56:14.40	+25:21:14.8	Gemini+GMOS	4000	4000	0.0323	0.0333
PTF11htb	21:55:37.01	+00:41:29.4	WHT+ISIS	5400	5400	0.0493	0.0481
PTF11khk	17:02:58.03	+40:31:28.6	WHT+ISIS	3600	3600	0.0306	0.0305
PTF11kjn	22:45:03.93	+33:59:46.0	WHT+ISIS	3600	3600	0.0234	0.0223
PTF11kx	08:09:13.20	+46:18:42.8	Gemini+GMOS	4000	4000	0.0467	0.0472
PTF11lih	23:10:58.93	+31:51:36.0	WHT+ISIS	3600	3600	0.0720	0.0709
PTF11mty	21:34:05.21	+10:25:24.6	WHT+ISIS	3600	3600	0.0770	0.0759
PTF11okh	23:06:04.85	+34:06:27.7	WHT+ISIS	3600	3600	0.0191	0.0180
PTF11opu	22:07:50.02	+27:47:47.0	WHT+ISIS	3600	3600	0.0649	0.0638
PTF11pfm	21:44:13.80	+00:56:34.1	Keck+LRIS	1800	1800	0.0795	0.0784
PTF11v	15:08:23.42	+49:39:57.6	Gemini+GMOS	2400	2400	0.0373	0.0376

PTF11vl	16:28:40.27	+27:43:39.7	Gemini+GMOS	4000	4000	0.0454	0.0455

[1]The exposure time for red or blue gratings/grisms in units of seconds.
[2]Here we present two redshifts based on heliocentric or CMB frame.
[3]'Galaxy Zoo Supernova project' discovered SNe.

Table A.2: The host photometric measurements in this thesis.

Host photometric properties[1]							
SN name	$M_{\rm stellar}-$	$M_{\rm stellar}$ ($M_\odot$)	$M_{\rm stellar}+$	logSFR–	logSFR ($M_\odot yr^{-1}$)	logSFR+	R_{SN}/R_{gal}[2]
PTF09a	9.66	10.02	10.14	0.20	0.20	0.88	0.43(0.0157)
PTF09agm	10.22	10.23	10.24	···	···	···	0.04(0.0127)
PTF09agy	10.15	10.55	10.84	0.89	0.89	0.93	···
PTF09ahf	11.20	11.73	11.87	···	···	0.66	···
PTF09akb	10.76	10.76	10.91	···	···	···	0.75(0.0016)
PTF09alu	10.82	10.84	11.45	···	···	0.28	0.94(0.0054)
PTF09aly	11.00	11.64	11.67	···	···	0.43	0.39(0.0007)
PTF09amm	10.94	10.95	11.09	···	···	-0.08	0.10(0.0003)
PTF09aro	8.12	8.31	8.41	···	···	-0.54	···
PTF09atw	7.65	8.75	8.82	-1.32	-0.88	-0.85	0.10(0.0190)
PTF09aus	10.59	10.66	10.73	-0.63	-0.63	0.55	0.61(0.0001)
PTF09aux	10.07	10.25	10.26	···	···	···	0.02(0.0044)
PTF09aws	9.98	10.13	10.23	0.36	0.37	0.47	0.40(0.0084)
PTF09azf	11.47	11.48	11.65	···	···	···	0.08(0.0000)
PTF09bak	9.69	9.78	10.14	···	···	0.92	0.45(0.0011)
PTF09bau	10.33	10.61	10.78	0.75	0.75	0.90	0.59(0.0034)
PTF09biq	11.47	11.49	12.19	···	···	0.92	0.23(0.0002)
PTF09bjs	11.69	11.72	11.85	···	···	0.50	0.03(0.0000)
PTF09c	11.05	11.11	11.16	···	···	···	0.62(0.0004)
PTF09cbu	8.84	9.12	9.66	-0.10	0.20	0.46	···
PTF09cex	11.70	11.76	11.83	···	···	0.54	1.73(0.0005)
PTF09dhx	8.00	8.12	8.39	-0.76	-0.76	-0.65	0.16(0.0051)
PTF09dic	9.26	9.31	9.39	-0.35	-0.32	-0.27	0.90(0.0018)
PTF09djc	10.59	10.60	10.77	···	···	···	2.23(0.0006)
PTF09dlc	8.49	8.92	9.08	-0.66	-0.64	-0.03	···
PTF09dmk	10.95	11.01	11.09	···	···	0.90	0.04(0.0150)
PTF09dnl	8.00	8.06	8.12	···	···	-0.77	0.20(0.0031)
PTF09dnp	10.55	10.58	10.73	···	···	···	0.64(0.0005)

PTF09dpy	10.77	10.84	10.89	-0.52	-0.52	-0.31	0.43(0.0015)
PTF09dsr	9.55	9.61	9.65	0.72	0.72	0.76	0.83(0.0033)
PTF09dsw	9.86	9.91	9.97	-0.63	-0.47	-0.13	···
PTF09dxo	10.21	10.25	10.75	···	···	-0.36	0.66(0.0093)
PTF09dxw	9.41	9.41	9.64	-0.35	-0.18	-0.17	0.39(0.0047)
PTF09dyc	10.54	10.62	10.82	0.06	0.81	0.86	0.05(0.0247)
PTF09dza	10.27	10.43	10.52	0.45	0.49	0.59	0.55(0.0119)
PTF09edr	11.29	11.30	11.40	···	···	0.15	0.50(0.0073)
PTF09eoi	9.26	9.39	9.42	···	···	···	0.51(0.0205)
PTF09eop	11.07	11.09	11.20	···	···	-0.01	0.65(0.0095)
PTF09fb	10.48	10.52	10.71	0.76	0.90	0.94	···
PTF09fim	11.08	11.14	11.24	···	···	0.05	0.09(0.0009)
PTF09fox	10.25	10.31	10.35	0.47	0.49	0.54	0.74(0.0084)
PTF09foz	10.39	10.54	10.58	···	···	···	0.30(0.0043)
PTF09fqj	9.75	9.80	9.88	0.18	0.20	0.23	···
PTF09fr	10.84	11.30	11.38	0.92	0.92	1.42	1.03(0.0052)
PTF09gce	10.27	10.43	10.44	···	···	···	2.22(0.0097)
PTF09gdy	10.61	10.76	10.84	0.88	0.92	1.05	1.29(0.0007)
PTF09ggb	9.80	9.93	10.07	0.12	0.15	0.27	0.35(0.0017)
PTF09gjf	11.27	11.28	11.34	···	···	···	···
PTF09gjj	10.58	11.21	11.27	···	···	-0.07	0.33(0.0099)
PTF09gm	10.12	10.39	10.55	0.69	0.69	1.35	···
PTF09gnm	8.83	9.20	9.42	-0.33	-0.33	0.22	0.39(0.0196)
PTF09gon	11.23	11.24	11.32	···	···	0.00	0.73(0.0000)
PTF09gpu	10.69	10.77	10.98	1.01	1.12	1.19	0.67(0.0008)
PTF09gqo	9.77	9.83	10.06	0.01	0.19	0.20	0.44(0.0027)
PTF09gqu	9.29	9.33	9.46	···	···	···	0.12(0.0050)
PTF09gul	11.00	11.11	11.14	-0.31	-0.31	-0.03	0.10(0.0057)
PTF09gzj	9.46	9.96	10.14	0.12	0.12	0.19	0.06(0.0200)
PTF09hhv	9.45	9.53	9.57	···	···	···	0.65(0.0158)
PTF09hpl	10.62	10.73	10.92	0.92	1.01	1.10	0.56(0.0045)
PTF09hpq	10.37	10.40	10.53	···	···	···	···
PTF09hql	9.39	9.46	9.53	-0.29	-0.25	-0.17	0.08(0.0006)

PTF09hqp	10.82	10.82	10.82	0.98	0.98	43.99	···
PTF09iaf	10.60	10.74	10.81	···	···	···	0.56(0.0026)
PTF09iag	11.34	11.44	11.45	-0.02	-0.02	0.31	1.14(0.0001)
PTF09idb	9.98	10.01	10.62	···	···	···	0.53(0.0057)
PTF09ifh	10.29	10.29	10.29	1.39	1.39	45.00	···
PTF09pr	8.87	8.92	8.94	···	···	···	0.10(0.0042)
PTF09ri	10.20	10.71	10.85	-0.39	-0.39	0.09	0.51(0.0104)
PTF09s	8.95	9.31	9.41	-0.47	-0.47	-0.37	0.03(0.0027)
PTF09sg	10.62	10.66	10.89	0.89	1.07	1.08	1.16(0.0035)
PTF09si	11.18	11.26	11.31	-0.19	0.63	1.14	0.44(0.0011)
PTF09sj	11.30	11.45	11.86	···	···	···	0.35(0.0001)
PTF10aaiw	10.11	10.65	10.74	-0.52	-0.52	-0.43	···
PTF10aajv	7.93	8.04	8.14	-1.01	-0.90	-0.79	0.07(0.0216)
PTF10aawe	11.28	11.35	11.36	0.54	1.16	1.36	1.24(0.0039)
PTF10aawn	9.74	9.93	10.45	···	···	0.47	···
PTF10abbi	10.65	10.66	11.20	···	···	0.59	···
PTF10abhm	10.56	10.63	11.14	···	···	-0.07	0.35(0.0008)
PTF10abjm	7.07	7.37	7.62	-1.86	-1.54	-1.28	0.15(0.0398)
PTF10abjv	9.94	10.02	10.06	0.25	0.27	0.32	0.28(0.0097)
PTF10abkt	10.52	10.57	10.64	0.77	0.82	0.86	0.18(0.0031)
PTF10abnr	10.43	10.60	10.61	···	···	···	0.47(0.0042)
PTF10abwy	10.48	10.85	11.04	1.01	1.01	1.09	0.50(0.0208)
PTF10accd	9.05	9.12	9.14	0.23	0.23	0.25	0.18(0.0060)
PTF10acdh	10.30	10.34	10.34	···	···	···	1.02(0.0507)
PTF10acej	8.65	8.91	9.06	-0.87	-0.87	-0.16	···
PTF10acem	11.26	11.29	11.35	-0.13	0.04	0.18	0.46(0.0027)
PTF10acnz	10.62	10.63	10.67	···	···	···	1.36(0.0006)
PTF10acts	10.39	10.85	11.04	1.00	1.00	1.07	0.20(0.0018)
PTF10bfg	9.90	9.91	9.93	···	···	···	0.73(0.0069)
PTF10bix	9.74	9.75	9.83	0.15	0.21	0.22	0.15(0.0063)
PTF10bjs	9.99	10.02	10.10	···	···	1.21	1.12(0.0025)
PTF10bt	10.17	10.18	10.34	···	···	···	0.31(0.0005)
PTF10bvr	10.01	10.18	10.68	···	···	···	1.32(0.0003)

PTF10bvw	11.79	11.80	11.89	···	···	···	1.40(0.0008)
PTF10bxs	10.39	10.74	10.93	0.93	0.93	0.97	0.46(0.0031)
PTF10cko	10.25	10.38	10.45	0.59	0.60	0.72	0.64(0.0059)
PTF10cu	10.24	10.39	10.55	0.35	0.50	0.59	0.24(0.0153)
PTF10cwm	10.37	10.54	10.68	0.67	0.72	0.85	0.54(0.0117)
PTF10cwy	9.96	9.97	9.97	···	···	···	0.01(0.0079)
PTF10cxk	9.06	9.15	9.24	···	···	···	1.16(0.0006)
PTF10dal	10.49	10.54	10.66	···	···	···	0.67(0.0015)
PTF10dna	9.35	9.75	9.88	0.15	0.15	0.71	0.69(0.0040)
PTF10duy	9.19	9.24	9.32	-0.40	-0.35	-0.33	0.19(0.0028)
PTF10duz	9.88	10.19	10.32	0.56	0.62	1.06	1.79(0.0121)
PTF10eqf	9.15	9.78	9.89	-0.46	-0.46	-0.12	0.31(0.0143)
PTF10fj	10.89	10.93	11.04	···	···	···	0.40(0.0007)
PTF10fjg	11.27	11.28	11.40	···	···	0.21	1.95(0.0041)
PTF10fkk	8.07	9.06	9.21	···	···	-0.92	···
PTF10fln	9.48	9.54	9.71	-0.22	-0.12	-0.06	0.62(0.0051)
PTF10for	10.13	10.13	10.30	···	···	···	0.82(0.0016)
PTF10fps	10.35	10.35	10.42	···	···	···	0.39(0.0001)
PTF10ftb	7.83	7.97	8.77	···	···	-1.40	···
PTF10fxk	10.46	10.51	11.14	···	···	-0.13	0.93(0.0036)
PTF10fxl	10.55	10.62	11.10	···	···	0.01	0.45(0.0004)
PTF10fyk	10.27	10.44	10.57	0.08	0.50	0.61	0.57(0.0025)
PTF10fyl	10.13	10.14	10.29	···	···	···	0.41(0.0072)
PTF10fym	10.89	11.01	11.03	-0.42	-0.42	-0.14	1.36(0.0078)
PTF10gjx	9.30	9.34	9.41	-0.30	-0.26	-0.23	0.29(0.0088)
PTF10glo	9.20	9.23	9.31	-0.36	-0.35	-0.32	0.51(0.0073)
PTF10gmd	10.31	10.32	10.40	···	···	···	0.56(0.0033)
PTF10gmg	9.68	9.75	9.84	0.06	0.07	0.15	0.13(0.0121)
PTF10gnj	10.16	10.25	10.40	0.51	0.57	0.64	0.12(0.0011)
PTF10goo	10.49	10.69	10.90	0.62	0.88	0.94	0.45(0.0005)
PTF10goq	10.34	10.55	10.65	0.35	0.35	0.66	0.18(0.0187)
PTF10got	10.55	10.58	11.01	···	···	1.03	0.22(0.0112)
PTF10gqi	9.64	9.84	9.97	-0.12	-0.07	0.07	0.39(0.0004)

PTF10gwe	11.57	11.71	11.74	0.28	0.28	0.54	0.35(0.0063)
PTF10hdn	8.73	8.89	9.00	-0.20	-0.02	0.10	0.26(0.0120)
PTF10hdv	7.61	7.80	8.03	-1.32	-1.12	-0.87	2.99(0.0077)
PTF10hjw	8.82	8.82	8.82	-0.14	-0.14	44.48	···
PTF10hld	9.87	9.91	9.99	0.19	0.26	0.30	0.33(0.0190)
PTF10hml	9.86	9.97	9.98	···	···	1.06	0.86(0.0014)
PTF10hmv	8.37	8.38	8.47	···	···	-0.41	0.11(0.0061)
PTF10hoe	10.46	10.47	10.51	···	···	···	···
PTF10hoz	9.90	10.10	10.21	0.14	0.15	0.30	0.15(0.0063)
PTF10hrw	10.44	10.97	11.09	-0.13	-0.13	1.09	1.26(0.0004)
PTF10icb	9.56	9.60	9.81	-0.14	-0.01	0.01	0.19(0.0006)
PTF10ifj	10.68	10.81	11.08	0.81	1.10	1.15	0.75(0.0057)
PTF10ijv	8.71	8.81	9.23	-0.33	-0.11	0.09	···
PTF10iyc	10.53	10.57	11.18	···	···	0.63	0.41(0.0014)
PTF10izy	10.70	10.88	11.04	0.70	0.99	1.10	0.27(0.0050)
PTF10jdw	10.58	11.08	11.15	0.55	0.55	1.18	0.69(0.0062)
PTF10jkh	10.02	10.09	10.69	···	···	0.77	0.79(0.0002)
PTF10jtp	11.17	11.24	11.26	0.09	0.51	0.78	0.12(0.0074)
PTF10jvy	9.32	9.57	9.73	-0.15	-0.15	-0.08	0.73(0.0174)
PTF10jwx	10.39	10.51	10.67	0.68	0.75	0.85	0.16(0.0000)
PTF10jxa	10.79	10.80	10.91	···	···	-0.29	0.10(0.0342)
PTF10kdg	8.73	8.92	9.05	-0.82	-0.80	-0.12	0.63(0.0175)
PTF10kiw	8.36	8.54	8.66	-0.37	-0.37	-0.23	0.40(0.0114)
PTF10lot	9.83	9.85	9.95	···	···	···	0.14(0.0002)
PTF10lya	10.38	10.39	10.50	···	···	···	0.03(0.0152)
PTF10mla	10.47	10.48	10.49	···	···	···	0.11(0.0063)
PTF10mtd	9.81	9.88	9.98	-0.04	0.01	0.08	0.41(0.0070)
PTF10mwb	8.99	9.28	9.48	-0.34	-0.34	-0.30	0.11(0.0007)
PTF10nax	11.11	11.13	11.28	···	···	-0.03	0.94(0.0009)
PTF10nct	10.89	10.90	11.01	-0.51	-0.24	0.88	0.40(0.0025)
PTF10ndc	9.16	9.20	9.22	0.32	0.32	0.34	1.31(0.0131)
PTF10ndo	9.88	9.97	10.33	1.08	1.08	1.13	0.46(0.0037)
PTF10ndw	11.11	11.19	11.20	-0.30	-0.30	-0.26	0.07(0.0003)

PTF10nkd	9.53	9.70	9.89	0.03	0.03	0.65	0.33(0.0137)
PTF10nlg	10.02	10.02	10.02	0.46	0.46	44.84	···
PTF10nvh	9.83	9.95	10.04	0.18	0.19	0.29	0.76(0.0045)
PTF10oiq	10.38	10.45	10.60	0.67	0.78	0.83	0.96(0.0032)
PTF10ops	8.12	9.06	9.17	···	···	-1.17	4.82(0.0140)
PTF10ozy	10.84	10.85	11.03	···	···	···	0.49(0.0003)
PTF10pdf	10.93	11.06	11.25	0.93	1.23	1.27	1.03(0.0054)
PTF10pvi	10.15	10.27	10.43	0.49	0.55	0.64	0.44(0.0136)
PTF10qhp	10.72	10.89	10.90	···	···	···	0.08(0.0013)
PTF10qht	11.95	12.04	12.09	···	···	···	1.99(0.0033)
PTF10qjl	8.14	8.52	8.76	-0.81	-0.42	-0.15	0.40(0.0038)
PTF10qjq	10.05	10.11	10.14	0.32	0.33	0.38	0.08(0.0039)
PTF10qkf	10.28	10.41	10.59	0.29	0.55	0.62	0.06(0.0017)
PTF10qkv	10.38	10.47	10.63	-0.15	0.61	0.68	0.71(0.0029)
PTF10qky	10.44	10.53	10.65	0.78	0.83	0.90	1.14(0.0022)
PTF10qly	6.90	6.90	9.54	-2.06	-2.06	-0.53	0.15(0.0099)
PTF10qny	10.18	10.34	10.80	···	···	0.82	0.50(0.0001)
PTF10qnz	10.77	11.30	11.39	0.20	0.20	0.68	0.27(0.0024)
PTF10qok	10.01	10.14	10.24	0.34	0.38	0.48	0.27(0.0203)
PTF10qpb	9.46	9.58	10.03	-0.09	0.04	0.63	0.43(0.0083)
PTF10qsc	9.37	9.79	9.90	0.17	0.19	0.73	0.33(0.0128)
PTF10qwg	9.90	10.05	10.24	-0.20	0.19	0.27	0.31(0.0172)
PTF10qyr	8.71	8.79	9.07	-0.10	-0.10	-0.07	···
PTF10rab	7.81	7.92	8.96	-1.15	-1.04	-0.43	0.54(0.0193)
PTF10rbp	10.67	10.72	11.25	···	···	1.26	···
PTF10rcf	9.57	9.68	9.75	-0.08	-0.08	0.02	0.10(0.0031)
PTF10rcg	8.81	8.84	9.08	-0.81	-0.70	-0.68	0.24(0.0049)
PTF10rct	11.68	11.69	11.80	···	···	0.65	···
PTF10rhi	9.64	10.01	10.09	0.10	0.10	0.23	0.26(0.0019)
PTF10rka	10.74	10.80	10.81	···	···	···	···
PTF10rpg	9.95	9.96	10.12	···	···	···	0.04(0.0069)
PTF10stg	9.07	9.10	9.33	-0.58	-0.44	-0.42	0.52(0.0330)
PTF10stw	10.45	10.48	10.56	0.80	0.87	0.89	0.13(0.0686)

PTF10tce	10.38	10.51	10.70	0.65	0.75	0.84	0.86(0.0023)
PTF10tly	11.02	11.09	11.62	···	···	0.45	0.94(0.0002)
PTF10tqy	10.10	10.10	10.26	···	···	···	0.83(0.0046)
PTF10trp	10.14	10.24	10.37	0.42	0.48	0.59	···
PTF10trs	10.75	10.77	10.89	-0.32	-0.32	0.89	1.55(0.0032)
PTF10twd	9.84	9.91	9.98	0.24	0.26	0.31	0.10(0.0161)
PTF10ubm	10.06	10.08	10.08	0.41	0.41	0.43	0.48(0.0076)
PTF10ucl	10.66	10.68	11.19	···	···	0.12	1.29(0.0038)
PTF10ufj	10.73	10.77	10.80	···	···	···	2.52(0.0013)
PTF10umy	11.18	11.70	11.77	1.12	1.12	1.76	0.81(0.0012)
PTF10vfo	10.73	10.75	10.76	···	···	···	0.24(0.0080)
PTF10vh	10.68	10.78	10.87	0.80	0.85	0.94	0.02(0.0090)
PTF10viq	10.33	10.95	10.99	0.76	0.76	1.06	0.75(0.0008)
PTF10vnu	9.15	9.52	9.70	-0.10	-0.10	0.47	1.21(0.0028)
PTF10vty	9.95	10.35	10.50	0.44	0.44	0.60	1.04(0.0088)
PTF10vyv	9.08	9.10	9.18	···	···	···	0.37(0.0267)
PTF10wbb	9.89	9.98	10.10	···	···	···	0.14(0.2383)
PTF10whg	10.55	10.56	10.58	···	···	···	0.81(0.0062)
PTF10wix	11.14	11.34	11.43	0.88	1.01	1.48	0.55(0.0057)
PTF10wlw	10.88	10.97	11.17	0.65	1.20	1.22	1.16(0.0026)
PTF10wml	10.78	10.79	10.96	···	···	···	0.21(0.0002)
PTF10wnm	10.39	10.49	10.62	0.71	0.77	0.85	0.49(0.0041)
PTF10wnq	10.80	11.32	11.46	···	···	0.12	0.51(0.0017)
PTF10wnt	8.95	8.97	9.03	0.03	0.05	0.12	···
PTF10woa	10.04	10.07	10.18	0.33	0.41	0.42	0.69(0.0254)
PTF10wof	9.92	10.06	10.15	0.21	0.25	0.37	0.82(0.0001)
PTF10wor	10.91	10.94	11.58	···	···	···	0.74(0.0006)
PTF10wos	10.76	11.26	11.39	0.17	0.17	0.59	0.29(0.0138)
PTF10wrm	10.69	10.85	11.05	0.64	1.04	1.07	0.45(0.0062)
PTF10wxp	10.74	10.78	10.78	···	···	···	0.48(0.0024)
PTF10wyq	11.11	11.17	11.27	···	···	0.08	···
PTF10xfk	9.97	10.29	10.42	0.47	0.47	1.16	1.18(0.0118)
PTF10xfn	11.13	11.21	11.33	0.08	0.08	1.26	0.57(0.0014)

PTF10xir	10.84	10.91	11.04	···	···	···	1.60(0.0010)
PTF10xup	9.77	9.90	10.28	···	···	1.03	0.42(0.0107)
PTF10xya	9.60	9.65	9.70	···	···	···	0.75(0.0037)
PTF10xyl	9.73	10.31	10.45	0.35	0.35	0.50	0.39(0.0042)
PTF10xyt	9.51	9.64	9.71	-0.23	-0.20	-0.10	0.07(0.0013)
PTF10ycq	8.51	8.53	8.61	···	···	-0.28	0.54(0.0187)
PTF10yer	10.54	10.68	10.90	0.79	0.92	0.99	0.37(0.0042)
PTF10ygu	10.71	11.42	11.44	···	···	0.13	0.33(0.0012)
PTF10ymy	8.57	8.58	8.65	···	···	-0.23	0.34(0.0027)
PTF10yux	10.69	10.73	10.78	···	···	···	0.73(0.0014)
PTF10zai	10.76	11.29	11.38	0.15	0.15	0.19	1.13(0.0013)
PTF10zak	10.60	10.67	11.16	···	···	0.06	0.75(0.0015)
PTF10zau	10.07	10.42	10.67	0.60	0.60	0.68	0.17(0.0001)
PTF10zbe	9.85	9.97	10.07	0.16	0.17	0.29	···
PTF10zbk	10.61	10.79	10.84	0.08	0.16	0.88	0.16(0.0246)
PTF10zdk	9.11	9.17	9.31	0.18	0.25	0.40	···
PTF10zgo	10.42	10.95	11.02	-0.15	-0.15	0.56	0.03(0.0006)
PTF10zgq	10.67	11.15	11.22	···	···	-0.02	0.08(0.0028)
PTF10zgy	11.16	11.16	11.16	1.42	1.42	44.61	···
PTF11ael	9.92	10.23	10.54	0.49	0.49	0.55	0.60(0.0171)
PTF11ap	10.78	10.89	10.91	-0.57	-0.57	0.20	0.64(0.1969)
PTF11apk	10.75	10.76	10.93	···	···	···	0.51(0.0002)
PTF11apq	10.77	10.88	10.97	0.90	0.90	0.93	0.61(0.0051)
PTF11aqu	10.32	10.45	10.88	···	···	1.56	0.88(0.0049)
PTF11atu	9.36	9.45	9.74	···	···	0.54	0.20(0.0225)
PTF11avn	10.96	10.98	11.10	-0.34	-0.11	0.51	0.32(0.0757)
PTF11bas	9.70	9.71	9.89	0.05	0.17	0.19	0.37(0.0190)
PTF11bge	7.36	8.36	8.95	···	···	-0.37	0.38(0.0159)
PTF11bgv	8.85	9.36	9.45	-0.25	-0.23	0.17	0.67(0.0021)
PTF11biv	9.61	9.63	9.71	-0.79	-0.70	-0.50	0.04(0.0117)
PTF11bju	9.51	9.52	9.58	-0.12	-0.06	-0.05	0.18(0.0022)
PTF11bkd	10.38	10.53	10.54	···	···	···	0.48(0.0004)
PTF11bkf	11.12	11.18	11.29	···	···	···	0.05(0.0008)

PTF11blu	9.88	9.94	9.97	1.06	1.06	1.08	0.56(0.0007)
PTF11bmo	9.58	9.85	10.07	0.27	0.27	0.29	1.13(0.0013)
PTF11bnb	9.69	9.73	9.76	0.78	0.82	0.86	1.10(0.0022)
PTF11bnf	10.46	10.52	10.70	0.66	0.82	0.84	0.07(0.0830)
PTF11bnx	9.29	9.41	9.83	0.18	0.50	0.59	0.64(0.0012)
PTF11bof	10.02	10.03	10.15	0.32	0.43	0.44	···
PTF11bpw	9.94	10.02	10.58	···	···	0.11	1.68(0.0029)
PTF11bqc	11.15	11.65	11.79	0.56	0.56	1.70	0.20(0.0023)
PTF11bui	10.72	10.78	10.91	···	···	···	0.56(0.0020)
PTF11bup	11.60	11.61	11.74	···	···	0.41	0.51(0.0146)
PTF11byi	9.94	10.02	10.58	···	···	0.11	1.69(0.0047)
PTF11cao	9.87	9.90	10.07	0.18	0.31	0.32	0.42(0.0012)
PTF11cfm	11.30	11.36	11.50	0.19	0.19	0.29	0.37(0.0014)
PTF11cji	9.99	10.02	10.10	0.45	0.46	0.49	0.64(0.0087)
PTF11cmw	8.94	9.10	9.12	···	···	···	0.33(0.0211)
PTF11cnc	9.69	9.77	9.83	0.09	0.09	0.16	0.11(0.0036)
PTF11ctn	9.21	9.31	9.62	0.43	0.43	0.46	0.24(0.0067)
PTF11cwb	11.26	11.37	11.41	-0.06	-0.06	0.63	0.24(0.0083)
PTF11czq	8.94	9.10	9.12	···	···	···	0.99(0.3204)
PTF11czz	11.16	11.18	11.29	···	···	···	0.28(0.0006)
PTF11deg	9.38	9.45	9.55	-0.29	-0.24	-0.15	1.36(0.0253)
PTF11dej	10.57	10.61	10.63	0.98	1.00	1.04	···
PTF11dhq	9.60	9.71	9.75	-0.10	-0.09	-0.02	0.32(0.0158)
PTF11dif	8.13	8.23	8.29	-0.80	-0.69	-0.63	···
PTF11drz	9.40	9.45	9.85	···	···	0.66	0.07(0.0018)
PTF11dva	10.08	10.20	10.31	0.42	0.47	0.55	0.14(0.0168)
PTF11dxu	8.56	8.71	8.87	-0.38	-0.22	-0.05	···
PTF11dzm	9.93	9.93	10.10	···	···	···	0.45(0.0003)
PTF11ecn	10.98	11.61	11.67	···	···	0.36	0.92(0.0020)
PTF11eie	9.10	9.29	9.39	-0.63	-0.62	-0.46	0.32(0.0049)
PTF11eql	10.44	10.61	10.78	0.14	0.80	0.84	0.60(0.0014)
PTF11fp	9.88	9.92	10.08	···	···	···	···
PTF11fvq	11.45	11.48	11.61	0.13	0.38	1.36	0.42(0.0051)

PTF11fwe	10.84	10.98	11.18	0.87	1.16	1.25	0.20(0.0008)
PTF11gdh	10.29	10.46	10.59	0.53	0.63	0.72	0.27(0.0012)
PTF11gjh	9.69	9.71	9.85	-0.01	0.10	0.13	0.02(0.0028)
PTF11hfu	10.31	10.60	10.74	0.78	0.78	0.90	0.96(0.0004)
PTF11htb	8.48	8.54	8.93	-0.67	-0.38	-0.32	0.75(0.0166)
PTF11hub	10.72	10.78	10.91	···	···	···	1.58(0.0005)
PTF11hyh	7.84	7.91	8.70	···	···	-0.86	0.22(0.0362)
PTF11icm	9.95	10.03	10.10	0.22	0.25	0.30	···
PTF11ihr	7.73	8.66	8.99	-1.56	-1.56	-1.31	···
PTF11iid	10.40	10.44	10.99	···	···	1.03	···
PTF11ivb	9.47	9.53	9.65	-0.16	-0.10	-0.05	0.86(0.0017)
PTF11izs	10.98	10.99	11.07	···	···	···	0.87(0.0033)
PTF11jfm	9.85	9.85	9.94	-0.48	-0.39	-0.17	0.39(0.0008)
PTF11jri	10.19	10.23	10.81	···	···	0.87	0.44(0.0085)
PTF11kaw	10.00	10.20	10.30	0.30	0.31	0.44	···
PTF11kdk	10.96	11.13	11.54	···	···	···	1.73(0.0000)
PTF11khk	10.55	10.62	10.75	···	···	···	1.42(0.0003)
PTF11kiu	10.64	10.77	10.94	0.90	0.97	1.09	0.54(0.0031)
PTF11kjn	11.02	11.18	11.67	···	···	···	0.77(0.0011)
PTF11kjr	10.79	10.83	10.88	1.12	1.15	1.20	0.25(0.0035)
PTF11kju	11.70	11.80	11.80	···	···	0.49	0.08(0.0021)
PTF11klx	10.55	10.62	10.75	···	···	···	0.88(0.1496)
PTF11kml	9.03	9.05	9.21	-0.53	-0.49	-0.46	0.07(0.0045)
PTF11ksu	10.50	10.66	10.75	0.19	0.66	0.78	0.11(0.0039)
PTF11kx	10.15	10.24	10.48	0.43	0.60	0.62	0.74(0.0034)
PTF11lih	10.56	10.64	10.94	0.67	0.99	1.01	0.09(0.0007)
PTF11lm	10.67	10.71	10.84	···	···	···	0.10(0.0006)
PTF11lmz	10.65	11.23	11.28	0.54	0.54	1.33	0.04(0.0098)
PTF11md	10.07	10.26	10.39	0.33	0.39	0.53	0.53(0.0011)
PTF11mfy	10.32	10.54	10.61	0.60	0.61	0.76	0.52(0.0035)
PTF11mke	9.99	10.06	10.20	···	···	···	0.84(0.0026)
PTF11mkx	6.99	7.70	8.26	-1.22	-1.22	-0.92	0.76(0.0149)
PTF11moy	8.04	8.18	8.56	···	···	-0.62	0.30(0.0109)

PTF11mpa	7.04	7.19	7.64	···	···	-1.61	···
PTF11mty	9.87	9.90	9.98	0.27	0.33	0.34	0.47(0.0031)
PTF11mxk	10.34	10.36	10.43	-0.10	0.11	0.21	0.38(0.0128)
PTF11okh	10.78	10.96	11.45	···	···	···	1.01(0.0001)
PTF11opu	9.70	9.77	9.93	0.06	0.12	0.17	0.25(0.0059)
PTF11owc	11.01	11.51	11.65	···	···	0.31	0.07(0.0085)
PTF11pbp	11.15	11.16	11.21	1.48	1.52	1.53	0.64(0.0001)
PTF11pfm	8.81	8.90	9.14	0.01	0.01	0.04	···
PTF11phk	9.66	9.69	9.73	0.74	0.77	0.82	···
PTF11ppn	11.54	11.62	11.68	···	···	0.37	0.39(0.0001)
PTF11pra	10.85	10.92	11.02	···	···	···	0.27(0.0002)
PTF11qbq	10.16	10.31	10.41	0.51	0.53	0.65	0.86(0.0025)
PTF11qcl	11.30	11.31	11.42	···	···	0.01	0.75(0.0098)
PTF11qgy	11.26	11.27	11.39	···	···	-0.03	3.13(0.0224)
PTF11qko	9.80	9.85	10.42	···	···	0.51	0.57(0.0032)
PTF11qmn	9.37	9.43	9.46	0.53	0.53	0.56	0.27(0.0238)
PTF11qnr	10.77	10.92	10.92	···	···	···	0.61(0.0008)
PTF11qpc	10.06	10.14	10.53	···	···	1.28	0.95(0.0192)
PTF11qri	10.03	10.17	10.23	0.28	0.31	0.41	0.95(0.0098)
PTF11qrv	10.90	11.38	11.45	0.81	0.81	1.48	0.69(0.0096)
PTF11quu	10.07	10.19	10.31	0.43	0.49	0.56	0.48(0.0347)
PTF11rem	10.71	11.20	11.32	0.11	0.11	1.34	0.46(0.0021)
PTF11rnu	11.15	11.25	11.28	···	···	-0.14	1.78(0.0014)
PTF11rpj	10.94	10.97	11.08	-0.41	-0.13	0.45	···
PTF11rpz	9.93	10.01	10.36	···	···	0.54	···
PTF11rrq	9.93	10.16	10.28	0.46	0.48	1.16	0.74(0.0149)
PTF11sd	10.85	10.92	11.55	···	···	···	0.26(0.0074)
PTF11v	11.05	11.06	11.23	···	···	···	0.55(0.0001)
PTF11vl	9.68	9.77	10.18	···	···	0.92	0.61(0.0051)
PTF12aki	8.78	8.87	9.18	-0.02	-0.02	0.02	···
PTF12alp	10.52	10.67	11.15	···	···	0.45	0.04(0.0044)
PTF12aob	10.60	10.79	11.00	0.73	0.97	1.06	0.05(0.0014)
PTF12ass	11.54	11.55	11.66	···	···	0.35	0.87(0.0007)

PTF12awi	10.40	10.50	10.64	0.69	0.75	0.85	0.31(0.0002)
PTF12bmr	10.92	10.97	11.11	1.25	1.35	1.38	0.17(0.0118)
PTF12bok	10.39	10.46	10.57	···	···	···	1.39(0.0015)
PTF12box	6.89	7.14	7.31	-2.08	-1.82	-1.63	0.60(0.0191)
PTF12ccw	9.29	9.31	9.74	···	···	0.51	1.03(0.0037)
PTF12ccx	9.50	9.60	9.69	-0.13	-0.12	-0.03	1.14(0.0021)
PTF12ccy	10.05	10.15	10.21	0.40	0.41	0.48	0.81(0.0157)
PTF12ccz	10.18	10.19	10.36	···	···	···	1.30(0.0082)
PTF12cjg	9.79	9.92	10.04	0.12	0.16	0.26	0.35(0.0028)
PTF12cks	11.35	11.43	11.48	-0.04	0.80	1.47	0.54(0.0014)
PTF12cnl	9.05	9.45	9.57	-0.24	-0.18	0.34	0.94(0.0024)
PTF12csi	9.98	10.06	10.67	···	···	0.72	0.21(0.0053)
PTF12dco	10.65	11.06	11.27	1.25	1.25	1.30	1.01(0.0014)
PTF12dhb	10.31	10.35	10.41	0.69	0.72	0.77	0.41(0.0061)
PTF12dhk	8.45	8.93	9.06	-0.67	-0.65	-0.13	0.48(0.0181)
PTF12dhl	10.99	11.04	11.11	-0.25	-0.25	-0.09	0.07(0.0053)
PTF12dlz	9.85	9.86	9.93	0.21	0.26	0.29	···
PTF12dwm	10.06	10.44	10.68	0.73	0.73	0.74	0.03(0.0025)
PTF12dxm	11.02	11.03	11.08	···	···	···	0.90(0.0008)
PTF12eac	10.15	10.16	10.21	0.55	0.59	0.62	0.01(0.0255)
PTF12ecj	11.34	11.35	11.89	···	···	···	0.33(0.0005)
PTF12ecm	10.40	10.43	10.44	···	···	···	0.03(0.0022)
PTF12ecr	10.08	10.13	10.34	0.38	0.50	0.55	0.39(0.0019)
PTF12eer	10.24	10.33	10.51	0.56	0.65	0.72	0.20(0.0020)
PTF12efn	9.49	9.64	9.71	-0.16	-0.13	-0.05	0.30(0.0091)
PTF12emh	10.18	10.36	10.38	···	···	···	0.01(0.0072)
PTF12emp	9.28	9.36	9.46	···	···	···	0.09(0.0020)
PTF12ena	10.03	10.06	10.21	0.29	0.43	0.46	0.19(0.0003)
PTF12epf	7.92	8.40	8.67	-1.03	-0.54	-0.23	0.50(0.0028)
PTF12esv	10.07	10.14	10.72	···	···	0.71	0.31(0.0057)
PTF12eut	11.01	11.03	11.16	···	···	-0.12	0.35(0.0131)
PTF12evo	10.10	10.30	10.50	0.18	0.45	0.53	1.31(0.1604)
PTF12ewk	11.19	11.26	11.32	-0.19	-0.03	1.26	0.15(0.0011)

PTF12fjx	7.51	8.05	8.46	-1.45	-0.88	-0.43	···
PTF12fkj	8.41	9.61	10.59	···	···	0.73	···
PTF12fkk	10.33	10.34	10.42	···	···	···	0.08(0.0034)
PTF12for	6.36	7.16	7.91	-1.76	-1.76	-1.13	0.41(0.0229)
PTF12fsd	10.01	10.08	10.21	0.33	0.38	0.47	0.08(0.0026)
PTF12fuu	6.50	7.38	7.97	-1.51	-1.51	-1.26	0.66(0.0344)
PTF12fxn	10.62	10.70	10.83	···	···	···	0.11(0.0016)
PTF12gaz	10.92	11.17	11.29	0.81	0.93	1.31	···
PTF12gdq	10.48	10.53	10.60	0.30	0.60	0.66	0.37(0.0113)
PTF12ggb	10.48	10.58	10.75	0.80	0.87	0.96	0.42(0.0009)
PTF12ghy	10.66	10.67	10.82	···	···	···	0.83(0.0011)
PTF12giy	10.82	10.85	11.04	1.00	1.16	1.18	0.38(0.0035)
PTF12gkn	10.73	10.75	11.23	···	···	0.14	0.49(0.0065)
PTF12gmv	10.10	10.71	10.77	0.08	0.08	0.81	0.56(0.0053)
PTF12gqh	9.83	9.84	9.87	-0.05	0.01	0.03	0.91(0.0026)
PTF12grk	8.34	8.42	8.45	-0.47	-0.47	-0.44	0.22(0.0046)
PTF12gxc	9.95	10.44	10.51	-0.65	-0.65	0.09	···
PTF12hdq	10.67	10.70	10.71	···	···	···	0.03(0.0040)
PTF12hmx	10.48	10.66	10.82	0.80	0.86	0.97	···
PTF12hpc	9.53	9.85	9.96	0.08	0.08	0.77	···
PTF12hwb	9.70	10.05	10.21	0.16	0.16	0.29	0.15(0.0012)
PTF12iiq	10.54	10.55	10.69	···	···	···	0.19(0.0008)
PTF12ikt	10.34	10.96	11.02	0.44	0.44	1.06	0.79(0.0010)
PTF12ilb	10.86	10.89	10.98	-0.20	-0.20	0.42	0.28(0.0037)
PTF12izc	11.73	11.74	11.85	···	···	···	0.50(0.0017)
PTF12jfy	10.57	10.79	10.93	0.49	0.83	0.95	0.51(0.0114)
PTF12jge	10.44	11.02	11.12	0.60	0.60	1.15	0.33(0.0001)
PTF12jgg	10.37	10.53	10.60	0.65	0.66	0.78	1.23(0.0061)
PTF12jgl	10.36	10.86	10.93	-0.23	-0.23	0.49	0.06(0.0018)
PTF12jic	11.03	11.04	11.14	-0.38	-0.06	0.49	0.78(0.0059)
PTF12jma	10.42	10.71	10.99	1.04	1.04	1.06	1.23(0.0017)
PTF12jqh	10.31	10.43	10.61	0.50	0.63	0.69	0.59(0.0052)
PTF12jsi	10.47	10.48	11.02	···	···	-0.21	0.68(0.0011)

PTF12keu	8.42	8.56	8.64	-0.50	-0.36	-0.26	0.22(0.0119)
PTF12kgt	10.00	10.12	10.30	-0.20	0.26	0.34	···
PTF12kim	10.86	11.33	11.41	0.95	0.95	1.45	0.41(0.0026)
PTF12kjh	10.43	10.59	10.60	···	···	···	···
PTF12kjl	10.04	10.66	10.73	-0.77	-0.77	0.71	0.26(0.0187)
PTF12lc	9.73	9.81	9.87	0.10	0.11	0.20	···
PTF12ldz	8.51	8.69	8.85	-1.07	-1.05	-0.35	···
PTF12lgq	10.80	10.85	10.91	0.08	0.88	0.93	0.41(0.0021)
PTF12lic	10.34	10.83	10.92	0.45	0.45	0.94	1.13(0.0111)
PTF12ltv	10.66	11.29	11.36	0.76	0.76	1.22	0.66(0.0043)
PTF12lvg	11.66	11.67	11.79	···	···	0.33	0.57(0.0027)
PTF12lz	8.63	8.67	8.85	···	···	-0.10	0.31(0.0364)
PTF12maw	10.91	11.44	11.55	0.31	0.31	0.98	1.50(0.0001)
PTF12mdb	11.64	11.72	11.78	···	···	···	···
PTF12mgm	10.03	10.04	10.19	···	···	···	0.11(0.0036)
PTF12mqz	9.92	9.93	9.94	···	···	···	0.65(0.0122)
PTF12ta	8.14	8.65	8.78	-1.33	-1.33	-1.15	0.82(0.0100)
PTF12tc	10.87	11.36	11.51	0.27	0.27	0.71	0.32(0.0070)
PTF12zp	11.87	11.89	12.03	···	···	···	0.33(0.0081)

[1]The host parameters determined by photometric data.

[2]R_{SN} is defined as the separation between the SN position and the host galaxy centre and R_{gal} is defined as the size of the host galaxy measured by SEXTRACTOR.

Table A.3: The host spectroscopic measurements in this thesis.

Host spectroscopic properties[1]					
SN name	12+log(O/H)	logSFR ($M_\odot yr^{-1}$)	[M/H]	logAge (Gyr)	AGN[2]
PTF09dav	8.698 ± 0.073	0.0778 ± 0.2001	-0.476	0.406	0
PTF09dlc	8.182 ± 0.069	-0.7730 ± 0.2002	-1.106	0.832	0
PTF09dnl	$\cdots$	-2.0440 ± 0.2003	-1.107	0.808	0
PTF09dnp	8.758 ± 0.081	< -1.5310	-0.130	1.110	1
PTF09dxo	8.732 ± 0.075	-0.1270 ± 0.2001	0.033	0.799	0
PTF09dxw	8.627 ± 0.072	-0.9420 ± 0.2001	-0.598	0.742	0
PTF09dza	8.688 ± 0.072	0.1926 ± 0.2001	-0.197	0.514	0
PTF09edr	8.760 ± 0.083	-0.5293 ± 0.2002	-0.111	1.045	1
PTF09eoi	8.518 ± 0.096	-0.8333 ± 0.2008	-0.454	0.211	0
PTF09fox	8.664 ± 0.071	0.5646 ± 0.2000	-0.216	0.243	0
PTF09foz	$\cdots$	< -1.7998	-0.033	0.735	0
PTF09gce	8.835 ± 0.073	-0.2271 ± 0.2001	-0.189	0.745	0
PTF09gon	$\cdots$	< -1.4682	0.052	0.994	0
PTF09gul	8.804 ± 0.074	-0.4125 ± 0.2001	-0.212	0.831	1
PTF09hpl	8.710 ± 0.072	0.5366 ± 0.2001	-0.292	0.674	0
PTF09hpq	$\cdots$	< -2.1847	0.122	0.932	0
PTF09hql	8.573 ± 0.081	-1.1066 ± 0.2001	-1.132	0.564	0
PTF09hqp	8.826 ± 0.070	0.8022 ± 0.2000	-0.132	0.585	0
PTF09ifh	8.724 ± 0.093	0.1958 ± 0.2008	-0.513	0.837	0
PTF10aaiw	8.854 ± 0.070	-0.6567 ± 0.2001	-0.349	0.944	0
PTF10accd	8.362 ± 0.087	-0.8841 ± 0.2002	-1.046	0.374	0
PTF10acnz	8.799 ± 0.079	-0.7896 ± 0.2023	0.074	0.890	1
PTF10bxs	8.718 ± 0.075	0.4785 ± 0.2002	-0.530	0.771	0
PTF10duz	8.571 ± 0.074	0.3213 ± 0.2001	-0.511	0.398	0
PTF10fps	8.751 ± 0.071	0.4652 ± 0.2000	0.083	0.413	0
PTF10fxl	8.752 ± 0.070	0.4853 ± 0.2000	-0.162	0.578	0
PTF10gmd	8.748 ± 0.084	< -1.9430	-0.075	0.722	1
PTF10gmg	8.396 ± 0.078	-0.3354 ± 0.2001	-1.148	0.994	0

PTF10hdn	8.224 ± 0.090	-0.2529 ± 0.2002	-1.297	0.695	0
PTF10hdv	8.101 ± 0.079	-1.1635 ± 0.2005	-1.099	0.734	0
PTF10hjw	8.618 ± 0.073	-0.0162 ± 0.2001	-1.081	0.654	0
PTF10hml	8.506 ± 0.077	0.0052 ± 0.2001	-0.210	0.249	0
PTF10icb	8.438 ± 0.074	-0.1586 ± 0.2001	-0.474	0.348	0
PTF10iyc	8.740 ± 0.087	-0.4100 ± 0.2002	-0.306	1.052	0
PTF10jdw	8.738 ± 0.089	0.4382 ± 0.2006	-0.605	0.765	0
PTF10jtp	8.779 ± 0.078	0.9699 ± 0.2001	-0.201	0.827	0
PTF10mwb	···	-1.3801 ± 0.2001	-1.179	0.605	0
PTF10nkd	8.570 ± 0.082	-0.6267 ± 0.2003	-1.116	0.614	0
PTF10nlg	8.552 ± 0.071	-0.2332 ± 0.2000	0.013	-0.252	0
PTF10pvi	8.621 ± 0.167	0.1395 ± 0.2034	-0.835	0.826	0
PTF10qjl	8.191 ± 0.214	0.0953 ± 0.2022	-0.905	0.730	0
PTF10qjq	8.678 ± 0.070	0.5050 ± 0.2000	-1.005	0.621	0
PTF10qkf	8.680 ± 0.087	-0.0993 ± 0.2003	-0.876	0.723	0
PTF10qkv	8.755 ± 0.082	0.0145 ± 0.2003	-0.209	0.810	0
PTF10qky	8.675 ± 0.071	0.7003 ± 0.2000	-0.073	0.312	0
PTF10qny	8.645 ± 0.078	0.7040 ± 0.2002	-0.408	0.404	0
PTF10qsc	···	-0.3717 ± 0.2006	-0.320	0.755	0
PTF10qwg	8.727 ± 0.072	-0.0504 ± 0.2000	-0.363	0.905	0
PTF10rab	8.098 ± 0.067	-1.3371 ± 0.2000	···	···	0
PTF10rbp	8.816 ± 0.075	0.2401 ± 0.2001	-0.153	0.665	0
PTF10tce	8.663 ± 0.145	-0.1912 ± 0.2030	-0.185	0.707	0
PTF10trp	8.623 ± 0.072	-0.0145 ± 0.2001	-0.860	0.534	0
PTF10twd	8.505 ± 0.072	0.0067 ± 0.2000	-0.693	0.572	0
PTF10ubm	8.664 ± 0.070	0.2402 ± 0.2000	-0.573	0.626	0
PTF10viq	8.822 ± 0.076	1.0179 ± 0.2003	-0.025	0.558	0
PTF10wnm	8.697 ± 0.119	0.4628 ± 0.2018	-0.131	0.482	0
PTF10wnq	···	< -1.0496	-0.130	1.035	0
PTF10wof	8.575 ± 0.100	-0.1685 ± 0.2011	-1.035	0.803	0
PTF10wor	8.903 ± 0.057	-0.7775 ± 0.2008	0.071	0.939	1
PTF10wos	···	< -2.0219	-0.117	0.916	0
PTF10xyt	8.397 ± 0.078	-0.4585 ± 0.2001	-1.047	0.443	0

PTF10yer	8.624 ± 0.071	0.4392 ± 0.2000	-1.011	0.781	0
PTF10ygu	$\cdots$	0.4154 ± 0.2041	-0.420	0.834	0
PTF10yux	8.711 ± 0.085	-0.6406 ± 0.2002	-0.199	0.922	1
PTF10zbk	8.768 ± 0.071	-0.0288 ± 0.2000	-0.203	0.820	0
PTF10zdk	8.431 ± 0.101	-0.4892 ± 0.2001	-0.402	0.005	0
PTF10zgy	8.827 ± 0.072	0.9997 ± 0.2000	0.010	0.601	1
PTF11apk	8.829 ± 0.074	-0.7912 ± 0.2002	-0.005	0.981	1
PTF11atu	8.559 ± 0.086	-0.6486 ± 0.2005	-0.842	0.711	0
PTF11bas	$\cdots$	0.0040 ± 0.2270	-1.084	0.735	0
PTF11bju	8.363 ± 0.072	-0.4429 ± 0.2000	-0.893	0.304	0
PTF11htb	8.235 ± 0.181	-0.6434 ± 0.2006	-1.135	0.640	0
PTF11khk	8.777 ± 0.081	0.4498 ± 0.2012	0.095	0.599	0
PTF11kjn	8.816 ± 0.074	-0.3221 ± 0.2010	0.108	0.993	1
PTF11kx	8.679 ± 0.072	-0.1617 ± 0.2001	-0.737	0.303	0
PTF11lih	8.747 ± 0.150	1.4264 ± 0.2038	-0.212	0.907	0
PTF11mty	8.584 ± 0.082	0.7431 ± 0.2004	-0.100	0.346	0
PTF11okh	8.811 ± 0.074	-0.0839 ± 0.2001	0.117	1.056	0
PTF11opu	8.319 ± 0.175	0.1381 ± 0.2024	-0.857	0.721	0
PTF11pfm	8.406 ± 0.070	-1.1024 ± 0.2000	-0.193	0.261	0
PTF11v	8.795 ± 0.076	-0.7488 ± 0.2004	-0.014	1.078	1
PTF11vl	8.581 ± 0.093	-0.6123 ± 0.2004	-1.020	0.664	0

[1]The host parameters determined either from emission line or stellar continuum measurements.

[2]The AGN tags for the host galaxies in this work. Normal galaxies are labeled as 0 and AGN hosts are labeled as 1.

Table A.4: The SN photometric measurements in this thesis.

SN photometric properties			
SN name	stretch (s)	colour ($\mathcal{C}$)	m_B (mag)
PTF09a	0.88 ± 0.05	···	···
PTF09dav	0.64 ± 0.04	···	···
PTF09dhx	1.70 ± 0.06	···	···
PTF09djc	0.82 ± 0.02	···	···
PTF09dlc	1.06 ± 0.01	0.02 ± 0.01	18.17 ± 0.02
PTF09dnl	1.05 ± 0.02	-0.02 ± 0.01	15.85 ± 0.02
PTF09dnp	0.98 ± 0.03	0.11 ± 0.02	17.09 ± 0.02
PTF09dsy	0.81 ± 0.02	···	···
PTF09dxo	1.08 ± 0.04	···	···
PTF09dxw	0.72 ± 0.05	···	···
PTF09dza	1.08 ± 0.44	···	···
PTF09edr	0.81 ± 0.11	···	···
PTF09fox	0.95 ± 0.04	0.03 ± 0.04	18.34 ± 0.06
PTF09foz	0.85 ± 0.04	0.00 ± 0.06	17.78 ± 0.09
PTF09gce	1.06 ± 0.05	-0.03 ± 0.03	17.70 ± 0.07
PTF09gul	0.89 ± 0.06	···	···
PTF09hpl	0.89 ± 0.05	···	···
PTF09hpq	0.82 ± 0.08	···	···
PTF09hql	1.11 ± 0.04	···	···
PTF09hqp	1.16 ± 0.03	···	···
PTF09qn	1.10 ± 0.12	···	···
PTF09s	1.06 ± 0.02	···	···
PTF10abjv	1.14 ± 0.02	···	···
PTF10accd	1.03 ± 0.02	-0.11 ± 0.02	16.60 ± 0.05
PTF10acnz	1.10 ± 0.01	0.10 ± 0.01	17.98 ± 0.01
PTF10bjs	1.12 ± 0.02	-0.11 ± 0.02	16.04 ± 0.03
PTF10bxs	1.08 ± 0.05	0.11 ± 0.09	18.81 ± 0.12
PTF10cko	1.19 ± 0.03	···	···
PTF10cwm	1.14 ± 0.08	···	···

PTF10cxk	0.90 ± 0.03	···	···
PTF10duy	1.16 ± 0.03	···	···
PTF10duz	0.97 ± 0.03	-0.01 ± 0.02	18.06 ± 0.03
PTF10elk	0.76 ± 0.05	···	···
PTF10fj	0.70 ± 0.04	···	···
PTF10fps	0.72 ± 0.02	0.12 ± 0.03	16.66 ± 0.05
PTF10fxl	0.97 ± 0.02	0.10 ± 0.01	16.76 ± 0.02
PTF10fyl	0.84 ± 0.05	···	···
PTF10fym	1.08 ± 0.12	···	···
PTF10glo	1.51 ± 0.05	···	···
PTF10gmd	0.78 ± 0.01	0.09 ± 0.01	18.35 ± 0.02
PTF10gmg	1.11 ± 0.02	-0.03 ± 0.02	17.91 ± 0.03
PTF10gmj	1.00 ± 0.11	···	···
PTF10gnj	1.00 ± 0.13	···	···
PTF10goo	1.11 ± 0.05	···	···
PTF10goq	1.22 ± 0.08	···	···
PTF10got	0.86 ± 0.10	···	···
PTF10gqi	0.77 ± 0.08	···	···
PTF10gvl	0.95 ± 0.04	0.10 ± 0.07	18.07 ± 0.10
PTF10hdn	1.09 ± 0.03	···	···
PTF10hdv	1.09 ± 0.01	-0.03 ± 0.01	17.56 ± 0.01
PTF10hjw	0.99 ± 0.02	-0.09 ± 0.04	16.99 ± 0.06
PTF10hld	1.09 ± 0.06	···	···
PTF10hmc	1.05 ± 0.02	0.08 ± 0.02	18.24 ± 0.02
PTF10hml	1.02 ± 0.01	-0.05 ± 0.03	17.71 ± 0.03
PTF10hmv	1.18 ± 0.09	0.22 ± 0.05	17.40 ± 0.07
PTF10icb	0.98 ± 0.03	0.06 ± 0.02	14.49 ± 0.03
PTF10iyc	1.06 ± 0.02	-0.03 ± 0.01	17.74 ± 0.01
PTF10jdw	0.84 ± 0.02	-0.03 ± 0.07	18.91 ± 0.09
PTF10jtp	0.87 ± 0.01	0.11 ± 0.02	18.69 ± 0.03
PTF10lot	1.02 ± 0.06	···	···
PTF10lya	1.04 ± 0.05	···	···
PTF10mtd	0.99 ± 0.03	···	···

PTF10mwb	0.92 ± 0.02	0.03 ± 0.03	16.82 ± 0.04
PTF10ncu	0.89 ± 0.05	···	···
PTF10nkd	0.92 ± 0.03	0.29 ± 0.04	20.14 ± 0.05
PTF10nlg	0.98 ± 0.03	0.10 ± 0.03	18.59 ± 0.03
PTF10nvh	1.29 ± 0.04	···	···
PTF10otc	0.72 ± 0.03	···	···
PTF10pvi	1.03 ± 0.02	-0.08 ± 0.02	18.43 ± 0.03
PTF10px	0.86 ± 0.05	···	···
PTF10qfo	1.10 ± 0.05	-0.07 ± 0.01	18.34 ± 0.02
PTF10qhp	0.92 ± 0.04	···	···
PTF10qjl	0.96 ± 0.02	-0.11 ± 0.02	17.82 ± 0.02
PTF10qjq	0.93 ± 0.02	0.00 ± 0.02	16.42 ± 0.03
PTF10qkf	1.03 ± 0.02	0.10 ± 0.03	18.95 ± 0.03
PTF10qkv	1.07 ± 0.04	0.17 ± 0.03	19.15 ± 0.03
PTF10qky	1.07 ± 0.02	-0.06 ± 0.02	18.14 ± 0.04
PTF10qny	1.10 ± 0.07	-0.02 ± 0.02	16.37 ± 0.05
PTF10qsc	1.15 ± 0.02	-0.07 ± 0.02	18.54 ± 0.02
PTF10qwg	0.93 ± 0.04	0.16 ± 0.07	18.58 ± 0.10
PTF10qyx	0.86 ± 0.02	-0.09 ± 0.02	18.25 ± 0.02
PTF10rab	1.06 ± 0.04	0.20 ± 0.06	19.15 ± 0.06
PTF10rbp	1.08 ± 0.03	0.09 ± 0.02	18.76 ± 0.03
PTF10rhi	1.03 ± 0.04	0.01 ± 0.05	18.67 ± 0.06
PTF10rks	0.87 ± 0.05	···	···
PTF10tce	1.08 ± 0.02	0.05 ± 0.02	17.19 ± 0.03
PTF10tqy	0.73 ± 0.03	···	···
PTF10trp	1.12 ± 0.02	0.59 ± 0.02	19.15 ± 0.03
PTF10trs	0.64 ± 0.02	-0.12 ± 0.02	18.29 ± 0.02
PTF10tum	1.14 ± 0.06	···	···
PTF10twd	1.08 ± 0.02	-0.07 ± 0.01	18.08 ± 0.03
PTF10ubm	1.06 ± 0.01	0.01 ± 0.01	17.98 ± 0.02
PTF10ucl	0.90 ± 0.03	···	···
PTF10ufj	0.97 ± 0.03	-0.10 ± 0.07	18.40 ± 0.09
PTF10vfo	0.84 ± 0.07	···	···

PTF10viq	1.13 ± 0.01	0.05 ± 0.02	16.62 ± 0.03
PTF10vnu	1.12 ± 0.08	···	···
PTF10wnm	1.04 ± 0.02	0.03 ± 0.01	18.20 ± 0.02
PTF10wnq	0.93 ± 0.02	-0.16 ± 0.02	18.10 ± 0.03
PTF10wof	0.99 ± 0.03	0.09 ± 0.04	17.95 ± 0.07
PTF10wor	0.68 ± 0.03	0.55 ± 0.05	20.03 ± 0.11
PTF10wos	0.93 ± 0.05	-0.04 ± 0.02	18.73 ± 0.04
PTF10xir	1.11 ± 0.04	···	···
PTF10xyl	0.75 ± 0.04	···	···
PTF10xyt	1.08 ± 0.03	0.22 ± 0.03	18.44 ± 0.04
PTF10yer	0.75 ± 0.06	···	···
PTF10ygu	1.01 ± 0.02	0.44 ± 0.03	17.27 ± 0.04
PTF10yux	0.84 ± 0.01	0.17 ± 0.02	18.52 ± 0.04
PTF10yyt	0.93 ± 0.03	···	···
PTF10zai	1.06 ± 0.04	···	···
PTF10zak	0.81 ± 0.04	···	···
PTF10zbk	0.78 ± 0.03	0.11 ± 0.06	19.28 ± 0.11
PTF10zdk	1.14 ± 0.01	0.06 ± 0.02	16.96 ± 0.04
PTF10zgy	1.16 ± 0.04	0.15 ± 0.03	18.00 ± 0.06
PTF11apk	0.75 ± 0.04	0.21 ± 0.04	18.32 ± 0.05
PTF11atu	0.81 ± 0.04	-0.06 ± 0.04	18.62 ± 0.10
PTF11bas	0.96 ± 0.02	0.06 ± 0.01	18.92 ± 0.02
PTF11bju	1.15 ± 0.01	0.02 ± 0.01	16.62 ± 0.01
PTF11blu	1.10 ± 0.02	···	···
PTF11bqc	1.00 ± 0.03	···	···
PTF11bui	1.10 ± 0.01	0.02 ± 0.02	16.51 ± 0.02
PTF11byi	1.18 ± 0.03	···	···
PTF11ctn	1.17 ± 0.11	···	···
PTF11deg	0.96 ± 0.04	···	···
PTF11dhq	1.24 ± 0.08	···	···
PTF11dva	0.96 ± 0.03	···	···
PTF11dxu	1.15 ± 0.04	0.01 ± 0.01	15.71 ± 0.02
PTF11dzm	0.86 ± 0.01	···	···

PTF11gdh	1.01 ± 0.03	···	···
PTF11htb	1.06 ± 0.02	0.01 ± 0.02	17.37 ± 0.04
PTF11hub	0.80 ± 0.01	···	···
PTF11kfk	0.82 ± 0.02	···	···
PTF11khk	0.59 ± 0.02	0.41 ± 0.04	17.97 ± 0.06
PTF11kjn	0.62 ± 0.01	0.28 ± 0.02	17.31 ± 0.03
PTF11klo	1.13 ± 0.06	···	···
PTF11kly	0.95 ± 0.01	0.06 ± 0.00	10.11 ± 0.01
PTF11kx	1.04 ± 0.02	···	···
PTF11lih	0.89 ± 0.01	0.10 ± 0.02	18.97 ± 0.03
PTF11lmz	0.75 ± 0.10	···	···
PTF11mty	1.05 ± 0.03	0.03 ± 0.03	18.44 ± 0.04
PTF11okh	0.53 ± 0.01	0.56 ± 0.03	18.17 ± 0.06
PTF11opu	1.34 ± 0.03	0.02 ± 0.03	19.39 ± 0.05
PTF11pfm	0.98 ± 0.21	···	···
PTF11qmo	1.09 ± 0.06	···	···
PTF11qpc	1.12 ± 0.08	···	···
PTF11tl	0.89 ± 0.04	···	···
PTF11v	0.78 ± 0.01	-0.00 ± 0.03	17.05 ± 0.04
PTF11vl	1.19 ± 0.58	-0.07 ± 0.15	17.15 ± 0.34
PTF11wv	0.97 ± 0.02	-0.13 ± 0.03	18.79 ± 0.03
PTF12awi	1.03 ± 0.12	···	···
PTF12cjg	0.94 ± 0.07	···	···
PTF12dco	1.14 ± 0.06	···	···
PTF12dhb	1.15 ± 0.03	···	···
PTF12dhl	0.82 ± 0.03	···	···
PTF12dwm	0.84 ± 0.03	···	···
PTF12dxm	0.83 ± 0.02	···	···
PTF12fsd	0.95 ± 0.03	···	···
PTF12ggb	0.87 ± 0.02	···	···
PTF12giy	1.08 ± 0.02	···	···
PTF12gkn	1.10 ± 0.01	···	···

PTF12mj	1.22 ± 0.03	···	···

Table A.5: The SN spectral measurements in this thesis.

	Si II λ6355		Ca II NIR (PVF)		Ca II NIR (HVF)	
SN name	velocity ($km\,s^{-1}$)	pEW (Å)	velocity ($km\,s^{-1}$)	pEW (Å)	velocity ($km\,s^{-1}$)	pEW (Å)
PTF09a	10445(26)	86(0.8)	...	...	...	...
PTF09dhx	11031(35)	99(0.8)	11258(300)	94(7.8)	16132(956)	30(6.6)
PTF09djc	12752(18)	167(1.0)	10937(247)	173(7.7)	22404(1322)	16(14.5)
PTF09dlc	10405(10)	87(1.2)	10286(41)	66(0.9)	20787(27)	97(1.2)
PTF09dnl	10796(3)	93(0.4)	10818(31)	119(0.6)	19449(125)	55(1.5)
PTF09dnp	11505(3)	86(0.4)	11328(52)	71(0.7)	18582(112)	12(0.9)
PTF09dsy	11057(12)	180(0.6)	8729(134)	158(3.9)	19213(2578)	10(10.0)
PTF09dxo	10649(10)	108(0.5)	...	...	...	...
PTF09fox	11603(13)	97(1.0)	...	...	...	...
PTF09foz	10079(5)	96(1.2)	...	...	...	...
PTF09gce	11425(17)	79(0.5)	...	...	...	...
PTF09gul	11086(35)	43(0.8)	...	...	...	...
PTF09qn	11442(9)	130(0.8)	10827(8)	132(0.5)	19476(17)	66(0.8)
PTF09s	8875(12)	73(0.6)	9169(80)	54(2.1)	16437(59)	24(0.6)
PTF10abjv	10527(24)	39(0.7)	...	...	...	...
PTF10bjs	14712(2)	67(0.1)	14554(16)	77(0.8)	22305(507)	5(0.9)
PTF10cko	11135(15)	143(0.6)	10615(1114)	115(27.2)	19340(69)	134(8.7)
PTF10cwm	10392(16)	108(1.7)	...	...	...	...
PTF10cxk	10684(12)	122(0.7)	10611(66)	128(2.6)	17494(12)	25(0.5)
PTF10duy	9468(13)	53(0.6)	10006(28)	24(0.5)	19385(35)	56(0.6)
PTF10duz	11328(34)	125(1.8)	11012(900)	154(29.4)	21270(3275)	65(31.4)
PTF10elk	9760(17)	99(1.0)	9563(827)	112(12.0)	17582(1097)	32(16.3)
PTF10fj	10649(14)	156(0.9)	8922(217)	163(10.1)	14727(608)	109(14.3)
PTF10fxl	11106(13)	108(0.8)	11373(583)	125(13.8)	18184(1028)	31(15.2)
PTF10fyl	10291(8)	94(0.4)	10007(231)	109(5.9)	20241(1445)	56(12.3)
PTF10fym	10260(43)	165(1.9)	8077(347)	182(31.1)	20455(2887)	71(44.6)
PTF10glo	10939(29)	87(1.2)	...	...	...	...
PTF10gmg	11925(22)	56(1.0)	...	...	...	...

PTF10gmj	11004(21)	76(1.5)	···	···	···	···
PTF10gnj	10816(13)	29(0.8)	···	···	···	···
PTF10goo	10557(33)	68(2.3)	···	···	···	···
PTF10goq	10837(84)	84(2.5)	···	···	···	···
PTF10got	11526(83)	53(2.7)	···	···	···	···
PTF10gqi	11070(7)	88(0.7)	10696(193)	73(2.7)	17706(579)	29(2.4)
PTF10gvl	11413(18)	138(1.1)	9935(284)	103(12.0)	15793(997)	67(20.7)
PTF10hld	13238(34)	73(0.3)	12659(158)	43(2.3)	19441(766)	15(5.2)
PTF10hmc	9911(76)	40(1.5)	···	···	···	···
PTF10hmv	10208(10)	51(0.8)	···	···	···	···
PTF10icb	10439(4)	94(0.5)	10676(14)	111(0.3)	18373(28)	49(0.4)
PTF10jtp	10304(12)	91(1.9)	10856(24)	48(4.6)	16069(2284)	7(11.4)
PTF10lot	12585(10)	173(0.7)	11214(485)	174(15.4)	18698(1024)	105(35.9)
PTF10lya	9017(148)	36(0.8)	···	···	···	···
PTF10mtd	11026(13)	70(1.0)	···	···	···	···
PTF10mwb	9711(4)	119(0.6)	8369(450)	126(11.8)	18970(1135)	25(12.2)
PTF10ncu	10330(16)	168(0.9)	···	···	···	···
PTF10nlg	12570(21)	90(0.6)	···	···	···	···
PTF10nvh	10549(8)	113(0.4)	···	···	···	···
PTF10otc	9932(59)	56(1.1)	···	···	···	···
PTF10pvi	11106(41)	96(2.8)	11171(394)	113(7.7)	17733(9)	22(1.2)
PTF10px	10048(15)	135(0.7)	8405(504)	134(19.0)	18410(3642)	76(33.0)
PTF10qfo	10818(19)	85(0.8)	···	···	···	···
PTF10qhp	11341(24)	140(1.2)	8948(416)	113(10.8)	21330(1403)	31(7.8)
PTF10qjl	10903(4)	75(0.9)	10122(665)	54(8.0)	19771(784)	66(19.3)
PTF10qjq	10717(5)	65(0.2)	10105(162)	54(2.3)	18895(1422)	9(3.3)
PTF10qkf	9854(61)	52(1.4)	···	···	···	···
PTF10qkv	9952(30)	80(1.2)	···	···	···	···
PTF10qky	10274(11)	76(1.3)	10455(393)	70(23.3)	20640(672)	62(9.2)
PTF10qny	11475(5)	36(0.5)	12165(23)	42(0.5)	19320(104)	14(0.9)
PTF10qsc	10336(14)	58(0.4)	10264(211)	50(5.7)	19620(621)	70(6.6)
PTF10qwg	12737(16)	100(0.6)	···	···	···	···
PTF10qyx	10117(39)	140(2.3)	9146(293)	154(11.9)	18473(710)	45(11.0)

PTF10rab	10956(90)	78(3.0)	9939(1341)	89(25.8)	20455(471)	162(21.7)
PTF10rhi	10971(27)	58(1.2)	...	...	...	...
PTF10rks	10844(13)	87(0.4)	8804(1068)	37(9.3)	21391(212)	10(0.9)
PTF10tce	12187(8)	107(0.8)	12469(206)	143(7.6)	20295(572)	46(8.9)
PTF10tqy	11315(14)	124(0.6)	11798(40)	178(1.1)	18905(44)	15(0.5)
PTF10trs	11045(6)	103(1.1)	11082(184)	92(1.6)	19050(113)	5(0.8)
PTF10tum	9718(15)	124(0.5)	9313(140)	108(3.6)	19120(250)	84(6.3)
PTF10twd	11369(20)	58(1.2)	...	...	...	...
PTF10ucl	10305(14)	90(1.4)	...	...	...	...
PTF10ufj	9842(11)	91(1.0)	9220(1458)	158(37.2)	20842(672)	69(12.6)
PTF10vfo	12254(61)	106(2.3)	...	...	...	...
PTF10viq	12380(9)	61(0.5)	13094(64)	60(2.1)	21196(1143)	31(5.6)
PTF10vnu	10078(11)	102(1.5)	...	...	...	...
PTF10wnm	10820(15)	74(1.0)	...	...	...	...
PTF10wnq	11429(51)	90(1.7)	...	...	...	...
PTF10wof	12111(6)	130(0.6)	11211(272)	117(5.8)	18187(534)	56(10.6)
PTF10wor	11045(14)	166(0.7)	8582(79)	158(6.6)	18091(1333)	34(31.2)
PTF10xir	10471(23)	93(0.8)	...	...	...	...
PTF10xyl	10685(12)	82(0.5)	...	...	...	...
PTF10xyt	12306(78)	75(2.0)	...	...	...	...
PTF10ygu	15273(10)	152(0.4)	14724(285)	153(6.0)	21214(62)	71(4.7)
PTF10yux	11665(19)	143(1.3)	9108(390)	119(8.7)	17251(4944)	...
PTF10yyt	10237(47)	117(0.9)	9713(115)	89(2.8)	17183(562)	20(6.0)
PTF10zai	8918(29)	54(0.9)	9631(15)	38(0.3)	17596(29)	33(0.4)
PTF10zak	11644(12)	131(0.6)	10957(120)	137(10.7)	18574(170)	49(3.2)
PTF10zgy	10849(46)	53(0.9)	...	...	...	...
PTF11apk	10115(13)	146(0.7)	8727(449)	182(15.5)	18495(2049)	50(20.8)
PTF11blu	10226(35)	91(2.0)	...	...	...	...
PTF11bqc	14286(44)	49(0.6)	...	...	...	...
PTF11bui	13898(46)	76(1.1)	13808(788)	63(9.5)	19967(892)	16(8.4)
PTF11byi	8475(13)	104(0.8)	...	...	...	...
PTF11ctn	9893(8)	43(0.9)	8675(220)	34(3.2)	20485(238)	25(5.1)
PTF11deg	11825(47)	148(2.1)	...	...	...	...

PTF11dhq	9739(56)	52(1.7)	···	···	···	···
PTF11dva	10071(16)	68(0.9)	···	···	···	···
PTF11dxu	10540(15)	48(0.7)	9699(119)	34(1.1)	19929(29)	46(1.1)
PTF11dzm	11008(52)	135(2.3)	10445(29)	130(1.6)	20207(923)	22(1.8)
PTF11gdh	9774(11)	18(0.3)	···	···	···	···
PTF11hub	11032(7)	121(0.3)	10440(15)	145(0.2)	19545(26)	54(0.2)
PTF11kfk	12207(48)	182(2.7)	10182(28)	164(1.0)	18020(55)	81(1.3)
PTF11khk	8980(9)	125(0.7)	···	···	···	···
PTF11klo	10247(17)	89(0.4)	···	···	···	···
PTF11kly	10317(27)	88(2.0)	···	···	···	···
PTF11kx	10826(36)	27(1.3)	···	···	···	···
PTF11lmz	13507(19)	104(0.5)	···	···	···	···
PTF11opu	9712(53)	73(1.4)	···	···	···	···
PTF11qmo	10112(5)	84(0.3)	10674(93)	110(18.5)	18294(1492)	75(22.5)
PTF11qpc	10494(24)	63(1.3)	10093(108)	29(4.9)	18137(966)	48(13.7)
PTF11tl	10196(78)	23(0.6)	···	···	···	···
PTF11v	12270(14)	133(0.7)	···	···	···	···
PTF12awi	9451(56)	44(1.4)	···	···	···	···
PTF12cjg	10773(20)	101(0.9)	10354(250)	88(7.7)	17317(1177)	19(15.7)
PTF12dco	13074(7)	109(0.9)	···	···	···	···
PTF12dhb	10521(26)	136(2.3)	9743(324)	60(5.0)	20459(2219)	64(9.6)
PTF12dhl	10200(49)	53(0.9)	···	···	···	···
PTF12dwm	9440(8)	78(0.4)	9008(881)	53(14.4)	15945(526)	21(12.3)
PTF12dxm	10251(9)	145(0.6)	···	···	···	···
PTF12fsd	10704(24)	83(1.5)	···	···	···	···
PTF12ggb	9643(39)	117(1.8)	···	···	···	···
PTF12giy	11558(92)	159(3.6)	10365(2109)	200(54.4)	20713(836)	81(18.7)
PTF12gkn	10401(6)	32(0.5)	···	···	···	···
PTF12mj	10157(14)	18(0.7)	···	···	···	···

Bibliography

Amanullah R., Goobar A., 2011, ApJ, 735, 20

Anderson J. P., Habergham S. M., James P. A., Hamuy M., 2012, MNRAS, 424, 1372

Anderson J. P., James P. A., 2008, MNRAS, 390, 1527

Arnett W. D., 1969, AP&SS, 5, 180

Arnett W. D., 1979, ApJ, 230, L37

Arnett W. D., 1982, ApJ, 253, 785

Bailey S. J. et al., 2009, in Bulletin of the American Astronomical Society, Vol. 41, American Astronomical Society Meeting Abstracts #213, p. 321.05

Baldry I. K. et al., 2012, MNRAS, 421, 621

Baldwin J. A., Phillips M. M., Terlevich R., 1981, PASP, 93, 5

Benetti S. et al., 2005, ApJ, 623, 1011

Bernstein J. P. et al., 2012, ApJ, 753, 152

Bertin E., Arnouts S., 1996, A&AS, 117, 393

Betoule M. et al., 2014, ArXiv e-prints

Betoule M. et al., 2013, A&A, 552, A124

Blondin S., Mandel K. S., Kirshner R. P., 2011, A&A, 526, A81

Bloom J. S. et al., 2012a, ApJ, 744, L17

Bloom J. S. et al., 2012b, PASP, 124, 1175

Branch D., Tammann G. A., 1992, ARA&A, 30, 359

Bravo E., Badenes C., 2011, MNRAS, 414, 1592

Brinchmann J., Charlot S., White S. D. M., Tremonti C., Kauffmann G., Heckman T., Brinkmann J., 2004, MNRAS, 351, 1151

Bronder T. J. et al., 2008, A&A, 477, 717

Brown T. M. et al., 2013, ArXiv e-prints

Calzetti D., 1997, in American Institute of Physics Conference Series, Vol. 408, American Institute of Physics Conference Series, Waller W. H., ed., pp. 403–412

Cappellari M., Emsellem E., 2004, PASP, 116, 138

Cardelli J. A., Clayton G. C., Mathis J. S., 1989, ApJ, 345, 245

Cenko S. B. et al., 2006, PASP, 118, 1396

Childress M. et al., 2013a, ApJ, 770, 108

Childress M. J. et al., 2013b, ArXiv e-prints

Childress M. J., Filippenko A. V., Ganeshalingam M., Schmidt B. P., 2014, MNRAS, 437, 338

Childress M. J. et al., 2013c, ApJ, 770, 29

Cid Fernandes R., Mateus A., Sodré L., Stasińska G., Gomes J. M., 2005, MNRAS, 358, 363

Colgate S. A., McKee C., 1969, ApJ, 157, 623

Conley A. et al., 2011, ApJS, 192, 1

Conley A. et al., 2008, ApJ, 681, 482

Cooper M. C., Newman J. A., Yan R., 2009, ApJ, 704, 687

Dalton G. et al., 2012, in Society of Photo-Optical Instrumentation Engineers (SPIE) Conference Series, Vol. 8446, Society of Photo-Optical Instrumentation Engineers (SPIE) Conference Series

D'Andrea C. B. et al., 2011, ApJ, 743, 172

de Jong R. S. et al., 2012, in Society of Photo-Optical Instrumentation Engineers (SPIE) Conference Series, Vol. 8446, Society of Photo-Optical Instrumentation Engineers (SPIE) Conference Series

Dilday B. et al., 2012, Science, 337, 942

Domínguez I., Höflich P., Straniero O., 2001, ApJ, 557, 279

Drory N. et al., 2009, ApJ, 707, 1595

Ellis R. S. et al., 2008, ApJ, 674, 51

Filippenko A. V., 1997, ARA&A, 35, 309

Filippenko A. V. et al., 1992a, AJ, 104, 1543

Filippenko A. V. et al., 1992b, ApJ, 384, L15

Fioc M., Rocca-Volmerange B., 1997, A&A, 326, 950

Foley R. J., 2012, ApJ, 748, 127

Foley R. J., 2013, MNRAS, 435, 273

Foley R. J. et al., 2008, ApJ, 684, 68

Foley R. J. et al., 2012a, AJ, 143, 113

Foley R. J. et al., 2012b, ApJ, 752, 101

Foster C. et al., 2012, A&A, 547, A79

Gallagher J. S., Garnavich P. M., Berlind P., Challis P., Jha S., Kirshner R. P., 2005, ApJ, 634, 210

Gallagher J. S., Garnavich P. M., Caldwell N., Kirshner R. P., Jha S. W., Li W., Ganeshalingam M., Filippenko A. V., 2008, ApJ, 685, 752

Gallazzi A., Charlot S., Brinchmann J., White S. D. M., Tremonti C. A., 2005, MNRAS, 362, 41

Gerardy C. L. et al., 2004, ApJ, 607, 391

Goobar A., 2008, ApJ, 686, L103

Gupta R. R. et al., 2011, ApJ, 740, 92

Guy J. et al., 2007, A&A, 466, 11

Guy J. et al., 2010, A&A, 523, A7

Guzman R., Gallego J., Koo D. C., Phillips A. C., Lowenthal J. D., Faber S. M., Illingworth G. D., Vogt N. P., 1997, ApJ, 489, 559

Hakobyan A. A., Mamon G. A., Petrosian A. R., Kunth D., Turatto M., 2009, A&A, 508, 1259

Hamuy M., Trager S. C., Pinto P. A., Phillips M. M., Schommer R. A., Ivanov V., Suntzeff N. B., 2000, AJ, 120, 1479

Hamuy M., et al., 1995, AJ, 109, 1

Hamuy M., et al., 1996, AJ, 112, 2391

Hayden B. T., Gupta R. R., Garnavich P. M., Mannucci F., Nichol R. C., Sako M., 2013, ApJ, 764, 191

Henry R. B. C., Worthey G., 1999, PASP, 111, 919

Hillebrandt W., Kromer M., Röpke F. K., Ruiter A. J., 2013, Frontiers of Physics, 8, 116

Hillebrandt W., Niemeyer J. C., 2000, ARA&A, 38, 191

Hoeflich P., Khokhlov A., Wheeler J. C., Phillips M. M., Suntzeff N. B., Hamuy M., 1996, ApJ, 472, L81

Hoeflich P., Wheeler J. C., Thielemann F. K., 1998, ApJ, 495, 617

Homeier D., Koester D., Hagen H.-J., Jordan S., Heber U., Engels D., Reimers D., Dreizler S., 1998, A&A, 338, 563

Hook I. M., Jørgensen I., Allington-Smith J. R., Davies R. L., Metcalfe N., Murowinski R. G., Crampton D., 2004, PASP, 116, 425

Hook I. M., McMahon R. G., Boyle B. J., Irwin M. J., 1994, MNRAS, 268, 305

Howell D. A., 2001, ApJ, 554, L193

Howell D. A. et al., 2009, ApJ, 691, 661

Hoyle F., Fowler W. A., 1960, ApJ, 132, 565

Hubble E. P., 1926, ApJ, 64, 321

Huterer D., Turner M. S., 1999, Phys. Rev. D, 60, 081301

Iben, Jr. I., Tutukov A. V., 1984, ApJS, 54, 335

Ivezić Ž. et al., 2007, AJ, 134, 973

Ivezic Z. et al., 2008, ArXiv e-prints

Jha S., Riess A. G., Kirshner R. P., 2007, ApJ, 659, 122

Johansson J. et al., 2013, MNRAS, 435, 1680

Kahabka P., Ergma E., 1997, A&A, 318, 108

Kauffmann G. et al., 2003, MNRAS, 346, 1055

Kelly B. C., 2007, ApJ, 665, 1489

Kelly P. L., Hicken M., Burke D. L., Mandel K. S., Kirshner R. P., 2010, ApJ, 715, 743

Kennicutt J. R. C., 1998, ARA&A, 36, 189

Kessler R. et al., 2009, ApJS, 185, 32

Kewley L. J., Dopita M. A., 2002, ApJS, 142, 35

Kewley L. J., Dopita M. A., Sutherland R. S., Heisler C. A., Trevena J., 2001, ApJ, 556, 121

Kewley L. J., Ellison S. L., 2008, ApJ, 681, 1183

Kimura M. et al., 2010, PASJ, 62, 1135

Kistler M. D., Stanek K. Z., Kochanek C. S., Prieto J. L., Thompson T. A., 2011, ArXiv e-prints

Kobayashi C., Nomoto K., 2009, ApJ, 707, 1466

Kobayashi C., Tsujimoto T., Nomoto K., Hachisu I., Kato M., 1998, ApJ, 503, L155

Kobulnicky H. A., Kewley L. J., 2004, ApJ, 617, 240

Koleva M., Prugniel P., Bouchard A., Wu Y., 2009, A&A, 501, 1269

Kroupa P., 2001, MNRAS, 322, 231

Lamareille F., Contini T., Le Borgne J.-F., Brinchmann J., Charlot S., Richard J., 2006, A&A, 448, 893

Lampeitl H. et al., 2010, ApJ, 722, 566

Law N. M. et al., 2009, PASP, 121, 1395

Le Borgne D., Rocca-Volmerange B., 2002, A&A, 386, 446

Le Fèvre O. et al., 2003, in Society of Photo-Optical Instrumentation Engineers (SPIE) Conference Series, Vol. 4841, Instrument Design and Performance for Optical/Infrared Ground-based Telescopes, Iye M., Moorwood A. F. M., eds., pp. 1670–1681

Leibundgut B. et al., 1993, AJ, 105, 301

Lentz E. J., Baron E., Branch D., Hauschildt P. H., Nugent P. E., 2000, ApJ, 530, 966

Li W. D., Filippenko A. V., Riess A. G., Treffers R. R., Hu J. Y., Qiu Y. L., 2000, in American Institute of Physics Conference Series, Vol. 522, American Institute of Physics Conference Series, Holt S. S., Zhang W. W., eds., pp. 91–94

Maguire K. et al., 2012, MNRAS, 426, 2359

Maguire K. et al., 2013a, MNRAS, 436, 222

Maguire K. et al., 2013b, ArXiv e-prints

Maguire K. et al., 2011, MNRAS, 418, 747

Mannucci F., Cresci G., Maiolino R., Marconi A., Gnerucci A., 2010, MNRAS, 408, 2115

Mannucci F., Della Valle M., Panagia N., 2006, MNRAS, 370, 773

Mannucci F., Della Valle M., Panagia N., Cappellaro E., Cresci G., Maiolino R., Petrosian A., Turatto M., 2005, A&A, 433, 807

Mannucci F., Salvaterra R., Campisi M. A., 2011, MNRAS, 414, 1263

Maoz D., Mannucci F., 2012, PASA, 29, 447

Maoz D., Mannucci F., Nelemans G., 2013, ArXiv e-prints

Maraston C., 2005, MNRAS, 362, 799

Markwardt C. B., 2009, in Astronomical Society of the Pacific Conference Series, Vol. 411, Astronomical Data Analysis Software and Systems XVIII, Bohlender D. A., Durand D., Dowler P., eds., p. 251

Mazzali P. et al., 2013, ArXiv e-prints

Mazzali P. A. et al., 2005a, ApJ, 623, L37

Mazzali P. A., Benetti S., Stehle M., Branch D., Deng J., Maeda K., Nomoto K., Hamuy M., 2005b, MNRAS, 357, 200

McGaugh S. S., 1991, ApJ, 380, 140

Miller C. J., Nichol R. C., Gómez P. L., Hopkins A. M., Bernardi M., 2003, ApJ, 597, 142

Miller J. S., Stone R. P. S., 1993, Lick Obs. Tech. Rep., No. 66

Minkowski R., 1941, PASP, 53, 224

Neill J. D. et al., 2009, ApJ, 707, 1449

Nomoto K., 1982, ApJ, 253, 798

Nomoto K., Iben, Jr. I., 1985, ApJ, 297, 531

Nomoto K., Nariai K., Sugimoto D., 1979, PASJ, 31, 287

Nugent P., Phillips M., Baron E., Branch D., Hauschildt P., 1995, ApJ, 455, L147+

Nugent P. E. et al., 2011, Nature, 480, 344

Oke J. B. et al., 1995, PASP, 107, 375

Osterbrock D. E., 1989, Astrophysics of gaseous nebulae and active galactic nuclei

Pan Y.-C. et al., 2014, MNRAS, 438, 1391

Patat F. et al., 2007, Science, 317, 924

Perlmutter S. et al., 1999, ApJ, 517, 565

Perrett K. et al., 2010, AJ, 140, 518

Pettini M., Pagel B. E. J., 2004, MNRAS, 348, L59

Phillips M. M., 1993, ApJ, 413, L105

Phillips M. M., Lira P., Suntzeff N. B., Schommer R. A., Hamuy M., Maza J., 1999, AJ, 118, 1766

Phillips M. M., Wells L. A., Suntzeff N. B., Hamuy M., Leibundgut B., Kirshner R. P., Foltz C. B., 1992, AJ, 103, 1632

Press W. H., Teukolsky S. A., Vetterling W. T., Flannery B. P., 1992, Numerical recipes in FORTRAN. The art of scientific computing

Rahmer G., Smith R., Velur V., Hale D., Law N., Bui K., Petrie H., Dekany R., 2008, in Society of Photo-Optical Instrumentation Engineers (SPIE) Conference Series, Vol. 7014, Society of Photo-Optical Instrumentation Engineers (SPIE) Conference Series

Rau A. et al., 2009, PASP, 121, 1334

Rest A. et al., 2013, ArXiv e-prints

Riess A. G. et al., 1998, AJ, 116, 1009

Riess A. G. et al., 1999, AJ, 117, 707

Riess A. G., Press W. H., Kirshner R. P., 1996, ApJ, 473, 88

Riess A. G. et al., 2007, ApJ, 659, 98

Rigault M. et al., 2013, ArXiv e-prints

Salpeter E. E., 1955, ApJ, 121, 161

Sánchez-Blázquez P. et al., 2006, MNRAS, 371, 703

Sarzi M. et al., 2006, MNRAS, 366, 1151

Savaglio S. et al., 2005, ApJ, 635, 260

Schaefer B. E., Pagnotta A., 2012, Nature, 481, 164

Schlafly E. F., Finkbeiner D. P., 2011, ApJ, 737, 103

Shaw R. L., 1979, A&A, 76, 188

Silverman J. M., Ganeshalingam M., Li W., Filippenko A. V., 2012a, MNRAS, 425, 1889

Silverman J. M., Kong J. J., Filippenko A. V., 2012b, MNRAS, 425, 1819

Smith A. M. et al., 2011, MNRAS, 412, 1309

Smith J. A. et al., 2002, AJ, 123, 2121

Smith M. et al., 2012, ApJ, 755, 61

Stanishev V., Rodrigues M., Mourão A., Flores H., 2012, A&A, 545, A58

Steele I. A. et al., 2004, in Society of Photo-Optical Instrumentation Engineers (SPIE) Conference Series, Vol. 5489, Society of Photo-Optical Instrumentation Engineers (SPIE) Conference Series, Oschmann Jr. J. M., ed., pp. 679–692

Sternberg A. et al., 2011, Science, 333, 856

Strateva I. et al., 2001, AJ, 122, 1861

Sullivan M. et al., 2010, MNRAS, 406, 782

Sullivan M. et al., 2011a, ApJ, 732, 118

Sullivan M., et al., 2006, ApJ, 648, 868

Sullivan M., et al., 2011b, ApJ, 737, 102

Suzuki N., et al., 2012, ApJ, 746, 85

Tanaka M., Mazzali P. A., Maeda K., Nomoto K., 2006, ApJ, 645, 470

Timmes F. X., Brown E. F., Truran J. W., 2003, ApJ, 590, L83

Trager S. C., Worthey G., Faber S. M., Burstein D., Gonzalez J. J., 1998, ApJS, 116, 1

Tremonti C. A. et al., 2004, ApJ, 613, 898

Tripp R., 1998, A&A, 331, 815

Tully R. B., Fisher J. R., 1977, A&A, 54, 661

Turatto M., 2003, in Lecture Notes in Physics, Berlin Springer Verlag, Vol. 598, Supernovae and Gamma-Ray Bursters, Weiler K., ed., pp. 21–36

Turatto M., Benetti S., Cappellaro E., Danziger I. J., Della Valle M., Gouiffes C., Mazzali P. A., Patat F., 1996, MNRAS, 283, 1

van den Heuvel E. P. J., Bhattacharya D., Nomoto K., Rappaport S. A., 1992, A&A, 262, 97

van Dokkum P. G., 2001, PASP, 113, 1420

Vazdekis A., Sánchez-Blázquez P., Falcón-Barroso J., Cenarro A. J., Beasley M. A., Cardiel N., Gorgas J., Peletier R. F., 2010, MNRAS, 404, 1639

Walker E. S. et al., 2011, MNRAS, 410, 1262

Wang L., 2005, ApJ, 635, L33

Wang L. et al., 2003, ApJ, 591, 1110

Wang X. et al., 2009, ApJ, 699, L139

Wang X., Wang L., Filippenko A. V., Zhang T., Zhao X., 2013, Science, 340, 170

Webbink R. F., 1984, ApJ, 277, 355

Wheeler J. C., Harkness R. P., 1990, Reports on Progress in Physics, 53, 1467

Whelan J., Iben, Jr. I., 1973, ApJ, 186, 1007

Woosley S. E., Weaver T. A., 1994, ApJ, 423, 371

Worthey G., 1994, ApJS, 95, 107

Yaron O., Gal-Yam A., 2012, PASP, 124, 668

York D. G. et al., 2000, AJ, 120, 1579

Yungelson L. R., 2005, in Astrophysics and Space Science Library, Vol. 332, White dwarfs: cosmological and galactic probes, Sion E. M., Vennes S., Shipman H. L., eds., pp. 163–173